AFRL-PR-WP-TR-2000-2064

PREDICTION AND MEASUREMENT OF HEAT TRANSFER IN A SWITCHED RELUCTANCE GENERATOR

EUGENE HIMES
DR. JOHN J. SCHAUER

UNIVERSITY OF DAYTON
MECHANICAL AND AEROSPACE ENGINEERING
300 COLLEGE PARK
DAYTON, OH 45469-0210

AUGUST 1998

FINAL REPORT FOR 01/01/1997 – 07/01/1998

APPROVED FOR PUBLIC RELEASE; DISTRIBUTION UNLIMITED

PROPULSION DIRECTORATE
AIR FORCE RESEARCH LABORATORY
AIR FORCE MATERIEL COMMAND
WRIGHT-PATTERSON AIR FORCE BASE OH 45433-7251

DTIC QUALITY INSPECTED 4

20000901 076

NOTICE

Using Government drawings, specifications, or other data included in this document for any purpose other than Government procurement does not in any way obligate the U.S. Government. The fact that the Government formulated or supplied the drawings, specifications, or other data does not license the holder or any other person or corporation; or convey any rights or permission to manufacture, use, or sell any patented invention that may relate to them.

This report is releasable to the National Technical Information Service (NTIS). At NTIS, it will be available to the general public, including foreign nations.

THIS TECHNICAL REPORT HAS BEEN REVIEWED AND IS APPROVED FOR PUBLICATION.

Edward B. Durkin

EDWARD B. DURKIN
Mechanical Engineer
Power Generation & Thermal Branch

Scott Rubertus

SCOTT RUBERTUS
Chief
Power Generation & Thermal Branch

FOR THE COMMANDER

Jerry E Beam 6/28/00

JERRY E. BEAM
Acting Chief, Power Division

Do not return copies of this report unless contractual obligations or notice on a specific document requires its return.

REPORT DOCUMENTATION PAGE

Form Approved
OMB No. 0704-0188

Public reporting burden for this collection of information is estimated to average 1 hour per response, including the time for reviewing instructions, searching existing data sources, gathering and maintaining the data needed, and completing and reviewing the collection of information. Send comments regarding this burden estimate or any other aspect of this collection of information, including suggestions for reducing this burden, to Washington Headquarters Services, Directorate for Information Operations and Reports, 1215 Jefferson Davis Highway, Suite 1204, Arlington, VA 22202-4302, and to the Office of Management and Budget, Paperwork Reduction Project (0704-0188), Washington, DC 20503.

1. AGENCY USE ONLY *(Leave blank)*

2. REPORT DATE
AUGUST 1998

3. REPORT TYPE AND DATES COVERED
FINAL REPORT FOR 01/01/1997 -07/01/1998

4. TITLE AND SUBTITLE
PREDICTION AND MEASUREMENT OF HEAT TRANSFER IN A SWITCHED RELUCTANCE GENERATOR

5. FUNDING NUMBERS
C F33615-94-C-2418
PE 62203
PR 3145
TA 01
WU C7

6. AUTHOR(S)
EUGENE HIMES
DR. JOHN J. SCHAUER

7. PERFORMING ORGANIZATION NAME(S) AND ADDRESS(ES)
UNIVERSITY OF DAYTON
MECHANICAL AND AEROSPACE ENGINEERING
300 COLLEGE PARK
DAYTON, OH 45469-0210

8. PERFORMING ORGANIZATION REPORT NUMBER

9. SPONSORING/MONITORING AGENCY NAME(S) AND ADDRESS(ES)
PROPULSION DIRECTORATE
AIR FORCE RESEARCH LABORATORY
AIR FORCE MATERIEL COMMAND
WRIGHT-PATTERSON AFB, OH 45433-7251
POC: ED DURKIN, AFRL/PRPG, 937-255-6241

10. SPONSORING/MONITORING AGENCY REPORT NUMBER
AFRL-PR-WP-TR-2000-2064

11. SUPPLEMENTARY NOTES

12a. DISTRIBUTION AVAILABILITY STATEMENT
APPROVED FOR PUBLIC RELEASE, DISTRIBUTION UNLIMITED.

12b. DISTRIBUTION CODE

13. ABSTRACT *(Maximum 200 words)*

The report is an experimental investigation of heat transfer convective film coefficients for a simulated high-speed electromachine rotor. The rotor geometry was matched to that of a switched-reluctance machine (SRM) for a USAF-funded integrated power unit (IPU) turbogenerator design, with an operating speed of 55 krpm. The experimental test of cooling a preheated rotor was achieved by convection to air that flowed axially through rotor pole gap cavities. The tests included a series of insulated rotors, with each rotor having a uniquely exposed (from insulation) rotor pole surface so to help determine the film coefficient for that specific surface. The coefficients for each surface, and the overall rotor surface film coefficient, were inferred by the cooling rates of the test rotors at given rotor speeds and axial airflow rates. The test rotors, with 4.3 in. maximum diameter, were operated at a speed range of 5--30 krpm, with an axial airflow range of 0.036--0.073 kg/sec. (Test rig limitations prevented higher rotor test speeds.) The resultant convective film coefficients are given in terms of Stanton and Nusselt numbers correlated to Reynolds number and velocity ratio of axial airspeed to rotor tip speed. Experimental variations from earlier analytical estimates were within 10--15%.

14. SUBJECT TERMS
Motor & Generators, Power Generation, Heat Transfer, Convection, Windage

15. NUMBER OF PAGES
218

16. PRICE CODE

17. SECURITY CLASSIFICATION OF REPORT
UNCLASSIFIED

18. SECURITY CLASSIFICATION OF THIS PAGE
UNCLASSIFIED

19. SECURITY CLASSIFICATION OF ABSTRACT
UNCLASSIFIED

20. LIMITATION OF ABSTRACT
SAR

TABLE OF CONTENTS

Chapter Page

1 Introduction 1
1.1 Problem Statement 1
1.2 Description of Integrated Power Unit 1
1.3 Rotor/Stator Geometry 4
1.4 Review of Previous Work 4
1.5 Technical Approach 6

2 Experimental Apparatus 10
2.1 General 10
2.2 Test Rotors 10
2.2.1 General 10
2.2.2 Rotor Core Material 14
2.2.3 Rotor Insulating Material 16
2.2.3.1 Formulation of Epoxy Insulation 18
2.2.3.2 Preparation and Casting of Rotor Cores 19
2.3 Rotor Thermal Test Rig 22
2.3.1 General 22
2.3.2 RTTR Components 22
2.4 Test Facility 29
2.4.1 General 29
2.4.2 Compressed Air Supply System 29
2.4.3 Purge Air Supply System 31
2.4.4 Axial Airflow Supply System 31

3 Experimental Methods and Measurements 32
3.1 Automatic Data Acquisition 32
3.2 Measurement of Physical Parameters 34
3.2.1 Air Temperature Measurements at Front and Rear Rotor Faces 34
3.2.2 Air Temperature Measurement in Rotor/Stator Gap 34
3.2.3 Bearing Temperature Measurement 35
3.4 Experimental Methods 37
3.4.1 Daily Experiment Preparation 37
3.4.2 Typical Data Collection 37
3.5 Test Matrix 41

4 Analysis 42
4.1 General 42

TABLE OF CONTENTS (Cont.)

4.2 Multi-lump Analysis of Rotors 42
4.3 Initial Conditions 44
4.4 Boundary Conditions 46
4.4.1 Convection from Front and Rear Rotor Faces 46
4.4.2 Shaft Temperature 47
4.5 Estimate of Convective Film Coefficient on Rotor 6 Peripheral Surface 49
4.5.1 Velocity Distribution 51
4.5.2 Temperature Distribution 55
4.5.3 Equations for Velocity and Temperature Distributions for Regions I through IV 59
4.5.4 Heat Transfer Analysis 60
4.6 Computer Model and Boundary Condition Verification Based on Rotor 6 Data 67
4.7 Estimate of Reference Temperatures for Rotors 1 through 5 70
4.7.1 Reference Temperature for Pole Face 1 70
4.7.2 Reference Temperature for Pole Faces 2, 3 and 4; Forced Axial Flow 77
4.7.3 Reference Temperature for Pole Faces 2, 3 and 4; No Forced Axial Flow 81

5 Results 85
5.1 General 85
5.2 Empirical Analysis of Results 87
5.3 Estimate of Temperature for use with Overall Film Coefficient 100
5.4 Discussion of Results 104

6 Conclusions and Recommendations 107
6.1 Conclusions 107
6.2 Recommendations for Further Study 108

Bibliography 111

Appendices

A. Material Properties Used in Analyses 113
B. Measurement of Thermophysical Properties of Epoxy with Glass Microspheres 116
C. Multi-Lump Analysis of the Rotors 127
D. Sensing Devices and Their Calibration 147
E. Analysis of Heat Conduction Through Thermocouple Wires 165
F. Calculation of Mass Flow Rate of Axial Airflow 179
G. Design Drawings 183
H. Measured Gap Spacing Between Rotor Pole Tip and Stator 192
I. Estimate of Time for Shaft Hub and Rotor Core to Reach Thermal Equilibrium 194
J. Experimental Validation of Using Forward Bearing Temperature as Shaft Temperature 196
K. MathcadTM Program Developed for High Speed, Wall-Driven Flow Analysis 199

LIST OF ILLUSTRATIONS

Figure Page

1 MEA-IPU Component Configuration (Adapted from [1]) 3
2 Isometric Sketch of Generator Assembly (Adapted from [1]) 3
3 Definition of Rotor Pole Faces Relative to Direction of Rotation 5
4 Photographs of Front and Rear of Rotor 1 12
5 Fabrication Drawing for Rotor 1 13
6 Photograph of Six Test Rotors Aligned in a Row 15
7 Photograph of Casting Epoxy Around Rotor Cores 21
8 Photograph of Rotor Thermal Test Rig (RTTR) 23
9 Photograph of Stator, Air Turbine and Installed Rotor 25
10 Photographs of IR Sensor Enclosure 27
11 Test Facility System Schematic 30
12 Thermocouple Installation for Measuring Gap Temperature 36
13 Rotor 3 Speed and Axial Airflow Data, Nominal 30,000 rpm and "Half" Axial Air Flow 39
14 Rotor 3 Temperature Data, Nominal 30,000 rpm and "Half" Axial Air Flow 40
15 Temperature Monitoring of Turbine Shaft Bearings 48
16 Velocity Distribution in Turbulent Wall Driven Flow 50
17 Static and Total Temperature Distribution in High Speed, Wall Driven Flow 64
18 Recovery Factor For High Speed, Wall Driven Flow 66
19 Predicted Value of Stanton Number as a Function of Re_{hg} for Wall Driven Flow 68
20 Control Volume in Gap Region Above Pole Face 1 71
21 Control Volume in Cavity Region, Forced Axial Flow 78
22 Control Volume in Cavity Region, No Forced Axial, Flow Induced by Pumping 82
23 Comparison of Measured and Predicted Core Temperature Versus Time for Rotor 1, 10,000 rpm, Full Axial Flow 86
24 Pole Face 1 (Rotor Tip) Stanton Number as a Function of Re_{hg} and V_{axial}/V_{tip} 89
25 Pole Face 1 (Rotor Tip) Nusselt Number as a Function of Re_{hg} and V_{axial}/V_{tip} 90
26 Pole Face 2 (Leeward Face) Stanton Number as a Function of Re_{HC} and V_{axial}/V_{tip} 91
27 Pole Face 2 (Leeward Face) Nusselt Number as a Function of Re_{HC} and V_{axial}/V_{tip} 92
28 Pole Face 3 (Cavity Trough) Stanton Number as a Function of Re_{HC} and V_{axial}/V_{tip} 93
29 Pole Face 3 (Cavity Trough) Nusselt Number as a Function of Re_{HC} and V_{axial}/V_{tip} 94
30 Pole Face 4 (Windward Face) Stanton Number as a Function of Re_{HC} and V_{axial}/V_{tip} 95
31 Pole Face 4 (Windward Face) Nusselt Number as a function of Re_{HC} and V_{axial}/V_{tip} 96
32 Overall and Individual Pole Surface Stanton Numbers 98
33 Overall and Individual Pole Surface Nusselt Numbers 99

LIST OF ILLUSTRATIONS (Cont.)

Figure Page

34 Overall Stanton Number as a function of Re_{HC} and V_{axial}/V_{tip} ... 101
35 Overall Nusselt Number as a Function of Re_{HC} and V_{axial}/V_{tip}... 102
36 Reference Temperature for Overall Heat Transfer Coefficient... 105
37 Comparison of Stanton Number for Face 1 (Pole Tip) Compared to Smooth Rotor ... 109
38 Specific Heat vs. Temperature for Epoxy with Glass Microspheres... 118
39 Predicted Temperature Distribution through Tin Epoxy Sample... 121
40 Epoxy Sample for Determination of Thermal Diffusivity (Not to Scale)... 123
41 Photograph of Epoxy Sample... 123
42 Estimate of Thermal Diffusivity of Epoxy With Glass Microspheres by Comparison of Experimental Data to Analytical Models... 125
43 Definition of Elements for Rotors 1-5 ... 129
44 Definition of Elements for Rotor 6... 130
45 One Dimensional Heat Transfer Through a Composite Wall and Electrical Analog (Adapted from [20])... 132
46 Thermal Resistance Between Abutting Elements... 133
47 Thermal Resistance Associated with Radial Heat Transfer... 134
48 Verification of Nulti-lump Analysis for Pure Radial Heat Flow in Rotor... 142
49 FE Model of Rotor 1 ... 144
50 Verification of Multi-lump Analysis for Rotor 1 ... 146
51 Typical Ice Bath for Thermocouple Reference Junctions (Adapted from [19]) ... 149
52 IR Sensor Calibration Test Specimen ... 155
53 IR Sensor Calibration Curve ... 158
54 Input 12 Differential Pressure Transducer Calibration Curve PX 163-120D5V; Nominal Range: -7.87 - 47.24 Inches Water Column... 161
55 Input 13 Differential Pressure Transducer Calibration Curve PX 162-027D5V; Nominal Range: 0 - 27.65 Inches Water Column... 162
56 Input 14 Differential Pressure Transducer Calibration Curve PX 164=010D5V; Nominal Range: 0 - 10 Inches Water Column ... 163
57 Input 15 Differential Pressure Transducer Calibration Curve PX 162-027D5V; Nominal Range: 0 - 27.65 Inches Water Column... 164
58 Thermocouple Installation for Measuring Gap Temperature... 167
59 Infinitesimal Thermodynamic System for Thermocouple Analysis... 170
60 Effect of Stator and Ambient Temperature on Thermocouple Bead Temperature Thermocouple Measuring Gap Temperature ... 178
61 Rotor Thermal Test Rig Assembly (Adapted from Tech Development, Inc., Dayton, Ohio... 184
62 Infrared Sensor Enclosure... 185
63 Rotor 1 Design Drawing (Adapted from Tech Development, Inc., Dayton, Ohio) 186
64 Rotor 2 Design Drawing (Adapted from Tech Development, Inc., Dayton, Ohio) 187
65 Rotor 3 Design Drawing (Adapted from Tech Development, Inc., Dayton, Ohio) 188
66 Rotor 4 Design Drawing (Adapted from Tech Development, Inc., Dayton, Ohio) 189
67 Rotor 5 Design Drawing (Adapted from Tech Development, Inc., Dayton, Ohio) 190
68 Rotor 6 Design Drawing (Adapted from Tech Development, Inc., Dayton, Ohio) 191

LIST OF ILLUSTRATIONS (Cont.)

Figure Page

69 Stator Locations for Rotor Pole Gap Measurements 192
70 Analysis of Thermal Resistance from Shaft to Forward Bearing 199

LIST OF TABLES

Table

Page

1 Features of Test Rotors 14
2 Formulation of Epoxy with Glass Microspheres 19
3 Inputs to DAS-TC/B Board 33
4 Test Matrix 41
5 Comparison of Experimental and Analytical Estimate of Film Coefficient for Rotor 6 69
6 Thermophysical Properties of Solids 114
7 Thermophysical Properties of Air as a Function of Temperature (SI units) 114
8 Thermophysical Properties of Air as a Function of Temperature (English units) 115
9 Infrared Sensor Specifications 152
10 Measured Gaps Between Rotor Poles and Stator Wall 193

NOMENCLATURE

A	Area, m^2 (ft^2)
APU	auxiliary power unit
AWG	American wire gage
Bi	Biot number, dimensionless $Bi \equiv \frac{h\,L_c}{k_{solid}}$
C_f	friction coefficient, dimensionless $C_f \equiv \frac{\tau_o}{1/2\,\rho\,V^2}$
C_N	Boundary layer re-start factor
C_p	constant pressure specific heat, J/Kg-K (Btu/lbm-°F)
C_v	constant volume specific heat, J/Kg-K (Btu/lbm-°F)
E	Energy, J (Btu)
Fo	Fourier Number, dimensionless $Fo \equiv \frac{\alpha\,t}{L_c^2}$
h	convective film coefficient, W/m^2-K $(Btu/hr\text{-}ft^2\text{-}F)$
i	specific enthalpy, J/kg (Btu/lbm)
h_g	gap height, m (ft)
H_c	cavity height, m (ft)
Hz	Hertz, 1 cycle/s
IPU	Integrated power unit

k	thermal conductivity, W/m-K (Btu/hr-ft-°F)
kw	kilowatts
L_c	characteristic length for calculation of Biot number
$\dot{m}$	mass flow rate, kg/s (lbm/s)
MEA	More electric aircraft
Nu	Nusselt Number, dimensionless $Nu \equiv \frac{h\,L_c}{k_{fluid}}$
Pe	Peclet number, dimensionless $Pe \equiv \frac{V\,L_c}{\alpha}$
Pr	Prandtl Number, dimensionless $\Pr \equiv \frac{\nu}{\alpha}$
Pr_t	turbulent Prandtl number, dimensionless $\Pr_t \equiv \frac{\varepsilon_M}{\varepsilon_H}$
$\dot{q}''$	heat flux rate, W/m^2 (Btu/hr-ft^2)
R	outside radius, m (ft)
r	radial position, m (ft)
r_c	recovery factor, dimensionless
Re	Reynolds Number, dimensionless
rpm	revolutions per minute
RTTR	Rotor Thermal Test Rig
St	Stanton Number, dimensionless $St \equiv \frac{h}{\rho\, c_p V}$
t	time, s
T	Temperature, K (F)

T_{aero}	aerodynamic heating term, K (F) $T_{aero} = r_c \frac{u_\infty^2}{2\,C_p}$
T_{aw}	adiabatic wall temperature, K (F)
T^*	stagnation temperature, K (F) $T^* = T + \frac{u^2}{2\,C_p}$
u	x-component of velocity, m/s (ft/s)
V	rotor tip speed, m/s (ft/s)
vDC	volts, direct current
α	thermal diffusivity, m^2/s (ft^2/s)
δ	boundary layer thickness
δ_1	boundary layer displacement thickness
δ_2	boundary layer momentum thickness
ε_H	eddy diffusivity for heat transfer, m^2/s (ft^2/s)
ε_M	eddy diffusivity for momentum, m^2/s (ft^2/s)
μ	dynamic viscosity, Pa-s (lbf-s/ft^2)
ν	kinematic viscosity, m^2/s (ft^2/s)
ρ	density, kg/m^3 (lbm/ft^3)
τ	shear stress, Pa (lbf/ft^2)
ω	angular velocity, rad/s

FOREWORD

The work documented in this report was performed by the University of Dayton between January 1997 and June 1998, for the Propulsion Directorate of the Air Force Research Laboratory, Wright-Patterson Air Force Base, Ohio. The effort was performed as Task 25 of DOD Contract F33615-94-C-2418, Scientific Research in Aerospace Power (SRP). Mr. Jeffrey A. Fox of University of Dayton Research Institute (UDRI) is the Program Manager of the Scientific Research Program.

Technical support and direction of this SRP Task was provided by Mr. Edward B. Durkin of AFRL/PRPG. Dr. John Schauer was the Task Principal Investigator and assisted by Gene Himes. The authors wishes to acknowledge the assistance of Mr. Micheal Morgan of the Power Division, Ms. Sheila Liskany, and Mr. Jeffrey Fox of UDRI, who provided the administrative support to make this work possible.

ABSTRACT

PREDICTION AND MEASUREMENT OF HEAT TRANSFER IN A SWITCHED RELUCTANCE GENERATOR

Himes, Jr., Marvin Eugene
University of Dayton, 1998

Advisor: Dr. John J. Schauer

This research is an experimental investigation of the convective film coefficients on the unique pole faces of a high speed rotor operating within a generator. The specific geometry studied is that of a switched reluctance generator under development by the United States Air Force for use on jet aircraft as an integrated power unit (IPU) to provide auxiliary and emergency power to the aircraft's electrical system. The generator consists of a four pole rotor, nominally 4.30 inches in diameter, housed within a stator assembly. The clearance gap between the rotor pole tip and the stator wall is nominally 0.020 inches. The rotor is designed to rotate at 55,000 rpm.

Rotor cooling is achieved by convection to air flowing axially through the rotor cavities. The convective film coefficient for each unique pole face, as well as an overall film coefficient for the four pole faces are inferred from the rate at which insulated test rotors cool when subjected to various rates of rotor rotational speed and axial airflows.

The high velocity of the rotor tips in close proximity to the stator wall results in aerodynamic heating of the air in the gap region. Convective film coefficients associated with high speed flow must be referenced to the adiabatic wall temperature to account for the effects of viscous heating. An estimate of the adiabatic wall temperature in the rotor gap region is developed analytically starting with the fundamental case of high-speed, wall-driven flow. These analytical results for wall-driven flow are verified experimentally using a smooth poled rotor. The analytically predicted film coefficients are within 10% of the experimental results.

Experiments are conducted for rotor speeds ranging from 5,000 to 30,000 rpm and axial airflows ranging from 0.036 to 0.073 kg/s (0.08 to 0.16 lbm/s). The convective film coefficients for each pole face as well as average values representing heat loss from the combined faces are presented in terms of Stanton and Nusselt numbers and correlated to two dimensionless parameters: Rotor Reynolds number and the ratio of axial velocity in the rotor cavities to the rotor pole tip speed. The correlations predict the experimental estimates of film coefficient within 15%.

ACKNOWLEDGMENTS

The author wishes to acknowledge the valuable direction provided by his Faculty Advisor, Dr. John J. Schauer. I would also like to express my appreciation to Tech Development, Inc., Dayton, Ohio, for the generous donation of the air turbine used in the experimental investigation. Messrs. Dennis Balster and Jim Brussel contributed significantly to the successful development and production of the test equipment.

The research was funded by the Aero Propulsion and Power Directorate of Wright Laboratory, Wright Patterson Air Force Base, Ohio under contract to the University of Dayton Research Institute (UDRI). Messrs. Eugene Hoffman and Ed Durkin of WL/POOS-1 were the technical monitors and provided helpful comments and suggestions.

I wish to thank the UDRI Aerospace Mechanics Division for their support during my research and academic studies. Mr. Blaine West, Head, and Mr. Mike Bouchard, Group Leader, generously provided access to the computers and facilities needed to complete this research. Ms. Linda Nianouris formatted and paginated this dissertation. However, the greatest resource afforded me by this Division was the daily interaction with the talented staff of engineers.

My deepest thanks go to my wife, Cynthia, for her love, encouragement and patience during the course of this research.

CHAPTER I

INTRODUCTION

1.1 Problem Statement

The subject of this research investigation is the experimental determination of the convective film coefficient on the pole faces of a four pole rotor rotating within a stator. The focus of the study is the specific rotor geometry associated with an integrated power unit (IPU) under development for the United States Air Force for application to jet aircraft. The investigation examines the film coefficients on the pole faces with and without axial air flow for multiple rotor speeds ranging from 5,000 to 30,000 rpm.

1.2 Description of Integrated Power Unit

The More-Electric Aircraft Integrated Power Unit (MEA-IPU) is a dual-use product which performs the combined operations of a conventional auxiliary power unit (APU) and emergency power unit (EPU) with one gas turbine. Its function is to provide power to an aircraft's 270 Vdc electrical bus. It is designed to provide a continuous power output of 125 kw as well as meet the intermittent demands of 250 kw for two minutes. It can be started for ground operations for performing ground checkout functions or rapidly started in flight to provide backup power in the event the engine generator fails or if a main engine flameout occurs[1].

The MEA-IPU is comprised of a switched reluctance generator mounted on a common shaft between the compressor discharge and the turbine and operates at speeds up to 55,000 rpm. The general component configuration of the IPU is presented in Figure 1. An isometric representation of the switched reluctance generator assembly illustrating its three primary components: rotor laminations, stator windings, and stator laminations is illustrated in Figure 2.

Heat is generated in the generator portion of the IPU by two modes. First, energy dissipation caused by viscous losses in the highly turbulent flow between the rotor poles and stator converts shaft power to heat. Second, generator component inefficiencies convert magnetic and electrical energy into heat.

The generator is cooled by the compressor discharge. While this heat addition to the core flow increases the internal energy of the air delivered to the turbine and has a net effect of reducing the amount of fuel required to power the IPU, increased temperatures negatively impact the performance of the generator. Thus, effective cooling of the rotor is a necessary concern in the many interrelationships involved in the design of the integrated system. The dominant mode of heat rejection from the generator rotor is convection from the rotor pole surfaces to the air discharge from the compressor. Therefore, characterizing the convective heat transfer on the faces of the rotor poles for the given rotor/stator geometry enables better modeling of the temperatures within the generator.

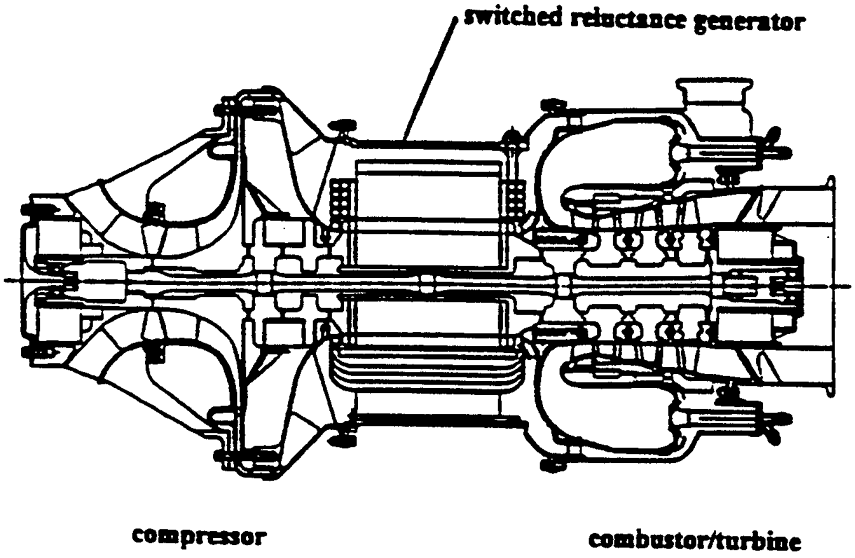
switched reluctance generator
compressor
combustor/turbine

Figure 1: MEA-IPU Component Configuration (Adapted from [1])

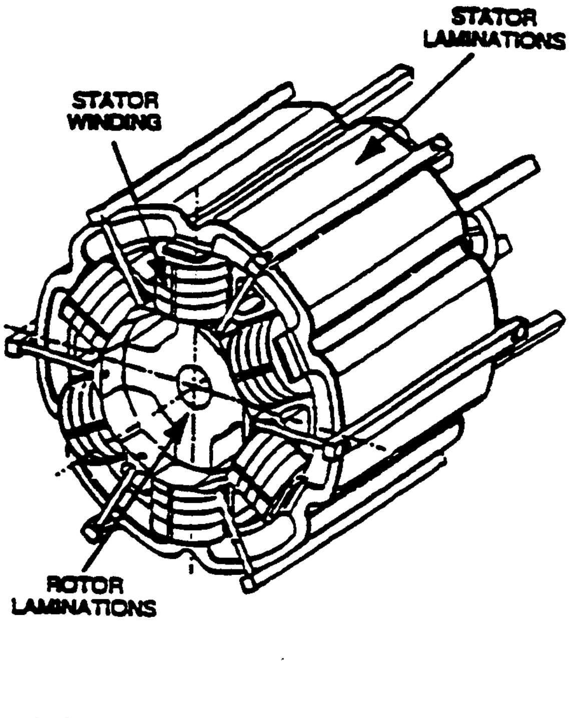
STATOR LAMINATIONS
STATOR WINDING
ROTOR LAMINATIONS

Figure 2: Isometric Sketch of Generator Assembly (Adapted from [1])

1.3 Rotor/Stator Geometry

A cross section of the specific rotor/stator geometry to be studied is shown in Figure 3. The outside diameter of the rotor poles is 4.30" with a cavity depth of 0.42". The nominal gap height between the rotor pole tip and stator wall is 0.020".

The rotor pole faces have been identified as faces 1 through 4 to establish their locations with respect to the rotational direction of the rotor. Face 1 is the pole tip area where significant shear forces occur associated with the large velocity gradient in the gap region. Face 2 is on the leeward face of the pole and will be in a wake region. Face 3 is the trough of the rotor. Face 4 is on the windward face of the pole.

1.4 Review of Previous Work

There have been significant theoretical and experimental investigations of heat transfer between concentric rotating cylinders. In 1958 Gazley[2] published results of experiments to measure the net heat transfer from a cylinder spinning inside a stator for two gap widths (0.017" and 0.24") with a nominal gap radius of 2.5". Both smooth and slotted rotor and stator surfaces were used. Tests were conducted with the inner cylinder rotating, 0 to 4,700 rpm, both with and without axial flow (axial velocities up to 300 ft/s). The experiments yielded data for the overall heat transfer associated with the inner and outer cylinders.

Hayase, Humphrey and Greif [3,4] present a numerical study for the flow and heat transfer in the space between a pair of coaxial cylinders with the outer cylinder fixed and the inner cylinder rotating. The papers investigate the cases where the inner cylinder has

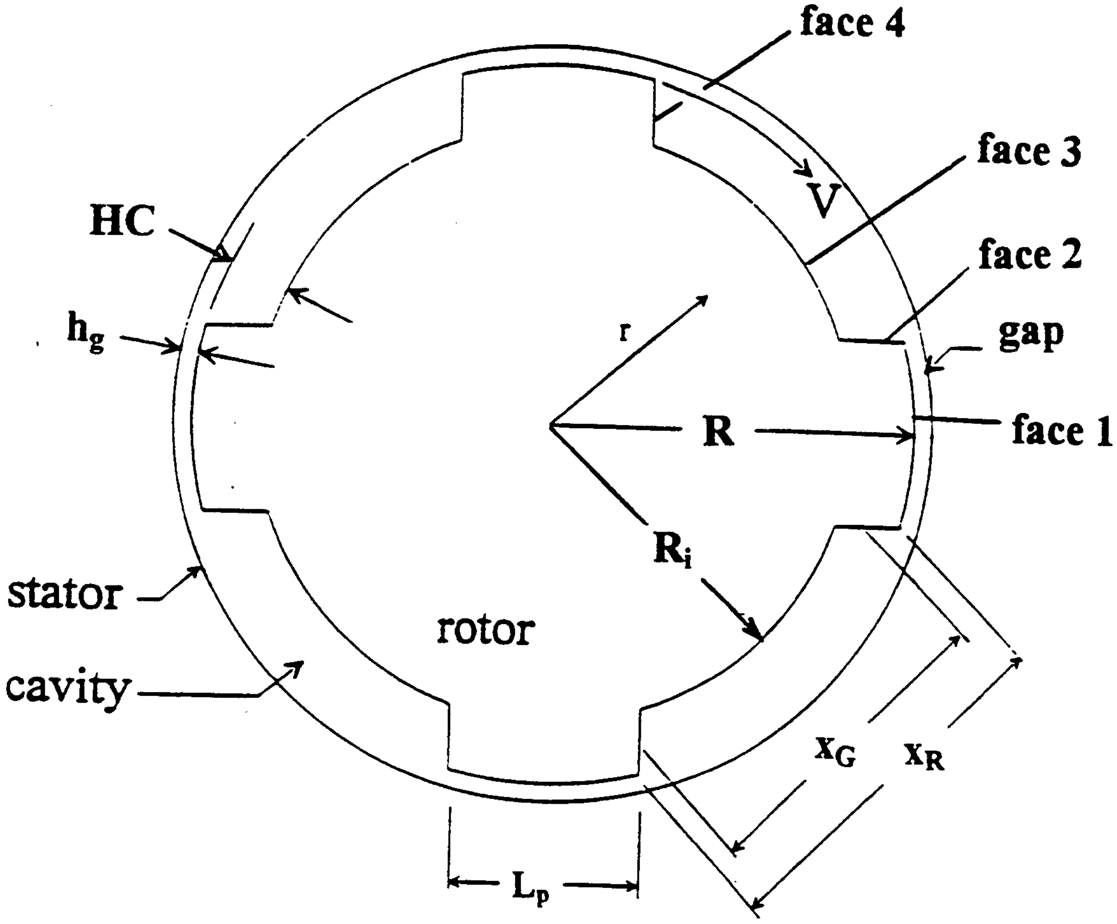
face 4
face 3
V
HC
face 2
gap
h_g
r
R
face 1
R_i
stator
rotor
cavity
x_G
x_R
L_p

Figure 3: Definition of Rotor Pole Faces Relative to Direction of Rotation

an axially grooved surface resulting in twelve circumferentially periodic cavities embedded in it and the ends of the cylinder are bounded by flat impermeable walls that are either fixed to the outer cylinder or rotate with the inner one. This geometry is common in electric motors. However, the heat transfer analysis assumes constant physical properties and rules out predicting the effects of body forces on fluid motion through variable density. Because the rotor of the switched reluctance generator operates at such high rotational speed, it is anticipated that centrifugal forces acting on the fluid in the cavities will significantly affect local heat transfer.

Hwang, Lin and Chen [5] experimentally measured the gross convective heat transfer between an inner slotted cylinder and smooth outer cylinder. However, the rotational speeds were limited to 2,400 rpm and again, the investigation considered the overall heat transfer between the cylinders.

Based upon the review of the literature, there has been no experimental investigation of the convective heat transfer characteristics of a rotor operating at the high rotational speeds of the rotor to be used in the IPU. Further, previous investigations examined average Nusselt numbers for the rotors with no attempt to characterize the variation in film coefficient based on location on the surface of the rotor poles.

1.5 Technical Approach

Convective heat loss from a body's surface can be inferred based on transient cooling of the body. A classic heat transfer problem is one in which a solid body at an initial uniform temperature T_i experiences a sudden change in its environment, T_∞. An example is a hot metal that is immersed in a cool liquid. If it can be assumed that as the body cools there are negligible spatial temperature gradients within the body, a simple solution exists that describes the temperature of the body as a function of time.

$$\frac{T-T_\infty}{T_i-T_\infty}=\exp\left[\left(\frac{-hA}{mc}\right)t\right] \tag{1-1}$$

where

T	temperature of the body, K
T_i	initial temperature of the body, at time t=0, K
T_∞	temperature of the surrounding fluid, K
h	convective film coefficient (W/m^2 K)
A	surface area through which heat is convected
m	mass of the body, Kg
c	specific heat of the body, J/Kg
t	elapsed time, s

This simple analysis is referred to as the lumped capacitance method and is a convenient method for analyzing transient conduction problems. Its accuracy depends on the validity of the assumption that at any time during the transient heat transfer process the temperature of the body is uniform (negligible internal temperature gradients).

Clearly for the above example, if a body were heated to a uniform temperature and then suddenly exposed to a cooler constant temperature environment and if its body temperature were recorded as a function of time during the cooling process, it would be possible to infer the value of the convective film coefficient, h. This is the concept employed in the experimental determination of the film coefficients for the rotor geometry.

Specifically, test rotors were fabricated consisting of highly thermally conductive aluminum cores that are insulated on all surfaces except for the rotor pole surfaces of interest. Each test rotor exposes the aluminum core on unique surfaces of the rotor poles.

I.e. Test Rotor 1 exposes face 1 on each of its four poles, Test Rotor 2 exposes face 2 on each of its four poles, etc. Ideally, the rotors can be heated, mounted on a test rig, enclosed circumferentially by a stator and spun at desired speeds with and without axial air flow while monitoring the temperature history of the aluminum core. If the insulation were perfect and there were no losses through the shaft to which the rotor were attached, all heat transfer would be through the exposed face areas. The convective film coefficient could then be inferred in the same manner as our simple example.

In reality, there are no perfect insulators (especially materials that can withstand the body and skin friction forces associated with such high rotational speeds). Also, since the rotor must be attached to a shaft during testing, the rotor core will lose heat to the shaft. So it is necessary to account for these heat losses through the insulation and shaft.

Further, the lumped capacitance method assumes negligible temperature gradients. The validity of the lumped capacitance method is often judged by a dimensionless parameter called the Biot number, Bi, which represents the ratio of the resistance to conduction within the body to resistance to convection across the fluid boundary layer [6].

$$Bi = \frac{h L_c}{k} \qquad (1\text{-}2)$$

where h is the convective film coefficient, L_c is a characteristic length customarily defined as the ratio of the solid's volume to surface area for convection, and k is the thermal conductivity of the solid material. A small value for Bi implies that heat more readily conducts within the body than convects from it, resulting in a more uniform temperature distribution within the body. For $Bi < 0.1$ the assumption of negligible temperature gradients is reasonable and the error associated with the lumped capacitance method is small.

The Biot numbers for the various rotor core configurations are not small enough to assume uniform temperatures. Although the high thermal conductivity of the aluminum contributes to a low Bi, high values of h are anticipated.

Other complicating factors are the fact that the various surfaces of the rotor convect heat to environments that are of different temperatures (front, rear and gap areas of the rotor) and these temperatures vary with time during the course of the experiments. Also, it is anticipated that in the gap region between pole face 1 and the stator, that the air temperature will be affected by viscous heating associated with the high shear stresses and velocity gradients in this region. This is a high speed boundary layer so the convective film coefficient must be referenced to the adiabatic wall temperature rather than simply a "free-stream" temperature.

Clearly a simple lumped capacitance model cannot adequately account for the complexity of heat dissipation from the rotors. A multi-lump model is developed that accommodates the complexity of the time varying boundary conditions and is used in the analysis of the experimental data to infer the values of h. Further, while it is attempted to measure the air temperature in the gap region, an analytical model for the average temperatures in the rotor gap and cavity regions is developed and used as the basis for inferring the values of film coefficient.

CHAPTER II

EXPERIMENTAL APPARATUS

2.1 General

Test rotors and a Rotor Thermal Test Rig (RTTR) were designed and manufactured for the purpose of collecting data to infer an average convective film coefficient over all faces of the rotor poles as well as a film coefficient for each of the four individual pole faces. This was accomplished by manufacturing full scale test rotors whose unique geometries exposed aluminum rotor core areas corresponding to the pole faces of interest. The RTTR consists of a drive mechanism upon which to mount the test rotors and spin them at the desired speeds, a stator assembly in which the rotors were spun and ancillary test equipment for the measurement of temperatures. A complete test facility was designed and built to house the RTTR and provide support services such as compressed air, purge air and axial airflow.

2.2 Test Rotors

2.2.1 General

Each test rotor is comprised of a 1" thick aluminum core whose unique profile has been designed specifically for that rotor. Epoxy insulation is cast around the core. After curing, the epoxy is machined to yield a test rotor with a profile identical to the IPU rotor.

The aluminum core is exposed on the pole faces of interest for that test rotor while, with some exceptions, all other surfaces are coated with 0.200" thick insulation.

Figure 4 presents a photograph of Rotor 1. The aluminum core is exposed at the four face 1 locations (as defined in Figure 3) and it is this test rotor that is used in determining the film coefficient for face 1. Note that on the front face of the rotor there is a 0.500" diameter opening in the insulating jacket which exposes the rotor core for measurement of its temperature by an infrared sensor. On the rear face, a 1.55" diameter area of the core is uninsulated where the rotor is bolted to the shaft hub of the RTTR.

A clearer understanding of the shape of the embedded rotor core and the insulating epoxy is realized by examining Figure 5. This figure is adapted from the design drawing for Rotor 1.

Six rotors were manufactured and designated as Rotor 1, Rotor 2, Rotor 3, ... Rotor 6. Complete design drawings for the six rotors are presented in Appendix G. For Rotors 1, 2, 3, and 4, their rotor number designation corresponds to the pole faces at which the aluminum core is exposed. Rotor 5 is used to determine an average overall convective film coefficient for the combined surface area of faces 1, 2, 3, and 4 so the aluminum core is exposed on all of the faces. Rotor 6 is not shaped like an IPU. While it is of the same thickness as the other test rotors, it is simply a disk with an outer diameter of 4.30" (the same as the outside diameter of the poles for rotors 1 - 5). Its front and rear surfaces are epoxy coated, however, its peripheral surface is uninsulated; the aluminum core extends to the outside diameter. The gap between rotor 6 and the stator wall is small compared to the radius of the rotor and the air velocity profile in the gap can be approximated as flat plate, wall driven flow. Based on this approximation, it is possible to

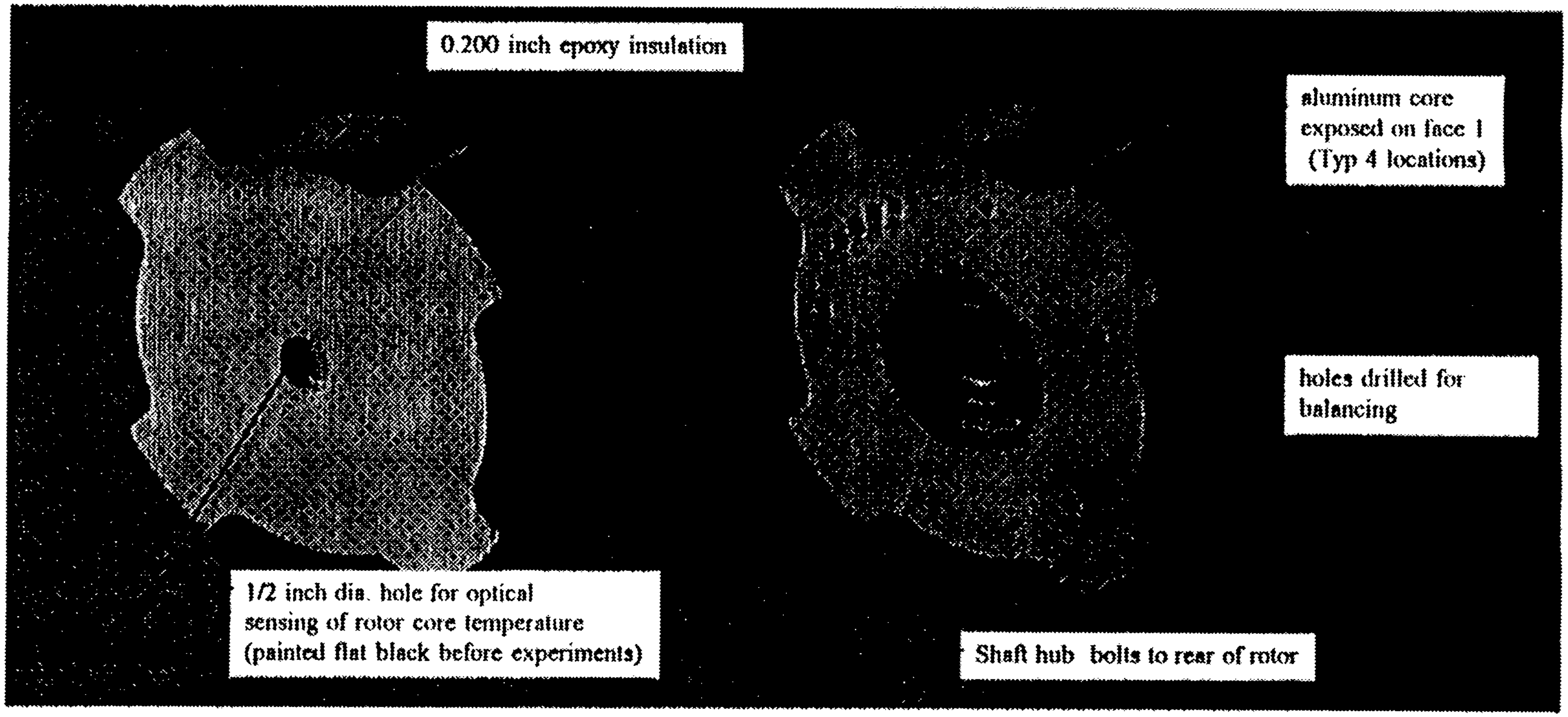
0.200 inch epoxy insulation
aluminum core exposed on face 1 (Typ 4 locations)
holes drilled for balancing
1/2 inch dia. hole for optical sensing of rotor core temperature (painted flat black before experiments)
Shaft hub bolts to rear of rotor

FrontView

Rear View

Figure 4: Photographs of Front and Rear of Rotor 1

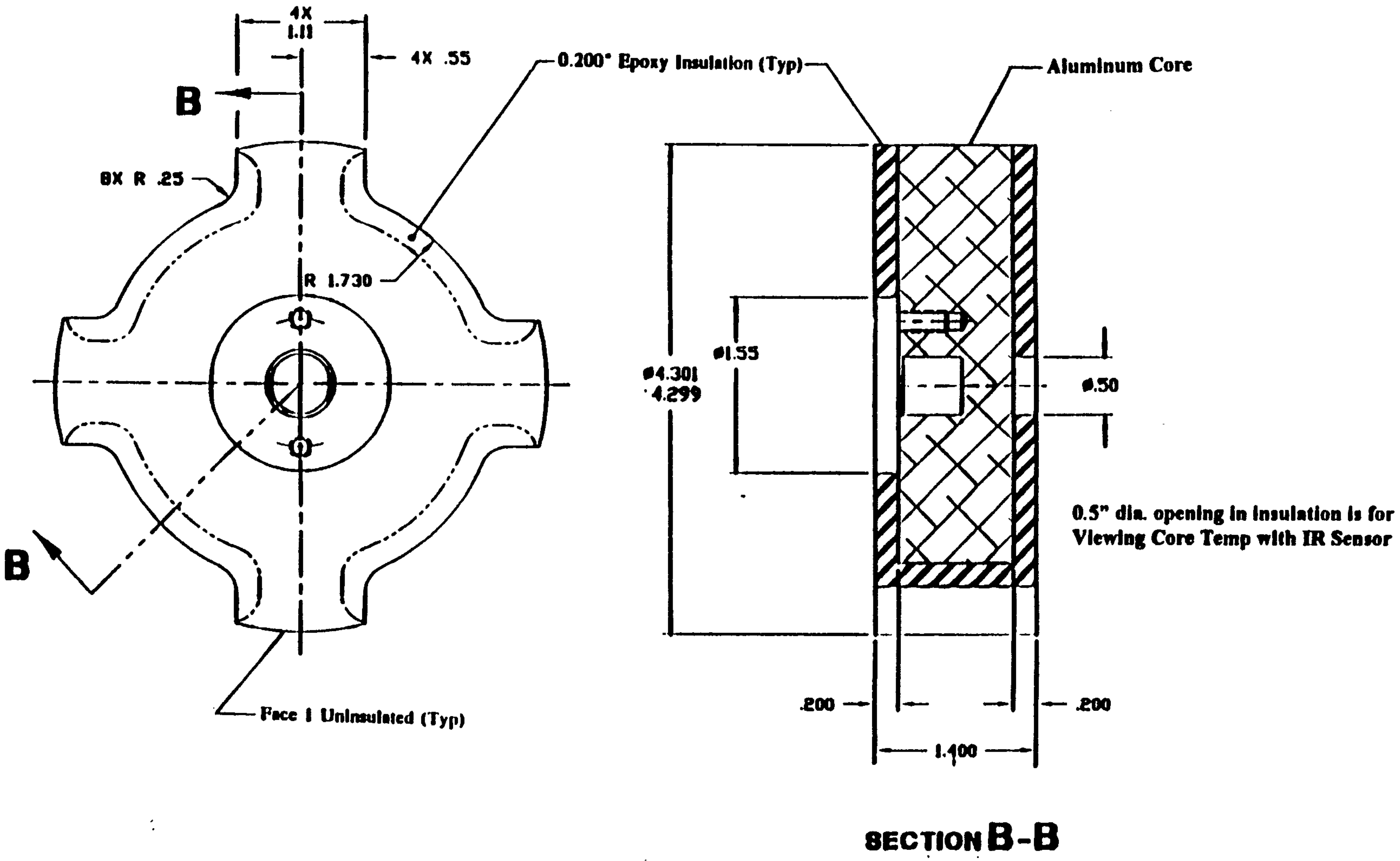
4X
1.11
4X .55
B
B
8X R .25
R 1.730
0.200" Epoxy Insulation (Typ)
Aluminum Core
Face 1 Uninsulated (Typ)
ø1.55
ø4.301
.4.299
ø.50
0.5" dia. opening in insulation is for
Viewing Core Temp with IR Sensor
.200
.200
1.400
SECTION B-B

Figure 5: Fabrication Drawing for Rotor 1

estimate the convective film coefficient on the exposed aluminum core surface with good accuracy. The purpose of rotor 6 is to validate the mathematical model of heat loss from the rotors and experimental data. It permits tuning of the model to account for heat loss through the insulation as well as through the shaft.

The unique features of the rotors may be readily observed upon examination of Figure 6. Here a photograph is presented of the six rotors touching front to back, aligned in a row. This photo was taken after all testing was completed, so the epoxy insulation has darkened due to repeated heating. Note that rotors 1 though 5 have the same outside dimensions, consistent with the profile of the IPU. Also, the locations on each rotor where the aluminum core is exposed are visible as shiny surfaces. Rotors 1 through 4 each have the core exposed in four unique locations consistent with Figure 3, Rotor 5 has all faces exposed and Rotor 6 is a disk. These features of the six test rotors are summarized in Table 1.

Table 1: Features of Test Rotors

Rotor Number	Profile	Exposed Pole Face
1	IPU Rotor	1
2	IPU Rotor	2
3	IPU Rotor	3
4	IPU Rotor	4
5	IPU Rotor	1, 2, 3, 4
6	4.3" dia. cylinder	Radial Perimeter

2.2.2 Rotor Core Material

The aluminum cores were machined from 7075-T651, a high strength Al-Zn-Mg-Cu alloy commonly used in aerospace applications. The selection of this material was influenced by the success of test rotors manufactured by the Air Force for

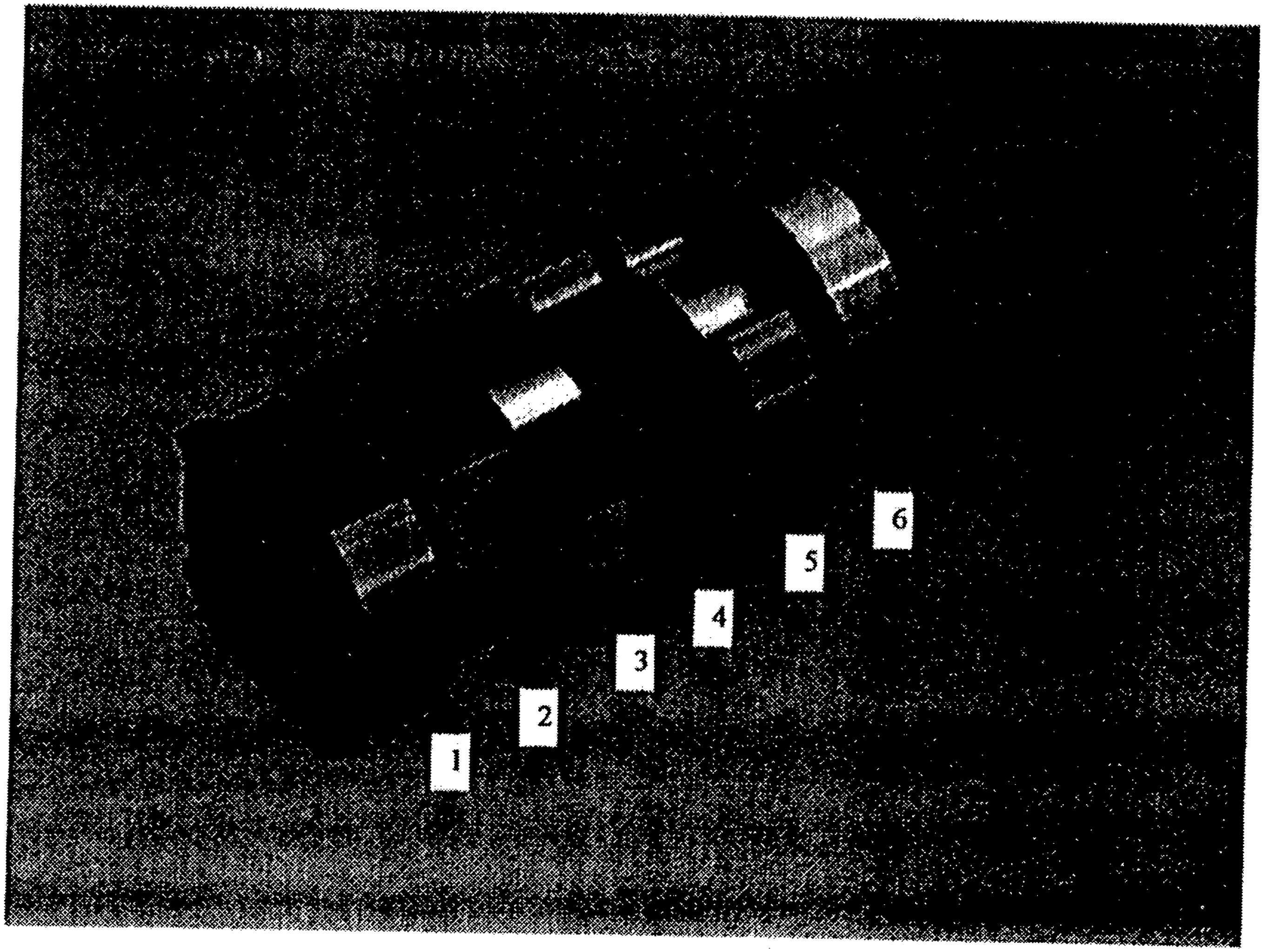

Figure 6: Photograph of Six Test Rotors Aligned in a Row

estimating rotor windage losses associated with axial air flow. In these tests, the entire rotor bodies were machined from 7075 aluminum to the shape of the IPU rotor.

2.2.3 Rotor Insulating Material

The selection of an insulating material required considerable investigation. There were several criteria that had to be met to assure that the insulating system was a success. These criteria are:

1. Low thermal conductivity. The lower the amount of heat loss through insulated surfaces, the greater the percentage of total heat loss through the uninsulated pole faces of interest and therefore a more accurate assessment of the film coefficient.
2. Good machineability. This is required to create finished test rotor profiles that are identical to the rotor of the IPU.
3. Good dimensional stability. The original design dimension of the gap between the outer rotor pole tip and stator was only 0.020", so elongation of the insulation caused by mechanical or thermal stresses could result in the spinning rotor contacting the stator wall. Such contact, especially at high rotational speeds, could destroy the rotor and the RTTR.
4. High Strength. The test rotors were designed for 55,000 rpm resulting in high centrifugal accelerations in the outer radial regions of the rotors. A 55,000 rpm rotor speed results in a centrifugal acceleration at the tip of approximately 185,000 times the acceleration of gravity. Also, at this high rate of rotation the tangential velocity in the tip region is 315 m/s (1032 ft/s or 704 mph), close to the speed of sound (343 m/s at 20°C). As a result, the insulation is subject to high shear stresses due to skin friction.

5. Good adhesion to aluminum. The insulation not only had to withstand stresses imposed by body and surface forces, it also had to bond to the aluminum rotor core. The adhesion had to be strong enough to accommodate the shear forces at the interface of the insulation to the aluminum.

The initial material considered as an insulator was expanded polystyrene board (Styrofoam). This material certainly has superior insulating qualities. Its thermal conductivity, 0.0288 W/m-°C (0.0167 Btu/hr-ft-°F), is only slightly greater than the conductivity of air. Also, on first consideration, the fact that it is a lightweight material (0.056 specific gravity) suggests that the body forces imposed by centrifugal acceleration would be small. However, Styrofoam has very low strength which rendered it unsuitable due to material failure at high speeds. Also, its low modulus of elasticity resulted in unacceptable dimensional growth. In a similar manner, spray polyurethane foam from a can was investigated as a potential candidate. The polyurethane was even lighter than Styrofoam and had marginally better insulating properties. However, it was found to be unsuitable for the same reasons as Styrofoam. Further, neither of these materials could be easily applied to the rotor cores nor did they possess good machining qualities.

Since the light weight foams lacked sufficient strength, denser materials with greater strength were considered. Epoxy seemed a good candidate since it meets essentially all of the criteria listed. Epoxies have high strength, relatively low thermal conductivity and many exhibit excellent machineability. Further, epoxy can be cast around the aluminum cores, assuring a reliable insulating shell maintained in place through surface adhesion to the aluminum as well as the cast rigidity of the epoxy.

The positive assessment of epoxy was bolstered by a 1996 investigation the author had performed.[7] That project was a thermal analysis of a calorimeter used by a government agency wherein epoxy was used to provide radial insulation of the calorimeter jacket. As part of that study, tests were performed on the epoxy to determine if its thermal conductivity could be further reduced by incorporating air encapsulated glass microspheres into the two part epoxy mixture. The material tests conducted in that study showed that the thermal conductivity of the original epoxy was 9.39 x 10^{-4} cal/cm-s-°C and that the addition of the prescribed quantities of glass microsphere beads reduced the thermal conductivity by 47% to 4.95 x 10^{-4} cal/cm-s-°C (.207 W/m-°C, 0.12 Btu/hr-ft-°F).

It was concluded that a glass microsphere augmented epoxy system presented a good compromise of thermal conductivity, strength, and machineability properties for application as the rotor insulation.

2.2.3.1 Formulation of Epoxy Insulation

The epoxy cited in [7] provided a good indication of anticipated thermophysical properties, however, that specific epoxy was not suitable for this application because it lacks sufficient strength and adhesion qualities. The manufacturer, Magnolia Plastics of Peachtree, Georgia, recommended Magnabond™ 6367, a two-part, high-strength, low-viscosity epoxy used in the repair of rotor blades on helicopters. The product exhibits high lap shear strength, 4,390 psi at 75°F (ASTM D1002, 2024 T-3 aluminum, FPL Etch) and peel strength, 4.0 PIW at 75°F (ASTM D-3167, 2024 T-3 aluminum, FPL Etch).

The glass microspheres used in the formulation are 3M Scotchlite™ Glass Bubbles, Product No. D32/4500. The two part epoxy was mixed with glass microspheres in the same ratio by weight as had been investigated in [7]. The formulation is presented in Table 2.

Table 2: Formulation of Epoxy with Glass Microspheres

Component	Parts by Weight	Parts by Volume
6367-A resin	100	2
6367-B hardener	44	1
Glass Microspheres	22	3

It should be noted that the Part A resin was very viscous and did not lend itself to weighing. A more manageable method of measuring the components was by volume with measuring cups. Note that while the glass microspheres represent only 13% of the total weight of the mixture (22/166), they represents 50% (3/6) of the pre-mixed volume. This gives a good indication of why the incorporation of the microspheres has such a favorable impact on the thermal conductivity. Since heat transfer is path dependent, the dispersion of these air encapsulated microspheres to occupy approximately half the volume dramatically increases the thermal resistance of the conduction path.

The measured thermophysical properties of this epoxy with glass microspheres formulation are comparable to the material used in the 1996 investigation. Its thermal conductivity was measured to be 0.216 ± .011 W/m K. Details of the measurement of these properties are presented in Appendix B.

2.2.3.2 Preparation and Casting of Rotor Cores

Proper surface preparation of the aluminum cores was essential to achieving a high strength bond at the epoxy-aluminum interface. The surface of each machined aluminum core was wiped with methyl ethyl ketone (MEK) and then grit blasted with 50-micron aluminum oxide. The cores were then submersed in a heated (150°F) alkaline cleaning solution for 10 minutes. Following cleaning, they were rinsed with deionized water and then submersed into a P2 etching solution (sulfuric acid/ferrous sulfate at 150°F) for 15 minutes. The cores were again rinsed with deionized water and then dried in an air-circulating oven at 150°F for 20 minutes. After cooling to room temperature, the rotors were sprayed with a primer.

It may be noted that the manufacturer's specifications for lap shear strength and peel strength are based on aluminum surfaces prepared with an FPL etch. The FPL (Forrest Park Laboratory) etch uses sodium dichromate which is a carcinogen and presents a hazardous waste. The P2 etch uses ferrous sulfate and has since been adopted by the military as a substitute for the FPL etch. Etching removes very weak oxide layers from the aluminum substrate and replaces them with a more stable oxide layer which improves bonding to the epoxy. The primer also improves bonding to the epoxy and extends the time period from when the aluminum surfaces are etched until the epoxy must be cast around the cores.

The epoxy formulation was mixed and cast around two cores at a time as shown in Figure 7. The epoxy is highly exothermic as it cures and large volumes are susceptible to violent boiling due to internal heat generation, causing voids in the epoxy. The curing epoxy was cooled by fabricating heavy aluminum casting bases to which the rotor cores were mounted. Thus, the mass of the aluminum cores and the casting bases acted as heat sinks to absorb heat generated by the epoxy while curing. Further, to help remove heat

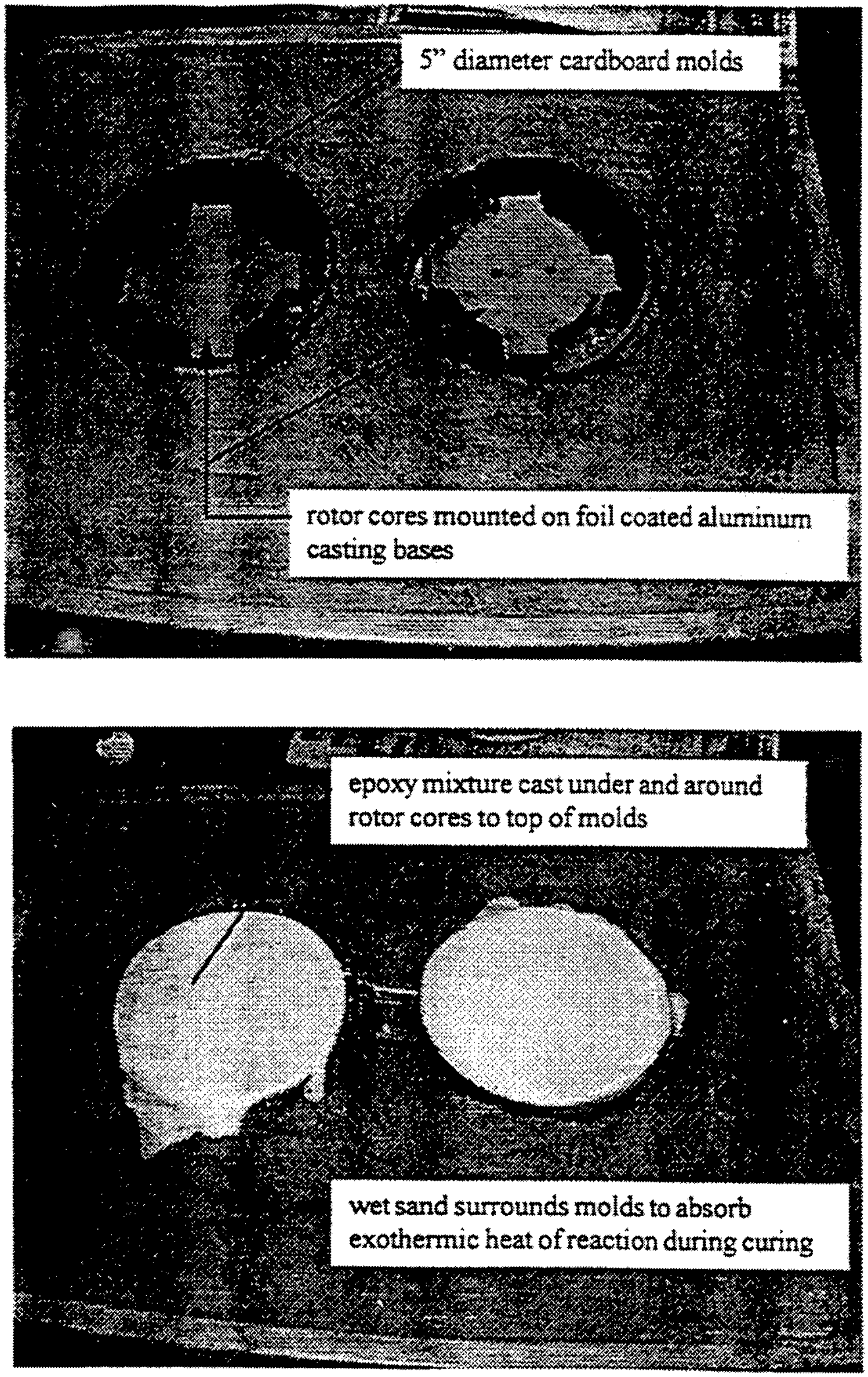
5" diameter cardboard molds
rotor cores mounted on foil coated aluminum casting bases
epoxy mixture cast under and around rotor cores to top of molds
wet sand surrounds molds to absorb exothermic heat of reaction during curing

Figure 7: Photograph of Casting Epoxy Around Rotor Cores

from the outer surfaces of the molds, wet sand was packed around the aluminum bases and the 5” diameter cardboard outer mold walls.

2.3 Rotor Thermal Test Rig

2.3.1 General

The purpose of the Rotor Thermal Test Rig (RTTR) is to spin the test rotor at desired speeds, simulate the spatial environment of the rotor within the stator and measure parameters during experiments for analysis of the transient heat loss of the rotor. During the course of experimentation, modifications to the RTTR were necessary to assure validity of test data. The specifics of these modifications and their reasons will be discussed further. A photograph of the final version of the RTTR is shown in Figure 8. The RTTR is comprised of four basic components: an air turbine and shaft, stator assembly, air inlet chamber and an IR sensor enclosure.

2.3.2 RTTR Components

Air Turbine and Shaft

The air turbine, manufactured and donated by Tech Development, Inc. of Dayton, Ohio is a model 45M TDI TURBOSTARTTWO™. Its commercial use is as an engine starter, typically for application to large diesel truck engines. The turbine is equipped with 28 vanes and 13 nozzles and driven by a compressed air source. The shaft, designed for attachment to the test rotors is 0.500” in diameter and fabricated from 17-4PH stainless steel. Stainless steel was selected as the shaft material, in part, because it has a relatively low thermal conductivity.

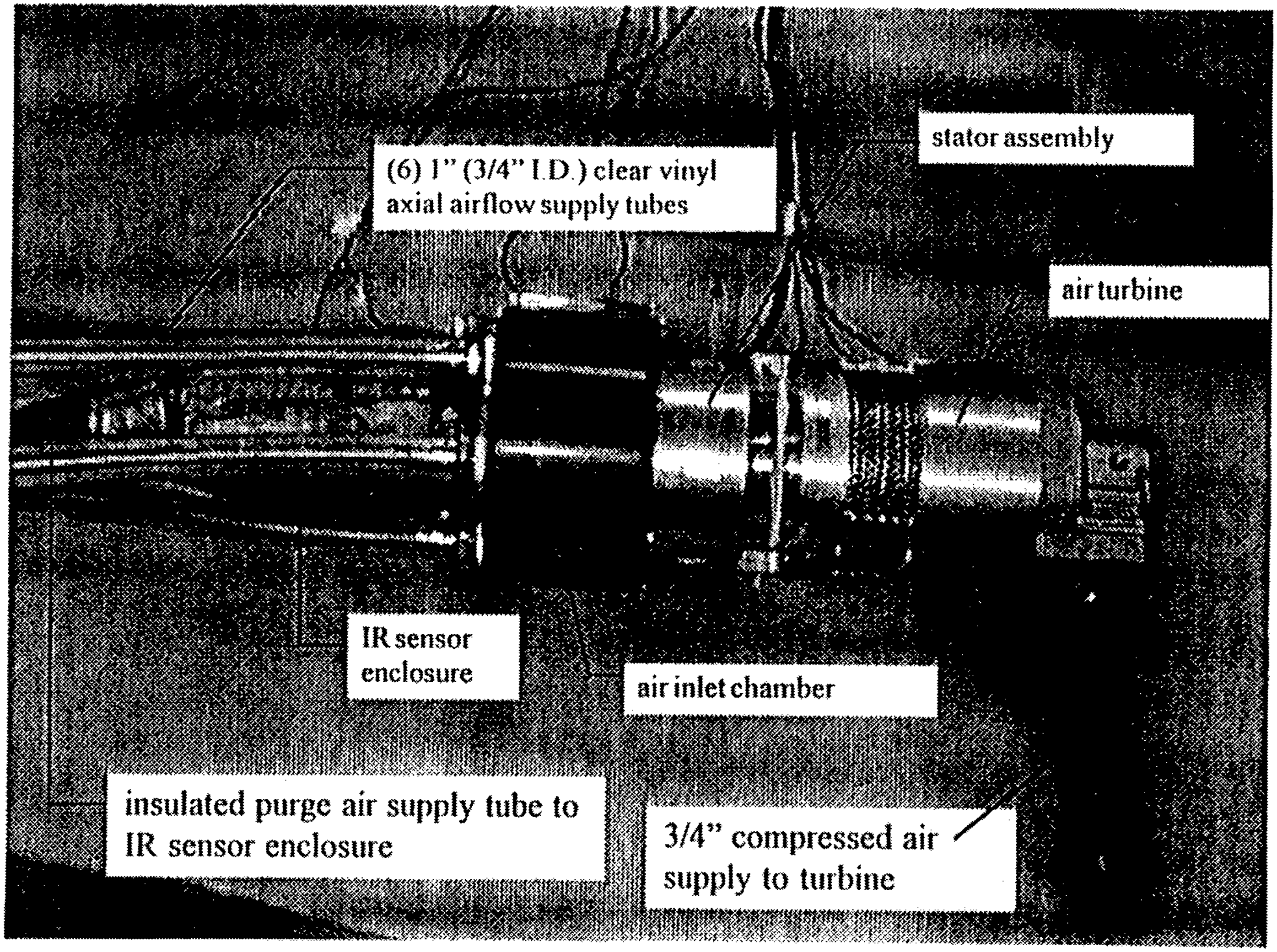
stator assembly
(6) 1" (3/4" I.D.) clear vinyl axial airflow supply tubes
air turbine
IR sensor enclosure
air inlet chamber
insulated purge air supply tube to IR sensor enclosure
3/4" compressed air supply to turbine

Figure 8: Photograph of Rotor Thermal Test Rig (RTTR)

The standard air starter donated for this experiment was modified in two ways. First, its outboard bearing was repositioned to be as close to the test rotor as possible. Second, the standard bearing was replaced with a larger bearing. These modifications yielded a first natural frequency for shaft bending of approximately 700 Hz or 42,000 rpm. These modifications were made after initial tests with the unmodified turbine resulted in catastrophic failure of the test rotors at approximately 16,000 rpm.

Stator Assembly

The stator is simply a cylindrical section fabricated from A356 cast aluminum which bolts to the face of the air turbine and surrounds the rotor. The outside diameter (OD) matches the OD of the air turbine. The inside diameter (ID) was originally designed to match the ID of the IPU stator and thus provide a 0.020" gap between the rotor pole tip and stator wall. However, during the course of experimentation, the ID was increased such that the gap between the rotor pole tips and stator was approximately 0.030". This change was made as an initial attempt to eliminate contact of the rotor with the stator when the first critical frequency was reached (16,000 rpm) and before addressing the problem through re-design of the air turbine bearings. A photograph of a test rotor mounted on the turbine shaft and installed within the stator assembly is illustrated in Figure 9.

Air Inlet Chamber and IR Sensor Enclosure

The design of the air inlet chamber and IR sensor enclosure were necessitated by the sensitivity of the IR temperature sensor to changes in ambient temperatures. Although the manufacturer's specifications state a 0 to 185°F ambient operating range for the IR sensor head, they do not stipulate that the environment must be steady. The original

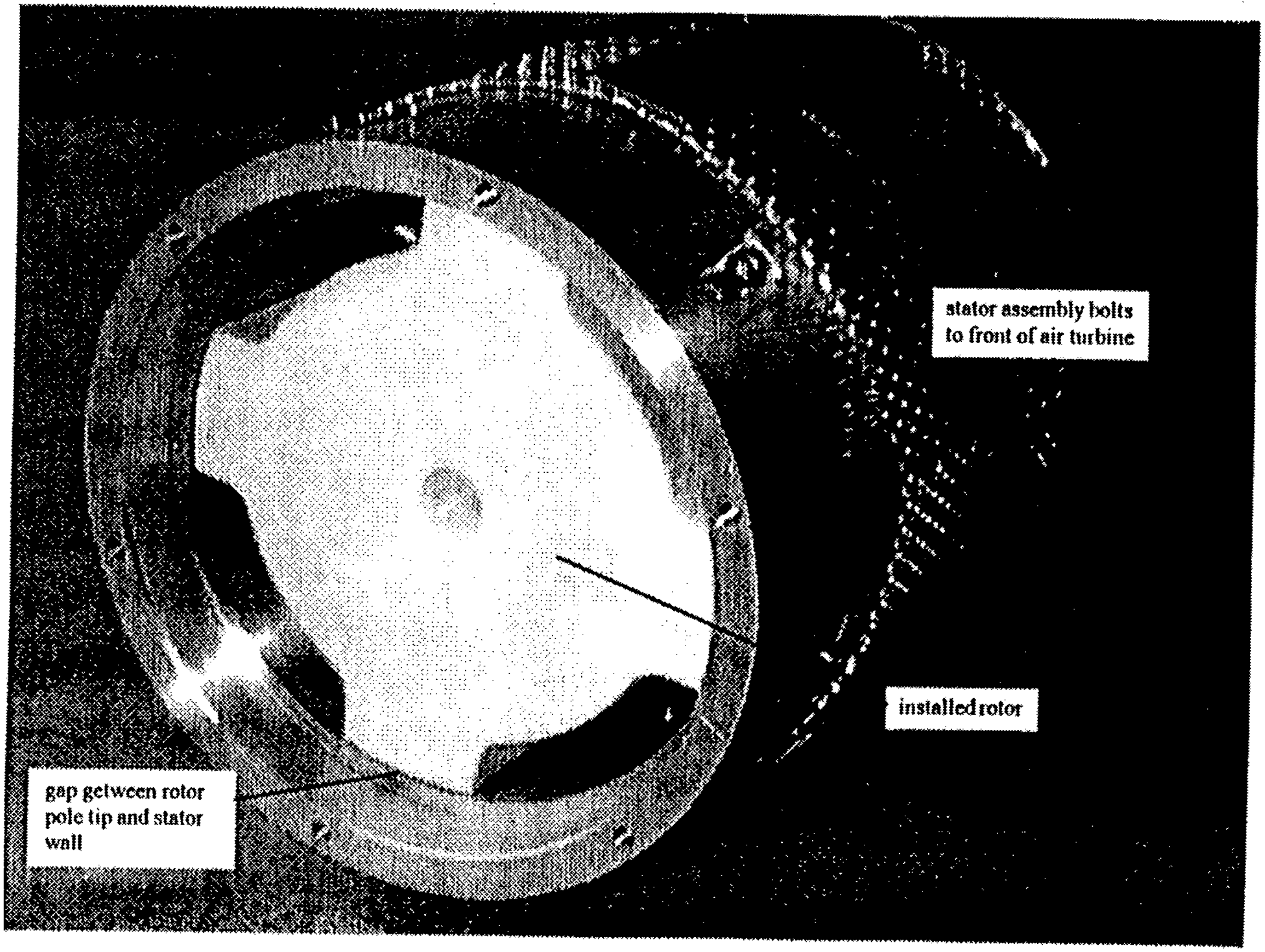
stator assembly bolts to front of air turbine
installed rotor
gap getween rotor pole tip and stator wall

Figure 9: Photograph of Stator, Air Turbine and Installed Rotor

design of the RTTR located the IR sensor lens 6" from the rotor core (as required for proper focusing on the 0.5" diameter exposed core) and centered within a cylindrical inlet housing through which axial airflow was ducted. IR sensor measurement errors associated with this design became apparent when the blower which furnishes axial air to the RTTR was energized. The supplied air was heated due to energy input by the fan (approximately 10°F above ambient) and the warm air passing over the IR sensor created temperature gradients within its body. These gradients resulted in IR sensor measurement errors as large as 23°F. As the blower continued to run, the system would achieve steady state conditions in about 30 minutes and the IR sensor would again provide accurate temperature measurements. Since the experiments to be conducted in this investigation were each of short duration (150 - 600 seconds) and required that the blower initially be off, it was clear that steady state conditions would never be achieved during the time period of each experiment and that the IR sensor readings would not be valid. This was clearly unacceptable, requiring a design modification to the RTTR.

The purpose of the IR sensor enclosure is to provide a constant temperature atmosphere by isolating the sensor from changes in the external environment. The enclosure, shown in Figure 10, mounts to the aft end plate of the air inlet chamber. It is fabricated from nylon to minimize thermal conduction to the sensor. A zinc selenide optical viewing window is located on the front of the enclosure where it attaches to the air inlet chamber. This window transmits radiant energy to the IR sensor, yet it eliminates infiltration of air supplied to the inlet chamber into the enclosure. To further assure steady state conditions within the enclosure, a constant temperature air purge is supplied to the rear of the enclosure and discharges through six (6) 0.201" diameter weep holes at the

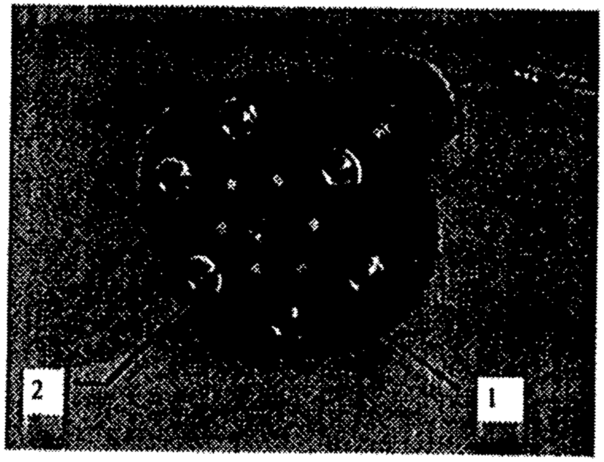

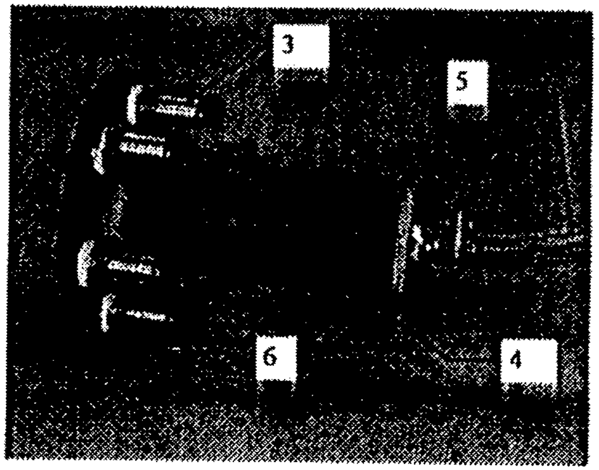

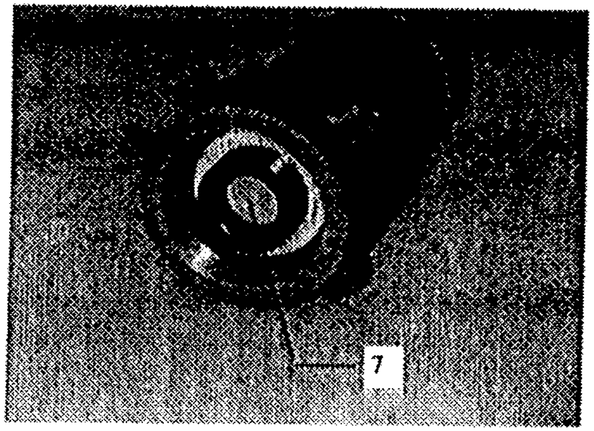

Notes:

1. Aft end plate of air inlet housing (PVC).
2. Zn-Se viewing window.
3. (6) 3/4" NPT x hose fittings for 3/4" I.D. axial airflow supply tubes.
4. IR sensor enclosure (nylon)
5. Purge air supply tube. Note that the cable from the IR sensor is routed inside this tube to minimize temperature gradients within the sensor.
6. (6) 0.201" purge air bleed holes drilled peripherally
7. Lens of IR sensor

Figure 10: Photographs of IR Sensor Enclosure

front. Purge airflow was estimated to provide in excess of 19 air change per second within the enclosure.

It may be noted that the enclosure was designed with four radial mounting tabs. These were provided so that the enclosure could be installed inside the original inlet housing of the RTTR with axial airflow would passing over the outside surfaces of the enclosure. The IR sensor enclosure was installed in the original inlet housing and tested. The enclosure greatly reduced the influence of supply air temperature variations on the accuracy of IR sensor measurements, however, the airflow continued to have a small, measurable effect.

The final major design modification to thermally isolate the sensor was to duct the supply airflow in tubes so that the air did not pass over the body of the enclosure. This modification resulted in the design and fabrication of the air inlet chamber. The air inlet chamber serves two functions. It acts as an air inlet plenum for axial airflow through the rotor. It also serves as a bracket upon which the IR sensor enclosure is mounted. Referring to Figure 7, the air inlet chamber is fabricated from 6" schedule 40 PVC pipe with 1/4" PVC plates screwed to each end. Axial airflow enters through six (6) 3/4" ID vinyl tubes equally spaced circumferentially on the aft end plate of the chamber. Axial air exits the chamber through a 4.36" ID hole in the front end plate of the chamber, aligned with the ID of the stator assembly.

Other measures taken to thermally isolate the sensor from the outside environment included insulating the outer surface of the enclosure (see Figure 8), attaching the sensor enclosure to the inlet chamber with nylon screws, and routing the sensor's electronics cable through the purge air line for a distance of approximately 3 feet to minimize conduction through the cable to the laboratory environment.

2.4 Test Facility

2.4.1 General

All tests were conducted at the University of Dayton in Kettering Laboratories room 19A. A schematic of the test system facility is illustrated in Figure 11.

It is apparent that in addition to the test rotors and the Rotor Thermal Test Rig discussed earlier, there are three ancillary air systems connected to the RTTR. These are a compressed air supply to power the air turbine, a purge air supply to the IR sensor enclosure and axial airflow supply to the RTTR.

2.4.2 Compressed Air Supply System

The compressed air supply system consists of an air compressor, filter/drier and a 400 gallon receiver rated for 200 psig maximum pressure. The rotational speed of the air turbine is governed by the pressure of the compressed air at the inlet to the turbine. Because the rate at which the turbine consumes compressed air is seldom equal to the rate that the air compressor delivers air to the system, the pressure in the receiver is almost always varying with time. The project budget could not accommodate an automated control system to meter compressed air to the air turbine to maintain a specified speed based on a feedback control loop from a speed monitor. However, reasonably accurate speed control was achieved by installing a pressure regulator between the primary air receiver and a secondary air reservoir. Air was supplied to the turbine from the secondary air reservoir and the rotor speed was manually regulated with a globe valve. During the

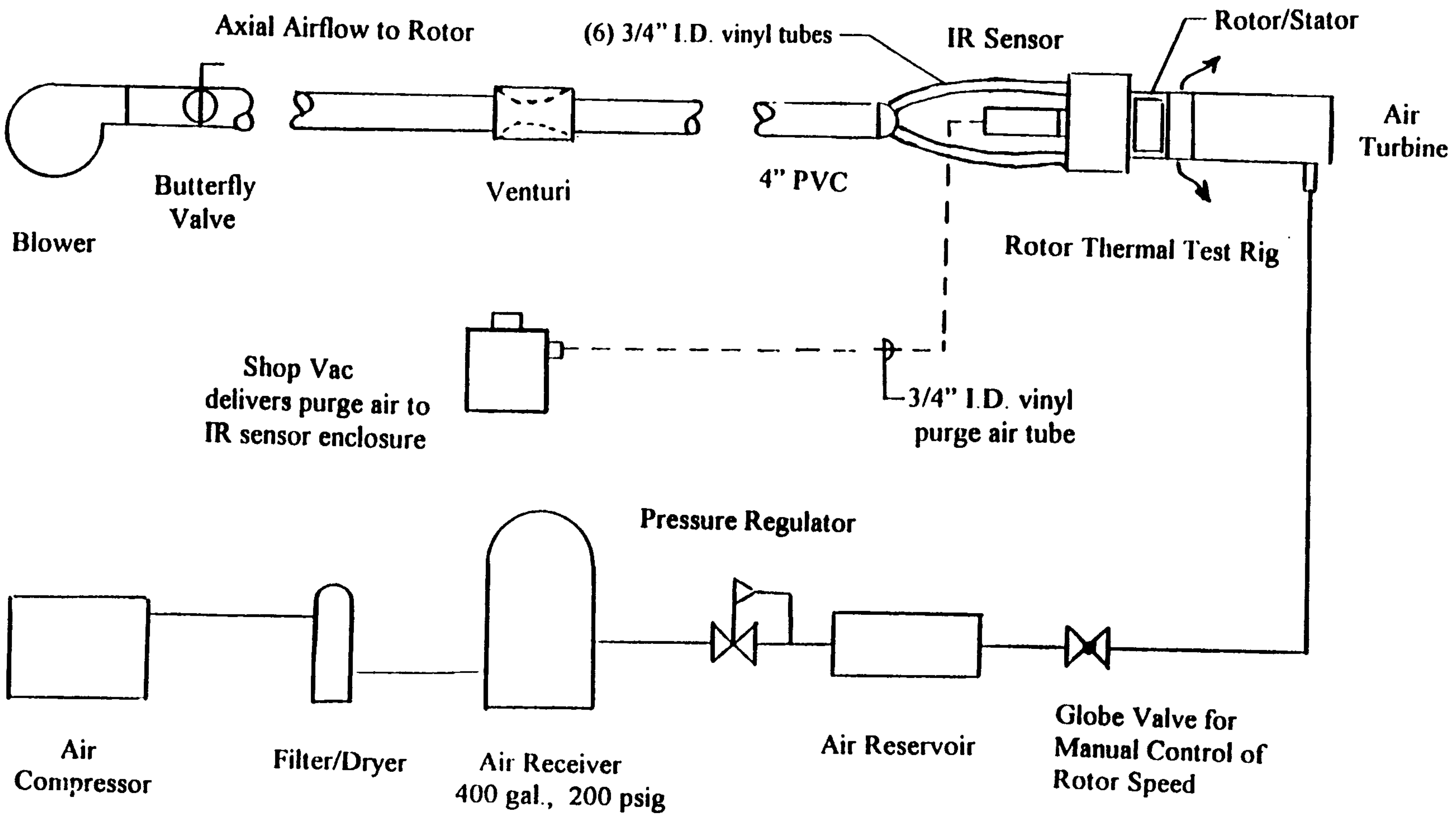
Axial Airflow to Rotor
(6) 3/4" I.D. vinyl tubes
IR Sensor
Rotor/Stator
Air Turbine
Blower
Butterfly Valve
Venturi
4" PVC
Rotor Thermal Test Rig
Shop Vac delivers purge air to IR sensor enclosure
3/4" I.D. vinyl purge air tube
Pressure Regulator
Air Compressor
Filter/Dryer
Air Receiver
400 gal., 200 psig
Air Reservoir
Globe Valve for Manual Control of Rotor Speed

Figure 11: Test Facility System Schematic

course of a test, the valve was continuously adjusted by the author in response to the rotor speed displayed by the data acquisition system.

2.4.3 Purge Air Supply System

The purge air system is simply a 10 gallon, 2 peak horsepower shop vac to which a 3/4" ID vinyl tube was attached to the discharge port. The purge air is routed approximately 30 feet from the shop vac to the IR sensor enclosure. The purpose for this long length is so that the air is cooled as it flows down the length of the tube before reaching the IR sensor. During steady state operation, discharge air from the shop vac was 105°F and entered the IR sensor enclosure at 85°F.

2.4.4 Axial Airflow Supply System

Axial airflow to the RTTR is furnished by a single width, single inlet blower nominally rated to deliver 1600 cfm at 1 psi discharge pressure. This fan was employed because it was already installed in the laboratory. Air is conveyed to the RTTR through 4" PVC pipe. Airflow is regulated with a butterfly valve at the fan discharge. The flow rate is monitored by a 3" venturi meter installed in a section of 3" pipe that assures 10 straight pipe diameters upstream and 5 straight pipe diameters downstream of the meter. The pipe supply header terminates with a 4" PVC cap from which six (6) 18" long, 3/4" ID vinyl hoses connect to the RTTR air inlet chamber.

CHAPTER III

EXPERIMENTAL METHODS AND MEASUREMENTS

3.1 Automatic Data Acquisition

Data acquisition was accomplished via an IBM compatible 486 computer using LABTECH NOTEBOOKpro™ Version 9.02 software. Two data acquisition boards were installed within the computer and each connected to a separate external terminal board with ribbon cable.

1. Keithley-Metrabyte CTM-05 counter-timer board. The CTM-05 board is designed for frequency measurements and event counting and accepts up to 5 inputs with a 7 MHz maximum input frequency. The board was used to measure the instantaneous speed of the air turbine.
2. Keithley-Metrabyte DAS-TC/B thermocouple and voltage input board. The DAS-TC/B board is specifically designed for thermocouple applications. The 16 channels can be individually configured to accept inputs from thermocouples or other voltage sources (up to 10 Vdc). The board was used for measuring temperatures as well as voltage inputs from differential pressure transducers.

The Labtech Notebook software allows the user to specify the data sampling rate. All data collected in the course of the experiments was recorded at a rate of 1 Hz. This rate was governed by the limitation of the scan rate of the data acquisition system. For the final data acquisition configuration which monitored multiple temperatures and voltages, a scan rate much greater than 1 Hz resulted in "jitter" where data was lost and/or not collected in the specified time increments. The 1 Hz sampling rate resulted in no jitter. Further, the parameters measured in these experiments did not change at rates that warranted a higher sampling rate.

The CTM-05 board had only a single input, the speed of the air turbine. The DAS-TC/B board, however, utilized all 16 inputs. Table 3 presents a listing of the inputs to this data acquisition board.

Table 3: Inputs to DAS-TC/B Board

Input	Symbol	Measured Parameter	Device
		Temperatures	
0	J-0	rotor core	IR Sensor (Type J Thermocouple)
1	T-1	air in front of rotor	20 AWG Type T Thermocouple
2	T-2	stator	Omega TMQSS-040E-6 Thermocouple
3	T-3	ambient air	Omega TMQSS-040E-6 Thermocouple
4	T-4	air behind rotor	20 AWG Type T Thermocouple
5	J-5	forward bearing	30 AWG Type J Thermocouple
6	J-6	aft bearing	30 AWG Type J Thermocouple
7	T-7	air behind rotor	34 AWG Type T Thermocouple
8	T-8	air in front of rotor	34 AWG Type T Thermocouple
9	K-9	air in rotor/stator gap	Omega KMQSS-040E-6 Thermocouple
10	T-10	air in oven heating rotors	20 AWG Type T Thermocouple
11	T-11	purge air supply to IR sensor	20 AWG Type T Thermocouple
		Differential Pressures	
12	DP-12	air entering venturi (gauge)	Omega PX163-120D5V
13	DP-13	differential across rotor	Omega PX162-027D5V
14	DP-14	differential across rotor	Omega PX164-010D5V
15	DP-15	differential across venturi	Omega PX162-027D5V

3.2 Measurement of Physical Parameters

The sensor hardware (and its calibration) used for the measurement of rotor speed, temperatures, pressures and axial air mass flow rate are discussed in detail in Appendix D.

3.2.1 Air Temperature Measurements at Front and Rear Rotor Faces

Redundant thermocouples were employed to measure the air temperatures fore and aft of the test rotors. At each location, 34 AWG and 20 AWG thermocouples were installed such that 18" of their length was exposed to the air stream to be measured. The added length of thermocouple wire minimized temperature gradients and isolated the beads from heat conduction through the wire.

The 34 AWG thermocouples were used for primary temperature measurement because the low thermal mass of their beads provided faster response than those of the 20 AWG wires. The purpose of redundant installation is that the 34 AWG is fragile and susceptible to breakage.

3.2.2 Air Temperature Measurement in Rotor/Stator Gap

It was desired to collect data on the "temperature in the gap". It is difficult to define exactly what this temperature represents. Certainly, the temperature in the gap between the rotor pole tip and stator wall is expected to be higher than the air temperature in the cavity region due to viscous heating. Thus, the measured "gap" temperature may represent an average temperature.

Accurate measurement of the air temperature in the gap between the outer rotor pole and the inner stator wall was challenging. The gap size of approximately 0.030" is too small to accommodate direct insertion of most thermocouples. Further, an exposed thermocouple bead would be vulnerable to damage during repeated mounting and dismounting of the test rotors.

Measurement of air temperature in the gap region was accomplished as illustrated in Figure 12. Since the thermocouple cannot be inserted into the gap region, the thermocouple bead is centered in a 0.062" diameter hole in the stator wall. Air flows from the gap region through the hole and out to the ambient atmosphere as a result of air pressure developed in the gap produced by rotor rotation.

A 1/4" OD nylon threaded rod was machined to have a 0.100" ID with air bleed holes near the top. The rod supports a 6" probe type K thermocouple at its top such that the thermocouple bead is centered in the 0.062" diameter hole in the stator wall. The length of nylon rod serves the purpose of insulating the thermocouple from the stator wall. Heat conduction through the thermocouple wire was minimized by using a type K thermocouple whose wires have low thermal conductivities. Further, heat conduction down the sheath of the probe was minimized by the flow of air from the gap over the length of the sheath inside the nylon support rod.

A detailed analysis of the thermocouple installation is presented in Appendix E where the temperature of the bead was estimated as a function of the temperature of the air in the gap, stator temperature, and ambient air temperature as well as the length of the nylon rod. For the design shown in Figure 12, the affect of stator and ambient air temperatures are negligible.

3.2.3 Bearing Temperature Measurement

Deep groove radial ball bearings support the shaft. The fore and aft shaft bearings temperatures were monitored with 30 awg type J thermocouples. The thermocouple

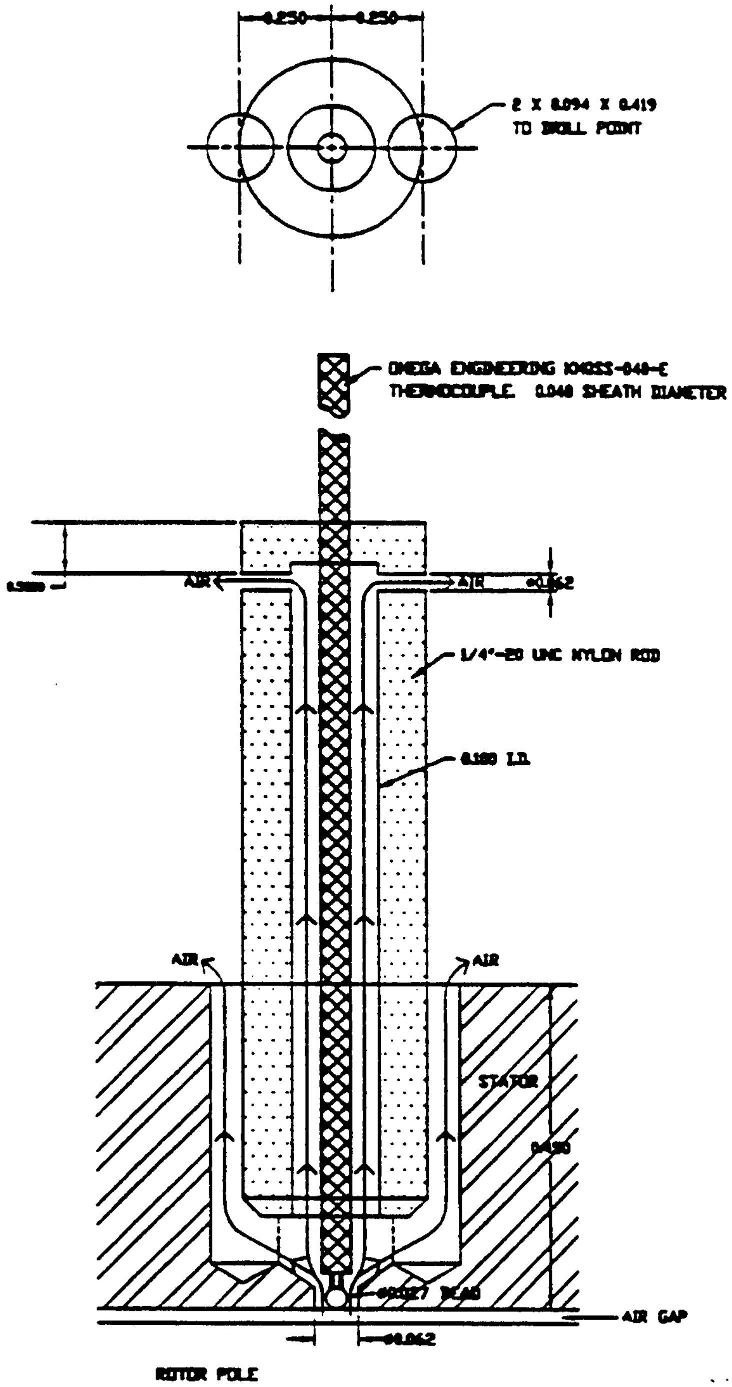
0.250
0.250
2 X 0.094 X 0.419
TO DRILL POINT
OMEGA ENGINEERING KMQSS-040-E
THERMOCOUPLE 0.040 SHEATH DIAMETER
AIR
AIR
Ø0.062
1/4"-20 UNC NYLON ROD
0.100 I.D.
AIR
AIR
STATOR
BEAD
AIR GAP
Ø0.062
ROTOR POLE

Figure 12: Thermocouple Installation for Measuring Gap Temperature

beads were embedded in thermally conductive epoxy and installed within 0.010 inch of the outside bearing sleeve.

3.4 Experimental Methods

3.4.1 Daily Experiment Preparation

Approximately three hours of experiment preparation was allotted each day before beginning data collection. This three hour period was conservative, however, it assured that the purge air supply to the IR sensor enclosure had reached steady state conditions, that the oven and rotor specimens had achieved a uniform temperature of approximately 250°F and that the thermocouple reference junction ice bath had achieved a constant temperature.

Throughout the day, ambient dry-bulb and wet-bulb temperatures were measured along with barometric pressure. This data was used in calculating the mass flow rate of the axial air flow measured with the venturi meter as presented in Appendix F. Further, once each day, the calibration of the IR sensor was validated in accordance with the method presented in Appendix D.

3.4.2 Typical Data Collection

A heated rotor specimen is removed from the oven and bolted to the shaft hub of the air turbine. The stator and air inlet chamber assembly are then slipped over the rotor and aligned with the six bolt holes in the air turbine. Three bolts are installed to secure the assembly to the turbine. The assembled RTTR is then placed on a support cradle. The compressed air hose is connected to the bottom of the air turbine and the six 3/4" ID vinyl tubes that supply axial air flow are attached to the air inlet chamber.

Approximately three minutes elapse from when the rotor test specimen contacts the shaft hub of the air turbine until data acquisition begins. The analyses of the test data assume an initial uniform temperature of the rotor core and shaft hub. Appendix I presents an analysis of the rotor and shaft hub that indicates that they approach thermal equilibrium in approximately 40 seconds, well before start of data collection.

The data acquisition system is started and the air turbine is brought up to desired speed by manually modulating the globe valve on the compressed air supply. For the cases where there is axial flow, the axial blower is started after the rotor reaches the desired test speed. The test continues until one of two conditions are met. Either the compressed air system cannot continue to deliver sufficient air to maintain the desired rotor speed (typically the case for high rotor speeds) or the temperature of the rotor core drops below approximately 120°F.

Upon completion of the test, the data file is saved as an ASCII space delimited text file (*.prn) and named in accordance with the following convention:

File name: r3_30k_2.prn

Axial flow (0, no flow; 1, full flow; 2, half flow)

Nominal rotor speed in thousands (10K, 10,000 rpm, etc.)

Rotor specimen number (r1, r2, ...r6)

Typical data collected during a test are presented in Figures 13 and 14. This particular data is for Rotor 3 operating at a nominal 30,000 rpm and "Half" axial air flow.

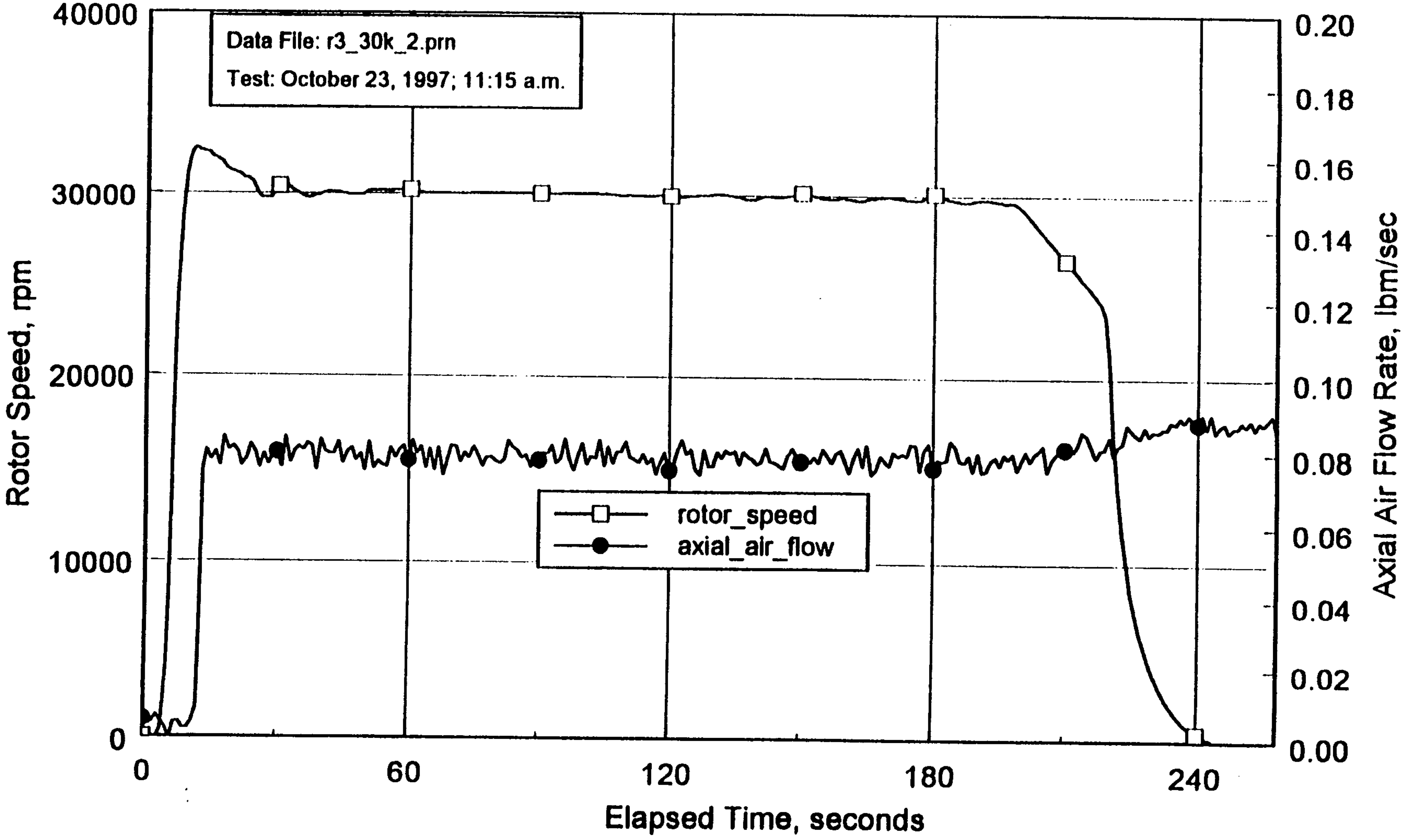

Figure 13: Rotor 3 Speed and Axial Airflow Data, Nominal 30,000 rpm and "Half" Axial Air Flow

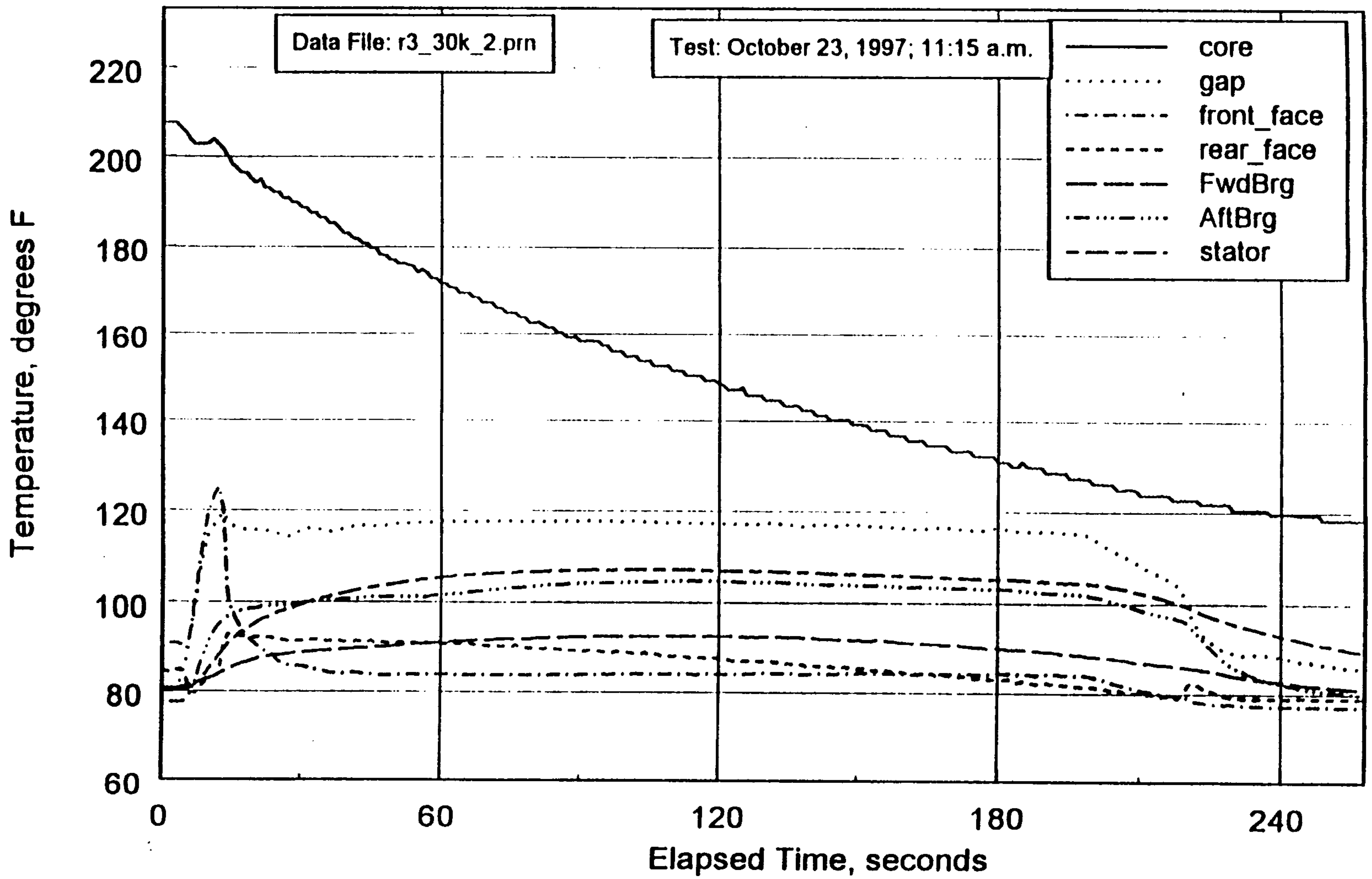

Figure 14: Rotor 3 Temperature Data, Nominal 30,000 rpm and "Half" Axial Air Flow

3.5 Test Matrix

Data was collected for a wide range of rotor speeds and axial flow conditions as indicated in Table 4.

Table 4: Test Matrix

No Axial Airflow						
Rotor Speed (rpm)	Rotor Number					
	1	2	3	4	5	6
5,000					x	
10,000	x	x	x	x	x	
15,000					x	
20,000	x	x	x	x	x	x
25,000					x	x
30,000	x	x	x	x	x	x

Full Axial Airflow (Approx. 0.16 lbm/s)						
Rotor Speed (rpm)	Rotor Number					
	1	2	3	4	5	6
5,000					x	
10,000	x	x	x	x	x	
15,000					x	
20,000	x	x	x	x	x	
25,000					x	
30,000	x	x	x	x	x	

Half Axial Airflow (Approx. 0.08 lbm/s)						
Rotor Speed (rpm)	Rotor Number					
	1	2	3	4	5	6
5,000					x	
10,000	x	x	x	x	x	
15,000					x	
20,000	Note 1	x	x	x	x	
25,000					x	
30,000	x	x	x	x	x	

Note 1: Infrared sensor failed on Tuesday October 27, 1997 just before this data was to be taken.

CHAPTER IV

ANALYSIS

4.1 General

The goal of the analysis is to infer the value of the convective film coefficient on the uninsulated rotor pole face based on the rate at which the center of the rotor core cools. This analysis actually requires the solution to two problems. First, it requires that the heat loss be estimated from all surfaces: front and rear faces, rotor pole faces (both insulated and uninsulated) and conduction losses through the shaft. Second, the film coefficient, h, must be based on a reference temperature which must be determined either through measurement or analysis.

4.2 Multi-lump Analysis of Rotors

The spatial and temporal temperature variations in the aluminum rotor core, epoxy insulation, stainless steel shaft hub and shaft are analyzed by discretizing the assembled system into 14 "lumps" or elements. Each lump is small and is considered to be at a uniform temperature at any given time. The temperature response of the elements is estimated by applying the law of conservation of energy to each individual element, accounting for heat fluxes at the boundaries of the element associated with conduction to adjacent elements or convection to air. The details of this analysis are presented in Appendix C.

Applying the law of conservation of energy to the 14 elements results in 13 simultaneous coupled, first-order, linear, ordinary differential equations. The reason there are 13 instead of 14 equations is because the temperature of element 14, the front end of the shaft, is known based on measurement. The differential equations are coupled because they are functions of each other's temperatures. Further, the equations are functions of the air temperatures surrounding the rotor due to convection at free surfaces. In fact, the analysis allows for unique temperatures for the front and rear surfaces of the rotor as well as each unique pole face.

A FORTRAN code called "Analyzer" was developed that solves this set of equations numerically using the Runge-Kutta method of Order Four. The code reads in all of the data collected by the data acquisition system during an experiment: elapsed time, rotor speed, rotor core temperature, stator temperature, inlet air temperature, outlet air temperature, gap temperature, shaft bearing temperatures, venturi differential pressure, static pressure at the inlet to the venturi, and differential pressure across the rotor. This data are stored in arrays and used to establish the time-varying boundary conditions of the model. The data was collected at a rate of 1 Hz. Thus, the boundary conditions of the multi-lump model are updated every second. The Runge-Kutta analysis uses a step size of 0.1 seconds and, based on the initial and boundary conditions, propagates in time a solution of the temperature distribution within the rotor. For rotors 1, 2, 3, and 4, only one face is exposed and the temperature of the center core is much more sensitive to changes in film coefficient on this pole face than on the insulated pole faces. Program Analyzer determines the value of the film coefficient for the uninsulated pole face such that the predicted time varying temperature of the center of the rotor core (element 1) best approximates the measured temperature of the center core at each point in time.

The difference between the measured and predicted temperatures of the center core are compared in a root mean square sense. For a test of "n" time increments, the rms error is calculated as:

$$RMS\ Error = \sqrt{\frac{1}{n}\sum_{i=1}^{n}\left(T_{core_{predicted}} - T_{core_{measured}}\right)_i^2} \tag{4-1}$$

Program Analyzer employs the root bisection method to find the value of film coefficient on the rotor poles that produces the minimum rms error. Typical values of rms error are between 0.5° and 1.0°F.

The multi-lump analysis and program Analyzer were verified for rotor 6 and rotor 1 against more precise solutions. These verifications are included in Appendix C.

4.3 Initial Conditions

Data acquisition commences at the same time that compressed air is supplied to the air turbine and the rotor begins ramping up to the desired speed. Although the rotor is brought up to speed as quickly as possible, typically 30 seconds elapse from initial start-up until a stable rotor speed is established. During this time, the rotor is cooling. At the time analysis begins, the rotor is not at a uniform temperature , spatial temperature gradients exist. Program Analyzer estimates the initial temperature distribution. The program requires three time inputs: initialization time, start time and ending time. The period between start and end times is when the program analyzes the data to determine the value of film coefficient. The period from initialization and start time is 10 seconds and serves to establish an initial temperature distribution in the rotor.

The initialization time of 10 seconds is based on the analytical model of an infinite cylinder. Arpaci[8], presents the solution for the temperature distribution within an infinite cylinder initially at a uniform temperature and then subjected to convective boundary condition.

$$\frac{T(r,t)-T_{\infty}}{T_{initial}-T_{\infty}} = 2\,Bi\,\frac{\sum_{n=1}^{\infty} e^{-\alpha\lambda_n^2 t} J_o(\lambda_n r)}{\left(\lambda_n^2 R_o^2 + Bi^2\right) J_o(\lambda_n R_o)} \tag{4-2}$$

where r is the radial distance from the center of the cylinder and R_o is the outside radius. The eigenvalues are the positive roots of the equation:

$$(\lambda_n R_o)\, J_1(\lambda_n R_o) - Bi\, J_o(\lambda_n R_o) = 0 \tag{4-3}$$

Heisler[9] has shown that for $Fo \equiv \frac{\alpha t}{R_o^2} \geq 0.2$, the series solution is well approximated by the first term in the series. Thus the time dependence of the temperature at any radial location in the cylinder is the same as the time dependence of the center of the cylinder. Therefore a constant, non-dimensionalized temperature gradient is established (at least for the case where the free-stream temperature is constant) given by:

$$\frac{T(r,t)-T_{\infty}}{T(0,t)-T_{\infty}} = J_o(\lambda_1 r) \tag{4-4}$$

A Fourier number of 0.2 corresponds to approximately 10 seconds for a cylinder 4.3 inches in diameter fabricated on 7075 aluminum.

Program Analyzer sets all of the elements of the model equal to the measure core temperature at time $t = t_{init}$. The analysis proceeds for 10 seconds until $t = t_{start}$. At this time, the temperature gradients are non-dimensionalized with respect to the measured gap temperature. The core temperature (element 1) is then set equal to the measured core temperature at time $t = t_{start}$ and the temperatures of the remaining elements are calculated using the non-dimensionalized temperature gradient. This establishes the "initial condition" of the rotor at time t_{start}.

4.4 Boundary Conditions

4.4.1 Convection from Front and Rear Rotor Faces

Heat loss from the front and rear faces was estimated based on the research by Popiel, et al.[10]. Popiel's investigation was for the case of a rotating disk in still air in an infinite medium. It is expected that these predicted values of film coefficient will be low for the front face when there is forced axial flow. These predicted values may be high for the front face when there is no axial flow because the air is recirculated within the air inlet housing. Popiel's model is used to give a reasonable first estimate of the film coefficient.

The value of the film coefficient on the front and rear faces was perturbated in the analyses to determine its effect on the final results.

The average film coefficient, $\bar{h}$, over the front and rear surface is estimated using the relation:

$$Nu_{avg} = \frac{\bar{h}\, R_o}{k} 0.0145\, \mathrm{Re}^{0.8} \tag{4-5}$$

where the Reynolds number for the disk is defined as:

$$\mathrm{Re} = \frac{\omega\, R_o^2}{\nu} \tag{4-6}$$

4.4.2 Shaft Temperature

It was not possible to directly measure the temperature of the end of the shaft where it transitions to the shaft hub (referred to as element 14 in the multi-lump analysis). This is because the rotor and air turbine are very closely coupled, and, similar to trying to measure the rotor core temperature, the speed of the shaft is too fast to use a direct contact device. Figure 15 presents a sketch of the shaft installed within the air turbine supported by front and rear steel ball bearings. Clearly, the front bearing surrounds the portion of the shaft identified as element 14. Further, the temperatures of the bearing housings are monitored with thermocouples. Since the bearing housing and roller bearings are manufactured from highly conductive steel, it may be a reasonable assumption that the temperature of the shaft is approximately the same as the bearing housing.

The validity of this assumption was tested using rotor 5 for the case where there is no forced flow and the rotor is stationary. The details of this study are presented in Appendix J. The results of the experiment gave a positive indication that the forward bearing temperature is a good estimate of the shaft temperature. However, this test is for the case when the shaft is not spinning and there is no heat generated within the bearing due to friction. A further verification that the bearing temperature is a reasonable estimate of the shaft temperature is based on rotor 6 experimental data.

Rotor 6 is used to validate the computer model and boundary conditions used in the analyses of rotors 1 through 5. Because rotor 6 is simply an insulated disk, it is possible to accurately estimate the convective film coefficient on its exposed peripheral face. The remaining boundary conditions are associated with conduction losses through the shaft and convection losses through the front and rear faces. If analysis of

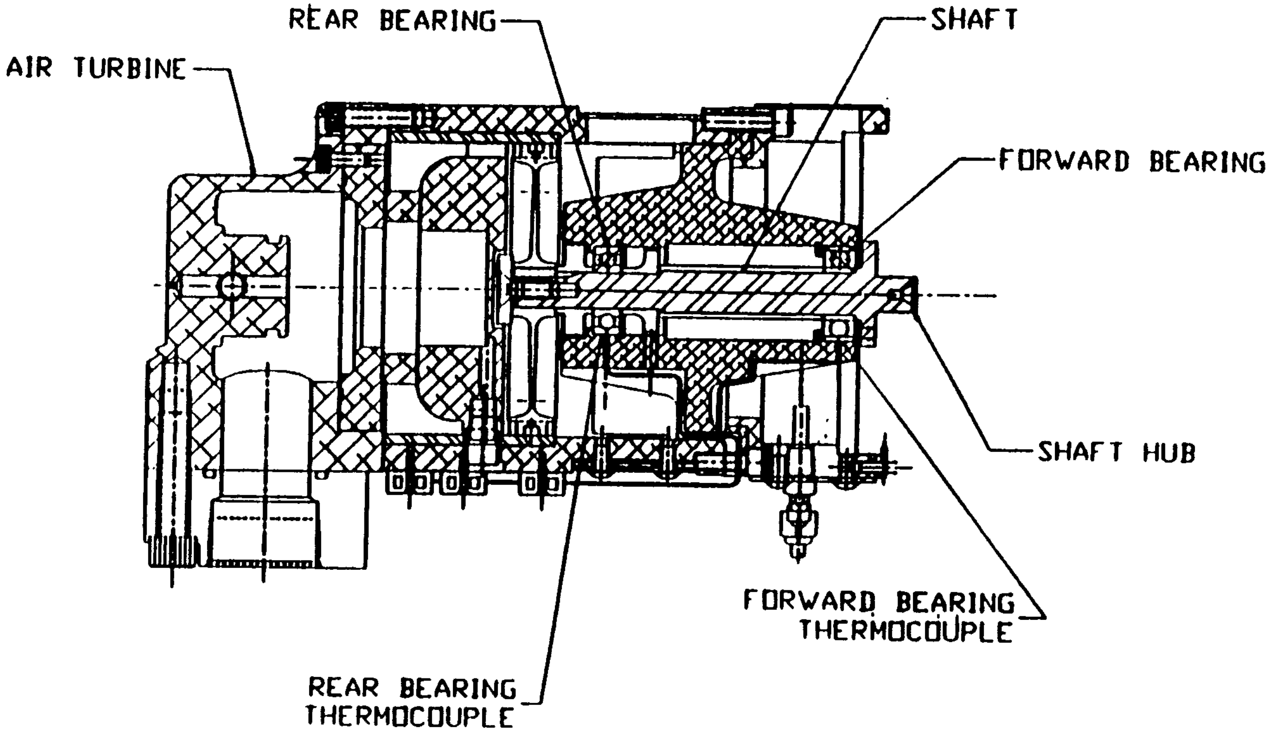
REAR BEARING
SHAFT
AIR TURBINE
FORWARD BEARING
SHAFT HUB
FORWARD BEARING THERMOCOUPLE
REAR BEARING THERMOCOUPLE

Figure 15: Temperature Monitoring of Turbine Shaft Bearings

experimental data predicts values of convective film coefficient on the peripheral surfaces consistent with the analytical model, then it is reasonable to conclude that the boundary conditions used in the model are valid.

4.5 Estimate of Convective Film Coefficient on Rotor 6 Peripheral Surface

The high rotational speeds of the rotor coupled with the small clearance gap between the smooth rotor and stator results in high shear stresses and large velocity gradients in the air in the gap. These cause viscous dissipation of mechanical to thermal energy, resulting in aerodynamic heating of the air. Previous investigators, such as Gazely[2] , did not account for viscous dissipation because the speed of their rotors were low and viscous effects were negligible.

Prediction of the convective film coefficient, accounting for aerodynamic heating effects, was accomplished by analyzing the air flow in the annular gap between the rotor and stator surfaces. The gap height, h_g, is much smaller than the rotor radius so that this flow may be considered as wall driven flow between two flat plates as shown in Figure 16.

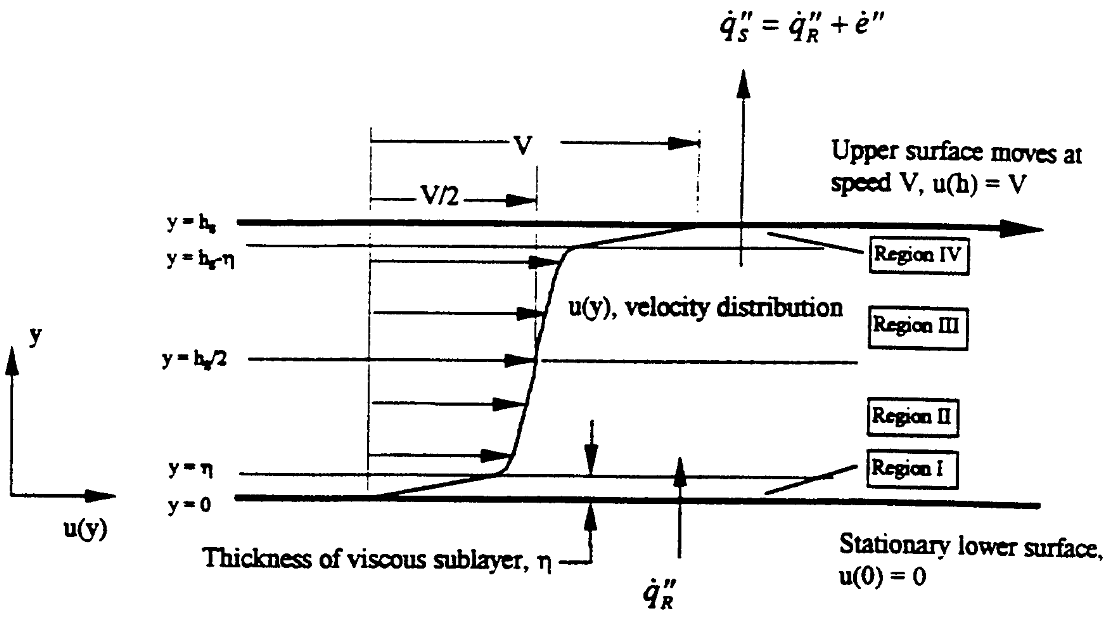
$\dot{q}_S'' = \dot{q}_R'' + \dot{e}''$
V
V/2
Upper surface moves at speed V, u(h) = V
y = h_s
y = h_s-η
y = h_s/2
y = η
y = 0
y
u(y)
u(y), velocity distribution
Region IV
Region III
Region II
Region I
Thickness of viscous sublayer, η
$\dot{q}_R''$
Stationary lower surface, u(0) = 0

Figure 16: Velocity Distribution in Turbulent Wall Driven Flow

In Figure 16 the rotor has been illustrated as the lower, stationary surface with heat flux $\dot{q}_R''$ transferred from the rotor to the air. The upper surface is shown as the stator surface with heat flux $\dot{q}_S'' = \dot{q}_R'' + \dot{e}''$ transferred from the air to the stator. Here $\dot{e}''$ is the rate of viscous energy dissipated per unit area in the form of heat due to shear work at the control surface between the moving plate and the air. Because the thermal mass of the air in the gap is small, the temperature distribution between the plates approaches a steady state profile almost instantaneously even when the rotor and stator temperatures vary with time. Thus, the analysis to determine the air temperature distribution assumes steady state conditions. In this figure the lower surface is shown as stationary and the upper surface is shown as moving to the right with speed, V, to be consistent with standard formulations of this problem. In reality, it is the rotor which moves and the stator that remains stationary; however, it is their relative motion which is of concern and the above model is an accurate portrayal of the problem.

4.5.1 Velocity Distribution

The "S" shaped velocity distribution illustrated qualitatively in Figure 16 is consistent with turbulent flow. Laminar wall driven flow is characterized by a linear velocity distribution. Laminar flow becomes unstable and transitions to turbulent flow for $\mathrm{Re}_{h_g} = \dfrac{V\,h_g}{\nu} \approx 3000$ [11]. This implies that for a gap height of 0.020 inches, laminar flow would prevail for rotor 6 disk speeds up to about 15,000 rpm. However, the flow is not between truly parallel plates and for a rotating inner cylinder a better parameter for assessing the stability of the flow is the Taylor number, Ta. For a small clearance between the inner rotating cylinder of radius r_0 and stationary outer cylinder of radius r_1, the critical value for instability is given by $Ta \equiv r_0\,(r_1 - r_0)^3\,\dfrac{\omega_0^2}{\nu^2} \approx 1700$ [11]

Applying this criterion to the rotor 6 geometry indicates that for a 0.020 inch clearance gap, the flow will transition to turbulent for rotational speeds greater than approximately 2,300 rpm. Further, Gazley[2] cites work by Taylor where the critical Reynolds number for transition is related to a dimensionless curvature factor, R/h_g such that $\left(\mathrm{Re}_{h_g}\right)_{crit} = 41.1\left(\dfrac{R}{h_g}\right)^{1/2}$

Applying this criterion, the flow transitions to turbulent for $\mathrm{Re}_{h_g} > 426$ which corresponds to a rotational speed of only 525 rpm. It is clear that for larger clearance gaps the transition to turbulence occurs at even lower speeds. Therefore, the flow will be assumed to be turbulent for all test conditions.

While the shear work imparted to the fluid by the high speed upper wall will affect the temperature distribution in the gap, it is reasonable to assume that the velocity distribution will be minimally affected by aerodynamic heating and that the velocity profile will be governed by the hydrodynamic law of the wall. For this analysis, the two layer law of the wall presented by Kays and Crawford [12] is employed which considers two distinct regions: a *viscous sublayer* for which we assume $\nu >> \varepsilon_M$ and a fully turbulent region for which $\varepsilon_M >> \nu$. Further, the law of the wall is for the current case where there is no pressure gradient in the flow direction (constant free-stream velocity) and solid walls (no transpiration). The law of the wall is based on experimental observations of the velocity distributions for many different fluids and velocities. It is found that when the data is plotted for in terms of dimensionless parameters, referred to as wall coordinates, the data from all of the experiments consistently collapse to a common form. The wall coordinates are defined as a dimensionless velocity, u^+, and a dimensionless distance from the wall, y^+ given by:

$$u^+ \equiv \frac{u}{u_\tau} \quad \text{and} \quad y^+ \equiv \frac{y\,u_\tau}{\nu}$$

where u_τ, the *friction velocity* or *shear velocity*, is a function of the shear stress at the wall, τ_o, and is defined as:

$$u_\tau \equiv \sqrt{\tau_o/\rho}\,.$$

For the viscous sublayer region, $0 \leq y^{+} \leq 10.8$, the law of the wall is given by:

$$u^{+} = y^{+} \tag{4-7}$$

and, for the fully turbulent region, $10.8 \leq y^{+} \leq 1{,}000$, the law of the wall is:

$$u^{+} = 2.44 \ln y^{+} + 5.0 \tag{4-8}$$

Equation (4-7) is quite accurate for $y^{+} < 5$ and equation (4-8) matches experimental data well for $y^{+} > 40$. In the intermediate region, the experimentally measured values of u^{+} are less than those predicted by this two layer model; suggesting that the effective sublayer extends further into the boundary layer.

Employing symmetry about the centerline, the region between the rotor and stator surfaces was divided into four regions as shown in Figure 16. Regions I and IV represent the near wall regions and Regions II and III represent the fully turbulent regions. The velocity profile in each region was modeled in accordance with the applicable hydrodynamic law of the wall.

The shear stress, τ_{yx}, is constant throughout the flow and the shear stress at the wall must be estimated to calculate the friction velocity, u_{τ}, for use in equations 4-7 and 4-8. The law of the wall is used to estimate τ_{o}. Although the logarithmic law of the wall best fits the experimental data, the data in the turbulent region can also be approximated by a power law of the wall given by:

$$u^{+} = 8.75\, {y^{+}}^{1/7} \tag{4-9}$$

Like the logarithmic law of the wall, this expression is restricted to constant free stream velocity with no transpiration. The advantage of the power law of the wall is that it allows τ_o to be solved for directly. Evaluating (4-9) at the edge of the boundary layer where $y = \delta$ and $u = u_\infty$ yields:

$$\frac{u_\infty}{\sqrt{\tau_o/\rho}} = 8.75\left(\frac{\delta\sqrt{\tau_o/\rho}}{\nu}\right)^{1/7} \tag{4-10}$$

and τ_o is calculated to be:

$$\tau_o = 0.0225\,\rho u_\infty^2\left(\frac{\delta\, u_\infty}{\nu}\right)^{-1/4} \tag{4-11}$$

Equation 4-11 is referred to as the Blasius relation[13] and estimates the shear stress on a flat plate due to the velocity distribution in a fully developed turbulent flow associated with a constant velocity free-stream. This equation is used to estimate the shear stress for the flow in the annular gap between the rotor and stator. The hydrodynamic boundary layer grows from both the upper and lower surfaces, meeting in the center. Taking the boundary layer thickness as half the gap height, $\delta = h_g/2$ and the free-stream velocity as $u_\infty = V/2$, the shear stress is evaluated as:

$$\tau_o = 0.00795\,\rho V^2\left(\frac{h_g\, V}{\nu}\right)^{-1/4} \tag{4-12}$$

Defining the Reynolds number based on gap height as:

$$\mathrm{Re}_{h_g} = \frac{V\, h_g}{\nu} \tag{4-13}$$

The shear stress can be written as:

$$\tau_o = 0.00795\,\rho V^2\,\mathrm{Re}_{h_g}^{-1/4} \tag{4-14}$$

Further, defining the skin friction coefficient as:

$$C_f \equiv \frac{\tau_o}{1/2\,\rho V^2} \tag{4-15}$$

the friction coefficient is related to the Reynolds number by

$$C_f = 0.0159\,\mathrm{Re}_{h_g}^{-1/4} \tag{4-16}$$

Using equation 4-14 as an estimate of the wall shear stress, the velocity distribution across the annular gap is approximated by applying the applicable law of the wall to each region and enforcing the conditions that the velocity profile be continuous at the boundaries between the regions and that $u(0) = 0$ and $u(h) = V$. The equations developed for the four domains satisfy all of the boundary conditions apriori except $u(h) = V$. This condition is achieved through an iterative calculation for the thickness of the viscous sublayer, η. A typical value of y^+ evaluated at the edge of the viscous sublayer is 11.6, which is in reasonable agreement with the applicable range of the law of the wall for this region.

It is found that the velocity varies linearly with y in the viscous sublayers and varies logarithmically in the turbulent domains.

4.5.2 Temperature Distribution

The temperature distribution across the gap is affected by the heat flux from the lower plate as well as the viscous dissipation of boundary work into heat. The total energy flux due to viscous dissipation, $\dot{e}''$, is equal to the rate of work done on the air in the gap at the control surface between the air and the plate moving at speed V.

$$\dot{e}'' = \tau_o V \tag{4-17}$$

While $\dot{e}''$ is the total energy flux due to viscous dissipation, the conversion from mechanical to thermal energy is not uniform across the gap. At any point in the flow, the viscous dissipation per unit volume is given by the product of the shear stress and spatial velocity gradient.

$$\dot{e}''' = \tau_{yx} \frac{\partial u}{\partial y} \tag{4-18}$$

The shear stress across the gap is constant, however, the velocity gradient varies continuously across the gap height and is greatest in the viscous sublayers. As a strong assumption, in this analysis it is assumed that all of the energy conversion occurs equally in the upper and lower viscous sublayers.

At any location in the flow, Fourier's law of heat conduction for turbulent flow can be written as:

$$\frac{\dot{q}''}{\rho c_p} = -(\alpha + \varepsilon_H)\frac{dT}{dy} \tag{4-19}$$

Similar to the hydrodynamic boundary layer, $\alpha >> \varepsilon_H$ in the viscous sublayer and $\varepsilon_H >> \alpha$ in the fully turbulent region.

In region I, the viscous energy dissipation varies linearly from 0 to $\dot{e}''/2$ and equation 4-19 can be written as:

$$\frac{\dot{q}''}{\rho c_p} = \frac{\dot{q}''_R}{\rho c_p} + \frac{\dot{e}''}{2\rho c_p}\left(\frac{y}{\eta}\right) = -\alpha \frac{dT}{dy} \tag{4-20}$$

This ordinary differential equation can be solved to give $T(y)$ for region I subject to the boundary condition that $T(0) = T_R$. The temperature is found to be a quadratic function of y.

In region II, the velocity gradients are much less than in the viscous sublayer and it is assumed that there is no viscous heat dissipation and that the heat flux is constant. Equation 4-19 can be written as:

$$\frac{\dot{q}''}{\rho c_p} = \frac{\dot{q}''_R}{\rho c_p} + \frac{\dot{e}''}{2\rho c_p} = -\left(\alpha + \varepsilon_H\right)\frac{dT}{dy} \tag{4-21}$$

In this turbulent region the value of $\left(\alpha + \varepsilon_H\right)$ must be determined. This term is estimated by employing the concept of turbulent Prandtl number. Kays and Crawford define turbulent Prandtl number in terms of eddy diffusivity for momentum and eddy diffusivity for heat transfer.

$$\mathrm{Pr}_t \equiv \frac{\varepsilon_M}{\varepsilon_H} \tag{4-22}$$

The value of Pr_t has been measured in the "logarithmic region" of the boundary layer (referring to the law of the wall) for different fluids and found that it ranges from about 0.7 to 0.9. Kays and Crawford report that most of the data suggests a turbulent Prandtl number around 0.85. It is interesting that the turbulent Prandtl number for common fluids such as air and water are essentially the same and there is little effect of the value of the molecular Prandtl number. The value $\mathrm{Pr}_t = 0.85$ will be used for this analysis.

Since in the turbulent region the eddy diffusivities for momentum and heat transfer are much greater than their molecular counterparts (which dominate in the viscous sublayers), the turbulent Prandtl number can also be approximated as:

$$\mathrm{Pr}_t \approx \frac{\nu+\varepsilon_M}{\alpha+\varepsilon_H} \tag{4-23}$$

and

$$\alpha+\varepsilon_H \approx \mathrm{Pr}_t \left(\nu+\varepsilon_M\right) \tag{4-24}$$

The eddy diffusivity for momentum is defined such that

$$\frac{\tau}{\rho}=\left(\nu+\varepsilon_M\right)\frac{\partial u}{\partial y} \tag{4-25}$$

Since for wall driven flow τ/ρ is constant, the value of ε_M varies with y to account for the variation in the velocity gradient. Solving for $\left(\nu+\varepsilon_M\right)$,

$$\left(\nu+\varepsilon_M\right)=\frac{\left(\dfrac{\tau_o}{\rho}\right)}{\left(\dfrac{du}{dy}\right)} \tag{4-26}$$

The velocity distribution for region II has been estimated and the velocity gradient can be calculated. It is found that $\left(\nu+\varepsilon_M\right)$ varies linearly with y. Multiplying this expression by Pr_t and substituting it for $\left(\alpha+\varepsilon_H\right)$ in equation 4-21 results in an ordinary differential equation in y. The solution to this differential equation is a logarithmic function of y.

Analyses in regions III and IV proceed in the same manner as regions I and II. Boundary conditions are applied such that $T(0) = T_R$ and that the temperature distribution is continuous across the gap. The temperature of the stator is not prescribed, but rather calculated. It is a function of the velocity profile, $\dot{q}''_R$, $\dot{e}''$, and T_R.

4.5.3 Equations for Velocity and Temperature Distributions for Regions I through IV

Region I $0 \le y \le \eta$

$$u_1(y) = \frac{\tau_o}{\rho v} y \tag{4-27}$$

$$T_1(y) = T_R - \frac{\dot{e}''}{4\alpha \rho c_p} \frac{y^2}{\eta} - \frac{\dot{q}_R'' y}{\alpha \rho c_p} \tag{4-28}$$

Region II $\eta \le y \le h_g / 2$

$$u_2(y) = 2.44\, u_\tau \ln\left(\frac{y}{\eta}\right) + u_1(\eta) \tag{4-29}$$

$$T_2(y) = T_1(\eta) - \frac{2.44\,\mathrm{Pr}_t}{u_\tau}\left(\frac{\dot{q}''}{\rho c_p} + \frac{\dot{e}''}{2\rho c_p}\right) \ln\left(\frac{y}{\eta}\right) \tag{4-30}$$

Region III $h_g / 2 \le y \le h_g - \eta$

$$u_3(y) = 2.44\, u_\tau \ln\left(\frac{h_g}{2(h_g - y)}\right) + u_2\left(\frac{h_g}{2}\right) \tag{4-31}$$

$$T_3(y) = T_2\left(\frac{h_g}{2}\right) - \frac{2.44\,\mathrm{Pr}_t}{u_\tau}\left(\frac{\dot{q}_R''}{\rho c_p} + \frac{\dot{e}''}{2\rho c_p}\right) \ln\left(\frac{y}{2(h_g - \eta)}\right) \tag{4-32}$$

Region IV $h_g - \eta \le y \le h_g$

$$u_4(y) = -\frac{\tau_o}{\rho v}(h_g - \eta - y) + u_3(h_g - \eta) \tag{4-33}$$

$$\begin{aligned} T_4(y) = T_3(h_g - \eta) + \frac{\dot{e}''}{2\rho c_p \alpha}\left(h_g y - \frac{y^2}{2}\right) - \frac{\dot{q}_R'' + \dot{e}''}{\rho c_p \alpha} y + \\ \frac{\dot{q}_R'' + \dot{e}''}{\rho c_p \alpha}(h_g - \eta) - \frac{\dot{e}''}{2\rho c_p \alpha \eta}\left[h_g (h_g - \eta) - \frac{(h_g - \eta)^2}{2}\right] \end{aligned} \tag{4-34}$$

4.5.4 Heat Transfer Analysis

Employing the above equations, the velocity and temperature field can be approximated for any combination of input parameters: rotor speed, gap height, rotor temperature and stator temperature. The resulting temperature field yields the heat fluxes $\dot{q}_R''$ and $\dot{q}_S''$. The convective film coefficient between the rotor and the air and the stator and the air can be calculated as:

$$h_{rotor} = \frac{\dot{q}_R''}{T_R - T_{aw}} \tag{4-35}$$

$$h_{stator} = \frac{\dot{q}_S''}{T_{aw} - T_S} \tag{4-36}$$

where T_{aw} is the adiabatic wall temperature.

The adiabatic wall temperature is used as the reference temperature to account for the effect of aerodynamic heating. Since the velocity gradients at the rotor and stator walls are the same, they will have the same convective film coefficient. Using the adiabatic wall temperature as the reference temperature results in a larger ΔT for the stator than the rotor, thus accounting for the fact that the heat rejected to the stator is equal to the heat input from the rotor surface plus the energy flux associated with viscous dissipation.

For the case of the high speed external boundary layer flow, Kays and Crawford[12] formulate an energy equation for the external turbulent boundary layer based on stagnation enthalpy.

$$\rho \bar{u} \frac{\partial \bar{i}^*}{\partial x} + \rho \bar{v} \frac{\partial \bar{i}^*}{\partial y} - \frac{\partial}{\partial y}\left(\frac{k_{eff}}{C_p}\frac{\partial \bar{i}^*}{\partial y}\right) = \left[\left(1 - \frac{1}{\mathrm{Pr}_{eff}}\right)\mu_{eff}\frac{\partial\left(1/2\, u^2\right)}{\partial y}\right] \tag{4-37}$$

where the stagnation enthalpy is defined as:

$$i^{*} = i + \tfrac{1}{2} u^{2} \tag{4-38}$$

Here, the effect of turbulence is accounted for using "effective" values of thermal conductivity, viscosity and Prandtl number defined as:

$$k_{eff} = k + k_{t} = k + \rho c_{p}\, \varepsilon_{H} \tag{4-39}$$

$$\mu_{eff} = \mu + \mu_{t} = \mu + \rho c_{p}\, \varepsilon_{M} \tag{4-40}$$

$$\Pr_{eff} = \frac{\mu_{eff}}{k_{eff} / c_{p}} \tag{4-41}$$

The advantage of this formulation of the energy equation is that for a fluid with Prandtl number equal to 1, the right hand side, which represents heat generation due to viscous shear, goes to zero. Assuming constant specific heats, equation 4-37 can be written in terms of the stagnation temperature, defined as:

$$T^{*} \equiv T + \frac{u^{2}}{2 C_{p}} \tag{4-42}$$

It is found that for high speed flow over a flat plate, the boundary conditions based on T^{*} are identical to the boundary conditions for low velocity flow where viscous heat dissipation is negligible. In the low velocity case, the solution to the energy equation was reduced to a local convection coefficient, h, such that the heat flux from the wall could be written:

$$\dot{q}_{o}'' = -k\left(\frac{\partial T}{\partial y}\right)_{0} = h\left(T_{0} - T_{\infty}\right) \tag{4-43}$$

For the high velocity case, it can be shown that

$$\dot{q}_o'' = -k\left(\frac{\partial T}{\partial y}\right)_0 = h\left(T_0 - T_\infty^{\bullet}\right) \tag{4-44}$$

In other words, for the case of high velocity flow and Pr = 1, replacing the free-stream temperature with the free-stream stagnation temperature accounts for the influence of aerodynamic heating. The adiabatic wall temperature is the temperature of the wall, T_0, at which there is no heat flux. It is apparent that the adiabatic wall temperature is equal to the free-stream stagnation temperature.

$$T_{aw} = T_\infty + \frac{u_\infty^2}{2\,C_p}; \quad \mathrm{Pr} = 1 \tag{4-45}$$

For gases, such as air, whose Prandtl numbers are not equal to 1, the adiabatic wall temperature is less than the free-stream stagnation temperature and is represented as:

$$T_{aw} = T_\infty + r_c\,\frac{u_\infty^2}{2\,C_p} \tag{4-46}$$

where r_c is known as the recovery factor. It is a measure of the external kinetic energy that is recovered as internal energy at the wall where the flow has been brought to rest by the frictional stresses in the boundary layer.[14] Values of r_c for external air flows typically vary from 0.87 to 0.91 and for turbulent flow a frequent approximation for the recovery factor is $r_c \approx \mathrm{Pr}^{1/3}$.

Employing the concept of an adiabatic wall temperature as the reference temperature for wall-driven flow, the recovery factor is calculated by setting the rotor heat flux to zero. The resulting temperature distribution is then based on the prescribed rotor temperature and the shear work imparted by the moving wall, τV. Unlike the case of an external boundary layer where there is a free-stream temperature, T_∞, a temperature must be defined within the gap analogous to the free-stream temperature. Two representative temperatures were investigated, T_{avg} and T_m defined as:

$$T_{avg} \equiv \frac{T_R + T_s}{2} \tag{4-47}$$

$$T_m \equiv \frac{1}{h_g}\int_0^h T(y)\,dy \tag{4-48}$$

Using these as reference temperatures, the adiabatic wall temperature can be written:

$$T_{aw} = T_{avg} + r_{c_1}\frac{u_\infty^2}{2\,C_p} \tag{4-49}$$

$$T_{aw} = T_m + r_{c_2}\frac{u_\infty^2}{2\,C_p} \tag{4-50}$$

where the "free-stream" velocity is taken to be the velocity at the mid-height of the gap, i.e. $u_\infty = V/2$.

In both cases the adiabatic wall temperatures are the same, the equations simply use different basis temperatures for which to calculate the recovery factor.

A typical air temperature distribution is presented in Figure 17. The static temperature, T, is plotted along with T^*. The velocity used in calculating T^* was defined separately over the lower half (domains I and II) and the upper region (domains III and IV) as follows:

Domains I and II: $T^* = T + \dfrac{u^2}{2\,C_p}$

Domains III and IV: $T^* = T + \dfrac{(V-u)^2}{2\,C_p}$

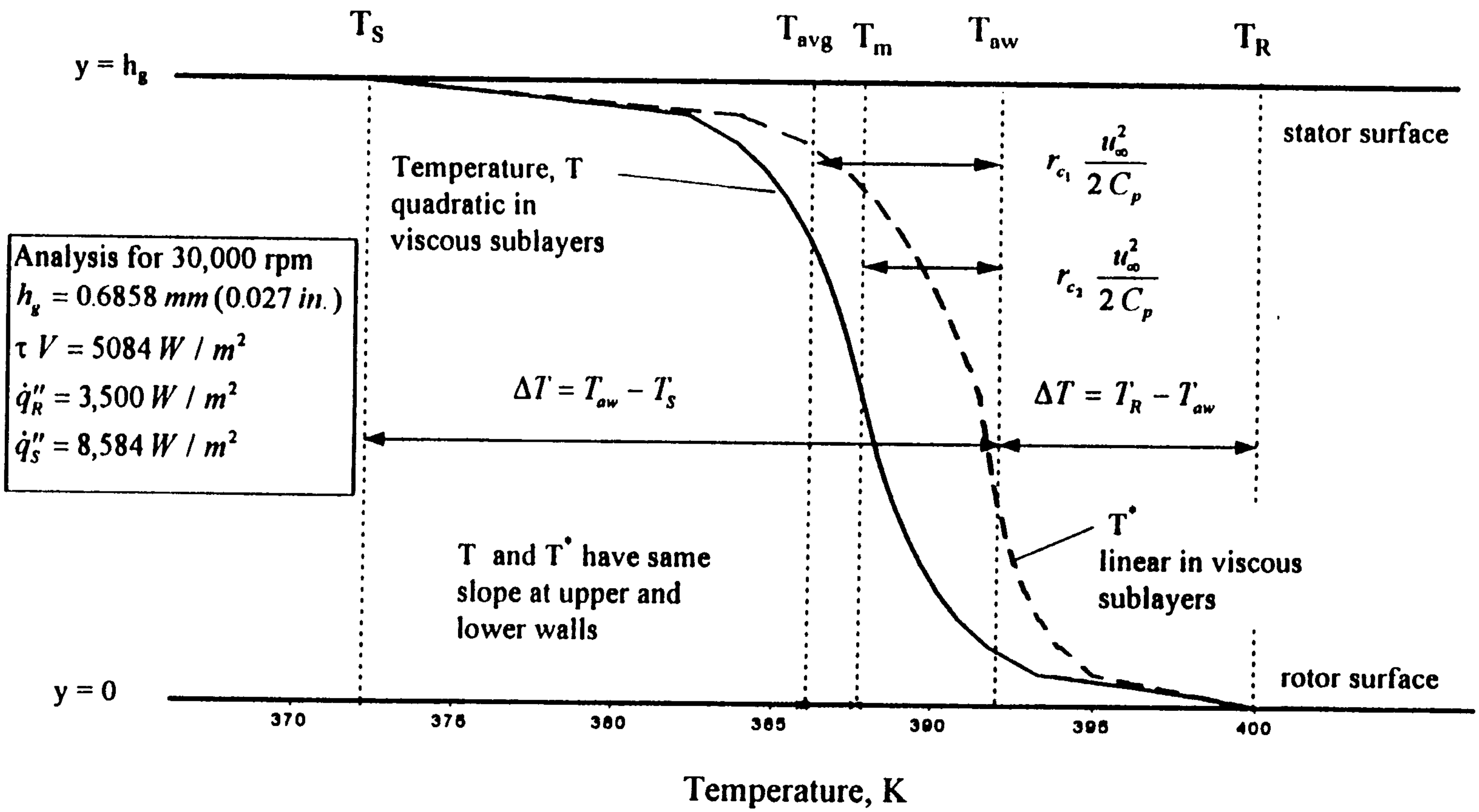

Figure 17: Static and Total Temperature Distribution in High Speed, Wall Driven Flow

Note the difference between the curves for T and T^*. The static temperature is quadratic in the viscous sublayers as a result of aerodynamic heating, whereas the profile for T^* is linear, consistent with no viscous heating. Both profiles have the same slope at the rotor and stator walls since they both accomplish the same heat transfer at the walls. Defining h based on the adiabatic wall temperature yields the same value of h for the rotor and the stator. Similar to the case of high speed flow over a flat plate, calculating the heat flux based on the temperature difference between the wall and the adiabatic wall temperature automatically accounts for the effect of viscous dissipation. I.e., $\dot{q}_R'' = h\left(T_R - T_{aw}\right)$ and $\dot{q}_S'' = h\left(T_{aw} - T_S\right)$. The fact that $T_{aw} - T_S > T_R - T_{aw}$ assures that heat rejected to the stator is larger than the heat flux from the rotor by the amount $\dot{e}'' = \tau V$.

A Mathcad™ program (see Appendix K) was prepared that calculates the temperature distribution and adiabatic wall temperature for wall driven flow as a function of gap height, rotor speed (wall speed) and rotor temperature. This program was employed to generate results using gap heights of 0.5080, 0.6858, 0.8890 and 1.016 mm (0.020, 0.027, 0.035 and 0.040 inch) and rotor speeds ranging from 5,000 to 55,000 rpm. Figure 18 presents the analytical results for the recovery factors, r_{c_1} and r_{c_2}. It was found that the values of recovery factor are solely functions of Reynolds number. Note that these values are generally greater than one, whereas, for external boundary layer flow, $r_c = 1$ was the maximum value. This is because, unlike a free-stream boundary layer where the shear varies from a maximum value at the wall to zero at the edge of the boundary layer, the shear stress in wall-driven flow is constant, resulting in greater viscous

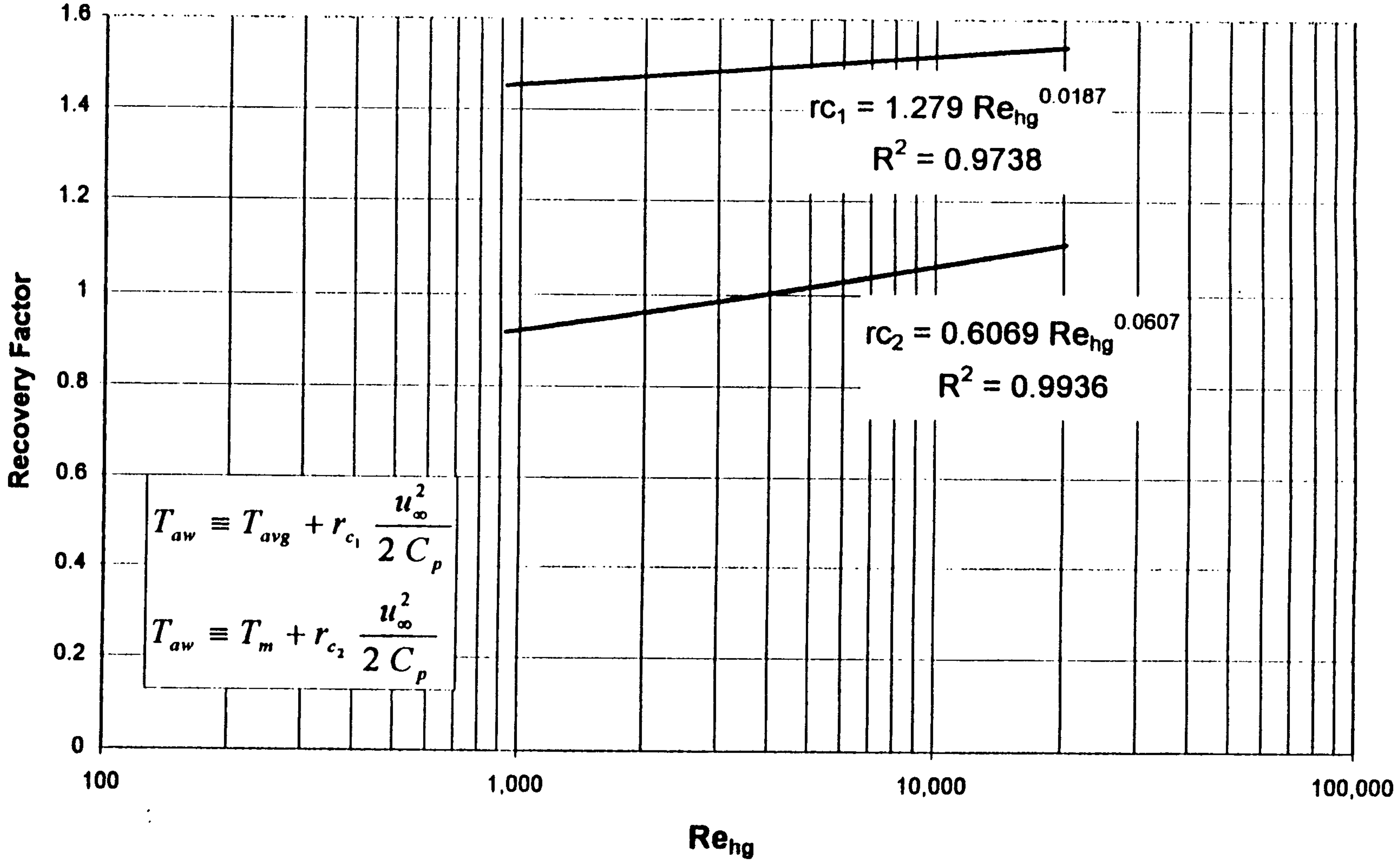

Figure 18: Recovery Factor For High Speed, Wall Driven Flow

dissipation. For air, these recovery coefficients, based on Blasius shear stress, can be characterized as:

$$r_{c_1} \cong 1.279\ \mathrm{Re}_{h_z}^{0.0187} \tag{4-51}$$

and $$r_{c_2} \cong 0.6069\ \mathrm{Re}_{h_z}^{0.0607} \tag{4-52}$$

Further, the analytical model verifies that when the heat transfer coefficient is based on the adiabatic wall temperature, it is solely a function of Reynolds number. The Stanton number, defined as $St \equiv \dfrac{h}{\rho\, C_p\, V}$, is presented in Figure 19 and is characterized by the empirical relation:

$$St \cong 0.0249\ \mathrm{Re}_{h_z}^{-0.2687} \tag{4-53}$$

It should be noted that an analytical investigation of high speed turbulent plane Couette flow was also conducted by Korkegi and Briggs[15, 16] and considers the effects of compressibility on the velocity distribution, friction coefficient and Stanton number. Their analysis was based on the von Karman mixing length model. A single differential equation is developed in terms of wall coordinates, density and the von Karman constant ($\kappa = 0.4$), representing the entire flow field between the two plates. Due to variations in density, the centerline is not a symmetry plane for the velocity field. Further, as the speed of the moving plate increases, the velocity gradients in the center region of the flow become greater, thus presenting an increased percentage of viscous heat generation in this region. However, Korkegi's investigation considers plate velocities up to Mach 10. The experimental data for the present investigation is limited to 30,000 rpm which yields a Mach number less than 0.5. At these relatively low speeds, Korkegi's prediction of the velocity distribution yields a relatively linear shape in the viscous sublayer and logarithmic profile in the fully turbulent region in agreement with the simpler four domain analysis. Further, the velocity gradients in the center turbulent region are appreciably less at these lower speeds and the assumption that most of the viscous heat generation occurs in the viscous sublayers adjacent to the walls is reasonable.

4.6 Computer Model and Boundary Condition Verification Based on Rotor 6 Data

As discussed in sections 4.4.1 and 4.4.2, rotor 6 is used to validate the FORTRAN Code that analyzes experimental data. It also validates the boundary conditions such as the film coefficient on the front and rear disk faces and the use of the forward shaft bearing temperature as the temperature of the shaft. Experimental data was collected for rotor 6 operating at 20,000, 25,000 and 30,000 rpm. The FORTRAN code analysis of the data estimated the values of h. Table 5 presents a comparison of the experimental and analytically predicted values of h. Also, the Stanton number for the experimentally determined values of h are plotted on Figure 19. The values of h are within ±8.3% of the analytically predicted values.

Table 5: Comparison of Experimental and Analytical Estimate of Film Coefficient for Rotor 6

rotor speed (rpm)	h inferred from experiment W/m^2-K (Btu/hr-ft^2-°F)	h based on empirical relation W/m^2-K (Btu/hr-ft^2-°F)	percent difference from empirical
20,000	369.6 (65.1)	341.1 (60.1)	8.3
25,000	383.2 (67.5)	401.9 (70.8)	-4.7
30,000	420.6 (74.1)	458.7 (80.8)	-8.3

A sensitivity analysis was performed by modifying the FORTRAN code such that the estimate of film coefficient on the front and rear faces was doubled. This had the

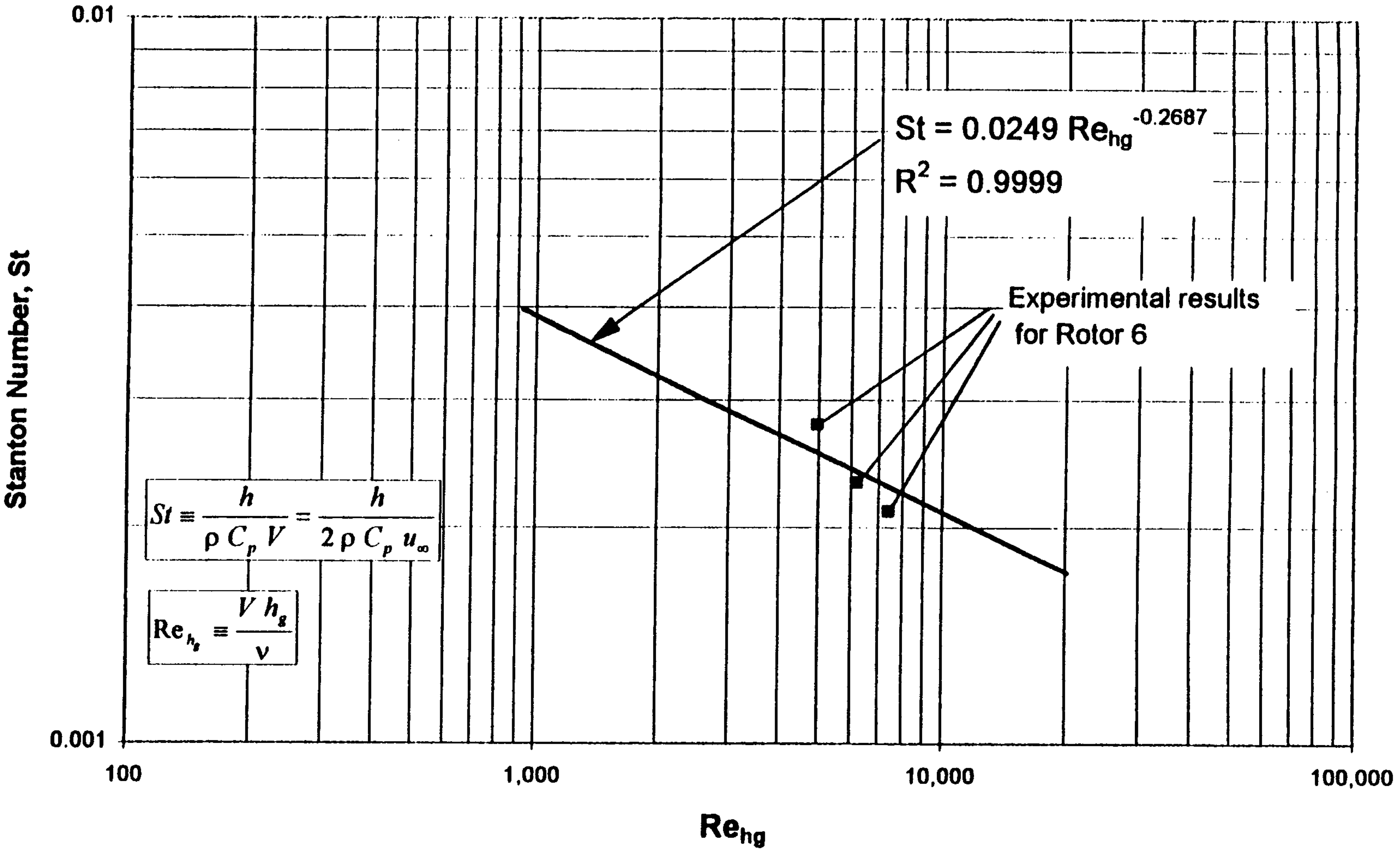

Figure 19: Predicted Value of Stanton Number as a Function of Re_{h_g} for Wall Driven Flow

affect of reducing the predicted values of film coefficient on the peripheral surface between 5.5% and 6.8%. So, the high thermal resistance of the epoxy insulation renders the analysis relatively insensitive to variations in the film coefficient on the front and rear surfaces.

A second, separate, sensitivity analysis was performed to assess the affect of varying the temperature of the shaft. While the original program assumes the shaft temperature (element 14) is equal to the temperature of the forward bearing, the program was modified such that the imposed shaft temperature was equal to the bearing temperature minus 10°F. This change resulted in greater heat loss through the shaft and had the affect of reducing the predicted values of peripheral surface film coefficient between 2.1% and 4.8%. The prescribed shaft temperature was then further lowered to be 20°F less than the forward bearing temperature with again comparable decrease in predicted value of h.

Based on the rotor 6 experimental results, the computer program successfully estimates the convective film coefficient on the peripheral surface. The perturbation study indicates a low sensitivity to variations in boundary conditions associated with estimated film coefficient on front and rear surfaces and measured shaft temperature.

4.7 Estimate of Reference Temperatures for Rotors 1 through 5

The reference temperatures were calculated based on control volume analyses of the regions in the annular gap above face 1 and the cavity region for faces 2, 3 and 4. Although the temperature in the gap region was measured, it was concluded that the temperatures did not accurately represent the reference temperatures for the two distinct regions of interest. Further, attempts to correlate the measured gap temperature to rotor, stator, inlet and outlet air temperatures were unsuccessful.

4.7.1 Reference Temperature for Pole Face 1

Viscous aerodynamic heating of the air occurs in the gap between rotor pole face 1 and the stator wall due to the high shear stresses and velocity gradients that are present, particularly at high rotational speeds. This aerodynamic heating contributes to increased mean temperature, T_m, over the pole face in the positive x-direction. A control volume of infinitesimal thickness, Δx, length, Δz, and finite height, h_g, is presented in Figure 20. Applying the law of conservation of energy to the control volume: $\dot{E}_{in} = \dot{E}_{out} + \frac{\partial E_{stored}}{\partial t}$,

yields:

$$\frac{\dot{m}_{tip}}{L_z} i\Big|_x \Delta z + \dot{q}''_R \, \Delta x \, \Delta z + \tau V \Delta x \, \Delta z = \frac{\dot{m}_{tip}}{L_z} i\Big|_{x+\Delta x} \Delta z + \dot{q}_S \, \Delta x \, \Delta z + \frac{\partial}{\partial t}\left(\rho c_v \, h_g \, \Delta x \, \Delta z \, T_1\right)$$

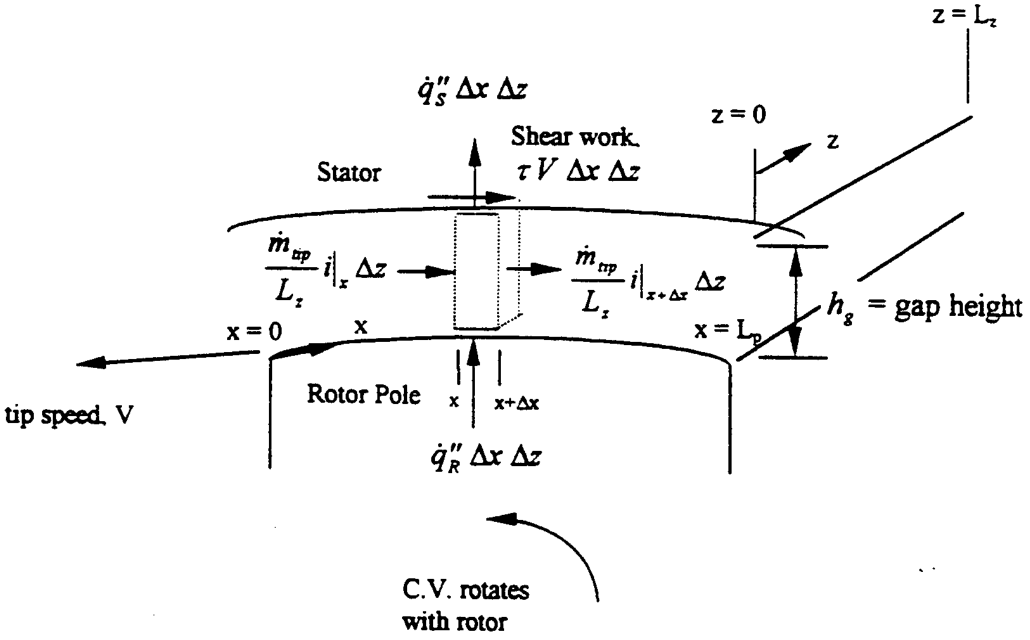
z = L_z
$\dot{q}''_S$ Δx Δz
z = 0
Shear work
τV Δx Δz
z
Stator
$\frac{\dot{m}_{tip}}{L_z} i|_x$ Δz
$\frac{\dot{m}_{tip}}{L_z} i|_{x+\Delta x}$ Δz
h_g = gap height
x = 0
x
x = L_p
tip speed, V
Rotor Pole
x
x+Δx
$\dot{q}''_R$ Δx Δz
C.V. rotates with rotor

Figure 20: Control Volume in Gap Region Above Pole Face 1

Note that the Δz terms can be canceled in this equation. This is because the control volume does not account for heat flux in the z-direction associated with either enthalpy flow or conduction. Because the gap between rotor pole face 1 and the stator is small compared to the rotor cavity dimensions, it is reasonable to assume essentially all axial air flow will occur in the cavities and that there will be negligible axial flow over face 1. Further, the thermal conductivity of air is low, so heat flux due to conduction will likewise be negligible. Similarly, heat conduction was not included at the control surfaces in the x-direction. The Peclet number; $Pe_{L_p} = \dfrac{V\,L_p}{\alpha} = \mathrm{Re}_{L_p}\,\mathrm{Pr}$, will be high. The Peclet number is a dimensionless parameter that represents the ratio of enthalpy flow to axial conduction and for Pe >> 1, enthalpy flow dominates the transfer of energy and axial conduction is negligible in comparison.

The mass flow rate of air over the face of the pole tip is assumed to be uniformly distributed in the z-direction and is given by:

$$\dot{m}_{ap} = 1/2\,\rho V L_z h_g \tag{4-54}$$

This equation can be written in terms of temperatures using the relation $i = c_p T$ (assumes calorically perfect gas), defining T_1 as the lumped temperature in the control volume over face 1 as a function of x, and employing the equation $\dot{q}'' = h\left(T_{surface} - T_{aw}\right)$, where T_{aw} is the adiabatic wall temperature.

$$\begin{aligned} &\frac{\dot{m}_{ap}}{L_z} c_p T_1\big|_x + h\left(T_R - T_{aw}\right)\Delta x + \tau\ V\ \Delta x = \\ &\qquad \frac{\dot{m}_{ap}}{L_z} c_p T_1\big|_{x+\Delta x} + h\left(T_{aw} - T_S\right)\Delta x + \rho c_v h_g\,\Delta x \frac{\partial T_1}{\partial t} \end{aligned} \tag{4-55}$$

Note that the adiabatic wall temperature is used as the reference temperature for convection to account for the effects of viscous heating and to assure that the value of the convective film coefficient, h, is unaffected by the wall heat transfer rates.

Dividing by Δx and taking the limit as $\Delta x \rightarrow 0$, yields:

$$\frac{\dot{m}_{tip}}{L_z} c_p \frac{\partial T_1}{\partial x} + 2hT_{aw} - \left[h(T_R + T_S) + \tau V\right] + \rho c_v h_g \frac{\partial T_1}{\partial t} = 0 \qquad (4\text{-}56)$$

Note that the airflow over the rotor tip occurs so quickly there is little time for a temporal variation in the mean air temperature. The length of the pole tip, L_p, is 2.85 cm (1.12 in.) and at the lowest experimental rotational speed of 5,000 rpm, the tip speed is 28.59 m/s (1,126 in/s) yielding a residence time of the air over the tip of 9.9×10^{-4} seconds. At the highest experimental speed of 30,000 rpm this residence time is only 1.7×10^{-4} seconds. So the temporal derivative of the mean temperature is considered negligible and will be dropped.

$$\frac{\dot{m}_{tip}}{L_z} c_p \frac{dT_1}{dx} + 2hT_{aw} - \left[h(T_R + T_S) + \tau V\right] = 0 \qquad (4\text{-}57)$$

The adiabatic wall temperature is defined as the mean temperature plus aerodynamic heating. $T_{aw} = T_1 + T_{aero}$. Substituting this expression yields:

$$\frac{dT_1}{dx} + \frac{2hL_z}{\dot{m}_{tip} c_p} T_1 + \frac{L_z}{\dot{m}_{tip} c_p}\left[2hT_{aero} - h(T_R + T_S) - \tau V\right] = 0 \qquad (4\text{-}58)$$

This expression can be simplified by defining the following constants:

$$C_1 \equiv \frac{2hL_z}{\dot{m}_{tip} c_p} \qquad (4\text{-}59)$$

and $$C_2 \equiv \frac{L_z}{\dot{m}_{tip} c_p}\left[2hT_{aero} - h(T_R + T_S) - \tau V\right] \qquad (4\text{-}60)$$

the equation can be written:

$$\frac{dT_1}{dx} + C_1 T_1 + C_2 = 0 \tag{4-61}$$

with boundary condition $T_1(x = 0) = T_0$ which has the solution:

$$T_1(x) = \left(T_0 + C_2/C_1\right)e^{-C_1 x} - C_2/C_1 \tag{4-62}$$

Note, however, that while the mean air temperature, T_1, over pole face 1 varies as a function of x, it also varies with z because the temperature of the air entering the control volume, $T_1(0)$, is equal to the temperature in the cavity, which varies with z. If mixing is ignored in the z direction, we find:

$$T_1(x, z) = \left(T_c(z) + C_2/C_1\right)e^{C_1 x} - C_2/C_1 \tag{4-63}$$

It is necessary to estimate the shear stress for the calculation of the term C_2. It was shown previously that for fully developed wall driven flow, the shear stress is approximated by the Blasius relation:

$$\tau_o = 0.0225\,\rho\,u_\infty^2 \left(\frac{\delta\,u_\infty}{\nu}\right)^{-1/4} = 0.00795\,\rho\,V^2\,\mathrm{Re}_{h_g}^{-1/4} \tag{4-64}$$

and the friction factor is given by:

$$C_f = 0.0159\,\mathrm{Re}_{h_g}^{-1/4} \tag{4-65}$$

However, the shear stress over pole face 1 will be greater than for a smooth-poled rotor due to the increased shear stress at the start of the boundary layer. Kays and Crawford [12] perform an approximate solution for the turbulent momentum boundary layer using an integral method and the power form of the law of the wall. The displacement thickness, δ_1, and the momentum thickness, δ_2 (a measure of the decrease in momentum flux caused by the boundary layer), are estimated in terms of the boundary layer thickness,

δ, by substituting the power law of the wall, $u^+ = 8.75\, y^{+\,1/7}$, into their respective definitions.

$$\delta_1 \equiv \int_0^\infty 1 - \frac{u\,\rho}{u_\infty \rho_\infty}\, dy \tag{4-66}$$

$$\delta_2 \equiv \int_0^\infty \frac{\rho\, u}{\rho_\infty u_\infty}\left(1 - \frac{u}{u_\infty}\right) dy \tag{4-67}$$

This results in the relations:

$$\frac{\delta_2}{\delta} = 0.097 \text{ and } \frac{\delta_1}{\delta} = 0.125$$

Further, the shape factor, H, is given by $\frac{\delta_1}{\delta_2} = 1.29$.

The Blasius shear stress can then be written in terms of the free-stream velocity and the momentum thickness (Kays and Crawford equation 11-19) as:

$$\tau_o = 0.0125\, \rho\, u_\infty^2 \left(\frac{\delta_2\, u_\infty}{\nu}\right)^{-1/4} \tag{4-68}$$

The momentum integral equation in axisymmetric body of revolution coordinates for the case of no transpiration at the walls is given by Kays and Crawford equation 6-7:

$$\frac{\tau_o}{\rho\, u_\infty^2} = \frac{d\,\delta_2}{d\,x} + \delta_2 \left[\left(2 + \frac{\delta_1}{\delta_2}\right) \frac{1}{u_\infty} \frac{d\,u_\infty}{d\,x} + \frac{1}{R} \frac{d\,R}{d\,x}\right] \tag{4-69}$$

Substituting the above expression for wall shear stress in terms of momentum thickness (equation 4-64), making use of the shape factor, and integrating yields:

$$\delta_2 = \frac{0.036\, \nu^{0.2}}{R\, u_\infty^{3.29}} \left(\int_0^x R^{5/4}\, u_\infty^{3.86}\, dx\right)^{0.8} \tag{4-70}$$

For this case, R and u_∞ are constant and the equation simplifies to Kays and Crawford equation 11-22:

$$\frac{\delta_2}{x} = \frac{0.036\, \nu^{0.2}}{u_\infty^{0.2}\, x^{0.2}} = 0.036\, \mathrm{Re}_x^{-0.2} \qquad (4\text{-}71)$$

The relation between boundary layer and momentum thickness can then be employed to yield the boundary layer thickness as a function of x:

$$\delta = 0.371\, x \left(\frac{u_\infty\, x}{\nu} \right)^{-0.2} \qquad (4\text{-}72)$$

Defining x_s as the distance from the start of the boundary layer until it is fully developed, i.e. where $\delta = h_g/2$, x_s is given by:

$$x_s = 1.221\, h_g\, \mathrm{Re}_{h_g}^{1/4} \qquad (4\text{-}73)$$

The total force acting on pole face 1 is found by integrating the shear stress over the face from the start of the boundary layer, x = 0, to where the boundary layer is fully developed, $x = x_s$, and from that point to the end of the pole face, $x = L_p$.

$$F = \int_0^{x_s} \tau_0\, L_z\, dx + \int_{x_s}^{L_p} \tau_o\, L_z\, dx \qquad (4\text{-}74)$$

$$F = \int_0^{x_s} 0.0225\, \rho\, u_\infty^2 \left[0.371\, x \left(\frac{u_\infty x}{\nu} \right)^{-0.2} \frac{u_\infty}{\nu} \right]^{-1/4} L_z\, dx + \int_{x_s}^{L_p} 0.0225\, \rho\, u_\infty^2 \left[\frac{\frac{h_g}{2}\,\frac{V}{2}}{\nu} \right]^{-1/4} L_z\, dx$$

Carrying out the integration yields:

$$F = 0.00971\, \rho\, u_\infty^2\, h_g\, L_z + 0.3182\, \rho\, u_\infty^2\, \mathrm{Re}_{h_g}^{-1/4}\, L_z \qquad (4\text{-}75)$$

The average shear stress over the face is

$$\tau_{ave} \equiv \frac{F}{L_p\, L_z} \tag{4-76}$$

Defining a boundary layer re-start coefficient, C_N, as the ratio of the average shear stress over the face to the shear stress associated with the fully developed flow gives:

$$C_N = 1 + 0.305\,\mathrm{Re}_{h_g}^{1/4}\ ;\ \text{for } \frac{L_p}{h_g} > 1.22\,\mathrm{Re}_{h_g}^{1/4} \text{ and turbulent flow.} \tag{4-77}$$

If the boundary layer does not become fully developed before the end of the pole, i.e. if $\frac{L_p}{h_g} < 1.22\,\mathrm{Re}_{h_g}^{1/4}$, then the total force on the pole face is:

$$F = \int_0^{L_p} 0.0225\,\rho\, u_\infty^2 \left[0.371\, x \left(\frac{u_\infty\, x}{\nu} \right)^{-0.2} \frac{u_\infty}{\nu} \right]^{-1/4} L_z dx \tag{4-78}$$

The average shear stress over the face is:

$$\tau_{ave} = \frac{F}{L_p L_z} = 0.0414\,\rho\, u_\infty^2\, \mathrm{Re}_{h_g}^{-0.2} \left(\frac{h_g}{L_p} \right)^{0.2} \tag{4-79}$$

and the boundary layer re-start factor is given by:

$$C_N = 1.29\,\mathrm{Re}_{h_g}^{0.05} \left(\frac{h_g}{L_p} \right)^{0.2} \text{ for } \frac{L_p}{h_g} < 1.22\,\mathrm{Re}_{h_g}^{1/4} \tag{4-80}$$

So, the shear stress in the gap region can be written as:

$$\tau = 1/2\,\rho V^2\, C_f\, C_N \tag{4-81}$$

Using these expressions to estimate the shear stress over pole face 1, the coefficient C_2 can be calculated and the temperature distribution, $T_1(x,z)$ can be estimated using equation 4-63. However, the z dependence of $T_1(x,z)$ comes from the temperature in the cavity region. $T_c(z)$ will be estimated in Section 4.6.2. Then it will be possible to estimate the mean temperature over pole face 1 defined as:

$$T_{m1} = \frac{1}{L_p L_z} \int_0^{L_z} \int_0^{L_p} T_1(x,z)\, dx\, dz \qquad (4\text{-}82)$$

4.7.2 Reference Temperature for Pole Faces 2, 3 and 4; Forced Axial Flow

The control volume depicted in Figure 21 represents one of the four cavities of the rotor. The control volume is attached to the rotor walls (faces 2, 3 and 4) and rotates with the rotor (no shear work on these surfaces). It is of infinitesimal thickness, Δz. The transverse dimensions extend from the rotor pole faces out to the stator wall. The temperature is considered to be lumped in the transverse direction (x and y). This control volume accounts for forced axial air flow into the control volume as well as airflow into and out associated with flow over the tips of the rotor pole.

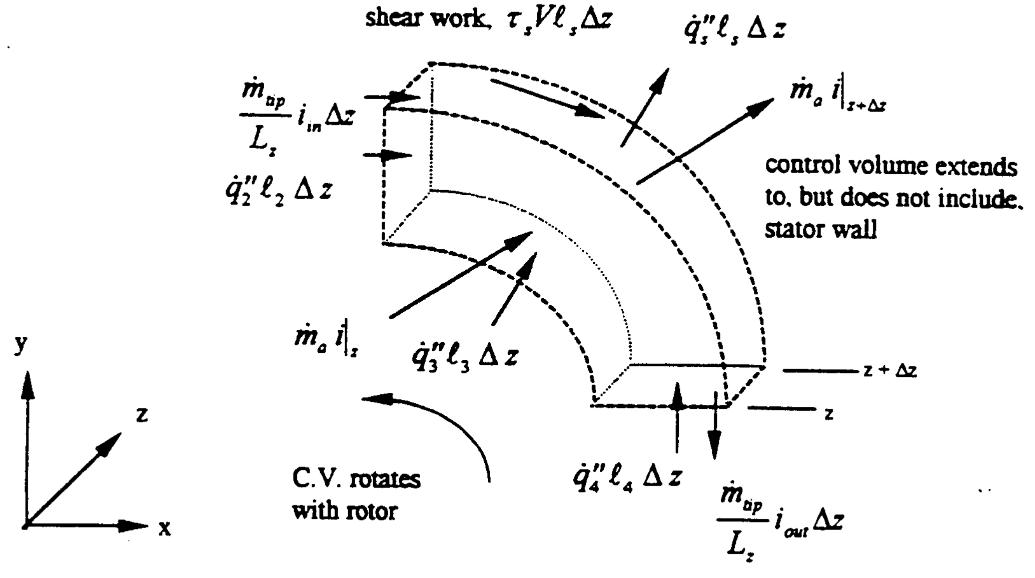
shear work, $\tau_s V \ell_s \Delta z$
$\dot{q}_s'' \ell_s \Delta z$
$\frac{\dot{m}_{tip}}{L_z} i_{in} \Delta z$
$\dot{m}_a i|_{z+\Delta z}$
$\dot{q}_2'' \ell_2 \Delta z$
control volume extends to, but does not include, stator wall
$\dot{m}_a i|_z$
$\dot{q}_3'' \ell_3 \Delta z$
y
z
x
z + Δz
z
C.V. rotates with rotor
$\dot{q}_4'' \ell_4 \Delta z$
$\frac{\dot{m}_{tip}}{L_z} i_{out} \Delta z$

Figure 21: Control Volume in Cavity Region, Forced Axial Flow

Applying the law of conservation of energy to the control volume: $\dot{E}_{in} = \dot{E}_{out} + \frac{\partial E_{stored}}{\partial t}$,

yields:

$$\frac{\dot{m}_{tip}}{L_z} i_{tip}\, \Delta z + \dot{m}_a i\big|_z + \dot{q}_2''\ell_2\Delta z + \dot{q}_3''\ell_3\Delta z + \dot{q}_4''\ell_4\Delta z + \tau_S V\ell_s\Delta z =$$

$$\frac{\dot{m}_{tip}}{L_z} i_{tip}\, \Delta z + \dot{m}_a i\big|_{z+\Delta z} + \dot{q}_S''\ell_S\Delta z$$

This equation can be written in terms of temperatures using the relation $i = c_p T$ (assumes calorically perfect gas), defining T_c as the lumped temperature in the control volume in the cavity as a function of z, and employing the equation $\dot{q}'' = h\left(T_{surface} - T_c\right)$. Note that in the cavity region, it is assumed that the velocity gradients are small enough that the static temperature is close to the adiabatic wall temperature.

$$\frac{\dot{m}_{tip}}{L_z} c_p T_1\left(L_p, z\right)\Delta z + \dot{m}_a c_p T_c\big|_z + h_2\ell_2\Delta z\left(T_2 - T_c\right) + h_3\ell_3\Delta z\left(T_3 - T_c\right) +$$
$$h_4\ell_4\Delta z\left(T_4 - T_c\right) + \tau_S V\ell_s\Delta z = \frac{\dot{m}_{tip}}{L_z} c_p T_c\, \Delta z + \dot{m}_a c_p T_c\big|_{z+\Delta z} + h_s\ell_s\Delta z\left(T_c - T_s\right) \tag{4-83}$$

Dividing by Δz and taking the limit as $\Delta z \to 0$, the equation can be written as:

$$\frac{dT_c}{dz} + \frac{1}{\dot{m}_a c_p}\left(\frac{\dot{m}_{tip}\, c_p}{L_z} + h_S\ell_S + h_2\ell_2 + h_3\ell_3 + h_4\ell_4\right) T_c -$$
$$\frac{1}{\dot{m}_a c_p}\left(h_2\ell_2 T_2 + h_3\ell_3 T_3 + h_4\ell_4 T_4 + h_s\ell_s T_s + \tau_s V\ell_s\right) - \frac{\dot{m}_{tip}\, T_1(L_p, z)}{\dot{m}_a\, L_z} = 0 \tag{4-84}$$

This differential equation can be simplified by defining the constants:

$$C_3 \equiv \left(\frac{\dot{m}_{tip}\, c_p}{L_z} + h_S\ell_S + h_2\ell_2 + h_3\ell_3 + h_4\ell_4\right) \tag{4-85}$$

and $$C_4 \equiv \left(h_2\ell_2 T_2 + h_3\ell_3 T_3 + h_4\ell_4 T_4 + h_s\ell_s T_s + \tau_s V\ell_s\right) \tag{4-86}$$

this equation can be written:

$$\frac{dT_c}{dz} + \frac{1}{\dot{m}_a c_p} C_3\, T_c - \frac{1}{\dot{m}_a c_p} C_4 - \frac{\dot{m}_{tip}}{\dot{m}_a L_z} T_1(L_p, z) = 0 \tag{4-87}$$

However, $T_1(L_p,z)$ is the air temperature leaving the region over pole face 1 and can be expressed as:

$$T_1(L_p,z) = \left(T_c(z) + C_2/C_1\right) e^{-C_1 L_p} - C_2/C_1 \tag{4-88}$$

Substituting into equation 4-87 yields:

$$\frac{dT_c}{dz} + \left(\frac{C_3}{\dot{m}_a c_p} - \frac{\dot{m}_{tip}}{\dot{m}_a L_z} e^{-C_1 L_p}\right) T_c + \left(-\frac{C_4}{\dot{m}_a c_p} - \frac{\dot{m}_{tip}}{\dot{m}_a L_z} \frac{C_2}{C_1}\left(e^{-C_1 L_p} - 1\right)\right) = 0 \tag{4-89}$$

Defining

$$C_5 \equiv \frac{C_3}{\dot{m}_a c_p} - \frac{\dot{m}_{tip}}{\dot{m}_a L_z} e^{-C_1 L_p} \tag{4-90}$$

and $$C_6 \equiv -\frac{C_4}{\dot{m}_a c_p} - \frac{\dot{m}_{tip}}{\dot{m}_a L_z} \frac{C_2}{C_1}\left(e^{-C_1 L_p} - 1\right) \tag{4-91}$$

The equation can be written as:

$$\frac{dT_c}{dz} + C_5 T_c + C_6 = 0 \tag{4-92}$$

with the boundary condition $T_c(0) = T_{inlet}$ which has the solution:

$$T_c(z) = \left(T_{inlet} + \frac{C_6}{C_5}\right) e^{-C_5 z} - \frac{C_6}{C_5} \tag{4-93}$$

It is necessary to estimate the shear stress, τ_s, for calculation of the term C_4. In experimental investigation of the same rotor profile, Schauer[17] develops an empirical relation to estimate power loss associated with rotor cavity mixing losses.

$$P_{RM} = 1/2\, \rho\, N\, V^3 C_f \left[7.28\left(\frac{h_g}{H_c}\right)^{0.25}\right] L_z\, x_R = \tau_s\, V\, L_z\, x_R \tag{4-94}$$

where N is the number of poles and L_z is the length of the rotor. Thus, the shear stress in the cavity region for the four pole rotor is estimated to be:

$$\tau_s = 14.56\,\rho\,V^2 C_f \left(\frac{h_g}{H_c}\right)^{0.25} \tag{4-95}$$

The mean temperature in the cavity, T_{mc}, can be calculated as follows:

$$T_{mc} = \frac{1}{L_z}\int_0^{L_z} T_c(z)\,dz = \frac{\left(T_{inlet} + \frac{C_6}{C_5}\right)}{C_5\,L_z}\left(1 - e^{-C_5 L_z}\right) - \frac{C_6}{C_5} \tag{4-96}$$

Also, now equation 4-93 for $T_c(z)$ can be substituted into equations 4-63 and 4-82 to estimate the mean temperature over pole face 1.

$$T_{m1} = \frac{1}{L_p L_z}\left\{\left[\frac{\left(T_{inlet} + \frac{C_6}{C_5}\right)\left(1 - e^{-C_5 L_z}\right)}{C_1\,C_5} + \left(\frac{C_2}{C_1} - \frac{C_6}{C_5}\right)\frac{L_z}{C_1}\right]\left(1 - e^{-C_1 L_p}\right)\right\} - \frac{C_2}{C_1} \tag{4-97}$$

4.7.3 Reference Temperature for Pole Faces 2, 3 and 4; No Forced Axial Flow

Note that equations 4-96 and 4-97, representing the mean reference temperatures, are not valid for the case of no forced axial airflow because the term $\dot{m}_a$ appears in the denominator of parameters C_5 and C_6. Further, when there is no forced axial airflow, air is induced into the cavities from both the front and rear faces of the rotor due to the pressure gradient that exists radially across the cavity. The control volume presented in Figure 22 represents the case of no forced axial airflow. The control volume is of finite dimension and occupies the entire volume in a single rotor cavity and extends out to the surface of the stator wall. A pressure gradient is established radially across the cavity due to the centripetal acceleration applied to the air particles as the rotor spins. This pressure gradient results in "pumping" of air into the cavity near the root of the rotor and discharge of air from the cavity in the higher pressure region near the stator wall. It is assumed that air is pumped into and out of the cavity equally from both the front and rear exposures of the cavity.

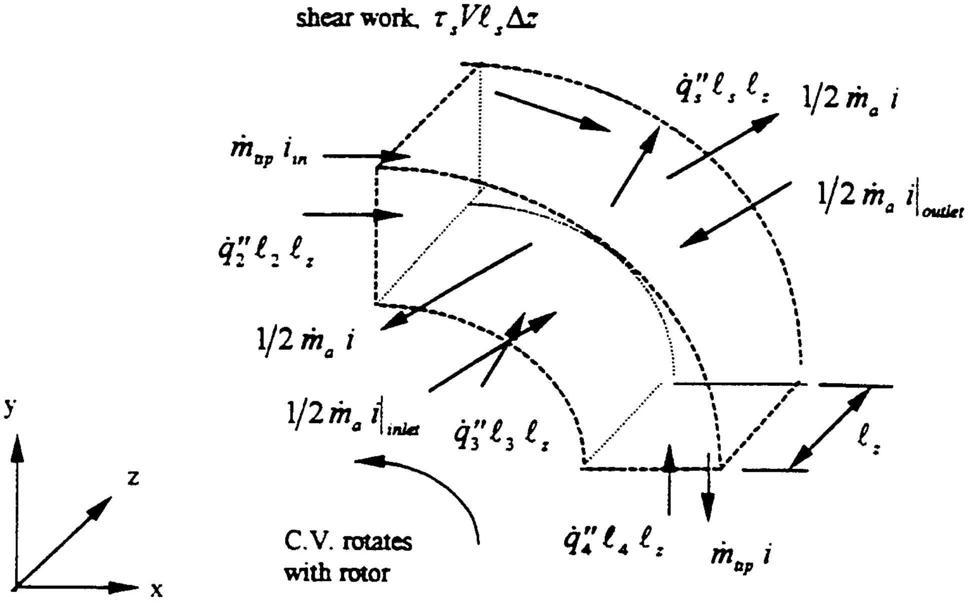
shear work, $\tau_s V \ell_s \Delta z$
$\dot q_s'' \ell_s \ell_z$
$1/2\, \dot m_a\, i$
$\dot m_{ap}\, i_{in}$
$1/2\, \dot m_a\, i|_{outlet}$
$\dot q_2'' \ell_2 \ell_z$
$1/2\, \dot m_a\, i$
$1/2\, \dot m_a\, i|_{inlet}$
$\dot q_3'' \ell_3 \ell_z$
ℓ_z
y
z
x
C.V. rotates with rotor
$\dot q_4'' \ell_4 \ell_z$
$\dot m_{ap}\, i$

Figure 22: Control Volume in Cavity Region, No Forced Axial, Flow Induced by Pumping

Applying the law of conservation of energy to the control volume: $\dot E_{in} = \dot E_{out} + \dfrac{\partial E_{stored}}{\partial t}$,

yields:

$$\dot m_{ap}\, i_{in} + 1/2\, \dot m_a\, i_{inlet} + 1/2\, \dot m_a\, i_{outlet} + \dot q_2'' \ell_2 \ell_z + \dot q_3'' \ell_3 \ell_z + \\ \dot q_4'' \ell_4 \ell_z + \tau_s V \ell_s \ell_z = 1/2\, \dot m_a\, i + 1/2\, \dot m_a + \dot m_{ap} i + \dot q_s'' \ell_s \ell_z$$

This equation can again be written in terms of temperature in the same manner as previously discussed. However, because this is not an infinitesimal control volume, the resulting equations are algebraic rather than differential.

It is found that the mean temperature in the cavity, T_{mc}, for the case of no forced axial flow is given by:

$$T_{mc} = \frac{C_8}{C_7} \tag{4-98}$$

where C_7 and C_8 are defined as:

$$C_7 \equiv C_3 + \frac{\dot{m}_a c_p}{L_z} - \frac{\dot{m}_{tip} c_p}{L_z} e^{-C_1 L_p} \tag{4-99}$$

$$C_8 \equiv C_4 + \frac{\dot{m}_{tip} c_p}{L_z} \frac{C_2}{C_1}\left(e^{-C_1 L_p} - 1\right) + \frac{1/2\, \dot{m}_a c_p}{L_z}\left(T_{inlet} + T_{outlet}\right) \tag{4-100}$$

Note that equation 4-98 is valid even for the case $\dot{m}_a = 0$. Note also that for the case of no forced axial flow (no net axial flow) the cavity temperature does not vary in the z direction because the control volume analysis lumps the temperature in the z direction. Thus, the mean temperature over rotor pole face 1 must be re-calculated for the case of no forced axial flow.

From equation 4-63, $T_1(x,z) = \left(T_c(z) + C_2/C_1\right) e^{-C_1 x} - C_2/C_1$.
But, now there is no functional relationship in z. $T(z) = T_{mc} = \dfrac{C_8}{C_7}$. So the mean temperature over pole face 1 can be calculated as:

$$T_{m1} = \frac{1}{L_p}\int_0^{L_p} T(x)\, dx = \frac{1}{L_p}\int_0^{L_p} \left(T_{mc} + \frac{C_2}{C_1}\right) e^{-C_1 x} - \frac{C_2}{C_1}\, dx \tag{4-101}$$

which results in the equation:

$$T_{m1} = \frac{1}{C_1 L_p}\left(T_{mc} + \frac{C_2}{C_1}\right)\left(1 - e^{-C_1 L_p}\right) - \frac{C_2}{C_1} \tag{4-102}$$

The shear stress in the rotor cavity region is again calculated using equation 4-95.

The mass flow rate into the control volume due to pumping was also investigated experimentally by Schauer[17] for rotors of identical cross-section but with lengths of 4.8 inches rather than the 1.4 inches used in the current study. His analytical and experimental study investigated the windage loss of rotors by measuring the spin-down rate of the rotor and determining the torque on the rotor by the rate of loss of angular momentum. He then postulated that total power loss due to windage, P, could be expressed as:

$$P = P_R + P_D + P_p \tag{4-103}$$

where:

P_R is the windage loss between the rotor and stator.

P_D is the windage loss occurring on the rotor ends, or disk loss.

P_P is the windage loss associated with pumping

Air induced into the cavities has no angular component of velocity, but leaves the control volume with approximately the velocity of the rotor, V, as an angular component. This results in a loss of power

$$P_P = \dot{m}_a V^2 \tag{4-104}$$

Here, $\dot{m}_a$ is the *total* mass flow rate induced into the rotor. The $\dot{m}_a$ used in the control volume analysis represented in Figure 4.8 is one fourth of the total induced mass flow rate.

In reference 17, Schauer develops analytical models for losses P_R and P_D. The pumping losses are the difference between the measured windage losses and those accounted for by analytical values of P_R and P_R. An empirical estimate of the total mass flow rate is developed as:

$$\dot{m}_a = C_{pumping}\, \rho N H \frac{x_R}{2} \sqrt{2}\; V \left[1 - \left(\frac{R_i}{R}\right)^2\right]^{1/2} \tag{4-105}$$

N is the number of poles and the pumping coefficient is

$$C_{pumping} = \mathrm{Re}_{x_R}^{-0.19} \tag{4-106}$$

CHAPTER V

RESULTS

5.1 General

The data from the experiments for rotors 1 through 4 were analyzed using the FORTRAN code, Analyzer. The output of each analysis was the value of film coefficient for the exposed pole face which caused the analytical model to most closely approximate the temperature history of the rotor core in the experiment.

Typical results from the analysis of the data are presented in Figure 23. This figure shows the experimental data for Rotor 1 operating at 10,000 rpm with full axial airflow. The FORTRAN code determines the optimum value of film coefficient for the exposed pole face such that the predicted core temperature versus time history of the analytical model best matches the experimental results. In this case, the root mean square deviation between the predicted and measured values over the course of the experiment is 0.96 °F. As an indication of the sensitivity of the model to changes in h on the exposed pole face, the value of h was decreased by 15%. These results are also plotted on Figure 23. It is apparent that the model is quite sensitive to changes in film coefficient. Conversely, changing the film coefficient on the insulated pole faces had minimal influence on the rotor core temperature.

The results of the individual analyses of rotors 1 through 4 were then verified using rotor 5 data. For example, the film coefficient results for r1_10k_1.prn, r2_10k_1.prn,

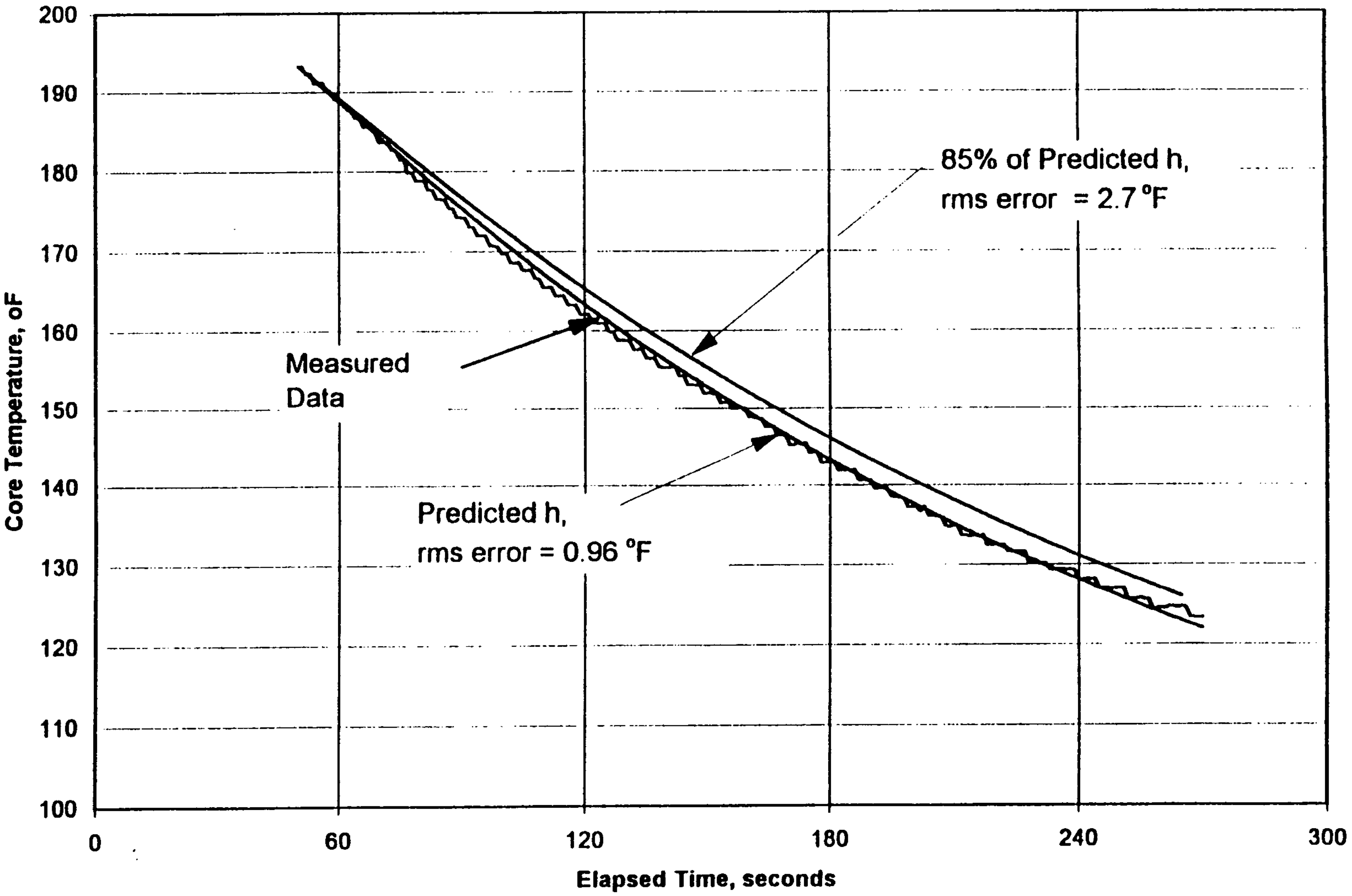

Figure 23: Comparison of Measured and Predicted Core Temperature Versus Time for Rotor 1, 10,000 rpm, Full Axial Flow

r3_10k_1.prn and r4_10k_1.prn, representing the film coefficients for the four rotor pole faces for the case of 10,000 rpm and full axial flow were applied to the analytical model of rotor 5. Using the time varying boundary conditions associated with r5_10k_1.prn, the predicted rotor core temperature was compared to the measured temperature versus time. In general, it was found that the estimated values of film coefficient for the faces were high and that when applied to the rotor 5 model, they predicted faster cooling of the rotor than occurred in the experiments. The values of film coefficient for the individual poles were adjusted for each experimental configuration (rotor speed and axial flow rate) to achieve the best overall agreement with the rotor 1 through 4 data and the rotor 5 data. The adjustments required were relatively minor. For each configuration, the final values of h, ±15%, encompass the experimental data of rotors 1 through 5. In general, the final values of film coefficient slightly under-predict the rate of cooling of rotors 1 through 4 and over-predict the cooling rate of rotor 5.

5.2 Empirical Analysis of Results

The final values of film coefficient are evaluated in terms of the Stanton and Nusselt numbers. The Stanton number is defined as:

$$St \equiv \frac{h}{\rho C_p V} \tag{5-1}$$

The Nusselt number is defined for pole face 1 as:

$$Nu \equiv \frac{h h_g}{k_{air}} \tag{5-2}$$

and is defined for pole faces 2, 3, and 4 as:

$$Nu \equiv \frac{h\,HC}{k_{air}} \tag{5-3}$$

where the gap height, h_g and the cavity height, HC are used as characteristic length scales. Note that they differ only by a multiplicative constant.

The two controlled variables in the experiments were rotor speed and axial air flow rate. The rate at which the rotors cooled, and thus the convective film coefficients, varied in response to these variables. Two dimensionless parameters that characterize these variables are: Reynolds number and $\frac{V_{axial}}{V_{tip}}$, the ratio of average axial air velocity through the rotor cavities to rotor tip speed. For each rotor pole face, an empirical relation is developed in the form $St \text{ or } Nu = f\left(\frac{V_{axial}}{V_{tip}}\right) g(\mathrm{Re})$. Similar to the definition of Nusselt number, the Reynolds number employs h_g as the characteristic length for pole face 1 and HC as characteristic length for rotors 2, 3 and 4.

The results are presented in Figures 24 through 31. In each plot, the abscissa is the product of $\left(\frac{V_{axial}}{V_{tip}}\right)^x \mathrm{Re}$. The value of the exponent, x, is chosen such that the line representing the empirical fit to the data is linear when plotted on a log-log scale. In most cases, the empirical relations accurately represent the experimental results within ±10%.

It is noted that the Nusselt number varies approximately with $\mathrm{Re}^{0.8}$, consistent with analytical and experimental results for turbulent flow over flat plates and in tubes. In developing empirical equations, it is assumed that the Nusselt number is also proportional to $\mathrm{Pr}^{1/3}$, as is the case for turbulent flow over flat plates and in tubes.

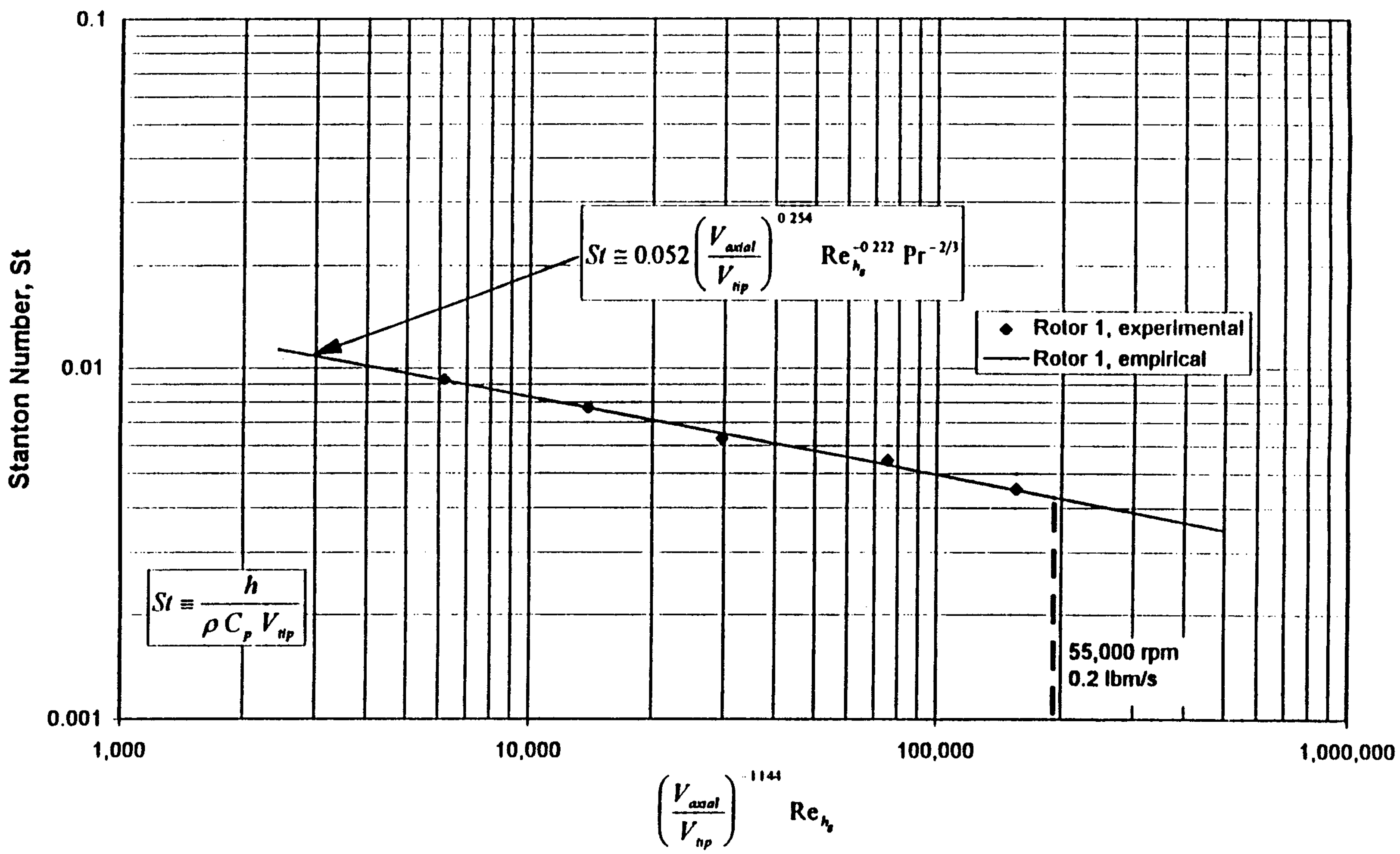

Figure 24: Pole Face 1 (Rotor Tip) Stanton Number as a Function of Re_{h_s} and $\frac{V_{axial}}{V_{tip}}$

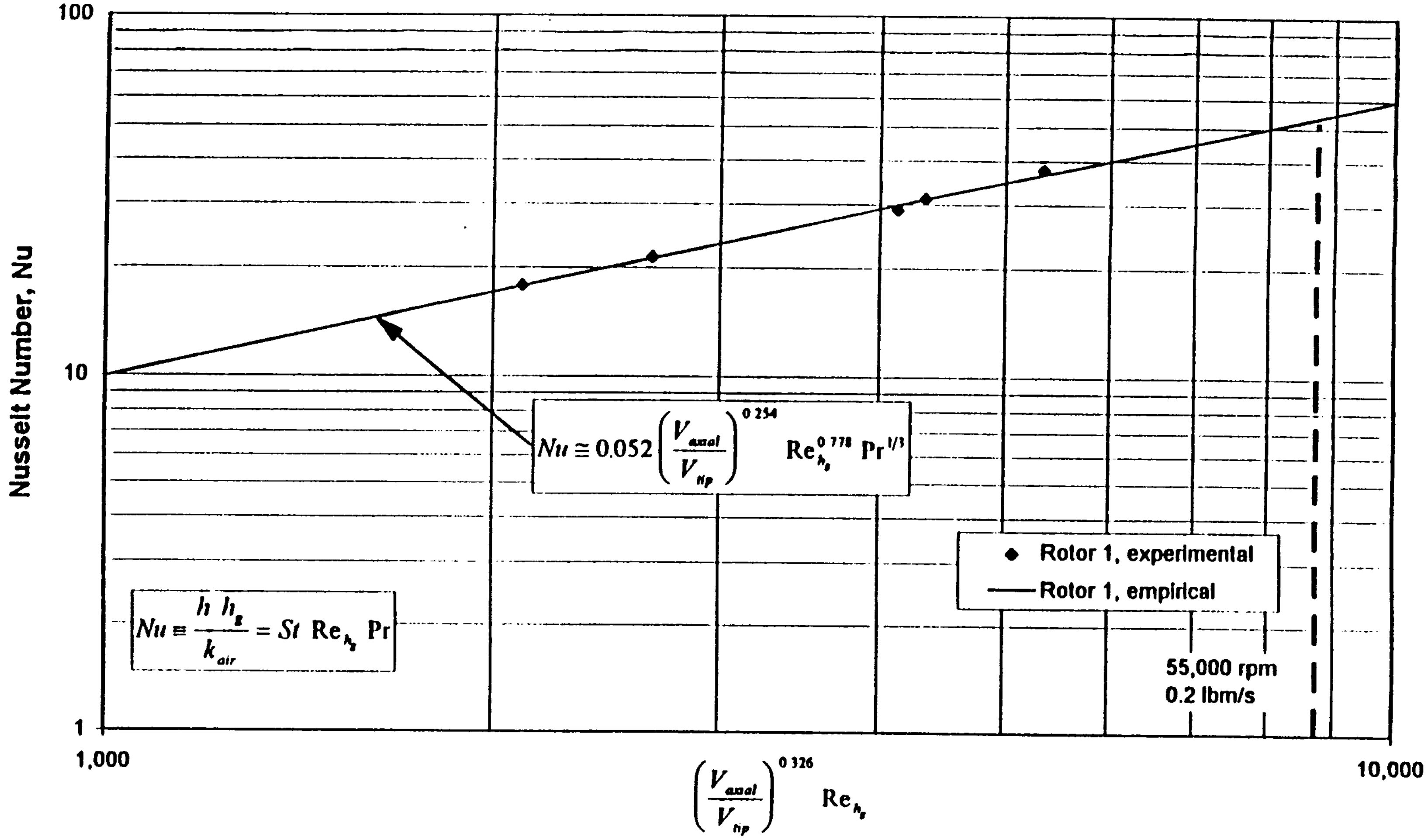

Figure 25: Pole Face 1 (Rotor Tip) Nusselt Number as a Function of Re_{h_g} and $\frac{V_{axial}}{V_{tip}}$

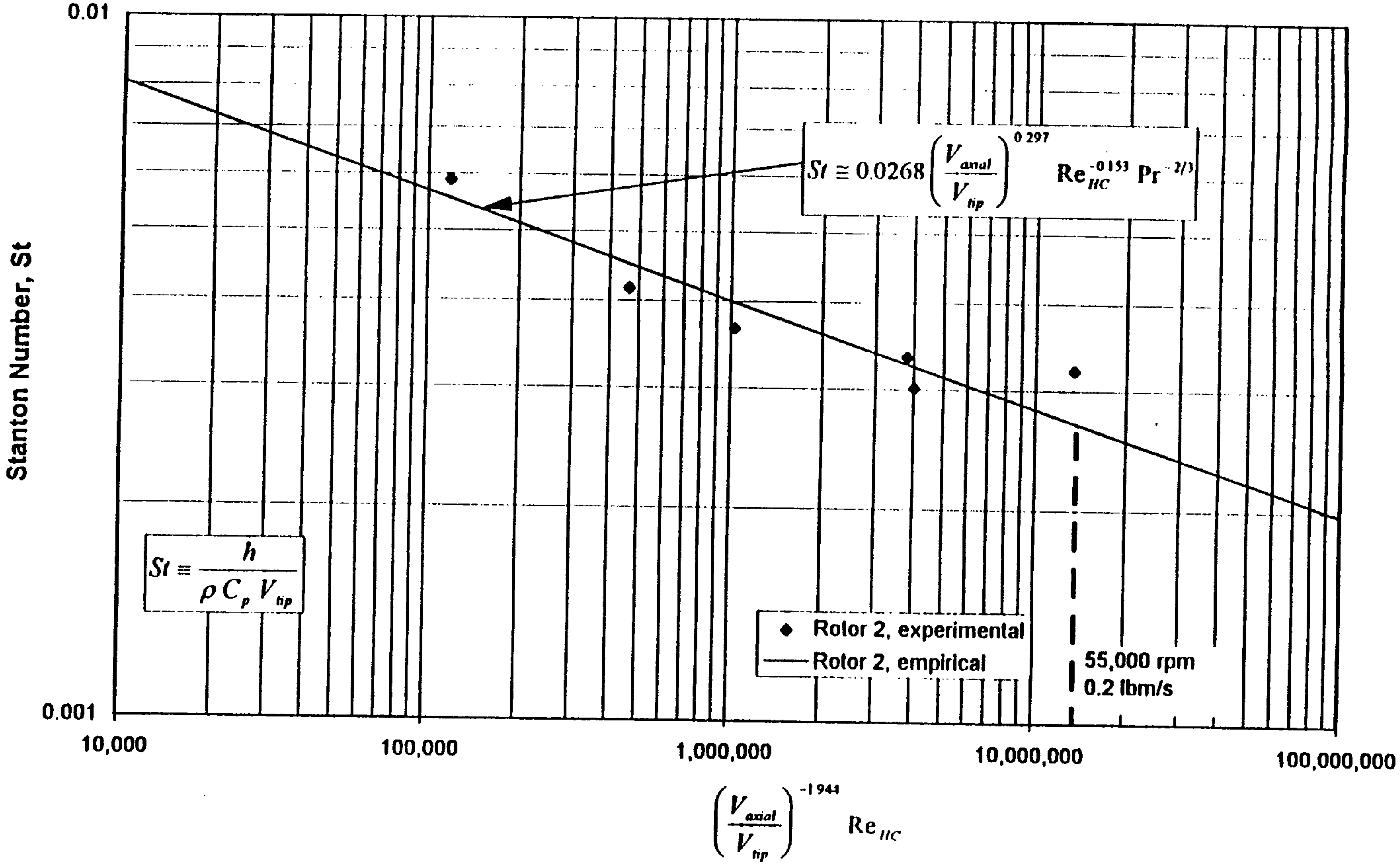

Figure 26: Pole Face 2 (Leeward Face) Stanton Number as a Function of Re_{HC} and $\frac{V_{axial}}{V_{tip}}$

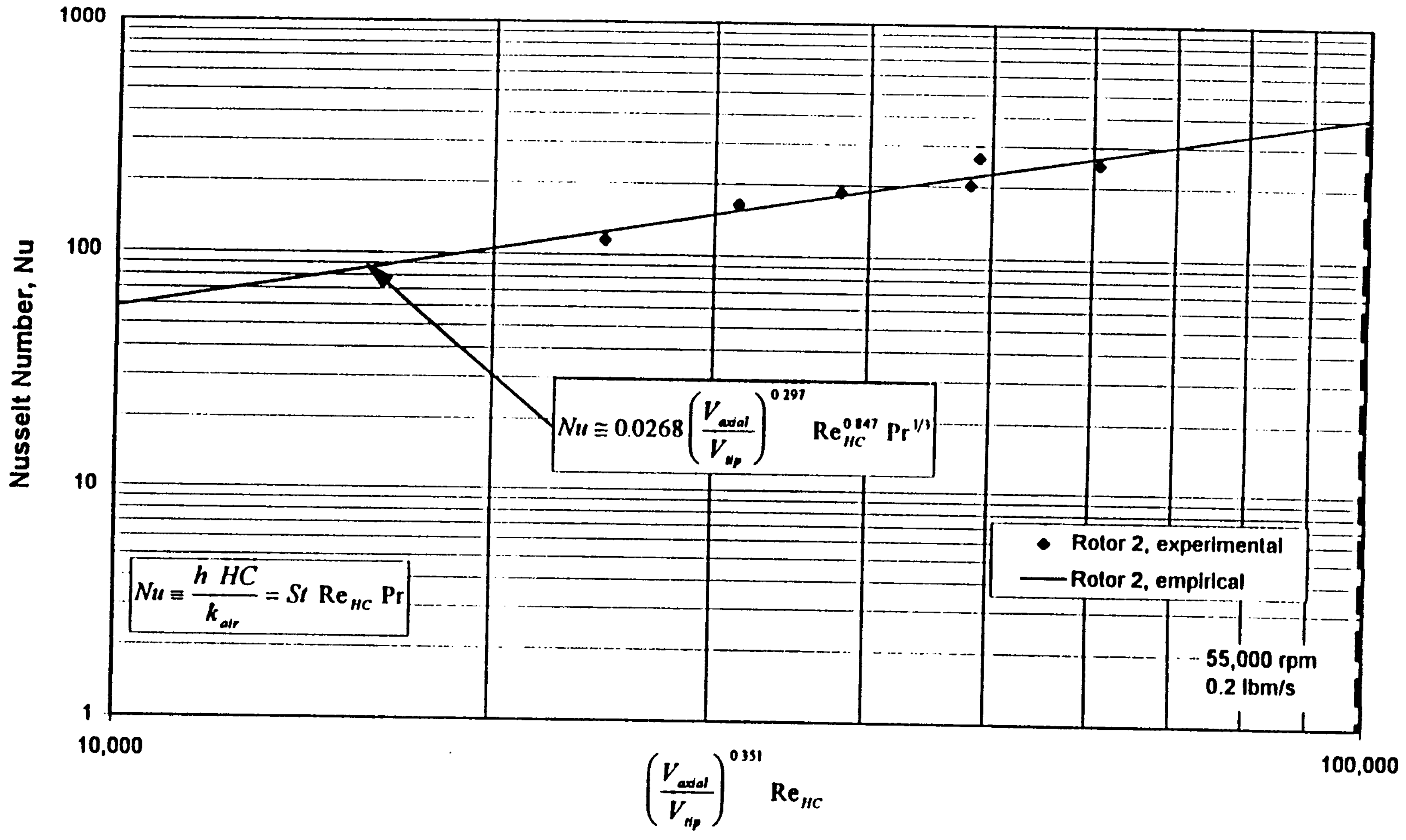

Figure 27: Pole Face 2 (Leeward Face) Nusselt Number as a Function of Re_{HC} and $\frac{V_{axial}}{V_{tip}}$

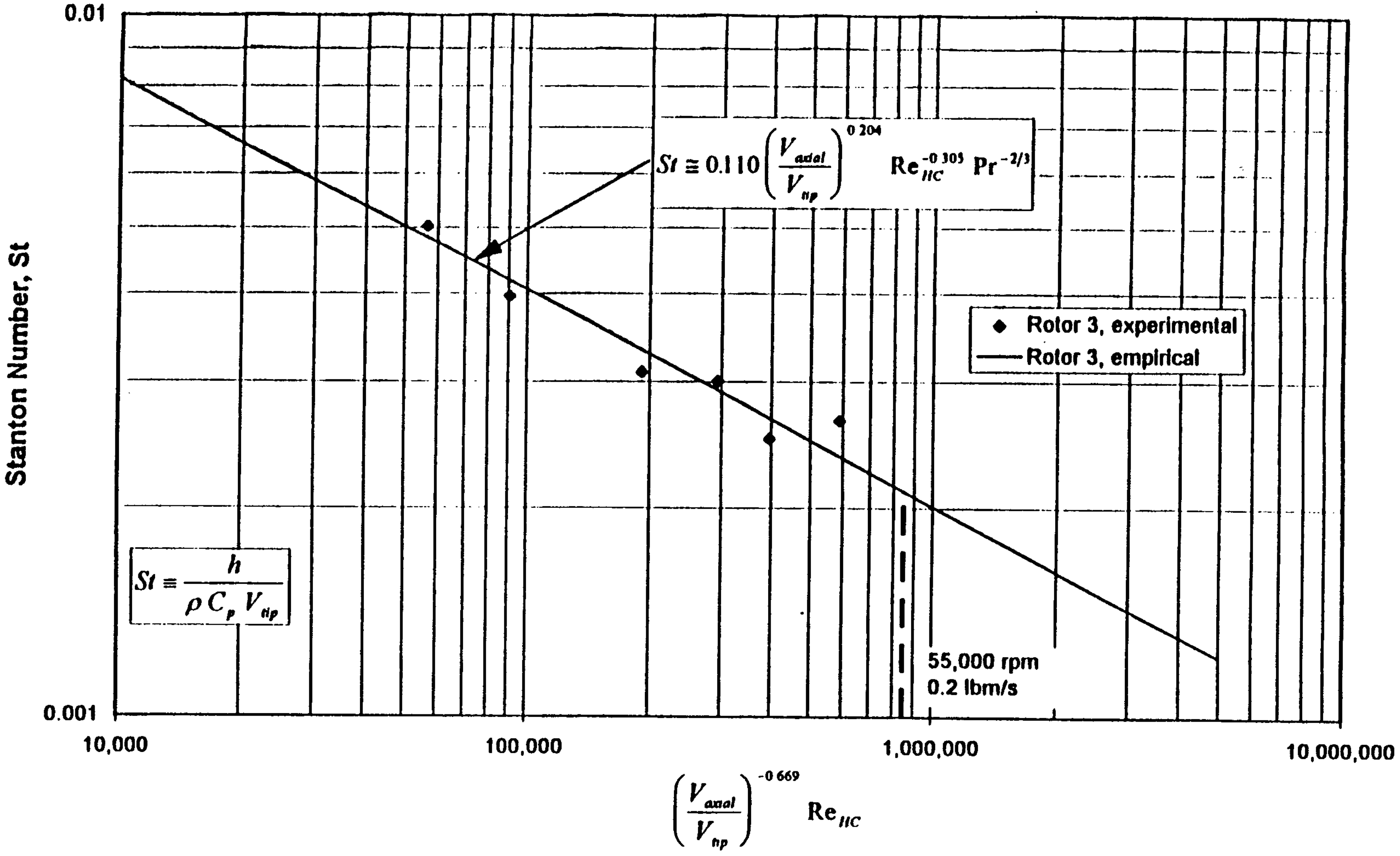

Figure 28: Pole Face 3 (Cavity Trough) Stanton Number as a function of Re_{HC} and $\frac{V_{axial}}{V_{tip}}$

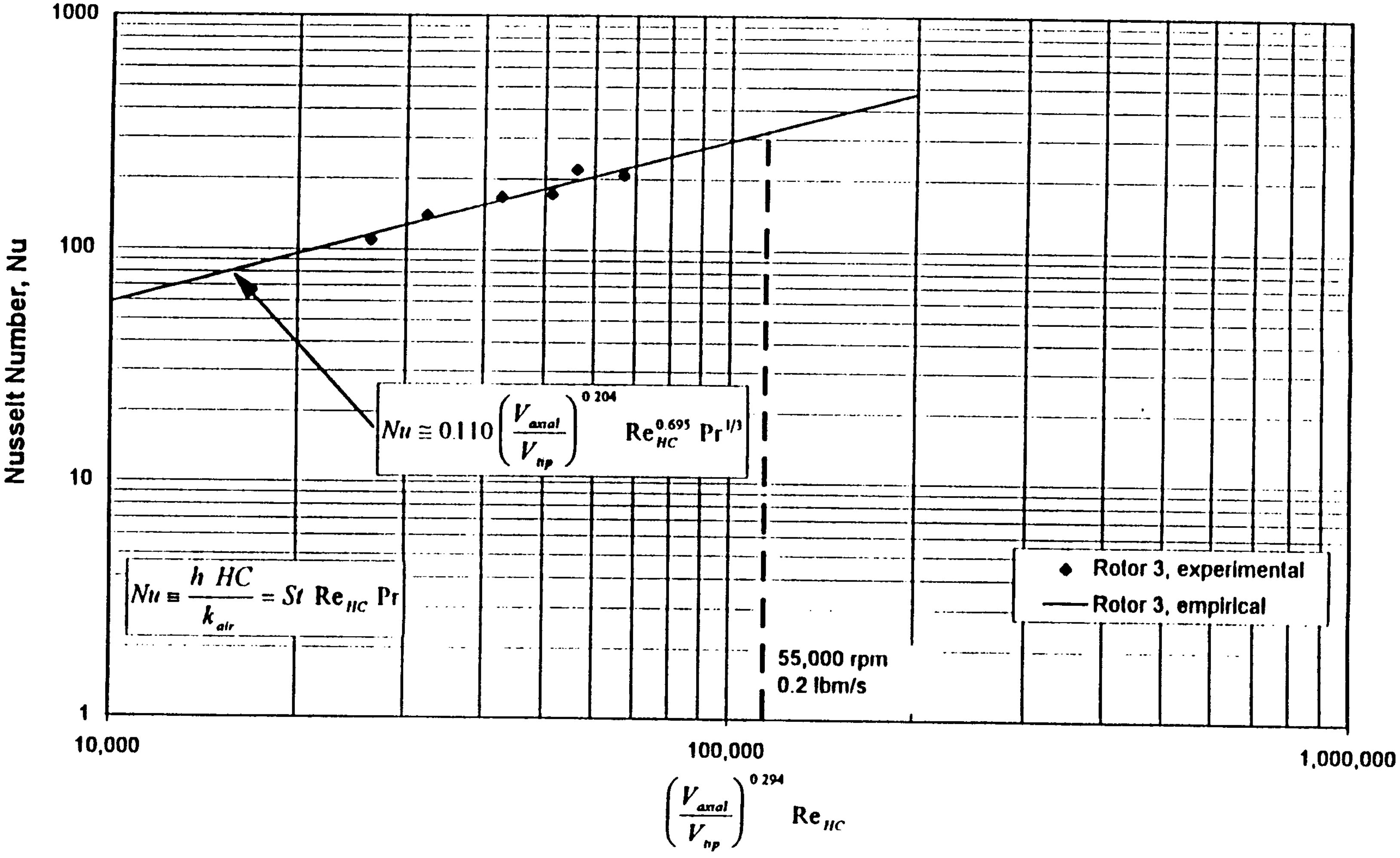

Figure 29: Pole Face 3 (Cavity Trough) Nusselt Number as a function of Re_{HC} and $\frac{V_{axial}}{V_{np}}$

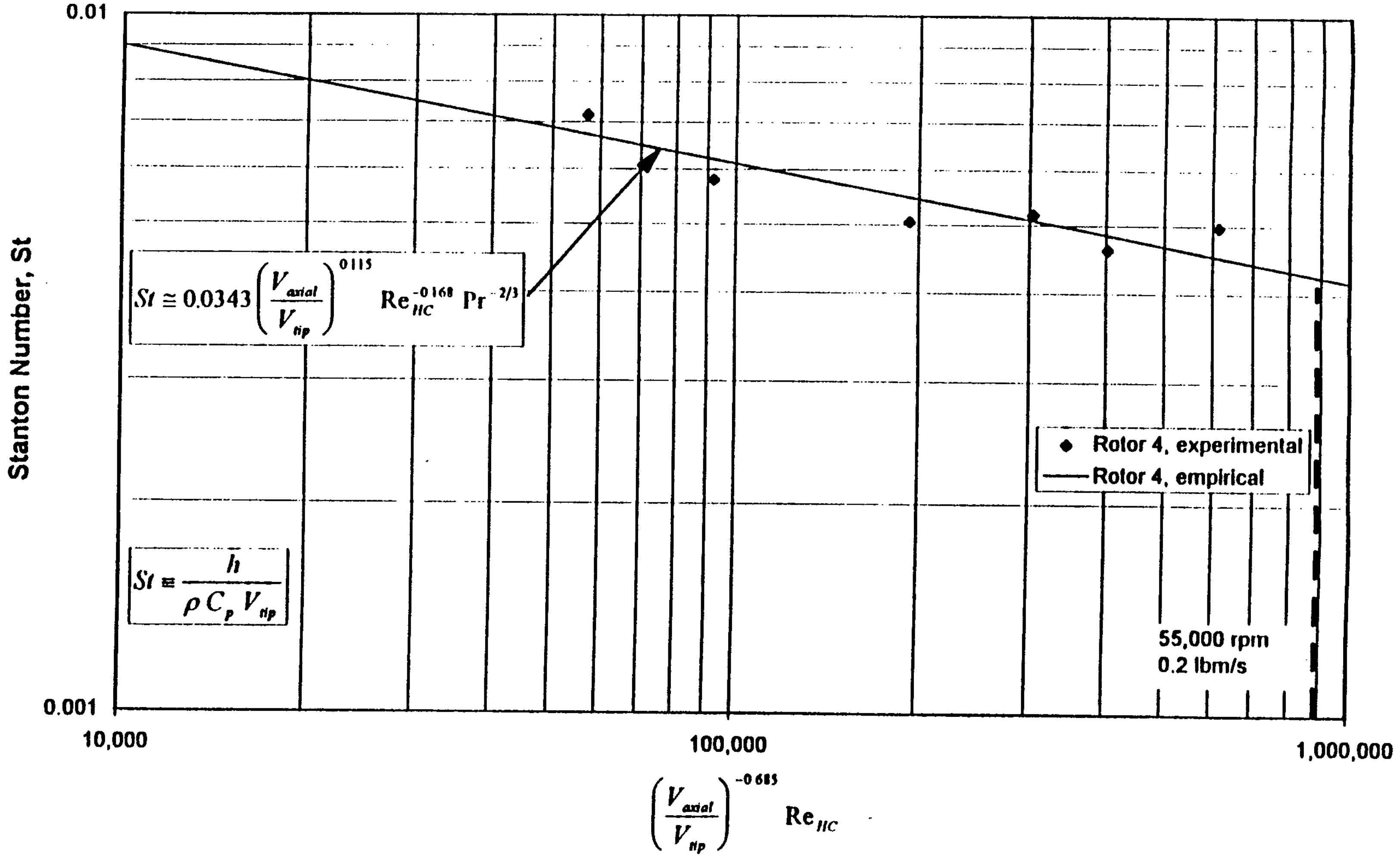

Figure 30: Pole Face 4 (Windward Face) Stanton Number as a function of Re_{HC} and $\frac{V_{axial}}{V_{tip}}$

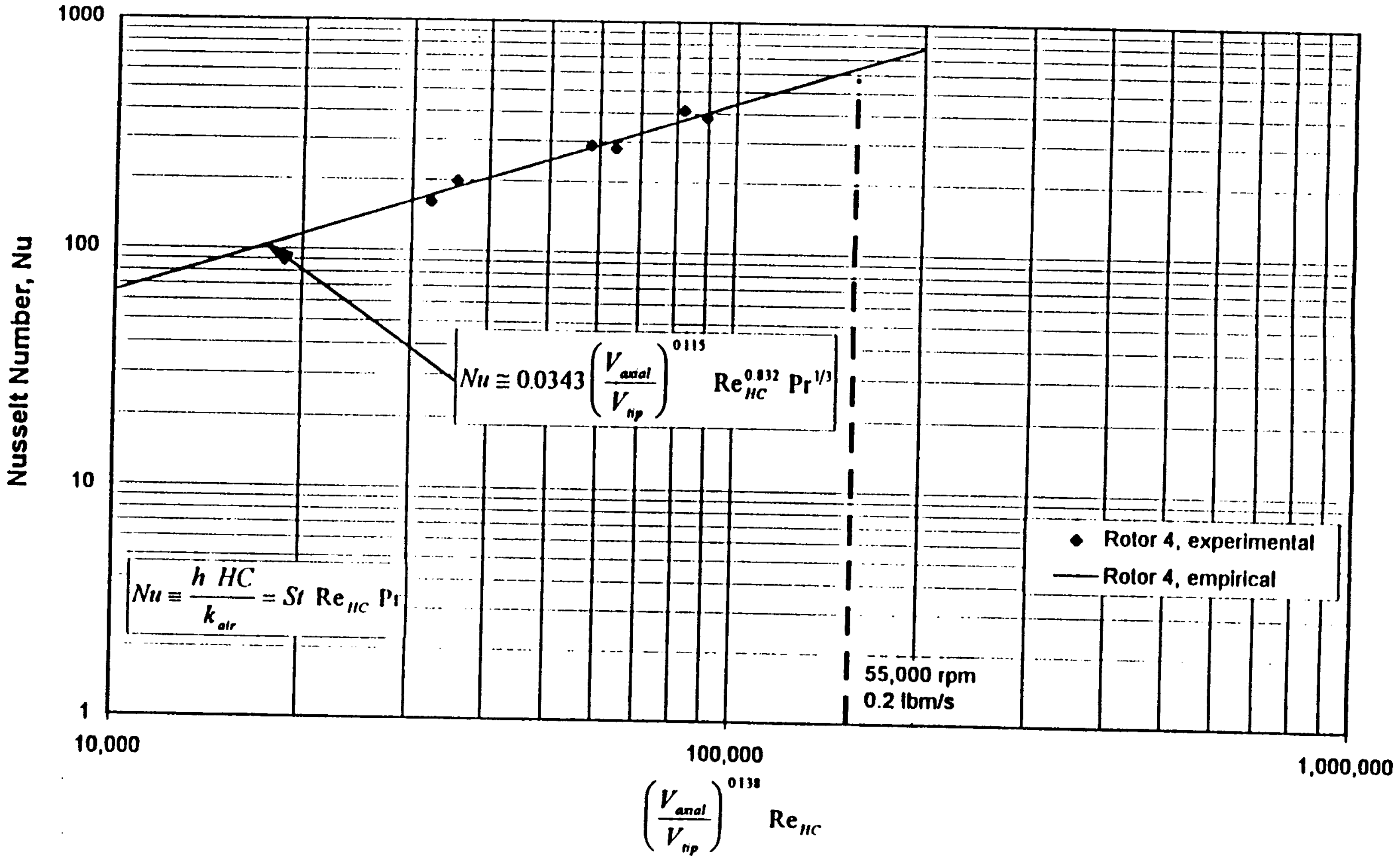

Figure 31: Pole Face 4 (Windward Face) Nusselt Number as a function of Re_{HC} and $\frac{V_{axial}}{V_{tip}}$

The empirical equations are summarized as follows:

Pole Face 1 (Rotor Tip)

$$St \cong 0.052\left(\frac{V_{axial}}{V_{tip}}\right)^{0.254} \mathrm{Re}_{h_t}{}^{-0.222}\,\mathrm{Pr}^{-2/3} \qquad (5\text{-}4)$$

$$Nu \cong 0.052\left(\frac{V_{axial}}{V_{tip}}\right)^{0.254} \mathrm{Re}_{h_t}{}^{0.778}\,\mathrm{Pr}^{1/3} \qquad (5\text{-}5)$$

Pole Face 2 (Leeward Face)

$$St \cong 0.0268\left(\frac{V_{axial}}{V_{tip}}\right)^{0.297} \mathrm{Re}_{HC}{}^{-0.153}\,\mathrm{Pr}^{-2/3} \qquad (5\text{-}6)$$

$$Nu \cong 0.0268\left(\frac{V_{axial}}{V_{tip}}\right)^{0.297} \mathrm{Re}_{HC}{}^{0.847}\,\mathrm{Pr}^{1/3} \qquad (5\text{-}7)$$

Pole Face 3 (Cavity Trough)

$$St \cong 0.110\left(\frac{V_{axial}}{V_{tip}}\right)^{0.204} \mathrm{Re}_{HC}{}^{-0.305}\,\mathrm{Pr}^{-2/3} \qquad (5\text{-}8)$$

$$Nu \cong 0.110\left(\frac{V_{axial}}{V_{tip}}\right)^{0.204} \mathrm{Re}_{HC}{}^{0.695}\,\mathrm{Pr}^{1/3} \qquad (5\text{-}9)$$

Pole Face 4 (Windward Face)

$$St \cong 0.0343\left(\frac{V_{axial}}{V_{tip}}\right)^{0.115} \mathrm{Re}_{HC}{}^{-0.168}\,\mathrm{Pr}^{-2/3} \qquad (5\text{-}10)$$

$$Nu \cong 0.0343\left(\frac{V_{axial}}{V_{tip}}\right)^{0.115} \mathrm{Re}_{HC}{}^{0.832}\,\mathrm{Pr}^{1/3} \qquad (5\text{-}11)$$

To visualize the relative film coefficients on the four pole face, Figures 32 and 33 present the Stanton number and Nusselt number, respectively, for all of the experiments

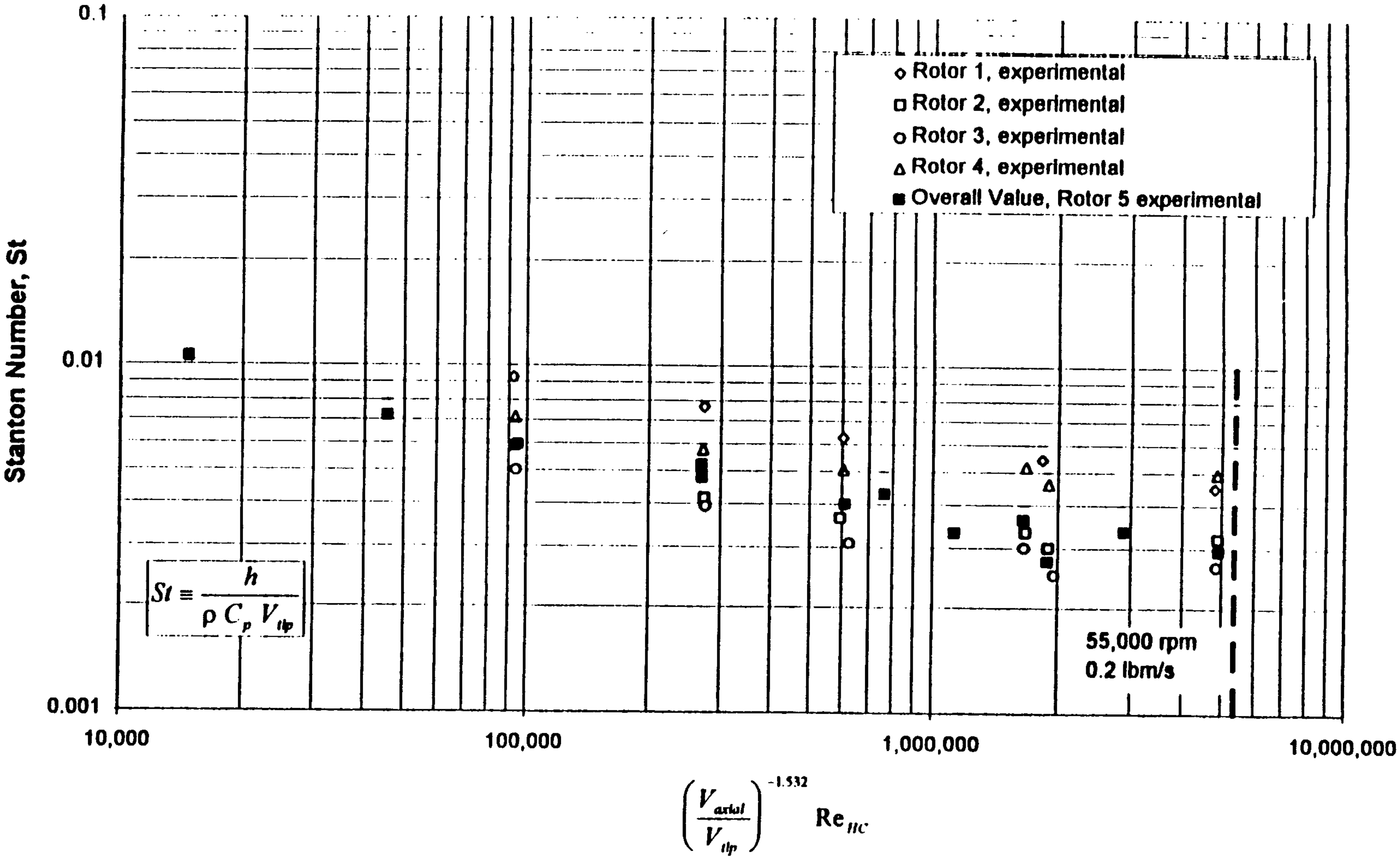

Figure 32: Overall and Individual Pole Surface Stanton Numbers

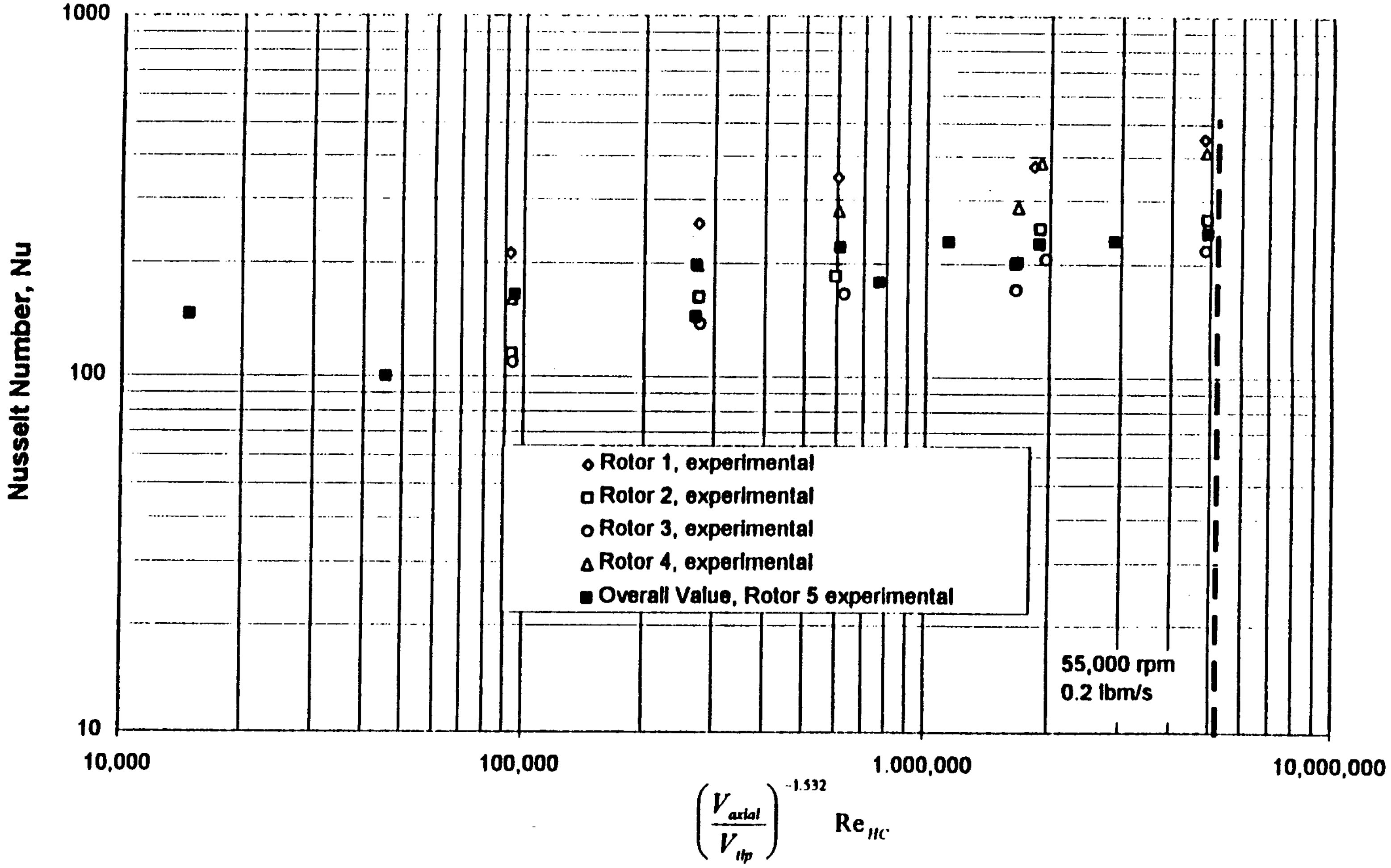

Figure 33: Overall and Individual Pole Surface Nusselt Numbers

using a common abscissa. As expected, pole face 1 has the highest film coefficient followed by face 4 (windward face), face 2 (leeward face) and face 3 (trough region).

Also plotted in Figures 32 and 33 are the overall Stanton and Nusselt numbers for the rotor pole surfaces. These are defined based on an overall film coefficient, $\bar{h}$, such that the total heat loss from the rotor pole tips is given by:

$$\dot{q}_{pole\ surfaces} = \bar{h}\left[A_1\left(T_1 - T_{m1}\right) + A_2\left(T_2 - T_{mc}\right) + A_3\left(T_3 - T_{mc}\right) + A_4\left(T_4 - T_{mc}\right)\right] \qquad (5\text{-}12)$$

The values of $\bar{h}$ were determined by analyzing rotor 5 data with program Analyzer to determine a single film coefficient which, when applied to all of the rotor pole surfaces, best approximates the temperature history of the rotor core in the experiment. The overall values of St and Nu are bounded by the values for the individual faces. The results for overall Stanton and Nusselt numbers are presented in Figures 34 and 35 respectively. Similar to the individual faces, empirical relations relating the overall Stanton and Nusselt numbers to $\frac{V_{axial}}{V_{tip}}$ and Re_{HC} were developed.

$$St_{overall} \cong 0.115\left(\frac{V_{axial}}{V_{tip}}\right)^{0.331} \mathrm{Re}_{HC}^{-0.275}\,\mathrm{Pr}^{-2/3} \qquad (5\text{-}13)$$

$$Nu_{overall} \cong 0.115\left(\frac{V_{axial}}{V_{tip}}\right)^{0.331} \mathrm{Re}_{HC}^{0.725}\,\mathrm{Pr}^{1/3} \qquad (5\text{-}14)$$

These empirical equations predict the experimental results within ± 15%.

5.3 Estimate of Temperature for use with Overall Film Coefficient

The overall film coefficients determined using program Analyzer were based on the difference in temperature between each exposed pole surface and the adiabatic wall

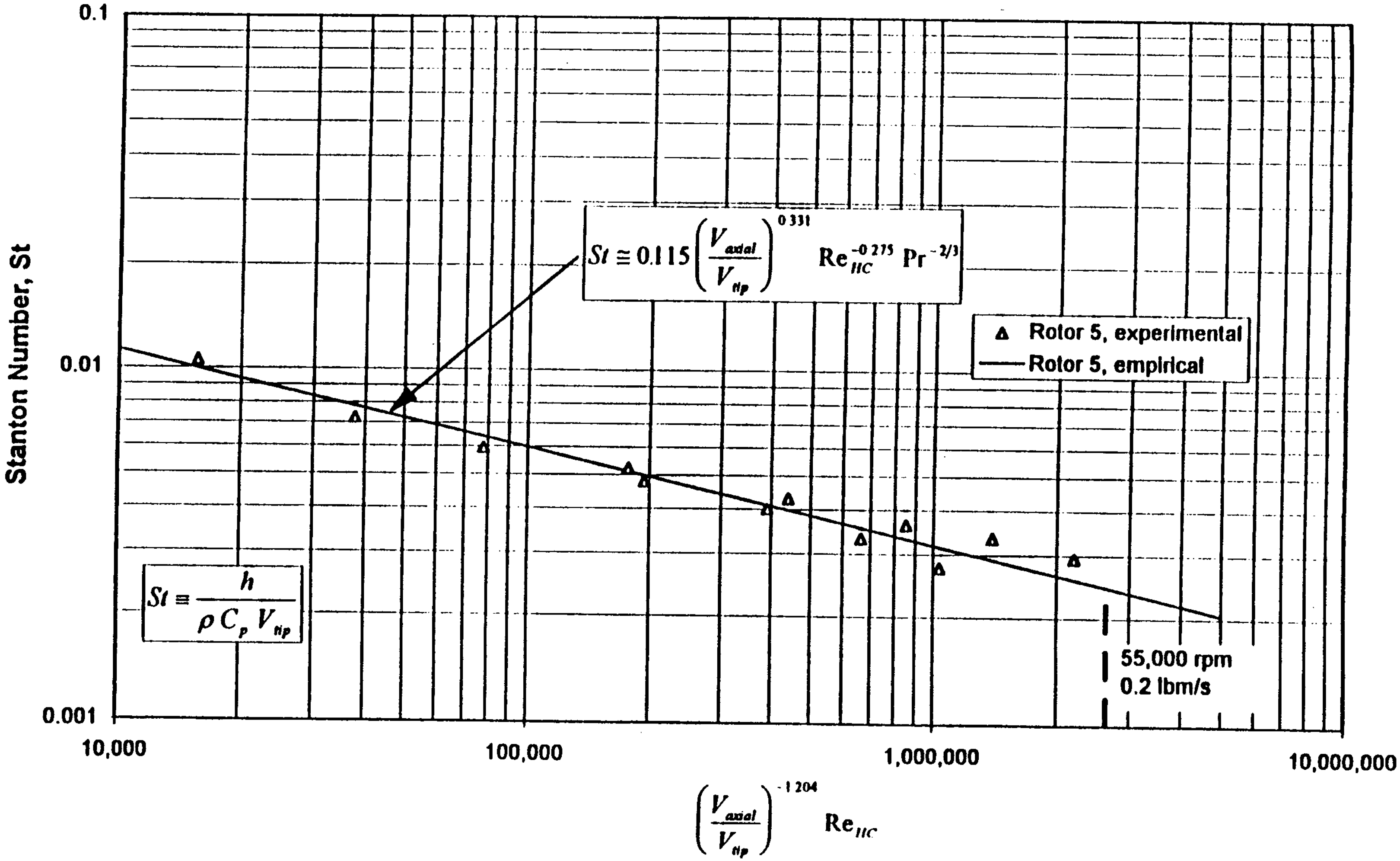

Figure 34: Overall Stanton Number as a Function of Re_{HC} and $\frac{V_{axial}}{V_{tip}}$

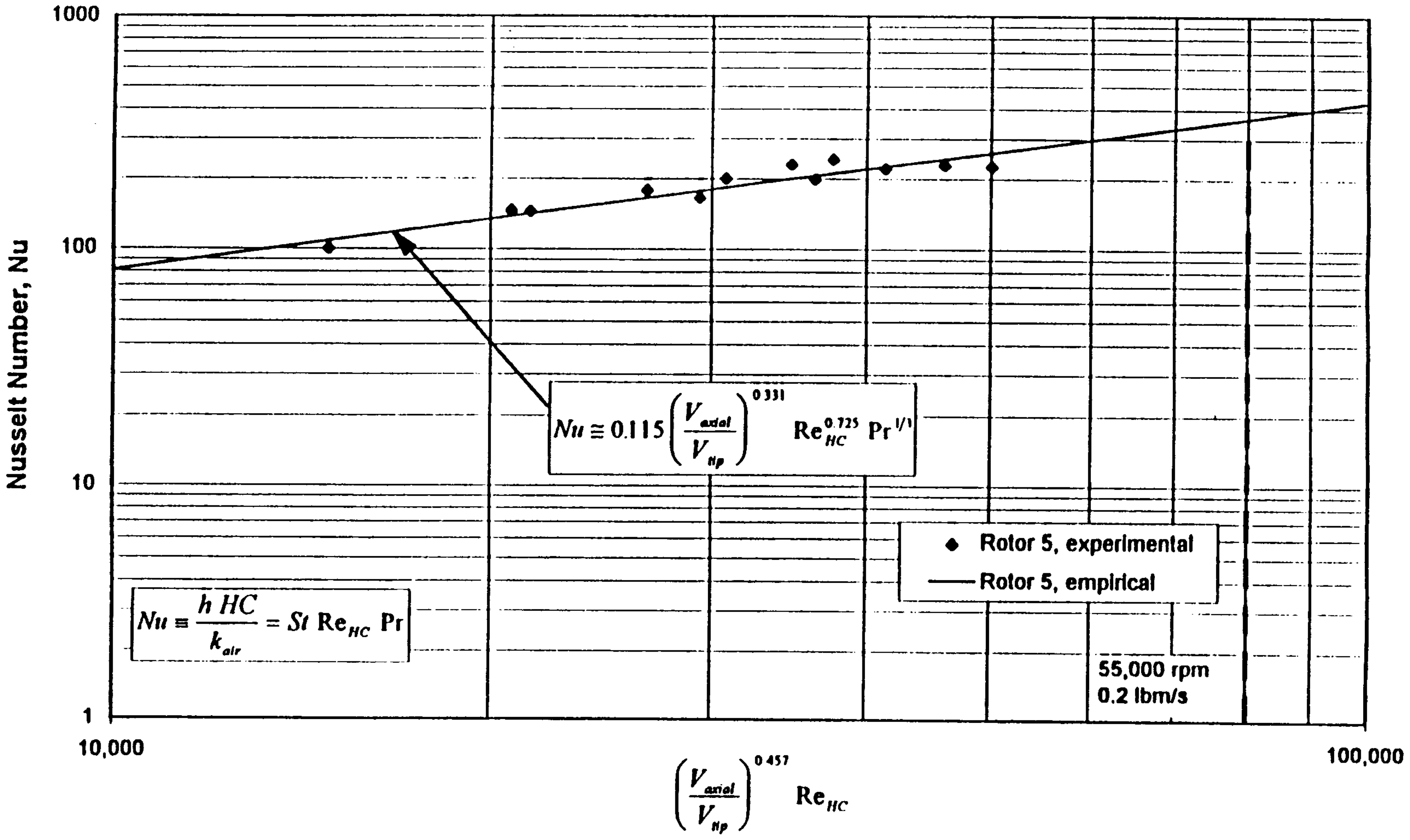

Figure 35: Overall Nusselt Number as a Function of Re_{HC} and $\frac{V_{axial}}{V_{tip}}$

temperature of the air to which it convects. Thus, pole face 1 convected to T_{m1} and faces 2, 3, and 4 convected to T_{mc}. Unfortunately, the analytical expressions for T_{m1} and T_{mc} are themselves functions of the film coefficients on the individual pole faces. It is possible to use the results for Nu for the individual pole faces to back substitute into the coefficients employed in the calculation of the reference temperatures.

However, it is desired to investigate a simpler method of using the results of this study to estimate the heat loss from the rotor poles. I.e., it is desired to employ the values of overall film coefficient in a simple equation to determine overall pole tip heat transfer defined as:

$$\dot{q}_{pole\ surfaces} = \bar{h}\left(A_1 + A_2 + A_3 + A_4\right)\left(T_{rotor\ core} - T_{reference}\right) \tag{5-15}$$

Note that this expression differs from equation 5-12 in that it is based on the difference between the rotor core temperature and a single reference temperature rather than the individual surface temperatures and their associated reference temperatures. Thus, this expression assumes that the rotor core temperature is a reasonable approximation of the pole face surface temperatures.

For each rotor 5 experiment, the heat transfer from the rotor pole tips was calculated at each second using equation 5-12. With the total heat loss from the pole known at each interval, the reference temperature was calculated using equation 5-15. The calculated reference temperature at each second was analyzed with respect to rotor, inlet air and stator temperatures. For each experiment, it was found that the reference temperature can be accurately represented as a linear combination of these three temperatures. These relationships were characterized as dimensionless parameters:

$\frac{T_{rotor} - T_{reference}}{T_{rotor} - T_{inlet}}$ and $\frac{T_{rotor} - T_{stator}}{T_{rotor} - T_{inlet}}$. These parameters are plotted in Figure 36 and represent rotor speeds ranging from 5,000 to 30,000 rpm and axial flow rates from 0.08 to 0.16 lbm/s. Although it was anticipated that the reference temperature would also be dependent upon the amount of axial airflow and rotor speed, there is no strong correlation to either of these influences based on the experimental data. The best fit to the data is a straight line given by:

$$\frac{T_{rotor} - T_{reference}}{T_{rotor} - T_{inlet}} = 0.500\frac{T_{rotor} - T_{stator}}{T_{rotor} - T_{inlet}} + 0.369 \tag{5-16}$$

which predicts the results within 3%.

5.4 Discussion of Results

The empirical correlation for St and Nu for the individual pole faces as well as the overall values accurately predict the experimentally inferred results. The empirical correlations for the individual pole faces predict the experimental results to within ±10% except for one data point. This lone data point is associated with pole face 2 and differs from the empirical value by 16%. The correlations for the overall Nu and St numbers predict the experimental values within ±15%. Such excellent correlation over a wide range of rotor speeds and axial flow rates suggests that the data is consistent and that the choice of Reynolds number and the ratio of axial air velocity in the cavity to rotor tip speed, $\frac{V_{axial}}{V_{tip}}$, are effective independent variables in characterizing the film coefficients.

While the overall values of St and Nu are bounded by the values for the individual faces, they tend toward the lower range. The values of $\bar{h}$ inferred from the rotor 5

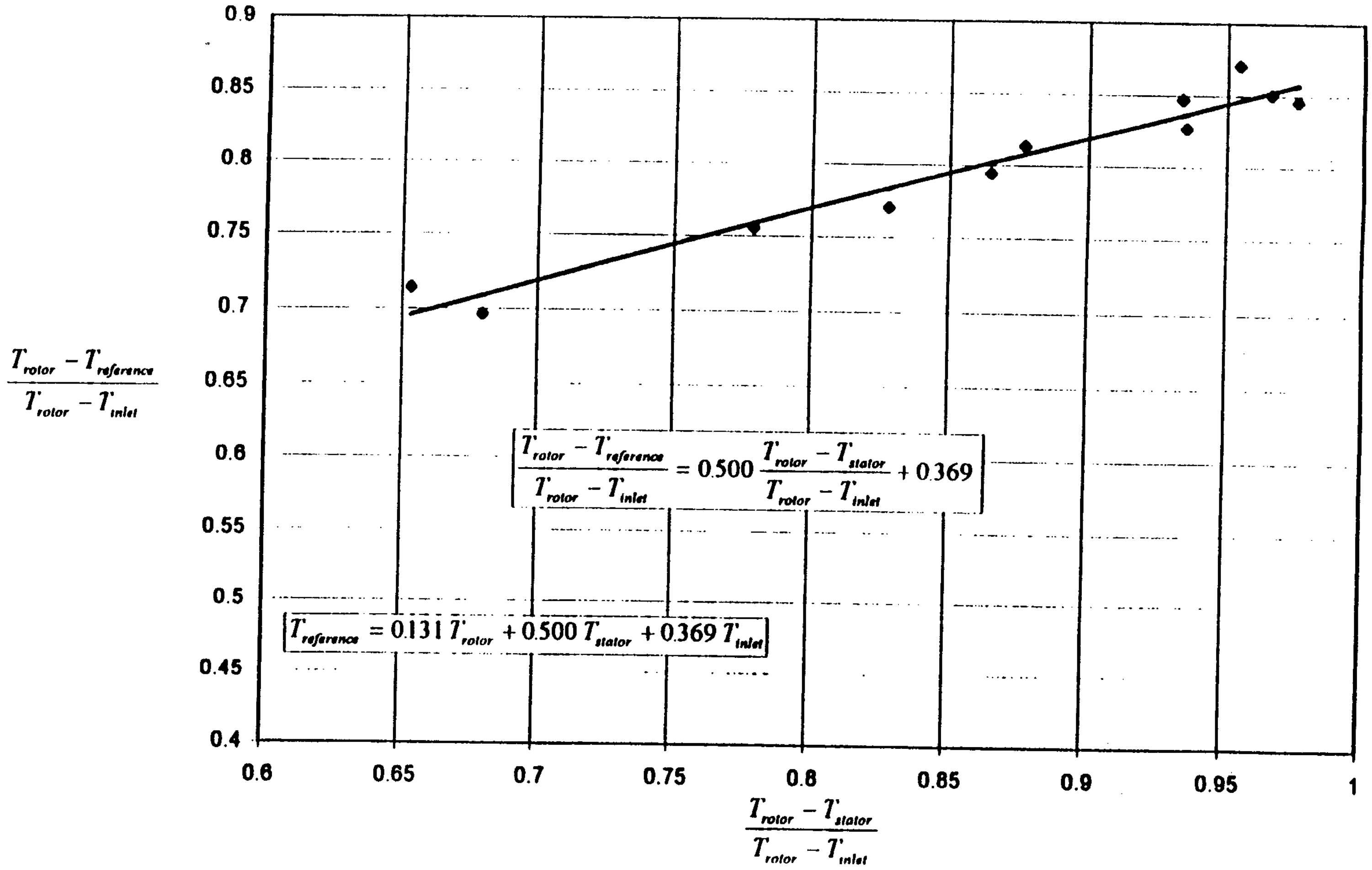

Figure 36: Reference Temperature for Overall Heat Transfer Coefficient

experimental data are probably more accurate than the values for the individual pole faces inferred from rotors 1 through 4. This is because a greater percentage of rotor 5 total heat loss flows through the uninsulated pole faces compared to rotors 1 through 4 and thus the rate of rotor cooling of the rotor core is more greatly influenced by convection at the rotor poles. Also, as previously discussed, the film coefficient values reported for the individual pole faces represent a compromise that under-predict the rate of cooling of rotors 1 through 4 and over-predict the cooling of rotor 5. So, these values of individual film coefficients may be high by approximately 15%.

The heat transfer coefficients for this specific rotor geometry are dependent on the speed of the rotor which dictates its tip speed, V_{tip}, and the amount of axial airflow which defines the average axial velocity through the cavities, V_{axial}. By characterizing the Nusselt number as the product of functions of Re and $\frac{V_{axial}}{V_{tip}}$, it is interesting to observe that the Nusselt numbers varies approximately with $\mathrm{Re}^{0.8}$. This result is analogous to and consistent with the empirical relations for turbulent flow over flat plates and inside tubes. The overall Nusselt number also varies with $\left(\frac{V_{axial}}{V_{tip}}\right)^{0.331}$. So, for a given rotor speed, the overall film coefficient varies with $V_{axial}^{1/3}$. Increasing the axial flow through the rotor by 10% will increase the film coefficient by approximately 3%.

CHAPTER VI

CONCLUSIONS AND RECOMMENDATIONS

6.1 Conclusions

The convective film coefficients for the unique rotor pole faces as well as an overall coefficient for the combined pole faces were successfully inferred from the experimental data. The analyses of the many experiments provided consistent results and excellent correlation of the Nusselt and Stanton numbers to Reynolds number and the dimensionless axial flow parameter, $\frac{V_{axial}}{V_{tip}}$. The overall film coefficient, expressed in terms of Stanton and Nusselt numbers is given by:

$$St_{overall} \cong 0.115\left(\frac{V_{axial}}{V_{tip}}\right)^{0.331} \mathrm{Re}_{HC}^{-0.275}\,\mathrm{Pr}^{-2/3} \tag{6-1}$$

$$Nu_{overall} \cong 0.115\left(\frac{V_{axial}}{V_{tip}}\right)^{0.331} \mathrm{Re}_{HC}^{0.725}\,\mathrm{Pr}^{1/3} \tag{6-2}$$

The values for the individual pole faces are of similar form. The empirical relations for the overall film coefficients predict the experimental results within 15% and the relations for the individual faces conform with the experimental results within 10%.

The Reynolds number dependence of the Nusselt number is very similar to the classic empirical relations associated with flow in tubes and over flat plates where the Nusselt number varies with $\mathrm{Re}^{0.8}$.

An analysis of high-speed, wall-driven heat transfer was developed and verified experimentally using smooth poled rotor 6. The analytical model was validated for $5{,}000 < Re_{h_r} < 7{,}500$ when it predicted the convective film coefficient within 10% of the experimental results. The analytical model was further verified by Gazely's[2] experimental results for a smooth poled at low speeds, $Re_{h_r} = 1{,}000$ where the affects of aerodynamic heating are minimal.

The film coefficient for the pole tip is best correlated when the effects of axial flow are included. The rotor 1 experimental results presented in Figure 24 are for the cases of full and half flow through the rotors. The correlation given by equation 5-4 predicts the experimental results within 3%. While it is clear that axial flow affects heat transfer on this face, it is interesting to analyze the data as a function of Reynolds number alone and compare the results to the analytical estimate for a smooth poled rotor with no axial flow.. Figure 37 presents a comparison of the Stanton number for Rotor 1 with axial flow and Rotor 6 with no axial flow as a function of Reynolds number alone. Clearly, the turbulence associated with the poled rotor, the increased shear stress over the pole face as a result of boundary layer restart and the effects of forced axial flow cause a substantial increase in convective film coefficient. In this case, the film coefficient is more than 2.5 times the smooth rotor.

6.2 Recommendations for Further Study

Enhanced heat transfer can be achieved by increasing the surface area for convection. The actual IPU rotor is comprised of material laminates. If the laminates were staggered such that the rotor surfaces were jagged, this would result in increased

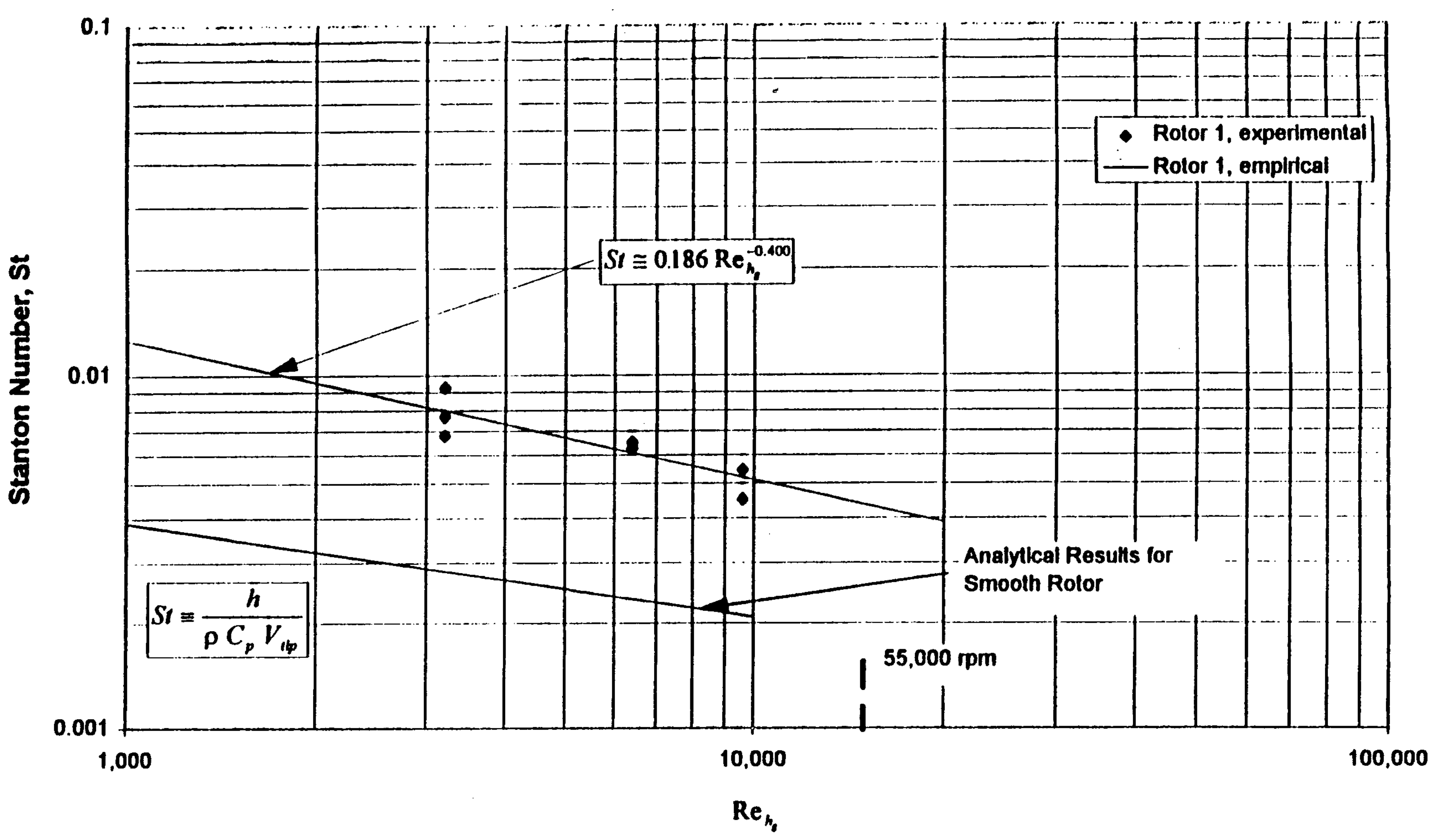

Figure 37: Comparison of Stanton Number for Face 1 (Pole Tip) Compared to Smooth Rotor

surface area for heat transfer as well as increased turbulence. The penalty for this configuration may be increased windage losses.

The current design of the IPU utilizes forced axial airflow to provide cooling of the rotors. An experimental configuration that should be studied is the use of partial shrouds at the inlet and outlet of the rotor. These shrouds would cause the rotor to induce axial airflow. The concept is to take advantage of the pressure gradient that exists in the cavity region of the rotor. The shroud at the inlet of the rotor exposes the lower half of the cavity cross section where the cavity pressure is low. The shroud at the outlet of the rotor exposes the outer portion of the cavity cross section where the pressure is high. This arrangement causes a natural pumping of air through the cavity.

BIBLIOGRAPHY

1. Klaass, R. M., & B. M. McFadden (1994). More-Electric Aircraft Integrated Power Unit Designed for Dual Use. *The Society of Automotive Engineers, Paper No 941159.*

2. Gazley, Jr., Carl (1958). Heat Transfer Characteristics of the Rotational and Axial Flow Between Concentric Cylinders. *Journal of Heat Transfer, Trans. ASME, Vol. 80, 79-90.*

3. Hayase, T., Humphrey, J.A.C., & Greif, R. (1992). Numerical Calculation of Convective Heat Transfer Between Rotating Coaxial Cylinders with Periodically Embedded Cavities. *Journal of Heat Transfer, Vol. 114, 589-597.*

4. Hayase, T., Humphrey, J.A.C., & Greif, R. (1990). Numerical Study of Three-Dimensional Flow and Heat Transfer Between a Fixed Outer Cylinder and a Rotating Inner Cylinder with Cavities. *3rd International Symposium on Transport Phenomena and Dynamics of Rotating Machinery, 239-254.*

5. Hwang, G.J., Lin, D.K., & Chen, L.T. (1990). Heat Transfer Between Rotating Cylinders. *3rd International Symposium on Transport Phenomena and Dynamics of Rotating Machinery, 161-176.*

6. Incropera, F. P., & D. P. DeWitt. (1990). *Fundamentals of Heat and Mass Transfer.* New York, NY: John Wiley & Sons.

7. Himes, M. E., T. J. Whitney, R. A. Brockman, & J. D. Wolf (1996). *Heat Transfer Analysis of Calorimeter Design.* University of Dayton Research Institute Report UDR-TR-96-44.

8. Arpaci, V.S. (1966). *Conduction Heat Transfer.* Reading, Massachusetts: Addison-Wesley Publishing Co.

9. Heisler, M.P. (1947). Temperature Charts for Induction and Constant Temperature Heating. *Transactions ASME, 227-236.*

10. Popiel, Cz. O., & L. Boguslawski. (1975). Local Heat Transfer Coefficients on the Rotating Disk in Still Air. *International Journal of Heat and Mass Transfer, Vol. 18, 170-174.*

11. White, F.M. (1991). *Viscous Fluid Flow* (Second Edition). New York: McGraw Hill, Inc.

12. Kays, W.M., & M.E. Crawford (1993). *Convective Heat and Mass Transfer* (Third Edition). New York: McGraw-Hill, Inc.

13. Schlichting, Herman (1979). *Boundary Layer Theory* (7th ed). New York: McGraw-Hill Book Company.

14. Young, A.D. (1989). *Boundary Layers*. Great Britain: Mackays of Chatham, Kent.

15. Korkegi, R.H., & R.A. Briggs (1970). Compressible Turbulent Plane Couette Flow with Variable Heat Transfer based on v on Karman Model. *AIAA Journal, Vol. 8, 817-819.*

16. Korkegi, R.H., & R. A. Briggs (1968). On Compressible Turbulent-Plane Couette Flow. *AIAA Journal, Vol. 6, 742-744.*

17. Schauer, J.J. (1995). *Prediction of Windage Losses in High Speed Generators.* University of Dayton Report for Contract F33615-94-C-2418

18. Materials Engineering (1972). 1973 Materials Selector, *Materials Engineering Magazine, Vol. 76, No.4.*

19. Miller, Richard W. (1996). *Flow Measurement Engineering Handbook* (Third Edition). New York: McGraw-Hill Book Company.

20. Military Standardization Handbook MIL-HDBK-5D (1983). Metallic Materials and Elements for Aerospace Vehicle Structures.

21. Benedict, Robert P. (1984). *Fundamentals of Temperature, Pressure and Flow Measurements* (3rd ed). New York: John Wiley & Sons.

22. Holman, J. P. (1972). *Heat Transfer* (Third Edition). New York: McGraw-Hill Book Company.

23. Holman, J. P. (1971). *Experimental Methods for Engineers* (2nd ed). New York: McGraw-Hill Book Company.

24. Myers, G. E. (1987). *Analytical Methods in Conduction Heat Transfer.* Schenectady, NY: Genium Publishing Corporation.

25. Burden, R.L., & J.D. Faires (1993). *Numerical Analysis* (Fifth Edition). Boston, MA: International Thomson Publishing

26. Keithley-Metrabyte. (April 1996). *DAS-TC/B User's Guide*. Part Number 95630.

27. Keithley-Metrabyte. (April 1993). *User Guide for the Keithley Data Acquisition CTM-05 Multi-Function Counter Timer Digital Expansion Board.* Part Number 24870.

28. Omega Engineering. *OS65 Series Infrared Pyrometers Operator's Manual*

29. Hibbitt, Karlsson & Sorensen, Inc. (1997). *ABAQUS/STANDARD USER'S MANUAL* (Version 5.6)

APPENDIX A

MATERIAL PROPERTIES USED IN ANALYSES

A.1 Introduction

The heat transfer analyses in this study require the input of thermophysical properties for the various materials comprising the systems and control volumes. Also, different systems of units were employed in different analyses (English and International System, SI). This appendix provides a summary of material thermophysical properties for a variety of different systems of units.

A.2 Thermophysical Properties of Solids

Many of the thermophysical properties of solid materials are temperature dependent; particularly specific heat and thermal conductivity. This temperature dependence was accounted for in the FORTRAN computer program that analyzed the experimental data from the rotors. For brevity in presentation, Table 6 presents average or representative values of property values for the temperature range of interest, 20°-120°C (68°-248°F). Specific values for temperature dependent properties as a function of temperature can be found from the reference sources noted in Table 6 or by viewing the appropriate material property subroutines in the FORTRAN code.

Table 6: Thermophysical Properties of Solids

Material	Density ρ			Thermal Conductivity k		Specific Heat C_p		Source*
	Kg/m^3	g/cm^3	lbm/in^3	W/m-°C	Btu/hr-ft-°F	Cal/g-°C Btu/lbm-°F	J/Kg-°C	
Epoxy w/ Glass Microspheres	819	0.819	0.0296	0.216	0.125	0.454	1,902	1
7075-T651 Aluminum	2,796	2.796	0.101	136.7	79	0.22	921	2
17-4PH Stainless Steel	7,833	7.833	0.283	16.8	9.7	0.12	502	3
Nylon	1,140	1.14	0.041	0.245	0.142	0.40	1,675	4

*Data Sources

1. UDRI Testing. See Appendix B.
2. Reference 20, MIL-HDBK-5D Change Notice 2, 1 May 1985.
3. Reference 20, MIL-HDBK-5D Change Notice 1, 1 January 1984.
4. Reference 18,Materials Selector 73, Materials Engineering Mid-September 1972, Vol 76 No. 4, pp 253-254.

A.3 Thermophysical Properties of Air

The thermophysical properties of air are presented in Tables 7 and 8 for SI and English units respectively. Both tables are based on data adapted from Reference 6, *Fundamentals of Heat and Mass Transfer*, Appendix A, Table A.4, page A15.

Table 7: Thermophysical Properties of Air as a Function of Temperature (SI units)

Temperature	Density ρ		Thermal Conductivity k	Specific Heat C_p		Kinematic Viscosity ν
°C	Kg/m^3	g/cm^3 x 10^3	W/m-°C x 10^3	Cal/g-°C	J/Kg-°C x 10^3	m^2/s x 10^6
-23.15 (250 K)	1.3947	1.3947	22.3	0.2403	1.006	11.44
26.85 (300 K)	1.1614	1.1614	26.3	0.2405	1.007	15.89
76.85 (350 K)	0.9950	0.9950	30.0	0.2410	1.009	20.92
126.85 (400 K)	0.8711	0.8711	33.8	0.2422	1.014	26.41

Table 8: Thermophysical Properties of Air as a Function of Temperature (English units)

Temperature	Density ρ	Thermal Conductivity k		Specific Heat] C_p	Kinematic Viscosity ν
°F	lbm/in^3 x 10^6	Btu/hr-ft-°F	Btu/s-in-°F x 10^6	Btu/lbm-°F	in^2/s
-9.67 (250 K)	50.39	0.0129	29.83	0.2403	0.0177
80.33 (300 K)	41.96	0.0152	35.18	0.2405	0.0246
170.33 (350 K)	35.95	0.0173	40.13	0.2410	0.0324
260.33 (400 K)	31.47	0.0195	45.21	0.2422	0.0409

APPENDIX B

MEASUREMENT OF THERMOPHYSICAL PROPERTIES OF EPOXY WITH GLASS MICROSPHERES

B.1 Introduction

Accurate thermophysical property data for the epoxy used to insulate the rotor cores was essential for estimating the heat loss from the aluminum rotor cores through the insulation. The purpose of incorporating a large portion of glass microspheres by volume into the two-part epoxy was to reduce the thermal conductivity of the final product . Estimating the thermophysical properties of the mixture: density, specific heat, and thermal conductivity, by employing applicable rules of mixture was too uncertain, particularly for the thermal conductivity. Thus, it was concluded that the thermal properties would be determined experimentally.

Although there are no published thermophysical properties for the mixture of epoxy and glass microspheres employed in this investigation, the author had performed a thermal analysis in 1996 where a similar epoxy (Magnolia Plastics 55-A resin and 932-B hardener) was mixed with the same glass microspheres in the same ratio by weight (100:44:22). The values of density, specific heat and thermal conductivity for that formulation were determined experimentally by the University of Dayton Research Institute and are presented in UDR-TR-96-44, Heat Transfer Analysis of Calorimeter Design. These values are used as a benchmark to validate the results of testing of the epoxy/glass microsphere formulation used in this study.

B.2 Epoxy/Glass Microspheres Formulation

The epoxy was Magnolia Plastics Magnabond™ 6367 part A resin and part B hardener. The glass microspheres used in the formulation were 3M Scotchlite™ Glass Bubbles, Product No. D32/4500. The two part epoxy was mixed with the glass microspheres in the following ratio.

Component	Parts by Weight	Parts by Volume
6367-A resin	100	2
6367-B hardener	44	1
glass microspheres	22	3

B.3 Density Measurement

The density of a cured sample was determined by machining it to a specific dimension and simply weighing it using a Metler PE 3600 electronic scale. The sample was 4.25" x 4.25" x 0.5" (same sample used in thermal conductivity testing). This sample registered a mass of 121.24 g ± 0.1 g. This results in a density of 0.819 g/cm^3 (0.0296 lbm/in^3). Note that the epoxy used in this formulation is less dense than the 1996 investigation for which the density of the epoxy/glass microsphere mixture was 0.854 g/cm^3.

B.4 Specific Heat Measurement

The specific heat of the samples was measured by the University of Dayton Research Institute, Materials Engineering Division, using differential scanning calorimetry (DCS) which monitors the amount of energy needed to raise the temperature of the samples. The test was performed at a rate of 10°C/min over the range 30° to 150°C. The results are presented in Figure 38. These results are comparable to the 1996 study for which the specific heat of the epoxy/glass microsphere sample was measured to be 0.400 cal/g-°C at 25°C and 0.525 cal/g-°C at 80°C.

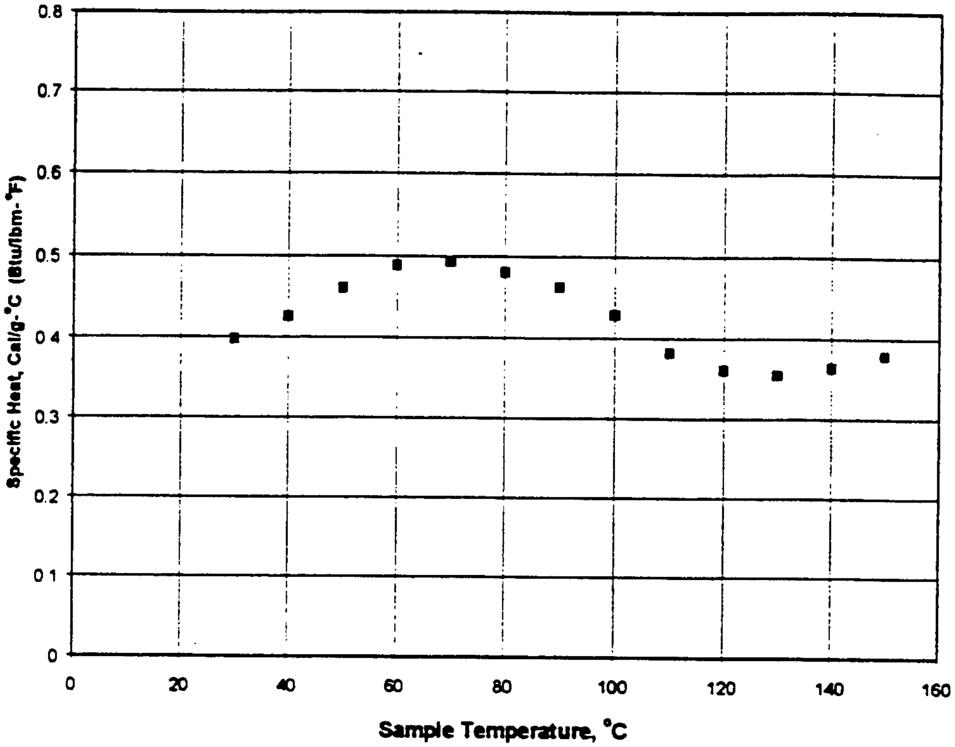

Figure 38: Specific Heat vs. Temperature for Epoxy with Glass Microspheres

B.5 Thermal Conductivity Measurement

Thermal conductivity can be calculated from knowledge of the thermal diffusivity. By definition, thermal diffusivity is given by $\alpha = \frac{k}{\rho c}$ in m^2/s, where k is thermal conductivity (W/m K), ρ is density (Kg/m^3) and c is specific heat (J/Kg K). Since the density and specific heat of the epoxy mixture have been measured, the thermal conductivity of the material can be inferred if the thermal diffusivity can be determined.

B.5.1 Experiment Concept

A simple, yet accurate, experiment was developed to determine the thermal diffusivity of the epoxy. The experiment represents a classic boundary value problem for one dimensional transient heat transfer that has an exact mathematical solution for the temperature distribution within the material as a function of location, x, time, t and thermal diffusivity, α. The concept is to determine the thermal diffusivity of the material by comparing the measured temperature within the center of a thin sample specimen as a function of time to the temperature variation predicted by theory.

Specifically, a sample whose thickness, 2L = 0.5", is much smaller than its 4.25" height and width is initially at a uniform room temperature. At time t = 0 the sample is immersed in a beaker of boiling water which imposes an instantaneous step change in wall temperature on the faces of the sample. The boiling water assures that the wall temperatures remain essentially constant. The temperature at the mid plane of the sample (x = L = 0.25") and at the exterior walls of the sample are monitored and input to the data acquisition system in 0.5 second intervals.

Because the sample's thickness is very small compared to its height and width, one dimensional heat transfer occurs in the center region of the sample and the temperature T(x,t) through the thickness of the sample can be modeled. The one dimensional heat equation for constant area heat transfer within a solid with constant thermal conductivity is given by:

$$\frac{\partial^2 T}{\partial x^2} = \frac{1}{\alpha}\frac{\partial T}{\partial t} \qquad 0 \le x \le 2L;\ t \ge 0 \qquad \text{(B-1)}$$

The boundary conditions for this experiment are:

$T(x,0) = T_{initial}$	Initial condition
$T(0,t) = T_{wall}$	Imposed boundary condition at time t = 0
$\frac{\partial T}{\partial x}(L,t) = 0$	Boundary condition at center plane due to symmetry

Defining $\Theta(x,t) = T(x,t) - T_{wall}$, the boundary value problem is transformed to yield a similar partial differential equation with two homogenous boundary conditions. The transformed problem is:

$$\frac{\partial^2 \Theta}{\partial x^2} = \frac{1}{\alpha}\frac{\partial \Theta}{\partial t} \qquad 0 \le x \le 2L;\ t \ge 0 \tag{B-2}$$

with boundary conditions:

$$\Theta(x,0) = \Theta_o = T_{initial} - T_{wall}$$

$$\Theta(0,t) = 0$$

$$\frac{\partial \Theta}{\partial x}(L,t) = 0$$

The solution is given by the Fourier series:

$$\frac{\Theta(x,t)}{\Theta_o} = \frac{T(x,t) - T_{wall}}{T_{initial} - T_{wall}} = \frac{2}{L}\sum_{n=1}^{\infty}\frac{1}{\lambda_n}e^{-\alpha\lambda_n^2 t}\sin\lambda_n x \tag{B-3}$$

where the eigenvalues, $\lambda_n = \frac{2n-1}{2L}\pi$.

The solution yields the temperature through the thickness of the sample for any location and any time. For example, for a value of $\alpha = 1.39 \times 10^{-7}$ m^2/s (0.000215 in^2/s) and a 0.5 inch sample thickness (L = 0.25"), the temperature distribution through the thickness of the sample has the profiles shown in Figure 39 at the times indicated.

For a specific location, such as the mid plane of the sample (x = L), the temperature can be predicted as a function of time. The only unknown in the equation is the value of α.

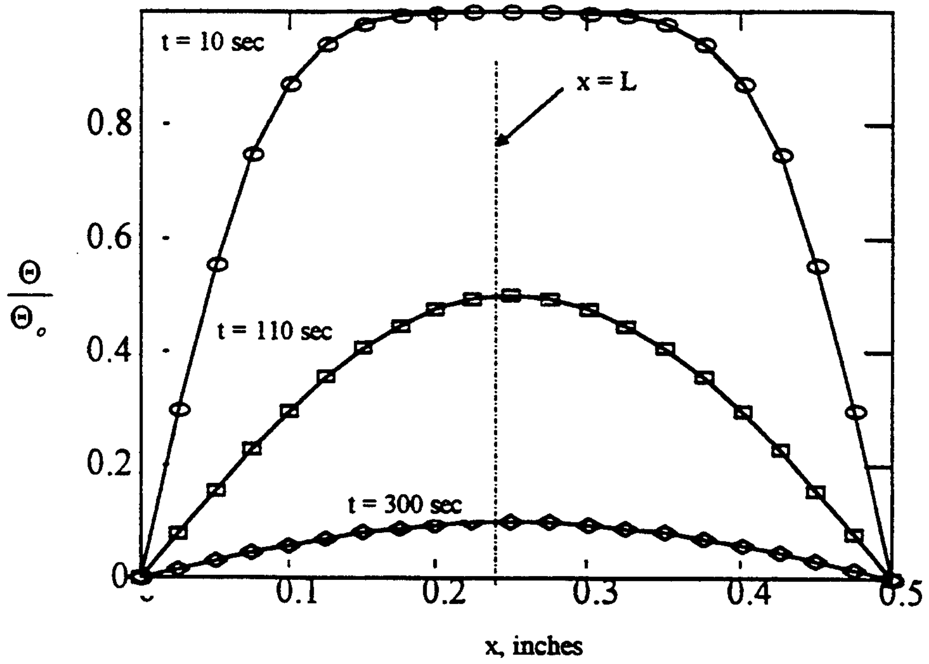

Figure 39: Predicted Temperature Distribution through Thin Epoxy Sample

Thus, it is possible to plot the normalized center plane temperature, $\frac{\Theta(L,t)}{\Theta_o} = \frac{T(L,t) - T_{wall}}{T_{initial} - T_{wall}}$, based on experimental data and on the same graph plot the distribution based on the mathematical solution to this problem for various values of α. The goal is to determine a range of values of α that bound the experimental curve for $\frac{\Theta(L)}{\Theta_o}$.

B.5.2 Sample Specimen

A 4.25" x 4.25" x 0.5" sample of epoxy with glass microspheres of the same formulation cast around the rotor cores was produced such that two thermocouples were located in the center of the sample as illustrated in Figure 40. This was accomplished by casting the epoxy mixture in a 4.25" x 4.25" mold to a thickness slightly greater than 0.25". The cured epoxy was then machined to 0.25" thickness. Two type T thermocouples fabricated of 34 awg (0.005" diameter) wire were placed on this machined face such that their beads were located adjacent to each other in the center of the face, but not touching. The thermocouple wires were fixed in place using a glue stick and were arranged such that the wires extended from the beads at the face center outward in opposite directions. The surface was thoroughly cleaned with acetone and a second layer of epoxy was cast over the face, encasing the two thermocouples. After the second layer of epoxy cured, the second surface was machined such that the total thickness was 0.5". A photograph of the finished sample is shown in Figure 41. The numbers written on the sample are the measurements of its thickness at the four edges.

Thus, a sample was prepared that encapsulated the thermocouples in the center of the sample. The purpose of embedding two thermocouples in the center of the sample was to verify that the beads had not shifted or floated out of position when the top layer of epoxy was cast. Thus, good consistency of readings between the two thermocouples gave this assurance. Further, the 34 awg wires are very fragile and susceptible to breakage. Small gage wire was used so that heat conduction from the boiling water at the boundary of the sample would not influence the temperature of the thermocouple beads. The thermocouples were modeled as 2" long fins encased in epoxy. The boiling water affected the temperature only in the first 0.5" of the wire.

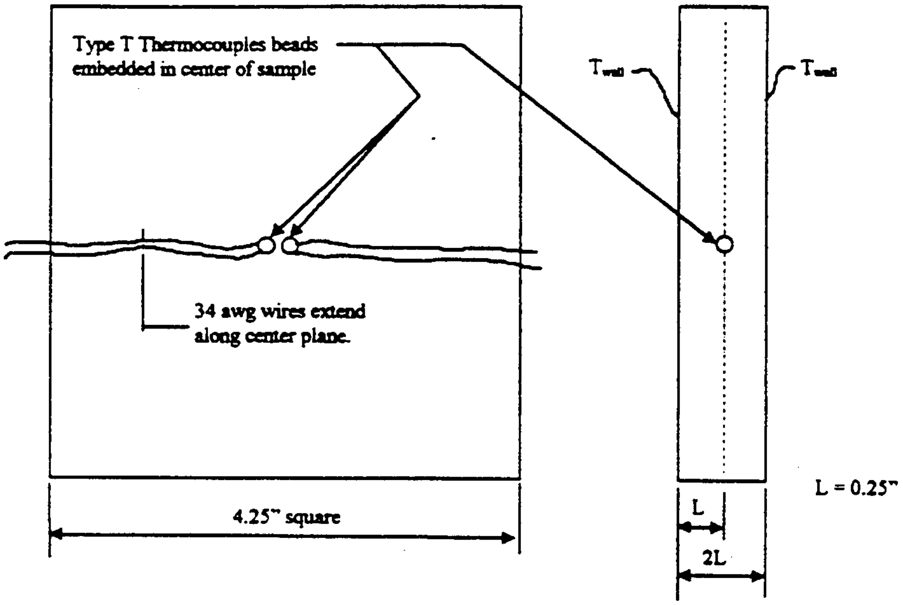
Type T Thermocouples beads embedded in center of sample
34 awg wires extend along center plane.
4.25" square
T_{wall}
T_{wall}
L
2L
L = 0.25"

Figure 40: Epoxy Sample for Determination of Thermal Diffusivity (Not to Scale)

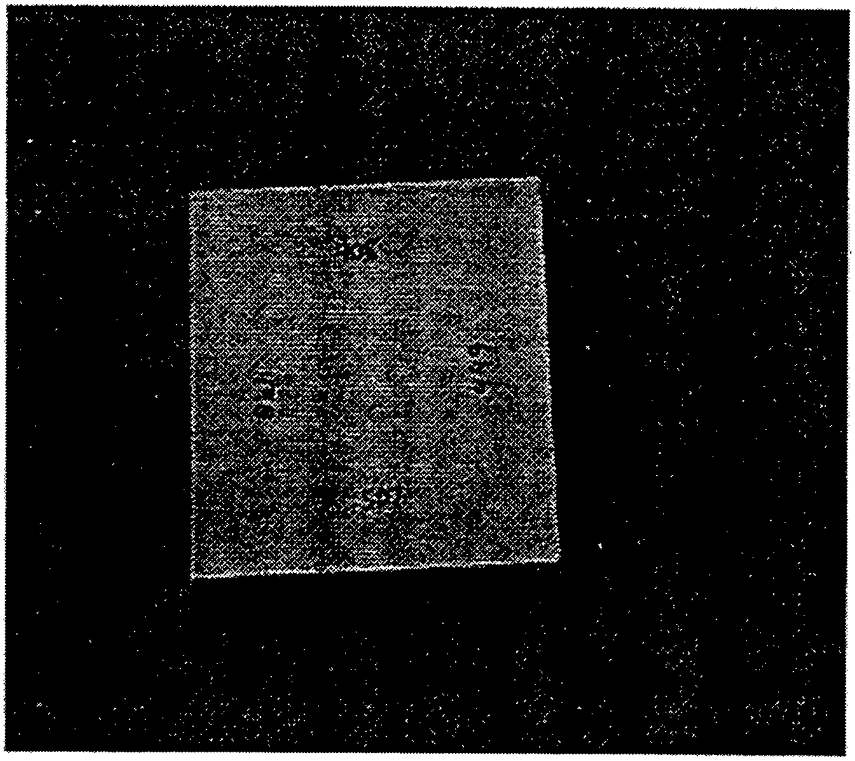

Figure 41: Photograph of Epoxy Sample

B.5.3 Results

The experiment was performed twice to assure consistent measurement. For each experiment, data was collected for approximately 500 seconds after immersion of the sample in the boiling water. In both experiments the temperatures indicated by the two embedded thermocouples were consistent with each other. The data is plotted in Figure 42 as the dimensionless temperature parameter $\frac{\Theta(L)}{\Theta_o}$ versus time. The two experiments yielded identical plots. Also plotted on the graph is the profile predicted by theory for a value of α that closely follows the profile of the experimental data. The value of α is perturbated by ± 5% resulting in profiles that bound the experimental data. Based on comparison of experimental measurement of the mid plane temperature to predicted values, the thermal diffusivity of the epoxy sample is 1.39×10^{-7} m^2/s ± 5%. It may be noted that while the profile predicted by theory closely approximates the experimental data there is evidence that the thermal diffusivity varies with the temperature of the material. However, the value stated is reasonable for the temperature range required for this investigation.

B.5.4 Conclusions

The thermal conductivity of the epoxy with glass microspheres can be estimated based on the inferred value of thermal diffusivity, $k = \alpha \rho c$

The density of the sample is 819 Kg/m^3. The average specific heat in the temperature range 0 - 100 °C is 1,902 J/Kg K. (0.454 Cal/g-°C). Using these values, the estimated value of thermal conductivity is 0.216 W/m K (0.125 Btu/hr-ft-°F).

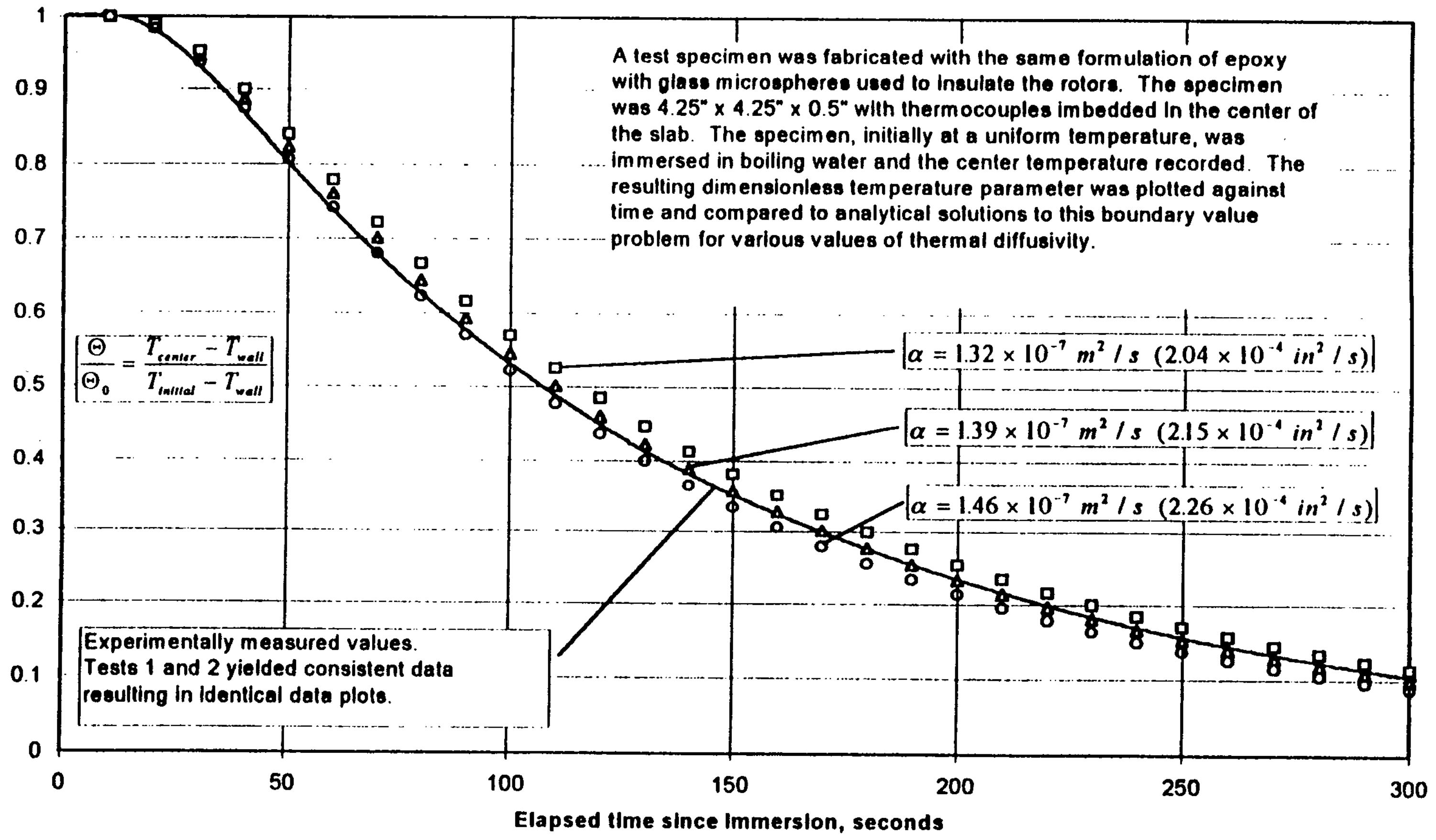

A test specimen was fabricated with the same formulation of epoxy with glass microspheres used to insulate the rotors. The specimen was 4.25" x 4.25" x 0.5" with thermocouples imbedded in the center of the slab. The specimen, initially at a uniform temperature, was immersed in boiling water and the center temperature recorded. The resulting dimensionless temperature parameter was plotted against time and compared to analytical solutions to this boundary value problem for various values of thermal diffusivity.

Experimentally measured values.
Tests 1 and 2 yielded consistent data resulting in identical data plots.

Figure 42: Estimate of Thermal Diffusivity of Epoxy With Glass Microspheres by Comparison of Experimental Data to Analytical Models

This value of thermal conductivity is comparable to the value reported in UDR-TR-96-44, Heat Transfer Analysis of Calorimeter Design for a similar epoxy (Magnolia Plastics 55-A resin and 932-B hardener) that was mixed with glass microspheres in the same ratio by weight (100:44:21). In that study, the thermal conductivity of the material was measured against a fused silica standard in accordance with ASTM C1045 and was reported to be 4.95 x 10^{-4} cal-cm/cm^2-s-C which is 0.207 W/m K (0.119 Btu/hr ft ^{0}F). The conductivity of the epoxy formulation of interest in this study, 0.216 W/m K, is only 4.4% greater than the 0.207 W/m K measured for the epoxy used in the Calorimeter Design study. It is reasonable to expect that these two epoxy formulations, mixed with glass microspheres in the same ratio by weight, would have comparable thermophysical properties. The fact that the thermal conductivities were independently measured to be so close in value further validates the results.

APPENDIX C

MULTI-LUMP ANALYSIS OF THE ROTORS

C.1 Introduction

If the epoxy coating on the rotors provided near perfect insulation and if it could be assumed that at any given time the rotor core was of uniform temperature, it would be reasonable to analyze the transient heat transfer from the rotor core using a single lump analysis. In reality, the epoxy coating, while a good insulator, is not near perfect and an appreciable amount of heat flows out the insulated surfaces. Further, the high convective film coefficients on the uninsulated rotor pole surfaces and the relatively large dimensions of the rotor cores cause temperature gradients. This means that the assumption of uniform temperature within the aluminum rotor core is not realistic.

Therefore, meaningful analysis of the experimental data requires a mathematical model that accounts for heat loss through the insulated surfaces as well as spatial variations within the entire rotor. Two models were developed to meet the analytical requirements of this study. One model is representative of the geometries of rotors 1 through 5. The second model is specific to the unique geometry of rotor 6.

C.2 Multi-Lump Models

The multi-lump analyses were developed by dividing the rotors into multiple lumps which can transfer heat with adjacent lumps as well as convect heat from their free surfaces. In this analysis, the rotor is divided into 14 "elements". Definition of the 14 elements is presented in Figure 43 for the model representative of rotors 1 through 5. (See Figure 44 for the definition of the 14 elements for the model representative of rotor 6). The front view is a true characterization of the shape of the 9 elements that comprise the center region of the rotor. Elements 6, 8 and 9 are all 0.200" thick, consistent with the thickness of the epoxy insulation coating the rotors. Thus, depending on which rotor is analyzed, one of these three elements will be assigned aluminum properties and the other two will be assigned epoxy properties. The remaining elements 1, 2, 3, 4, 5 and 7 are aluminum in all cases. The side view is a schematic representation of the 9 elements of the rotor core as well as the single elements, 10 and 11, that represent the front and rear epoxy insulation layers respectively. Elements 12, 13 and 14 represent the stainless steel shaft to which the rotor core is mounted.

In addition to numbering the unique elements that comprise the aluminum rotor core, epoxy insulation and stainless steel shaft, the regions surrounding the system have been numbered to allow application of boundary conditions specific to the front, rear and gap area around the rotor poles based on experimental measurements.

C.3 Analysis of Heat Conduction Between Elements

Each element is individually analyzed as a system. The law of conservation of energy, $\dot{E}_{in} = \dot{E}_{out} + \frac{\partial E_{stored}}{\partial t}$, is applied to each element as follows.

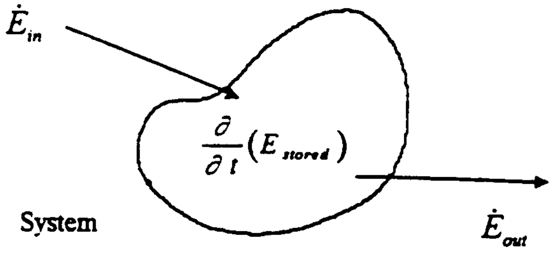

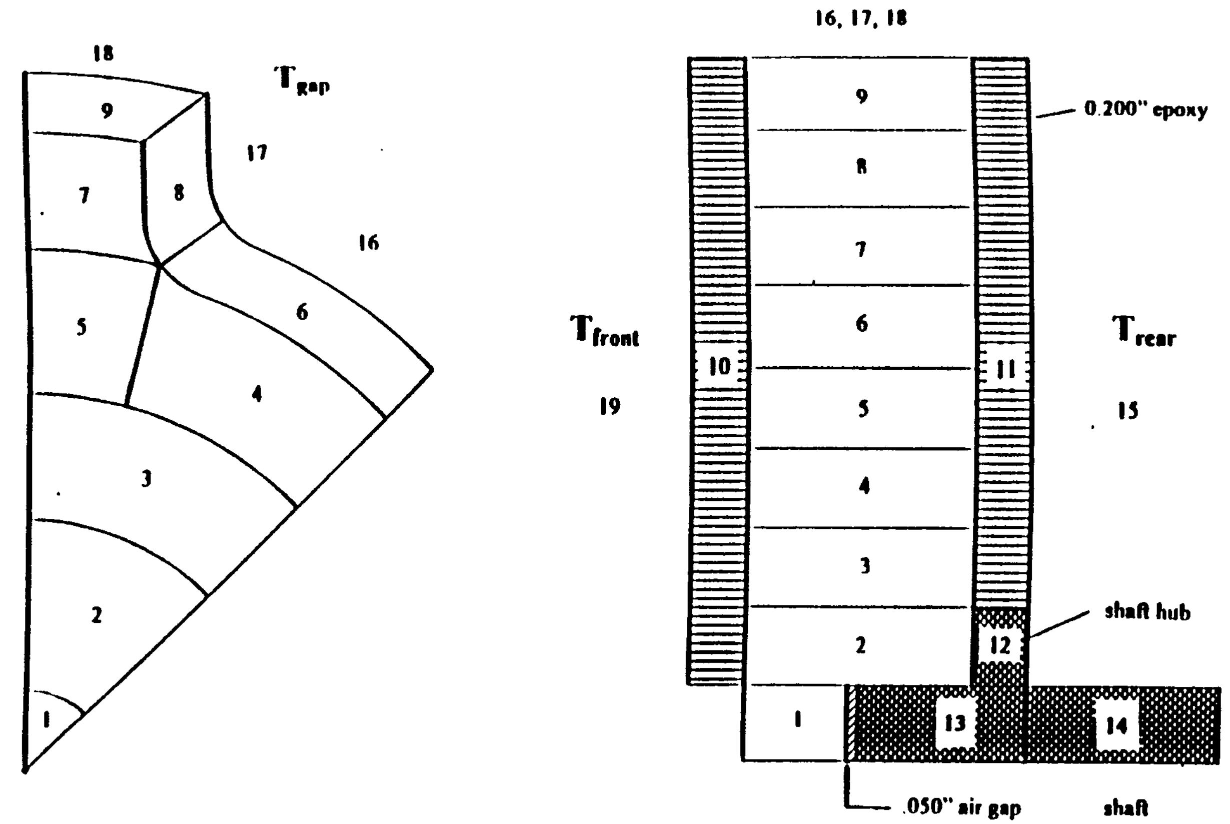
18
T_{gap}
9
17
7
8
16
5
6
4
3
2
1
16, 17, 18
9
8
7
6
T_{front}
10
11
T_{rear}
19
5
15
4
3
2
12
1
13
14
0.200" epoxy
shaft hub
.050" air gap
shaft

Definition of Elements
Front View
(Not to Scale)

Schematic Representation
Side View
(Not to Scale)

Figure 43: Definition of Elements for Rotors 1 - 5

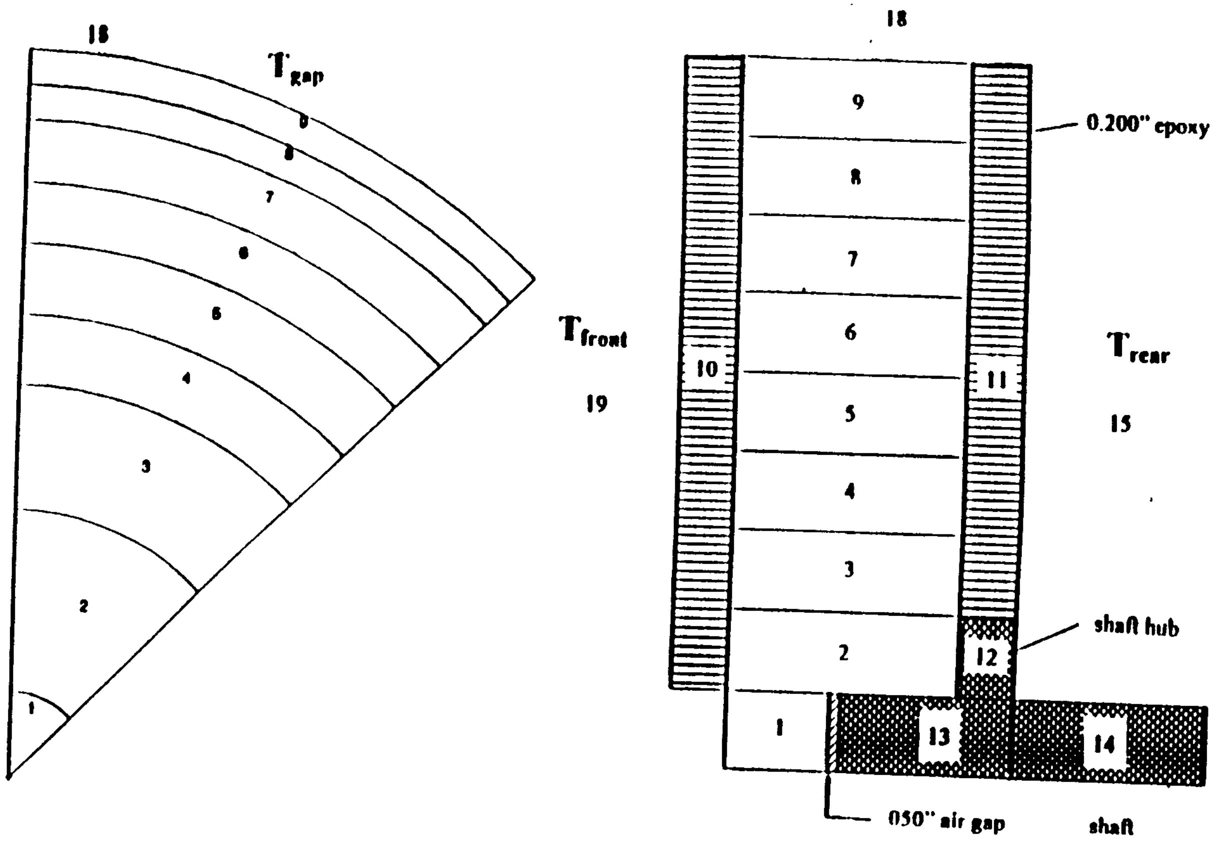
18
T_{gap}
9
8
7
6
5
4
3
2
1
T_{front}
19
18
9
8
7
6
5
4
3
2
1
10
11
12
13
14
0.200" epoxy
T_{rear}
15
shaft hub
050" air gap
shaft

Definition of Elements
Front View
(Not to Scale)

Schematic Representation
Side View
(Not to Scale)

Figure 44: Definition of Elements for Rotor 6

Energy exchange due to conduction between adjacent elements was characterized according to Fourier's Law for one dimensional heat conduction: $\dot{q} = \frac{dq}{dt} = -kA\frac{dT}{dx}$, where $\dot{q}$ is the heat transfer rate, k is the thermal conductivity of the solid material, A is the cross sectional area through which heat is transferred (orthogonal to direction of heat flow), and $\frac{dT}{dx}$ is the spatial temperature gradient in the direction of heat flow. For *steady state* heat transfer in a solid of uniform material composition, Fourier's law reduces to: $\dot{q} = -kA\frac{\Delta T}{\Delta x}$. This is often written as: $\dot{q} = \frac{\Delta T}{R_{th}}$ where R_{th} is the thermal resistance given by $R_{th} = \frac{\Delta x}{kA}$. For the case of heat conduction through materials of different material composition, an electric circuit analogy is applied. Consider the example of one dimensional heat transfer through a composite wall presented in Figure 45.

Because the same heat transfer rate exists through each cross section of the wall,

$$\dot{q} = -k_A A\frac{T_2 - T_1}{\Delta x_A} = -k_B A\frac{T_3 - T_2}{\Delta x_B} = -k_C A\frac{T_4 - T_3}{\Delta x_C}$$

The heat flow rate can also be written in terms of just the outer wall temperatures:

$$\dot{q} = \frac{T_1 - T_4}{\Delta x_A / K_A A + \Delta x_B / K_B A + \Delta x_C / K_C A} \quad \text{or}$$

$$\dot{q} = \frac{\Delta T_{overall}}{\sum R_{th}}$$

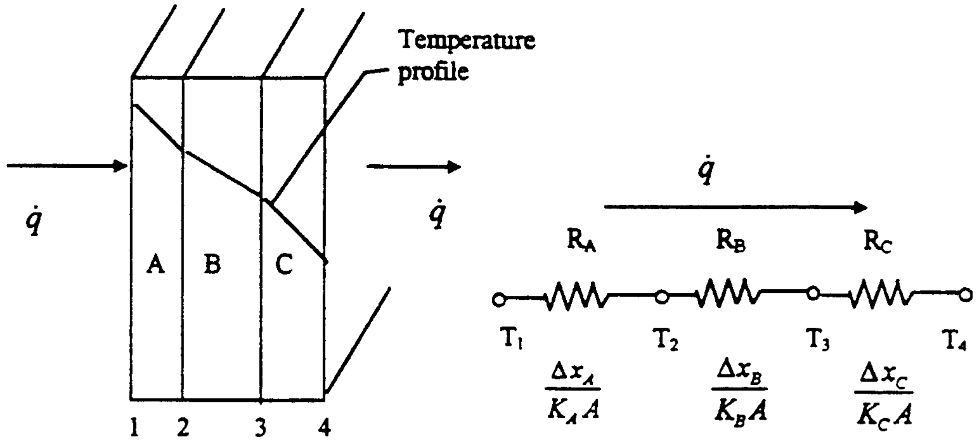
Temperature profile
$\dot{q}$
$\dot{q}$
A
B
C
1
2
3
4
$\dot{q}$
R_A
R_B
R_C
T_1
T_2
T_3
T_4
$\frac{\Delta x_A}{K_A A}$
$\frac{\Delta x_B}{K_B A}$
$\frac{\Delta x_C}{K_C A}$

Figure 45: One Dimensional Heat Transfer Through a Composite Wall and Electrical Analog (Adapted from [22])

For the case of the multi-lumped analysis, each lump or element is assumed to be at a uniform temperature at any given time. Further, to approximate the heat flow rate between adjacent elements, the heat flow rate at any given instant is assumed to be steady state.

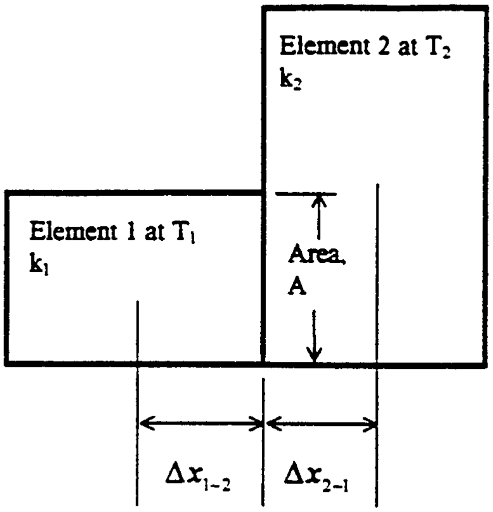

Figure 46: Thermal Resistance Between Abutting Elements

Resistance to heat flow between element 1 and 2 illustrated in Figure 46 is given by:

$$R_{1-2} = \frac{\Delta x_{1-2}}{k_1 A} + \frac{\Delta x_{2-1}}{k_2 A} = R_{2-1} \tag{C-1}$$

Here the convention was adopted that Δx_{1-2} is the distance from the midpoint of element 1 to the interface between elements 1 and 2. Similarly, Δx_{2-1} is the distance from the midpoint of element 2 to the interface between elements 1 and 2.

Because much of the heat flow between lumps can be approximated as radial one-dimensional heat transfer as shown in Figure 47, a more refined estimate for the resistances between the lumps can be developed.

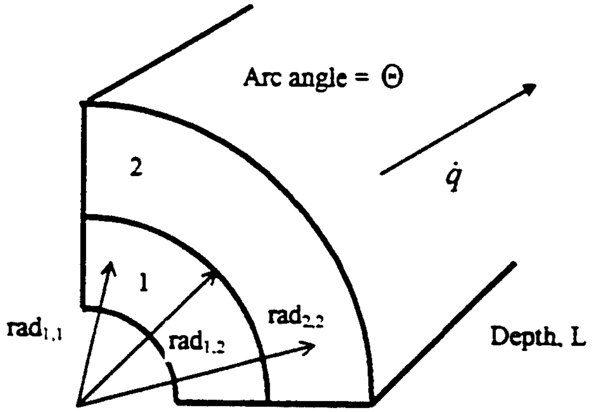

Figure 47: Thermal Resistance Associated with Radial Heat Transfer

Here, the nomenclature $rad_{1,2}$ is the radius to the interface between elements 1 and 2. Similarly, $rad_{1,1}$ and $rad_{2,2}$ are the radii to the centroids of elements 1 and 2 respectively. The centroid radii are defined as: $\bar{r} \equiv \dfrac{\int r\,dA}{\int dA} = \dfrac{\int_{r_1}^{r_2}\int_{\theta_1}^{\theta_2} r^2\,d\theta\,dr}{\int_{r_1}^{r_2}\int_{\theta_1}^{\theta_2} r\,d\theta\,dr} = \dfrac{2}{3}\dfrac{\left(r_2^3 - r_1^3\right)}{\left(r_2^2 - r_1^2\right)}$

The thermal resistance to radial heat transfer between elements 1 and 2 is given by:

$$R_{1-2} = R_{2-1} = \frac{\ln\left(\dfrac{rad_{1,2}}{rad_{1,1}}\right)}{\Theta\,k_1\,L} + \frac{\ln\left(\dfrac{rad_{2,2}}{rad_{1,2}}\right)}{\Theta\,k_2\,L} \tag{C-2}$$

All thermal resistances to heat conduction were calculated in accordance with equations C-1 or C-2. One area that was given additional consideration is the 0.050" air gap that exists between the end of the shaft and the rotor core. One method of analyzing the thermal resistance of this gap is to simply model the air as a solid, so that the resistance of the air gap is given by $\frac{\Delta x_{air}}{k_{air} A}$. This results in a very large resistance because the thermal conductivity of air is so low. Another approach is to consider the heat transfer through the air as a convective process from one surface to the air and then from the air to the next surface. If temperature gradients through the air space are neglected, the resistance to heat flow is given by $R = \frac{1}{h_1} + \frac{1}{h_2}$. For large values of h (250 W/m^2-K) the calculated thermal resistance is only 17% of the value associated with the pure conduction model. Since an accurate determination of this thermal resistance is not possible, the value of this resistance was varied from the high value associated with direct conduction through the air to a value of zero. The effect of changing this resistance to these extremes had negligible influence on the temperature profile of T_1 which represents the temperature sensed by the IR sensor.

C.4 Energy Balances for Model Representing Rotors 1 through 5

The law of conservation of energy is applied to each of the 13 lumps (the temperature of element 14 is known based on measurement), resulting in a system of 13 coupled, linear, first-order, ordinary differential equations (ODE's). Each element has an initial condition at time t = 0. This system of equations is solved numerically using the Runge-Kutta method of Order Four. The resulting ODE's are:

Element 1

$$h_1 \, A_{1-19} \, (T_{front} - T_1) + \frac{T_2 - T_1}{R_{1-2}} + \frac{T_{13} - T_1}{R_{1-13}} = \frac{d}{dt}(m_1 \, c_1 \, T_1)$$

or

$$\frac{dT_1}{dt} = \frac{1}{(\rho V c)_1}\left[\frac{T_2 - T_1}{R_{1-2}} + \frac{T_{13} - T_1}{R_{1-13}} + h_1\, A_{1-19}\,(T_{front} - T_1)\right]$$

Similar analyses for the remaining 12 elements yield the following equations:

Element 2

$$\frac{dT_2}{dt} = \frac{1}{(\rho V c)_2}\left[\frac{T_1 - T_2}{R_{2-1}} + \frac{T_3 - T_2}{R_{2-3}} + \frac{T_{10} - T_2}{R_{2-10}} + \frac{T_{12} - T_2}{R_{2-12}} + \frac{T_{13} - T_2}{R_{2-13}}\right]$$

Element 3

$$\frac{dT_3}{dt} = \frac{1}{(\rho V c)_3}\left[\frac{T_2 - T_3}{R_{3-2}} + \frac{T_4 - T_3}{R_{3-4}} + \frac{T_5 - T_3}{R_{3-5}} + \frac{T_{10} - T_3}{R_{3-10}} + \frac{T_{11} - T_3}{R_{3-11}}\right]$$

Element 4

$$\frac{dT_4}{dt} = \frac{1}{(\rho V c)_4}\left[\frac{T_3 - T_4}{R_{4-3}} + \frac{T_5 - T_4}{R_{4-5}} + \frac{T_6 - T_4}{R_{4-6}} + \frac{T_{10} - T_4}{R_{4-10}} + \frac{T_{11} - T_4}{R_{4-11}}\right]$$

Element 5

$$\frac{dT_5}{dt} = \frac{1}{(\rho V c)_5}\left[\frac{T_3 - T_5}{R_{5-3}} + \frac{T_4 - T_5}{R_{5-4}} + \frac{T_7 - T_5}{R_{5-7}} + \frac{T_{10} - T_5}{R_{5-10}} + \frac{T_{11} - T_5}{R_{5-11}}\right]$$

Element 6

$$\frac{dT_6}{dt} = \frac{1}{(\rho V c)_6}\left[\frac{T_4 - T_6}{R_{6-4}} + \frac{T_8 - T_6}{R_{6-8}} + \frac{T_{10} - T_6}{R_{6-10}} + \frac{T_{11} - T_6}{R_{6-11}} + h_6\, A_{6-16}(T_{gap-3} - T_6)\right]$$

Element 7

$$\frac{dT_7}{dt} = \frac{1}{(\rho V c)_7}\left[\frac{T_5 - T_7}{R_{7-5}} + \frac{T_8 - T_7}{R_{7-8}} + \frac{T_9 - T_7}{R_{7-9}} + \frac{T_{10} - T_7}{R_{7-10}} + \frac{T_{11} - T_7}{R_{7-11}}\right]$$

Element 8

$$\frac{dT_8}{dt}=\frac{1}{(\rho Vc)_8}\left[\frac{T_6-T_8}{R_{8-6}}+\frac{T_7-T_8}{R_{8-7}}+\frac{T_9-T_8}{R_{8-9}}+\frac{T_{10}-T_8}{R_{8-10}}+\frac{T_{11}-T_8}{R_{8-11}}+h_8\,A_{8-17}(T_{gap-2}-T_8)\right]$$

Element 9

$$\frac{dT_9}{dt}=\frac{1}{(\rho Vc)_9}\left[\frac{T_7-T_9}{R_{9-7}}+\frac{T_8-T_9}{R_{9-8}}+\frac{T_{10}-T_9}{R_{9-10}}+\frac{T_{11}-T_9}{R_{9-11}}+h_9\,A_{9-18}(T_{gap-1}-T_9)\right]$$

Element 10

$$\frac{dT_{10}}{dt}=\frac{1}{(\rho Vc)_{10}}\left[\frac{T_2-T_{10}}{R_{10-2}}+\frac{T_3-T_{10}}{R_{10-3}}+\frac{T_4-T_{10}}{R_{10-4}}+\frac{T_5-T_{10}}{R_{10-5}}+\frac{T_6-T_{10}}{R_{10-6}}+\frac{T_7-T_{10}}{R_{10-7}}+\right.$$
$$\frac{T_8-T_{10}}{R_{10-8}}+\frac{T_9-T_{10}}{R_{10-9}}+h_{10}A_{10-19}\left(T_{front}-T_{10}\right)+h_9A_{10-18}\left(T_{gap-1}-T_{10}\right)+$$
$$\left.h_8A_{10-17}\left(T_{gap-2}-T_{10}\right)+h_6A_{10-16}\left(T_{gap-3}-T_{10}\right)\right]$$

Element 11

$$\frac{dT_{11}}{dt}=\frac{1}{(\rho Vc)_{11}}\left[\frac{T_3-T_{11}}{R_{11-3}}+\frac{T_4-T_{11}}{R_{11-4}}+\frac{T_5-T_{11}}{R_{11-5}}+\frac{T_6-T_{11}}{R_{11-6}}+\frac{T_7-T_{11}}{R_{11-7}}+\frac{T_8-T_{11}}{R_{11-8}}+\right.$$
$$\frac{T_9-T_{11}}{R_{11-9}}+\frac{T_{12}-T_{11}}{R_{11-12}}+h_{11}A_{11-15}\left(T_{rear}-T_{11}\right)+h_9A_{11-18}\left(T_{gap-1}-T_{11}\right)+$$
$$\left.h_8A_{11-17}\left(T_{gap-2}-T_{11}\right)+h_6A_{11-16}\left(T_{gap-3}-T_{11}\right)\right]$$

Element 12

$$\frac{dT_{12}}{dt}=\frac{1}{(\rho Vc)_{12}}\left[\frac{T_2-T_{12}}{R_{12-2}}+\frac{T_{11}-T_{12}}{R_{12-11}}+\frac{T_{13}-T_{12}}{R_{12-13}}+h_{12}\,A_{12-15}(T_{rear}-T_{12})\right]$$

Element 13

$$\frac{dT_{13}}{dt}=\frac{1}{(\rho V c)_{13}}\left[\frac{T_1-T_{13}}{R_{13-1}}+\frac{T_2-T_{13}}{R_{13-2}}+\frac{T_{12}-T_{13}}{R_{13-12}}+\frac{T_{shaft}-T_{13}}{R_{13-14}}\right]$$

C.5 Energy Balances for Model Representing Rotors 6

Similar analyses are performed on each element comprising the model for Rotor 6. The resulting ODE's are:

Element 1

$$h_1\,A_{1-19}\,(T_{front}-T_1)+\frac{T_2-T_1}{R_{1-2}}+\frac{T_{13}-T_1}{R_{1-13}}=\frac{d}{dt}(m_1\,c_1\,T_1)$$

or

$$\frac{dT_1}{dt}=\frac{1}{(\rho V c)_1}\left[\frac{T_2-T_1}{R_{1-2}}+\frac{T_{13}-T_1}{R_{1-13}}+h_1\,A_{1-19}\,(T_{front}-T_1)\right]$$

Similar analyses for the remaining 12 elements yield the following equations:

Element 2

$$\frac{dT_2}{dt}=\frac{1}{(\rho V c)_2}\left[\frac{T_1-T_2}{R_{2-1}}+\frac{T_3-T_2}{R_{2-3}}+\frac{T_{10}-T_2}{R_{2-10}}+\frac{T_{12}-T_2}{R_{2-12}}+\frac{T_{13}-T_2}{R_{2-13}}\right]$$

Element 3

$$\frac{dT_3}{dt}=\frac{1}{(\rho V c)_3}\left[\frac{T_2-T_3}{R_{3-2}}+\frac{T_4-T_3}{R_{3-4}}+\frac{T_{10}-T_3}{R_{3-10}}+\frac{T_{11}-T_3}{R_{3-11}}\right]$$

Element 4

$$\frac{dT_4}{dt}=\frac{1}{(\rho V c)_4}\left[\frac{T_3-T_4}{R_{4-3}}+\frac{T_5-T_4}{R_{4-5}}+\frac{T_{10}-T_4}{R_{4-10}}+\frac{T_{11}-T_4}{R_{4-11}}\right]$$

Element 5

$$\frac{dT_5}{dt} = \frac{1}{(\rho V c)_5}\left[\frac{T_4 - T_5}{R_{5-4}} + \frac{T_6 - T_5}{R_{5-6}} + \frac{T_{10} - T_5}{R_{5-10}} + \frac{T_{11} - T_5}{R_{5-11}}\right]$$

Element 6

$$\frac{dT_6}{dt} = \frac{1}{(\rho V c)_6}\left[\frac{T_5 - T_6}{R_{6-5}} + \frac{T_7 - T_6}{R_{6-7}} + \frac{T_{10} - T_6}{R_{6-10}} + \frac{T_{11} - T_6}{R_{6-11}}\right]$$

Element 7

$$\frac{dT_7}{dt} = \frac{1}{(\rho V c)_7}\left[\frac{T_6 - T_7}{R_{7-6}} + \frac{T_8 - T_7}{R_{7-8}} + \frac{T_{10} - T_7}{R_{7-10}} + \frac{T_{11} - T_7}{R_{7-11}}\right]$$

Element 8

$$\frac{dT_8}{dt} = \frac{1}{(\rho V c)_8}\left[\frac{T_7 - T_8}{R_{8-7}} + \frac{T_9 - T_8}{R_{8-9}} + \frac{T_{10} - T_8}{R_{8-10}} + \frac{T_{11} - T_8}{R_{8-11}}\right]$$

Element 9

$$\frac{dT_9}{dt} = \frac{1}{(\rho V c)_9}\left[\frac{T_8 - T_9}{R_{9-8}} + \frac{T_{10} - T_9}{R_{9-10}} + \frac{T_{11} - T_9}{R_{9-11}} + h_9\, A_{9-18}(T_{gap-1} - T_9)\right]$$

Element 10

$$\frac{dT_{10}}{dt} = \frac{1}{(\rho V c)_{10}}\left[\frac{T_2 - T_{10}}{R_{10-2}} + \frac{T_3 - T_{10}}{R_{10-3}} + \frac{T_4 - T_{10}}{R_{10-4}} + \frac{T_5 - T_{10}}{R_{10-5}} + \frac{T_6 - T_{10}}{R_{10-6}} + \frac{T_7 - T_{10}}{R_{10-7}} + \right.$$

$$\left. \frac{T_8 - T_{10}}{R_{10-8}} + \frac{T_9 - T_{10}}{R_{10-9}} + h_{10}\, A_{10-19}\left(T_{front} - T_{10}\right) + h_9\, A_{10-18}\left(T_{gap-1} - T_{10}\right)\right]$$

Element 11

$$\frac{dT_{11}}{dt}=\frac{1}{(\rho Vc)_{11}}\left[\frac{T_3-T_{11}}{R_{11-3}}+\frac{T_4-T_{11}}{R_{11-4}}+\frac{T_5-T_{11}}{R_{11-5}}+\frac{T_6-T_{11}}{R_{11-6}}+\frac{T_7-T_{11}}{R_{11-7}}+\frac{T_8-T_{11}}{R_{11-8}}+\right.$$
$$\left.\frac{T_9-T_{11}}{R_{11-9}}+\frac{T_{12}-T_{11}}{R_{11-12}}+h_{11}A_{11-15}\left(T_{rear}-T_{11}\right)+h_9A_{11-18}\left(T_{gap-1}-T_{11}\right)\right]$$

Element 12

$$\frac{dT_{12}}{dt}=\frac{1}{(\rho Vc)_{12}}\left[\frac{T_2-T_{12}}{R_{12-2}}+\frac{T_{11}-T_{12}}{R_{12-11}}+\frac{T_{13}-T_{12}}{R_{12-13}}+h_{12}A_{12-15}(T_{rear}-T_{12})\right]$$

Element 13

$$\frac{dT_{13}}{dt}=\frac{1}{(\rho Vc)_{13}}\left[\frac{T_1-T_{13}}{R_{13-1}}+\frac{T_2-T_{13}}{R_{13-2}}+\frac{T_{12}-T_{13}}{R_{13-12}}+\frac{T_{shaft}-T_{13}}{R_{13-14}}\right]$$

C.6 Verification of Multi-lump Analyses

A FORTRAN computer code was written to numerically model the temperatures within the rotors using the Runge-Kutta method. The code required thermophysical properties of the elements, initial conditions (temperatures), boundary conditions (air temperature and convective film coefficients) and input of a time step for incrementation of the numerical analysis. The validity of the results returned by the multi-lump analyses were verified by comparing to standards.

Test scenarios were developed for both models. In each case the time step chosen for analysis was 0.1 second. This seemed a good choice since data from experimental work would be collected at a rate of 1 Hz. The effect of decreasing the time step was checked for both scenarios and decreasing the time step from 0.1 to 0.05 second had no effect on the results.

For the case of rotor 6, the cylinder, verification was achieved by considering the case of radial heat transfer only. I.e. there was no heat flux through the shaft or out the front or rear epoxy insulated faces of the rotor. This was done because their is an exact, closed form solution to the temperature distribution in an infinitely long cylinder given by[8]:

$$\frac{T(r,t)-T_\infty}{T_o-T_\infty} = 2\,Bi\sum_{n=1}^{\infty}\frac{e^{-\alpha\lambda_n^2 t}J_o(\lambda_n r)}{\left(\lambda_n^2 R_o^2 + Bi^2\right)J_o(\lambda_n R_o)} \qquad \text{(C-3)}$$

where r is the radial distance from the center of the cylinder and R_o is the outside radius of the cylinder. The eigenvalues, λ_n, are the positive roots of the equation:

$$(\lambda_n R_o)J_1(\lambda_n R_o) - Bi\,J_o(\lambda_n R_o) = 0\,. \qquad \text{(C-4)}$$

In these equations the Biot number is defined as $Bi = \frac{hR_o}{k}$.

A test case was considered for which the aluminum cylinder was initially at 200°F. At time t = 0, the cylinder convected heat to the surroundings at 70°F with a convective film coefficient h = 90 Btu/hr-ft^2-°F (511 W/m^2-K). This boundary value problem was solved by the computer program using the 14 lump analysis as well as the above exact solution. Further, for this case the Biot number is 0.20. Although a single lump analysis is typically considered a good approximation for Bi < 0.1, a single lump analysis was also conducted. The results are presented in Figure 48. Variation between the exact solution and the multi-lump analysis results were typically less than 1°F. Based on these results the multi-lump analysis successfully predicts the center temperature of rotor 6.

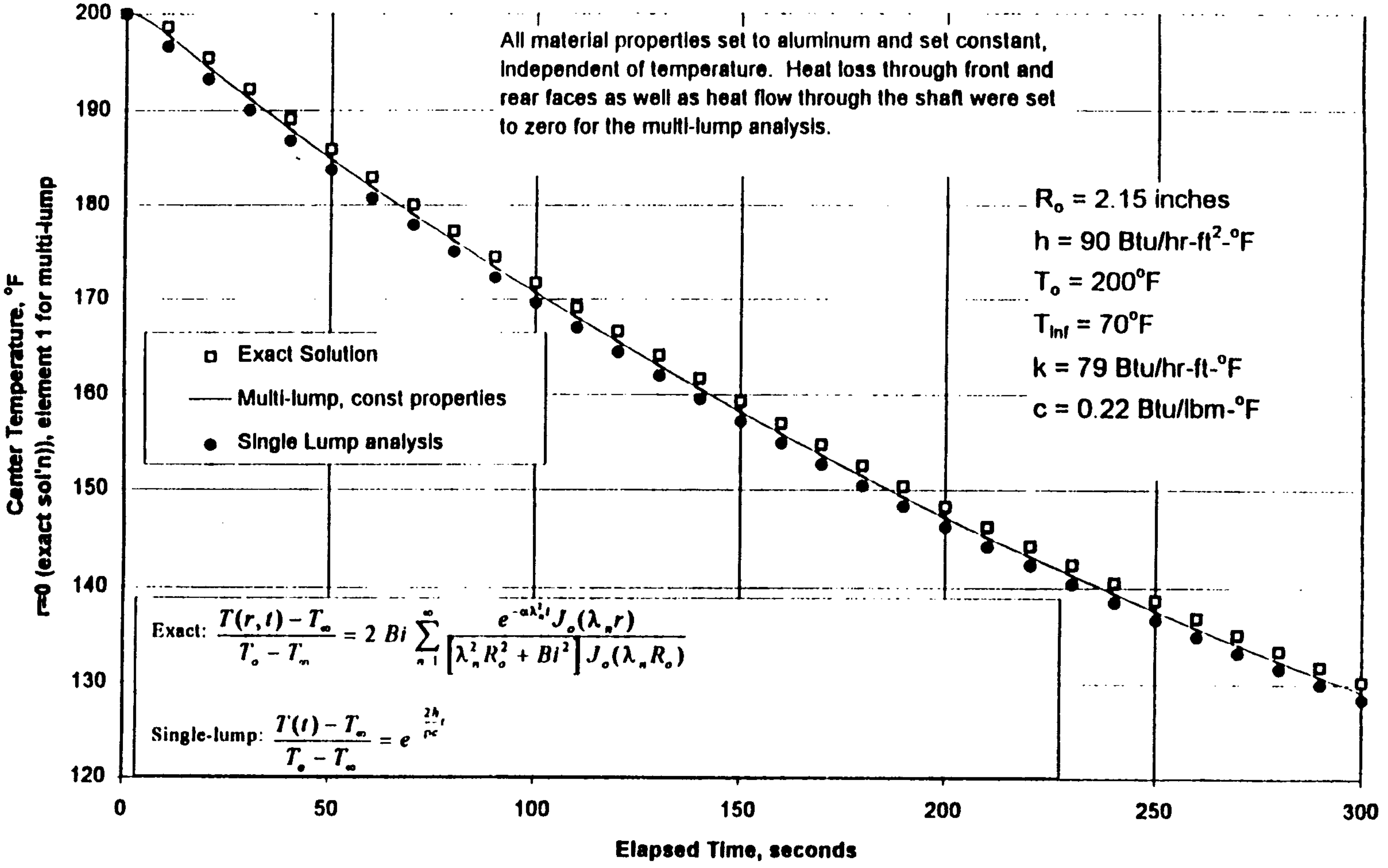

Figure 48: Verification of Multi-lump Analysis for Pure Radial Heat Flow in Rotor

There is no closed form solution of the partial differential equation governing heat conduction in rotors 1 through 5 because of the complex geometry and boundary conditions associated with these rotors. However, a close approximation to an exact solution can be achieved using finite element analysis (FEA). FEA is a powerful method of attacking complex engineering problems that defy closed form solution by transforming the problems from continuous regions to discrete regions. A three dimensional finite element model was constructed of the rotor core, epoxy insulation and shaft hub to use as a standard of comparison for the multi-lump analysis. The commercial FEA code used for this investigation was ABAQUS. P3/PATRAN was used to define the geometry, create the finite element mesh, and generate the ABAQUS input deck. The analyses were performed on a Silicon Graphics Indigo 2 work station. Similar to the multi-lump analysis, the FEA model employs one eighth symmetry and is comprised of 2,905 nodes and 2,316 elements. The elements are DC3D8 8-node linear heat transfer bricks. An isometric representations of the finite element mesh is shown in Figure 49.

The validity of the multi-lump analysis was verified for rotors 1 through 5 by comparing the temperature predicted for element 1 in the multi-lump analysis to the temperature of node 2610 of the finite element analysis. Node 2610 is the at the very center surface of the rotor core where the IR sensor is focused. A test case was considered for rotor 1. Rotor 1 was selected as a worst case because face 1 is furthest away from the center resulting in the greatest temperature gradients. The rotor, initially at 200°F is spun at 30,000 rpm. It is estimated that the average film coefficient on the front and rear insulated surfaces are 42 Btu/hr-ft^2-°F and the value at the pole faces is taken to be 176 Btu/hr-ft^2-°F (1,000 W/m^2-K). The ambient temperature as well as the shaft

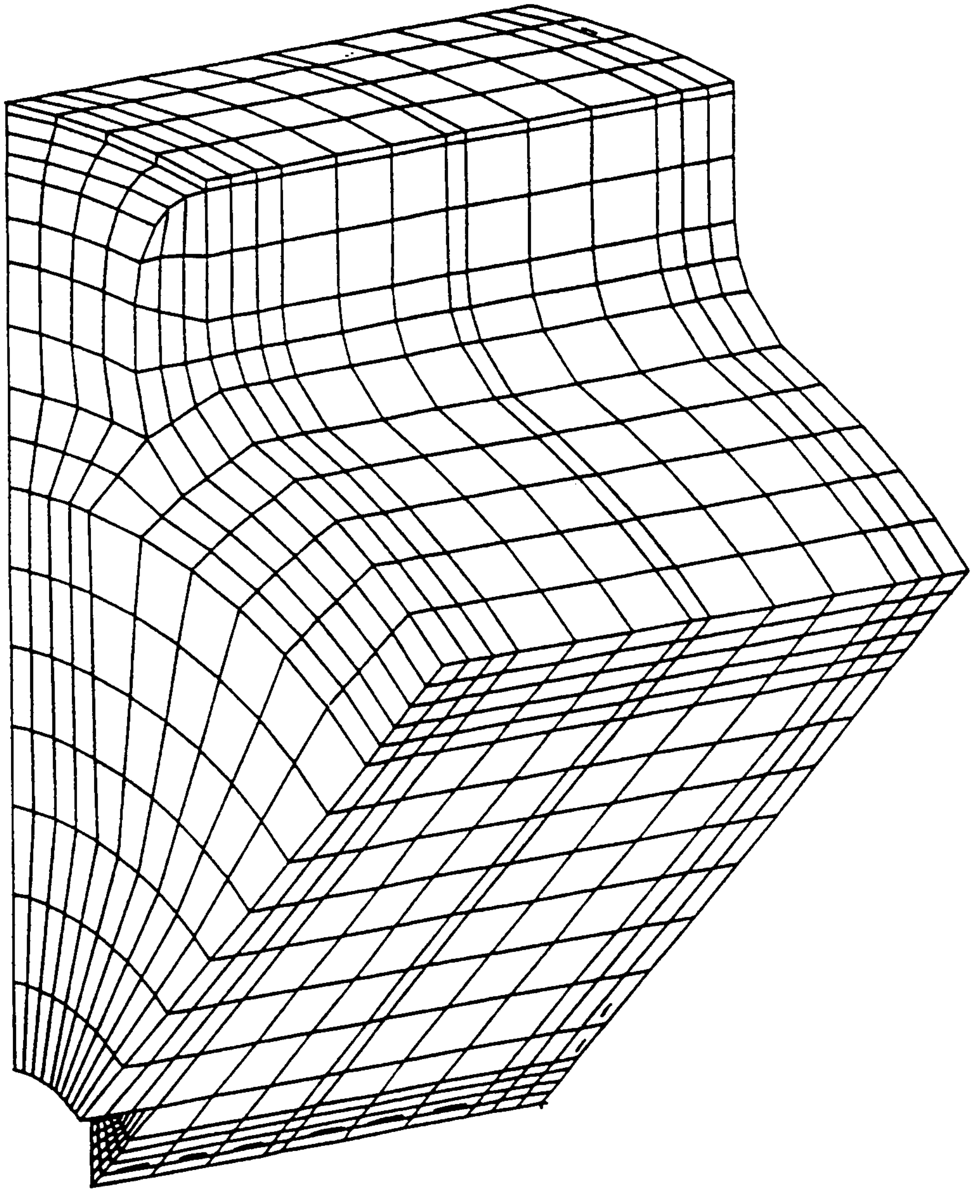

Figure 49: FE Model of Rotor 1

temperature are maintained at a constant 100°F. Results from the FEA and multi-lump analyses are presented in Figure 50. It is apparent that the multi-lump analysis compares very well to the "exact" solution provided by finite element analysis. As expected, the exact solution always yields a higher temperature than that predicted with the multi-lump analysis. This is because smaller temperature gradients exist in the rotors than are represented by the multi-lump model.

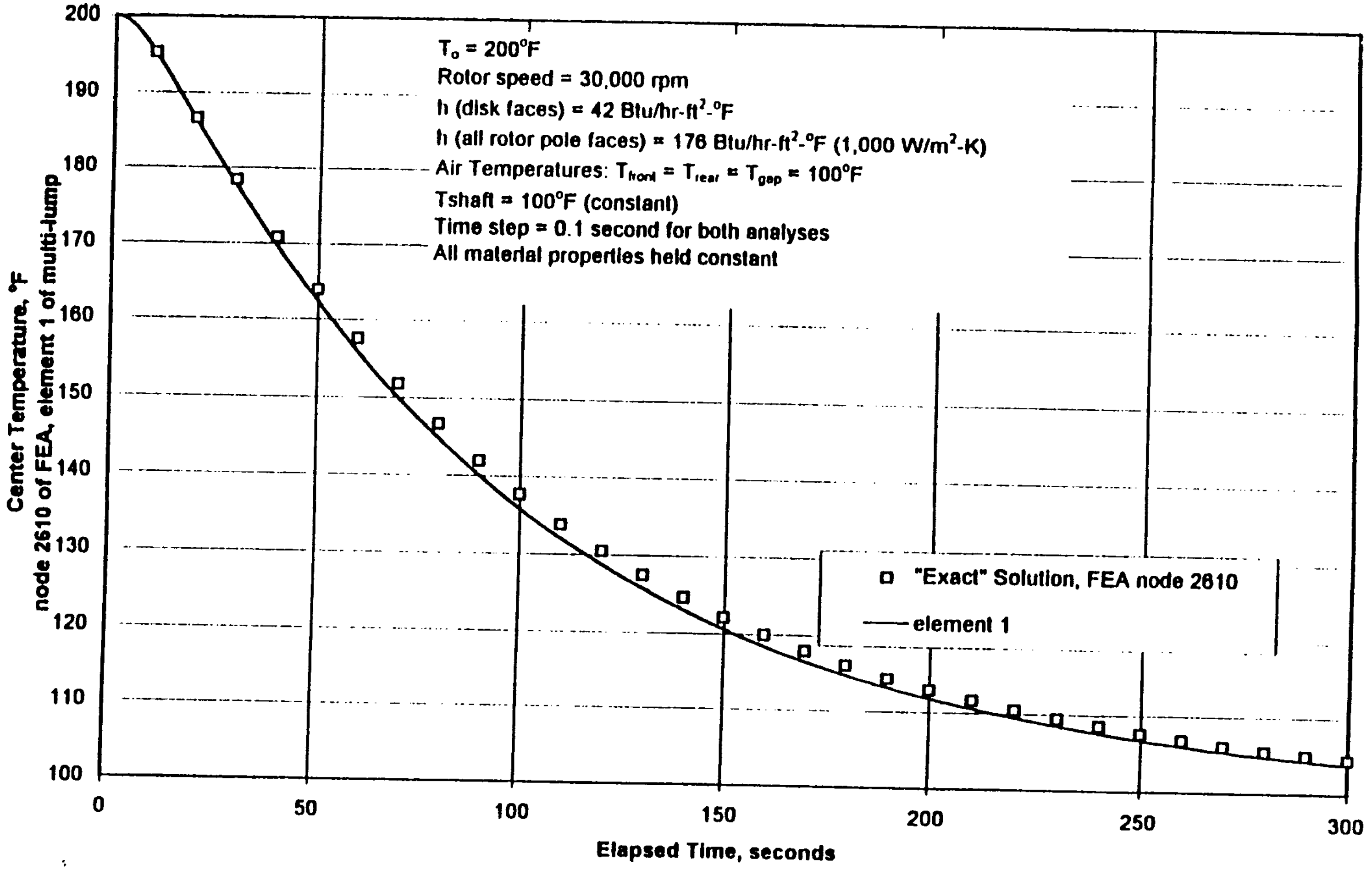

Figure 50: Verification of Multi-lump Analysis for Rotor 1

APPENDIX D

SENSING DEVICES AND THEIR CALIBRATION

D.1 General

This appendix addresses the specification and calibration of the sensors employed in the measurement of rotational speed, temperature, differential pressure and air mass flow rate.

D.2 Rotor Speed Measurement

D.2.1 Magnetic Proximity Pick-up Specification

Rotor speed measurement was accomplished with an Electro Products Model 3080 magnetic proximity pick-up installed within the housing of the air turbine in close proximity to the teeth of a 30 tooth gear installed on the air turbine shaft. Each time a gear tooth passes by the pickup, a voltage pulse is directed to an Electro Products Model MZA 102 signal conditioner which provides a consistent 0.5 volt output to the Keithley-Metrabyte CTM-05 board. Because the gear has 30 teeth, the pulse frequency is equal to one-half the instantaneous shaft speed measured in rpm. At 30,000 rpm, the gear inputs a pulse to the data acquisition board at a rate of 15 Khz, well below the maximum input frequency of 7 Mhz.

D.2.2 Rotational Speed Measurement Calibration

The rotor speed indicated by the data acquisition system was verified using a stroboscope. It is reasonable to conclude that the signal produced by the magnetic pick-up and processed by the data acquisition system is a more reliable standard than the stroboscope. Speeds were verified with the stroboscope up to a speed of approximately 7,000 rpm. It was deemed dangerous to observe the shaft spinning at higher speeds since there was no personal protection. The speeds reported by the data acquisition system and the stroboscope were in excellent agreement for the entire range of speeds verified.

D.3 Temperature Measurement

D.3.1 General

All temperature measurements employed thermocouples except for the rotor core temperature. An electronic infrared (IR) pyrometer was used to measure the rotor core temperature. However, the output of the IR sensor circuit board was factory calibrated to give a millivolt output identical to a type J thermocouple. Thus, all temperature sensors were input to the DAS-TC/B board as thermocouples.

D.3.2 Ice Bath Reference

The Keithley-Metrabyte DAS-TC/B terminal board is equipped with a cold junction compensator (CJC) thermistor to permit thermocouples to be directly wired to the terminal board. However, the accuracy of the CJC is ±1.2° C (±2.16° F). This error was essentially eliminated by the use of an external ice bath.

The ice bath configuration employed was to solder the ends of the positive and negative thermocouple wires to copper lead wires and maintain both junctions at the ice point as illustrated in Figure 51. A nominal 1 gallon thermos bottle was used as the ice bath. It had a 6" diameter top opening and was approximately 12" tall. An insulating top was made of 1" thick Styrofoam. 1/4" diameter x 7-1/2" long test tubes were filled with oil and inserted through the Styrofoam top such that the lower 5" of the tubes were suspended in ice water. Each individual junction of a thermocouple and copper lead wire was immersed in its own oil filled test tube to eliminate any stray electric currents that could occur if all of the many junctions were directly inserted into the ice bath. The copper leads were then routed to the nearby screw terminal panel of the thermocouple data acquisition board.

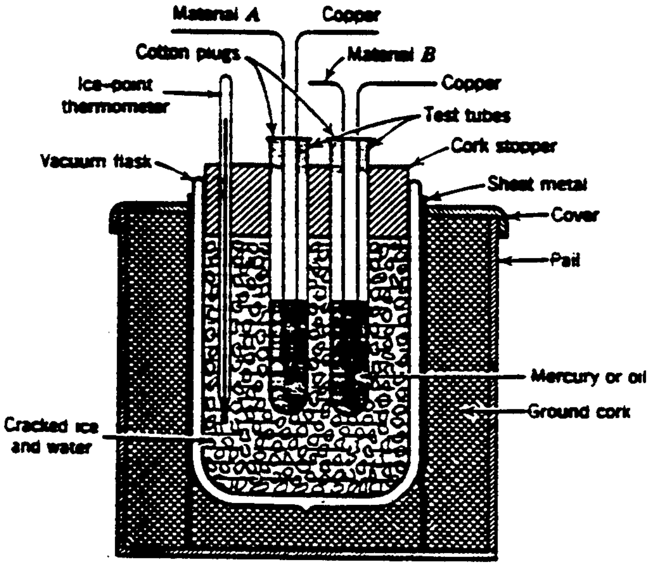
Material A
Copper
Cotton plugs
Material B
Ice-point thermometer
Copper
Test tubes
Cork stopper
Vacuum flask
Sheet metal
Cover
Pail
Mercury or oil
Ground cork
Cracked ice and water

Figure 51: Typical Ice Bath for Thermocouple Reference Junctions (Adapted from [21])

D.3.3 Thermocouples

D3.3.1 Thermocouple Specifications

The thermocouple is a simple temperature measurement device that is quite accurate when properly applied. The output (Seebeck) voltage of a thermocouple is a function of the temperature of its junction (bead) where two dissimilar metal wires are joined, the composition of the wires and the temperature of the reference junction where the voltage between the wires is measured. In this experiment, the reference junction was maintained at 0° C by means of an ice bath as discussed in Section D.3.2.

Thermocouple type refers to the composition of the two thermocouple wires. Three of the most common thermocouple types were employed in this investigation:

Type T: Copper/Constantan ($Cu_{57}Ni_{43}$)

Type J: Iron/Constantan ($Cu_{57}Ni_{43}$)

Type K: Chromel ($Ni_{90}Cr_{10}$)/Alumel ($Ni_{94}Mn_3Al_2Si_1$)

Both factory manufactured thermocouple probes and field fabricated thermocouples were used in the experiment. Field fabricated thermocouples were made from 34 awg (0.005" diameter) and 20 awg (0.032" diameter) thermocouple wire by welding together the dissimilar metals at one end.

Factory manufactured thermocouples are listed in Table 3 as Omega Engineering models KMQSS-040E-6 and TMQSS-040E-6. These are types K and T respectively. They are 6" long subminiature probes with 0.040" diameter stainless steel sheaths and exposed junctions. The individual wires within the sheaths are 34 awg and their beads are approximately 0.027" diameter.

D.3.3.2 Thermocouple Calibration

The thermocouples were calibrated against a calibrated thermometer (standard) by immersing the thermocouples and reference thermometer in a water filled beaker that was continuously stirred and gradually heated. An Omega Engineering Model GT-35554Y-CC, serial number 5N666, 76 mm. mercury, partial immersion thermometer was used as the reference thermometer. Its range was -1° to 101°C with divisions of 0.1°C. The manufacturer certified the accuracy to be ±0.3°C. All thermocouples were calibrated over a range from 20° to 99°C. In all cases, the temperatures indicated by the thermocouples were within the 0.3°C tolerance of the reference thermometer. Therefore, no corrections were applied to the thermocouple readings.

D.3.4 Infrared Temperature Sensor

D.3.4.1 Infrared Temperature Sensor Specifications

The infrared (IR) sensor is an Omega Engineering infrared pyrometer. The microprocessor-based electronic circuitry provides a type J thermocouple output with a range (R3) of 0 to 250 °F. The ordering suffix -4 indicates that the field of view is 24:1 which provides a minimum spot size for focus of 1/4" at 6". The manufacturer's performance specifications are presented in Table 9.

Table 9: Infrared Sensor Specifications

Manufacturer	Omega Engineering
Model	OS 65-J-R3-4BB
Serial Number	12171
Sensing Range	-18 to 121°C (0 to 250°F)
Accuracy	±1% of reading or ±2°F (1°C) whichever is greater
Repeatability	±0.50% of reading, ±1°C
Spectral Response	8-14 microns
Response Time	300 ms (10 to 90%)
Power	9-30 VDC, 40 ma (24 VDC applied)
Ambient Operating Range	
Sensing Head	-18 to 85°C (0 to 185°F)
Electronics	0 to 49°C (32 to 120°F)

Power was supplied to the sensor electronics with a Hewlett Packard Model 6224B DC power supply, S/N 1102A01225 adjusted to 24 VDC.

D.3.4.2 Description of IR Sensor Operation

Total integrated emissive power from the object viewed by the sensor is focused by a lens mechanism onto a hermetically sealed detector. The detector has a small window which transmits radiant energy in the 8 - 14μm bandwidth. Inside the detector is a spider type design of chromel-alumel thermocouples comprising a thermopile. All chromel junctions are on a piece of 0.0005 inch thick aluminum which has been painted with platinum black. This is the target of the detector. All alumel junctions are electrically isolated but attached to a thermally uniform ring outside the radiation field of view. Radiant exchange of energy between the detector target and the viewed object establishes the temperature of the aluminum target. There is another thermocouple which measures the ambient temperature. The output of the thermopile is calibrated against the ambient. EMF output is calibrated against a blackbody and the values stored in a PROM on the circuit board. In operation, the voltage generated by the thermopile is compared with the values in the PROM and an output is generated consistent with a type J thermocouple.

D.3.4.3 Infrared Sensor Calibration

The OS65-J infrared sensor has two emissivity pots in its circuit board that may be adjusted based on the surface characteristics of the object whose temperature is being measured. These pots allow emissivity adjustments ranging from 0.00 to 0.99 and act as a gain adjustment on the amplifier of the IR sensor circuit board. The instrument comes factory set to $\varepsilon = 0.99$ which is essentially equivalent to a black body radiator. Aluminum has a low emissivity and flat black paint was applied to the surfaces to increase the emissivity. The IR sensor was calibrated with the emissivity set to 0.99.

While the sensing head may be used in environments between 0 to 185°F, it is imperative that its environment remain relatively stable. I.e. there must me minimal spatial or temporal temperature gradients within the body of the sensing head. This requirement, though not stated in the manufacturer's marketing literature or owner's manual, was discovered during data collection when the blower was started and axial air flow to the RTTR flowed directly over the body of the sensor. The temperature of the air discharging from the blower was as much as 15°F greater than the ambient air (and the sensor temperature prior to activation of the blower). This resulted in IR indicated temperature errors in excess of 20°F. This problem was solved by enclosing the IR sensor in a nylon housing to shield it from air currents as well as physically removing the IR sensor from the air stream.

To remove the sensor from the axial air stream to the rotor it was necessary to install a viewing window such that the IR sensor could continue to view the center of the rotor but yet be isolated from the air flow. The viewing window used is a 2" diameter x 0.25" thick ZnSe (zinc selenide) lens manufacture by II-VI, Inc. The lens was coated on both sides with a broadband anti-reflective coating, BAR-05-0001 for the 8-12 μm wavelength range. Further, since the nylon sensor housing was directly connected to the RTTR, conduction of heat through the nylon to the IR sensor was a concern. This was addressed by installing an air purge to the housing. The source of the purge air was a 2 HP shop vac connected to the enclosure with approximately 30 feet of nominal 1" vinyl tubing (3/4" I.D.). The vinyl tubing connected to the rear of the sensor housing. Purge air was discharged from the housing through six (6) 0.201" diameter holes located peripherally around the enclosure near the zinc selenide viewing lens, downstream of the IR sensor. Air flow rate was measured with a pitot static tube and 0-2" inclined manometer. The centerline velocity pressure was 1.6" w.c. which is about 5,066 ft/min (84.4 ft/sec or 1,013 in/sec). The flow is turbulent and assuming that the centerline velocity is representative of the velocity across the cross-section, the flow rate is approximately 15.5 ft^3/min and an air exchange rate within the IR sensor enclosure in excess of 19 air changes/second.

Calibration was performed using two test specimens. One was a spare 7075 aluminum rotor core (without any epoxy insulation) shown in Figure 52, and the other was a rectangular 1-1/4" x 1-3/8" x 4-5/8" 7075 aluminum block. Flat black paint was applied to both specimens in the region to be viewed by the IR sensor in the same manner as was applied to the actual test rotors used during data gathering. A small hole was drilled in the

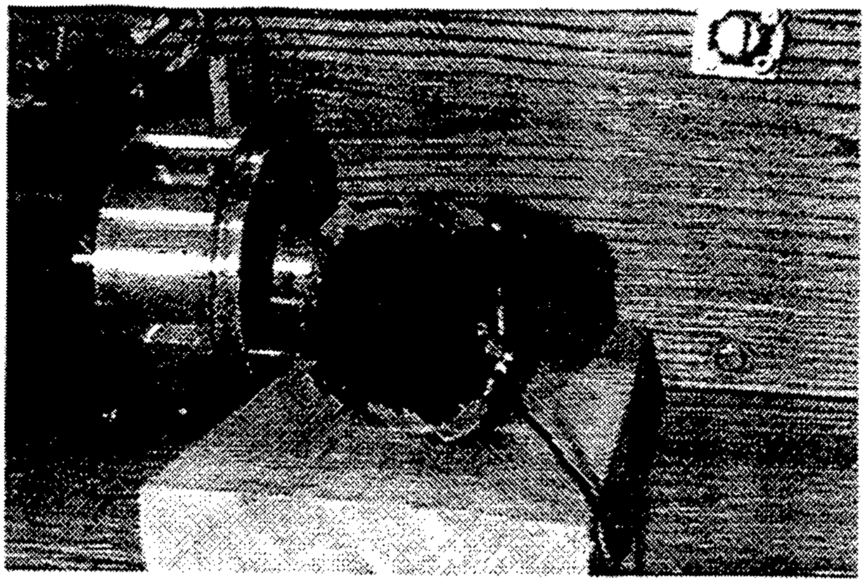

Figure 52: IR Sensor Calibration Test Specimen

aluminum specimens just below and parallel to the surface of the specimen whose temperature was to be measured. In this hole was inserted a calibrated thermocouple coated with heat conductive grease. Because the test specimen is aluminum (high thermal conductivity, k), cooling is through natural convection (for cases 1 and 2) and the thermocouple is measuring the temperature of the aluminum just below the surface ($L_c<<1$) the Biot number is small and it is reasonable to assume that the temperature of the painted surface of the specimen is the same as the temperature measured by the embedded thermocouple. Therefore, the calibrated thermocouple was used as the reference standard to which the IR sensor was calibrated.

A total of 13 calibration runs were performed September 30 through October 2, 1997. They were done over a period of several days to verify the repeatability of the calibrations. Also, calibrations were performed for three different configurations or cases:

Case 1 represents the configuration where the test rotor specimen is heated and placed inside the RTTR. There is no axial air flow and the rotor cools slowly due to natural convection. This is a worst case condition because there is significant time for heat to conduct to the IR sensor.

Case 2 represents calibration when the test rotor or a rectangular aluminum test specimen is not mounted inside the RTTR but rather is simply set on the workbench and the IR sensor is focused on it.

Case 3 is the same as Case 1 except that full axial airflow causes rapid cooling of the test rotor.

In addition to these three cases, efforts were made to further affect the temperature of the reference thermocouple in the body of the IR sensor. These efforts included directing cold compressed air (from a Vortec Corporation Model 606 cold air gun) over the body of the sensor enclosure.

The IR sensor was calibrated installed within the nylon housing as it would be during actual data acquisition. I.e. it was installed inside the nylon enclosure with the ZnSe viewing lens in place and attached to the PVC air inlet housing with purge air flowing. The sensor enclosure was insulated with foam insulation and wrapped with duct tape. The test specimen was then heated in an oven. When the specimen was hot (greater than 200°F), the thermocouple was inserted to act as the primary standard temperature. Calibration data was collected with the data acquisition system at a rate of 1 Hz. At each second, the temperature of the test specimen was record as measured by the calibrated thermocouple and the IR sensor.

Temperature corrections were calculated by comparing the temperature indicated by the IR sensor to the actual temperature of the aluminum rotor core based on the embedded thermocouple. The temperature correction is given by:

$$T_{correction} = T_{actual} - T_{indicated} \tag{D-1}$$

The required corrections for cases 2 and 3 were very similar while calibration runs for case 1 required smaller corrections. The apparent reason for this is that case 1 required that the rotor specimen be installed inside the RTTR for long periods of time, typically about 50 minutes. This allowed time for conduction of heat to the IR sensor which in turn caused the sensor to read higher than normal. In actual operation, cases 2 and 3 are more representative of the conditions under which the sensor and enclosure will operate. I.e., data collection is typically about 5 minutes in duration. Also, the rotors are insulated which will decrease the operating temperature inside the RTTR. It was concluded that the most reasonable calibration of the sensor would be achieved by curve fitting the results of cases 2 and 3. This was accomplished using Jandel Scientific TableCurve 2D™. The curve which best fit the data is given by:

$$Correction,\ ^{\circ}F = -93.82 + 20.53 \log_e \left(IR\ Indicated\ Temperature,\ ^{\circ}F\right) \tag{D-2}$$

The calibration curve for the IR sensor is presented in Figure 53. The correction is considered to be accurate within +/- 1.4°F.

While the temperature corrections are rather large, the calibration is repeatable. It is apparent that the lens blocks some of the infrared power from reaching the sensor. Part of this is attributable to the fact that the IR sensor is designed for the 8-14 μm band while the zinc selenide viewing lens is designed for the 8-12 μm range.

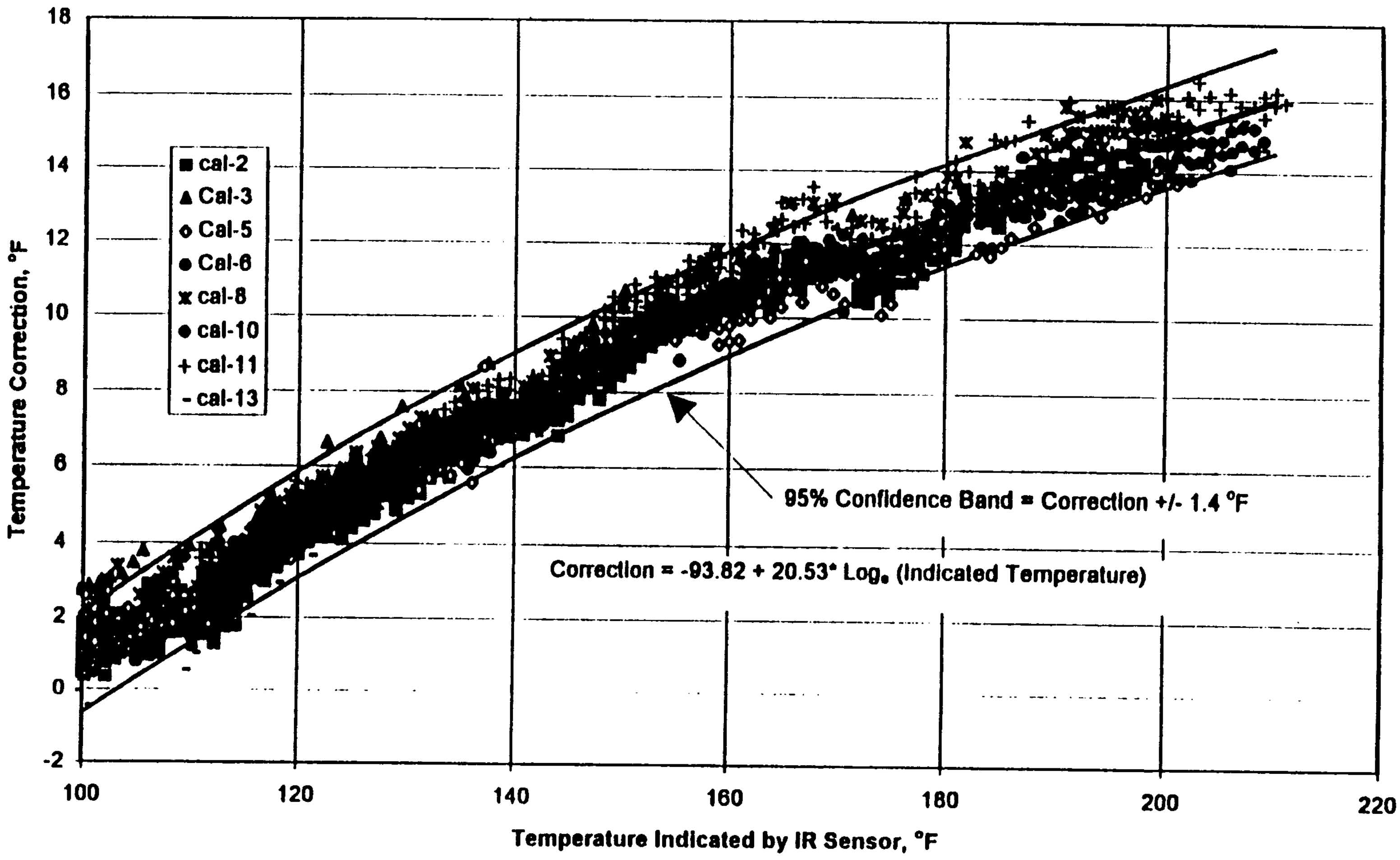

Figure 53: IR Sensor Calibration Curve

D.4 Differential Pressure Measurement

D.4.1 Differential Pressure Transducer Specifications

Four Omega Engineering PX162, PX163 and PX164 series transducers were used in the measurement of differential pressures. These are solid state pizoresistive devices. Each sensor requires a regulated DC voltage, typically 8 vDC. The output from the transducers was a linear 1 to 6 vDC output voltage proportional to the differential pressure between the measuring ports. The specifications for the four specific transducers used in the experiment are:

Input 12: PX 163-120D5V, nominal 1-6 vDC output for range -7.87 - 47.24 in. w.c.
Input 13: PX 162-027D5V, nominal 1-6 vDC output for range 0 - 27.65 in. w.c.
Input 14: PX 164-010D5V, nominal 1-6 vDC output for range 0 - 10 in. w.c.
Input 15: PX162-027D5V, nominal 1-6 vDC output for range 0 - 27.65 in. w.c.

D.4.2 Differential Pressure Transducer Calibration

The pressure transducers were calibrated against a U-tube and inclined manometer as standards. The inclined manometer was a Dwyer Model 246, 0 - 6 inches water column range with a smallest division of 0.02 inches. For differential pressures greater than 6 inches of water column, the U-tube manometer was employed and its smallest divisions were 0.125 inches.

At least three tests were run for each differential pressure transducer and their results averaged. A differential pressure between the ports of the transducer was created by use a squeeze bulb (similar to those used in blood pressure measurement) connected to port P2 and a manometer. Port P1 was left unconnected and sensed room pressure. Similarly the other end of the manometer was open to atmospheric pressure in the room. Thus the differential pressure indicated by the manometer was the same as the differential pressure between ports P1 and P2 of the transducer. The differential pressure was systematically increased. The output voltages were recorded as they were displayed via the data acquisition system.

A linear calibration curve was generated for each of the four transducers by a least-squares fit of the measured differential pressure to the average voltage output of the transducer. The calibration curves are presented in Figures 54, 55, 56 and 57.

D.5 Airflow Measurement

D.5.1 Venturi Meter Specifications

Mass flow rate of axial air delivered to the rotor thermal test rig was measured with a venturi meter. The meter, manufactured by Lambda Square, Inc. was a Model 2300, nominal 3 inch schedule 40 pipe size, 3.0680 inch ID inlet with a 1.4500 inch diameter throat. The meter was of PVC construction and furnished complete with integral inlet and throat static pressure sensing ports. The flow coefficient for the meter is 0.9797 and represents the ratio of true flow rate divided by theoretical flow rate. The mass flow rate of air through the venturi is based on the difference in static pressure between the inlet and throat and the details of the calculation are presented in Appendix F.

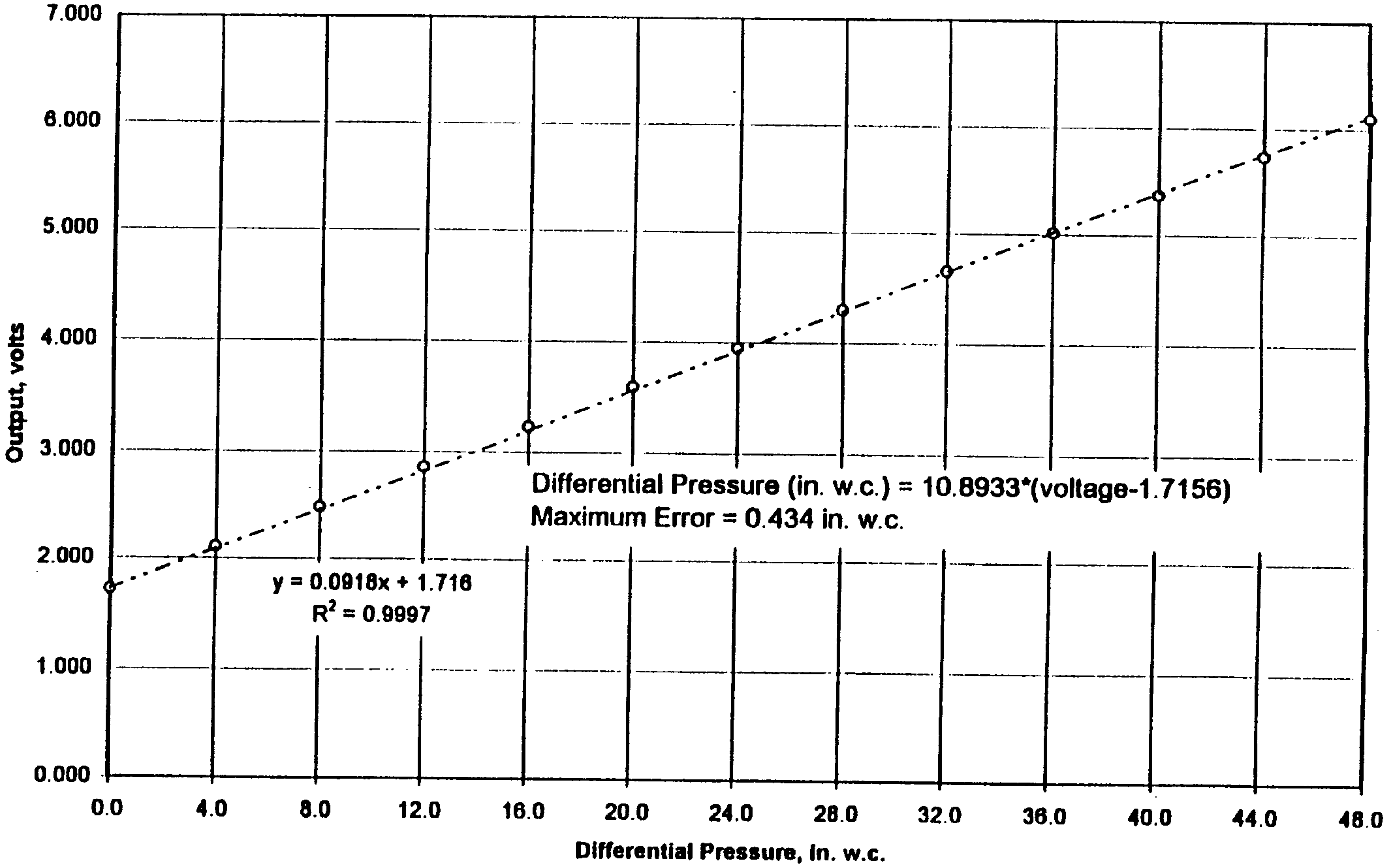

Figure 54: Input 12 Differential Pressure Transducer Calibration Curve PX 163-120D5V; Nominal Range: -7.87 –47.24 Inches Water Column

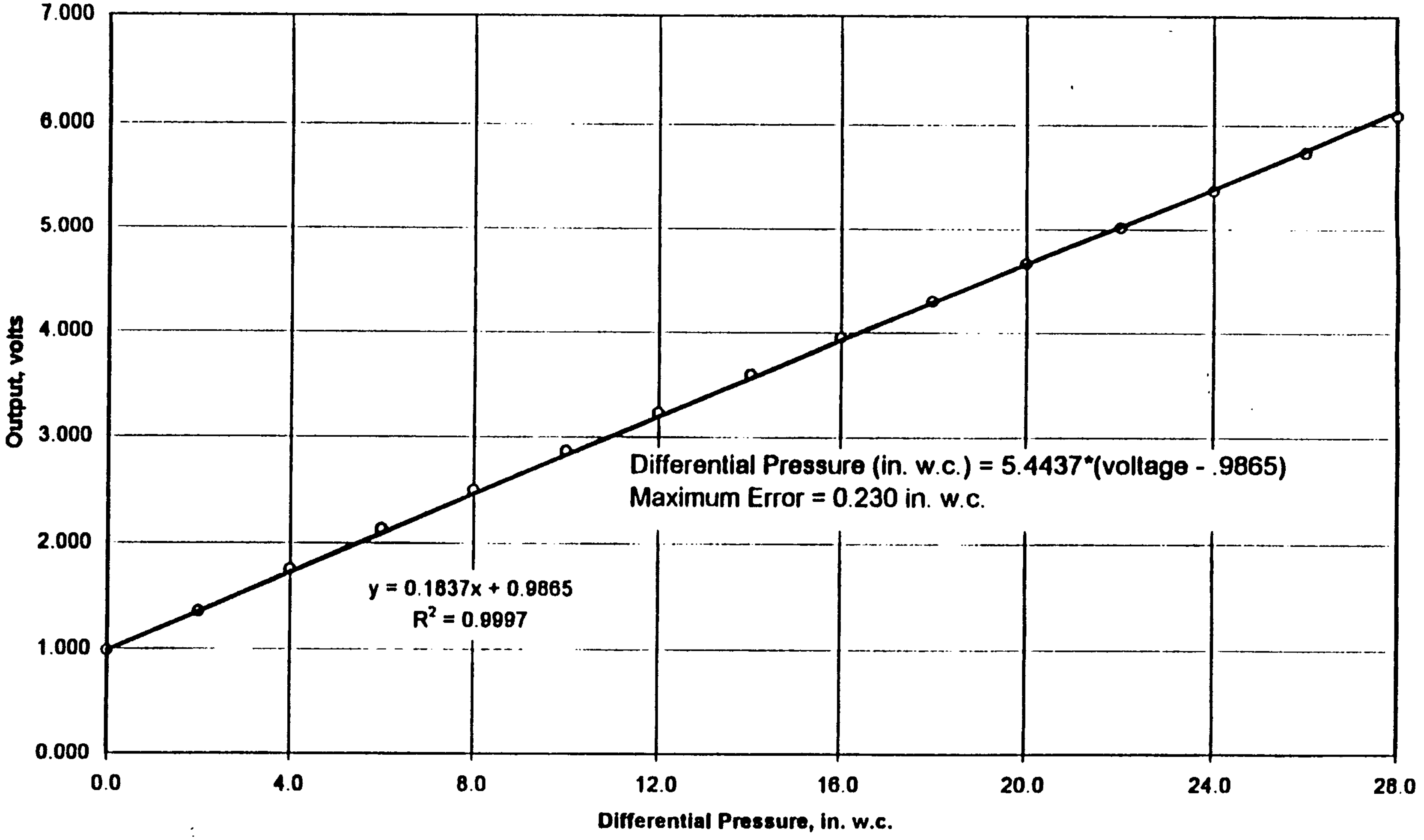

Figure 55: **Input 13 Differential Pressure Transducer Calibration Curve PX 162-027D5V; Nominal Range: 0 - 27.65 Inches Water Column**

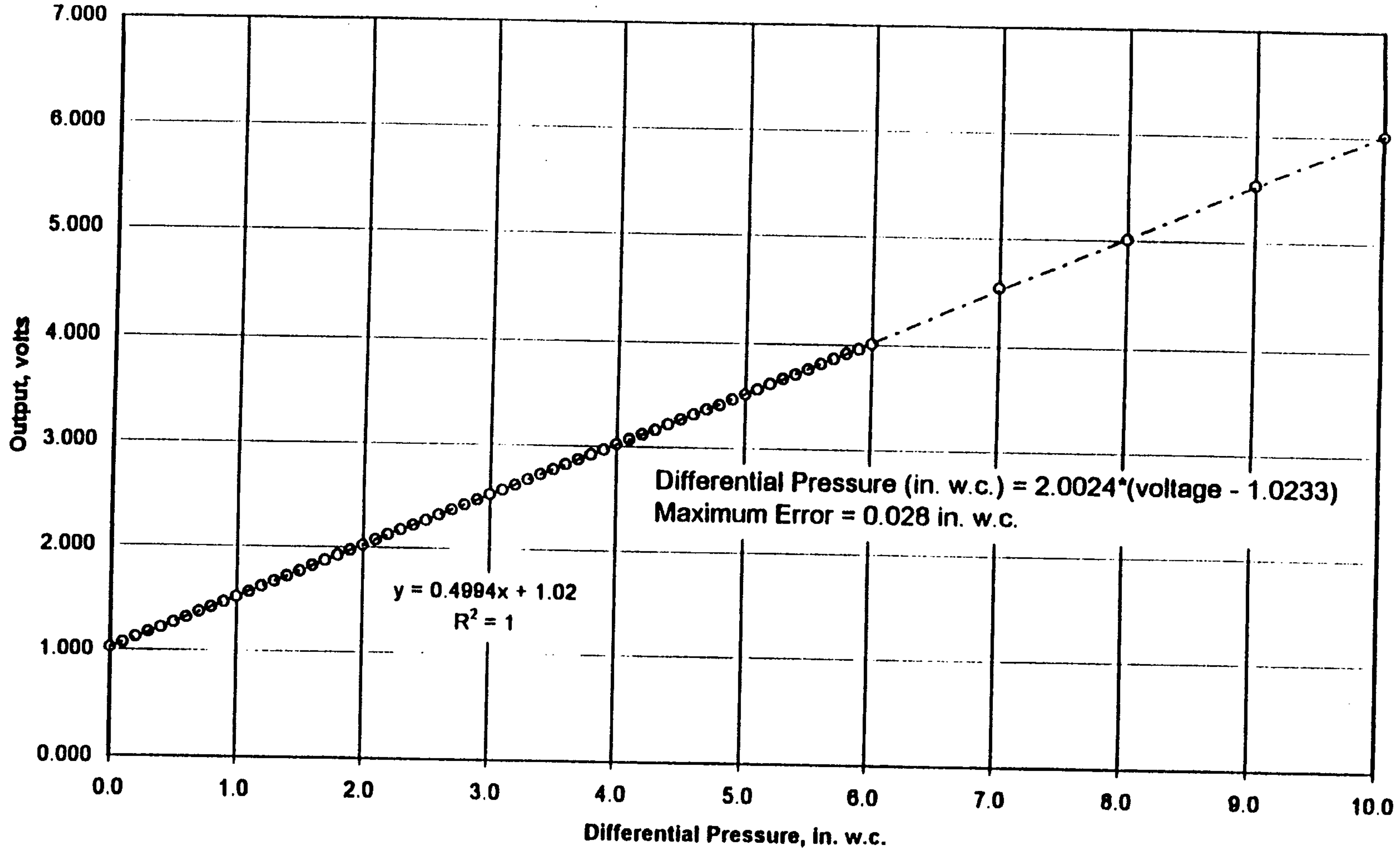

Figure 56: Input 14 Differential Pressure Transducer Calibration Curve PX 164-010D5V; Nominal Range: 0 - 10 Inches Water Column

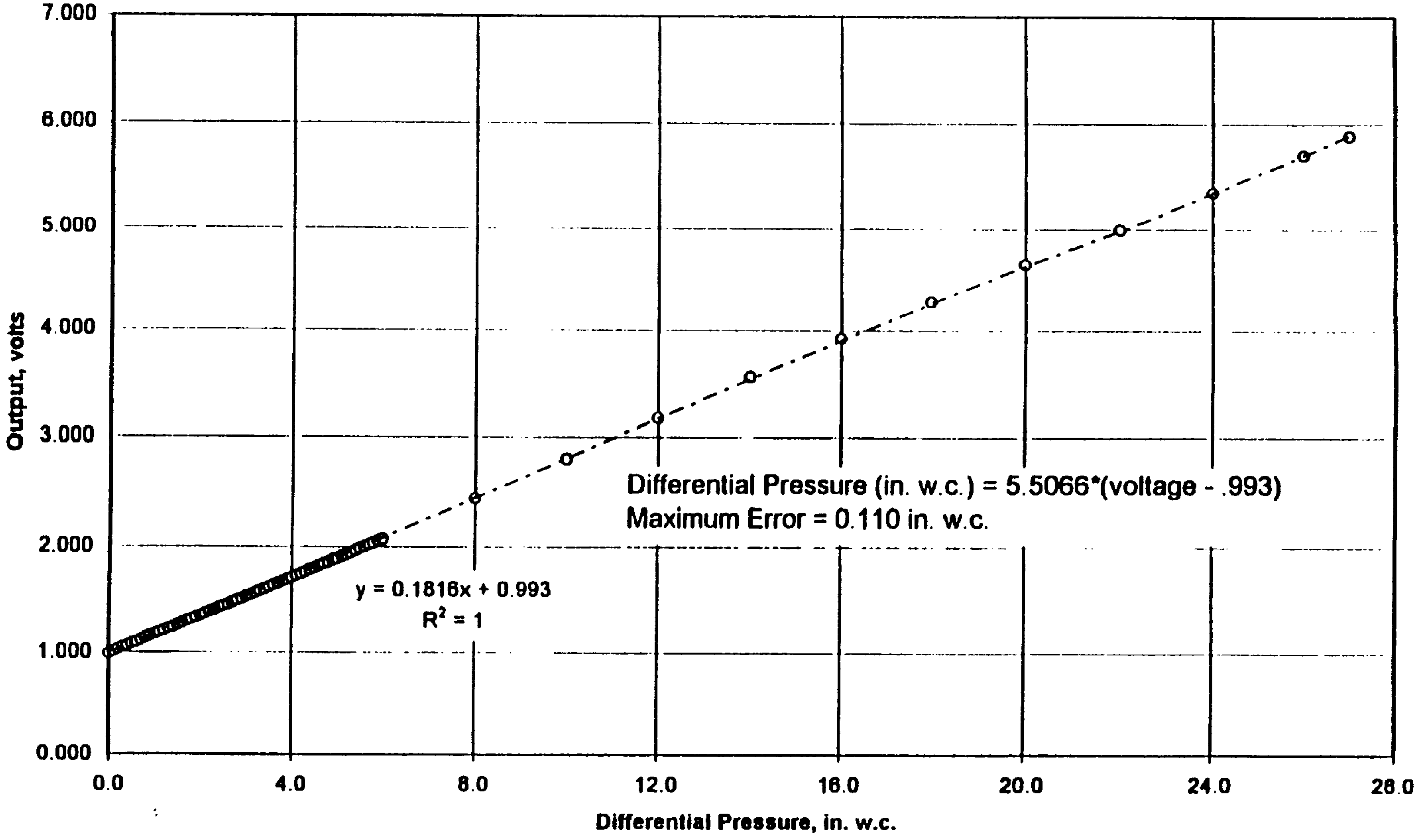

Figure 57: Input 15 Differential Pressure Transducer Calibration Curve PX 162-027D5V; Nominal Range: 0 - 27.65 Inches Water Column

APPENDIX E

ANALYSIS OF HEAT CONDUCTION THROUGH THERMOCOUPLE WIRES

E.1 Introduction

This appendix addresses the accurate measurement of air temperature using thermocouples. Calibration of the thermocouples verified that they are quite accurate. In fact, their deviation from the calibrated reference thermometer that was used as a standard was less than the tolerance of the standard. However, this calibration simply verified that the thermocouples provide an accurate millivolt output corresponding to the temperature of the thermocouple *bead*. During calibration it was easy to assure that the temperature of the thermocouple beads and standard thermometer were the same as the stirred water bath because the convection coefficient associated with forced convection of liquids is high.

Measurement of air temperature requires careful consideration. The temperature indicated by the thermocouple is the temperature of the bead. Care must be taken to minimize the difference between the bead temperature and the air temperature. This is accomplished by using small diameter beads with low thermal mass so that they respond quickly to changes in air temperature. Also, temperature gradients are minimized in the thermocouple wires near the bead so that minimal heat is conducted to/from the beads through the wires.

E.2 Thermocouple Analysis for Measuring Gap Temperature

At the outset of the experiment, it was recognized that the temperature in the annular gap between the rotor pole tip and stator would be of interest since the basis for defining a convective heat transfer coefficient is a reference temperature. Although the measured temperature in the gap may not be the appropriate reference temperature, it is instructive to measure the temperature for consideration as a reference temperature.

The space between the rotor tip and stator wall ranged from 0.027 to 0.035 inches which precluded the direct insertion of a thermocouple. Further, even if a thermocouple were inserted in this small gap, it most certainly would have been damaged during the repeated mounting of the rotors within the stator.

Gap temperature measurement was accomplished by drilling a small 0.062" dia. hole through the stator wall. Centered in this opening at the inner surface of the stator was a 0.027" diameter Type K thermocouple bead. The concept was that rotation of the rotor causes an increase in pressure within the annular gap due to the centrifugal loads applied to the air in the pole cavities. The increased air pressure causes air to flow from the gap region through the hole in the stator wall, over the thermocouple bead centered within the hole, over the thermocouple sheath within the nylon rod and to discharge to the atmosphere. A sketch of the stator wall and thermocouple installation is illustrated in Figure 58.

Figure 58 shows an Omega Engineering KMQSS-040-E thermocouple inserted through a 1/4" nylon rod that is threaded into the aluminum stator. A type K thermocouple was used because chromel and alumel have lower values of thermal

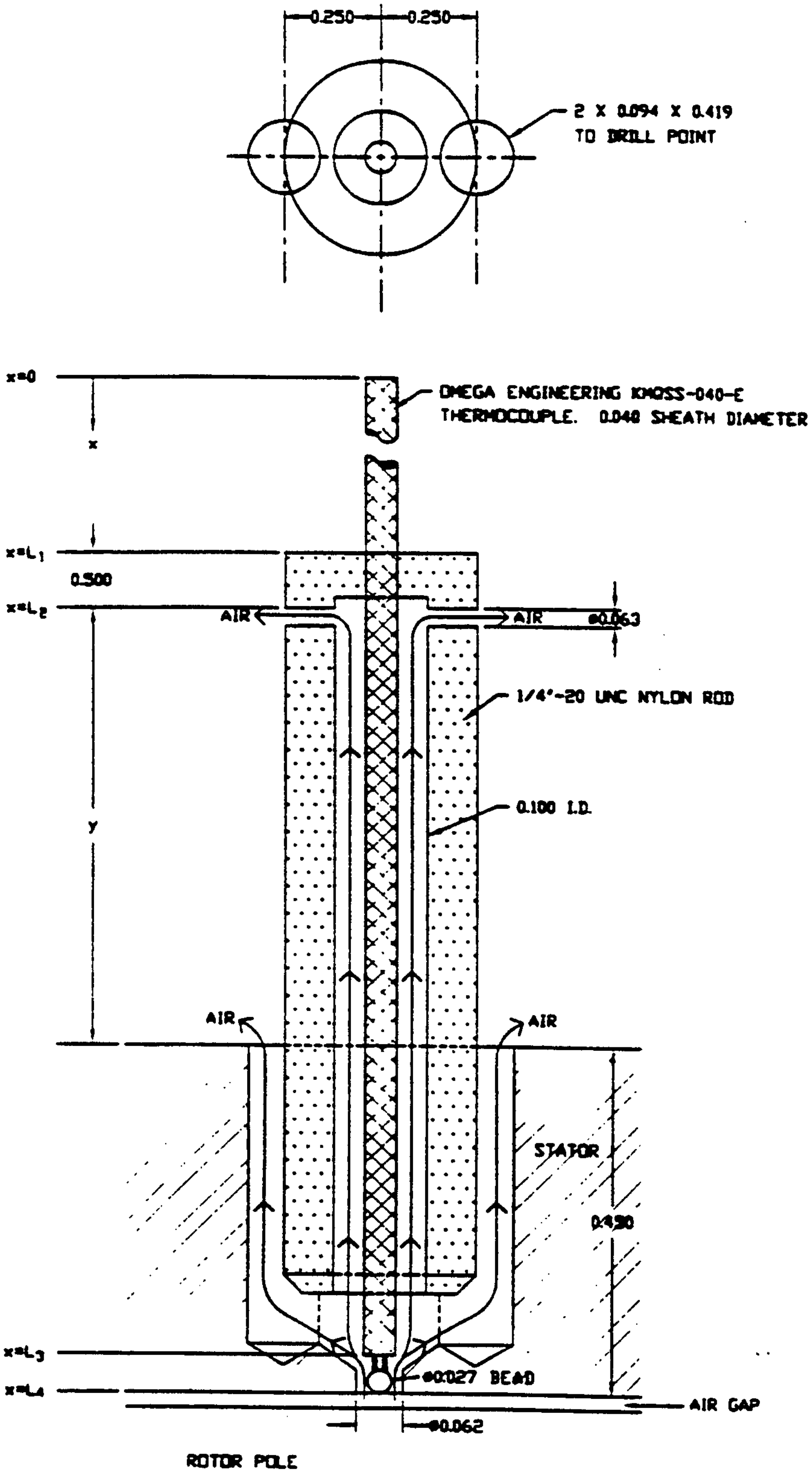
0.250
0.250
2 X 0.094 X 0.419
TO DRILL POINT
x=0
x
OMEGA ENGINEERING KMQSS-040-E
THERMOCOUPLE. 0.040 SHEATH DIAMETER
x=L$_1$
0.500
x=L$_2$
AIR
AIR
Ø0.063
1/4"-20 UNC NYLON ROD
0.100 I.D.
y
AIR
AIR
STATOR
0.430
x=L$_3$
Ø0.027 BEAD
x=L$_4$
AIR GAP
Ø0.062
ROTOR POLE

Figure 58: Thermocouple Installation for Measuring Gap Temperature

conductivity than the copper wires associated with Types J and T. The thermocouple support was carefully designed to minimize conduction of heat from the stator and the ambient air down the thermocouple to the thermocouple bead which would introduce errors in the measurement of the gap temperature. The height, y, above the stator wall where the thermocouple sheath contacts the nylon rod, affects the thermal resistance between these two elements. Also, this height affects the total length of sheath exposed to airflow at temperature, T_{gap}, which minimizes temperature gradients in the thermocouple wires. In general, it is expected that the greater the "y" dimension indicated in Figure 58, the more isolated the thermocouple bead will be from conduction of heat from the stator and the ambient air temperature. As will be seen from the results of the analysis, this is a correct observation.

Note also in Figure 58 that the length of the thermocouple is divided into four regions with the x-axis starting at the top of the thermocouple and ending at the end of the bead.

Goal: Estimate how closely the temperature of the thermocouple bead, T_{bead}, approaches T_{gap}, the temperature of the air flowing over it, in light of the influences of the temperature of the stator, T_{stator}, and the ambient temperature, T_{amb}.

Approach: Develop a one-dimensional mathematical model of heat conduction for each of four segments of the thermocouple with appropriate boundary conditions at the interfaces of the domains. The solution yields a piecewise continuous temperature distribution along the length of the thermocouple as a function of T_{stator} and T_{amb}.

Evaluating the function at $x = L_4$, yields the temperature of the thermocouple bead, T_{bead}.

A graph is then generated that plots the dimensionless parameters: $\frac{T_{gap} - T_{bead}}{T_{gap} - T_{amb}}$ versus $\frac{T_{stator} - T_{amb}}{T_{gap} - T_{amb}}$. It is desired to have $T_{bead} = T_{gap}$ and thus for the ordinate of the graph to be as close to zero as possible.

Assumptions:

1 Steady state analysis.

2. $T = T(x)$ only. (Lumped in the radial direction).

Analysis:

The Omega Engineering KMQSS-040-E thermocouple is a type K thermocouple (0.006" diameter Chromel and Alumel conductor wires). The wires are embedded in MgO insulation within a 0.040" diameter stainless steel sheath. Only a small length of wires are left exposed at the end of the thermocouple along with the bead. A thermodynamic system of infinitesimal length Δx is illustrated in Figure 59 that represents a portion of the thermocouple.

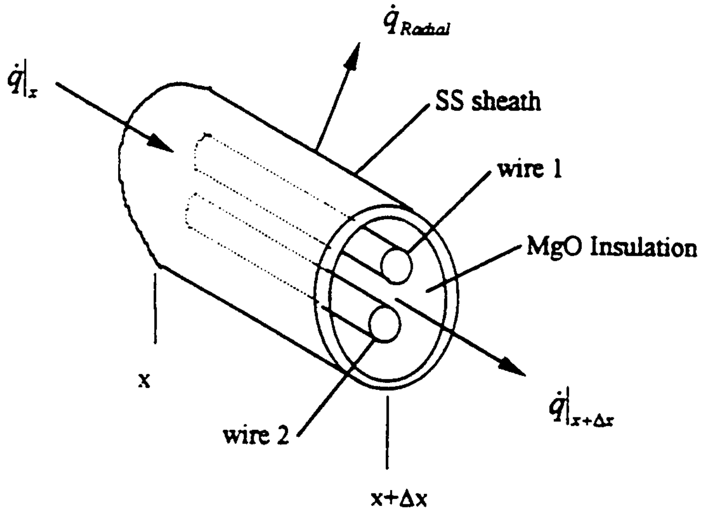

Figure 59: Infinitesimal Thermodynamic System for Thermocouple Analysis

Applying the first law of thermodynamics to this system for steady state yields:

$$\dot{q}_{in} = \dot{q}_{out} \qquad \text{(E-1)}$$

Employing Fourier's Law, this can be written:

$$-kA_c \frac{\partial T}{\partial x}\Big|_x = -kA_c \frac{\partial T}{\partial x}\Big|_{x+\Delta x} + \dot{q}_{radial} \qquad \text{(E-2)}$$

The radial heat loss may be due to convection or conduction, depending on what region of the thermocouple is being considered.

For radial convection to a free stream temperature, T_∞, the radial heat loss can be expressed as:

$$\dot{q}_{radial} = h(2\pi r\, \Delta x)(T - T_\infty) \qquad \text{(E-3)}$$

For radial conduction where the sheath of the thermocouple contacts the nylon threaded rod, the radial heat loss can be written as:

$$\dot{q}_{radial} = \frac{\Delta x \left(T - T_{stator}\right)}{\frac{1}{2\,\pi\,k_{nylon}} \ln\left(\frac{r_{nylon}}{r_{sheath}}\right)} \tag{E-4}$$

The radial heat loss can be generally expressed as:

$$\dot{q}_{radial} = \frac{\Delta x \left(T - T_{ref}\right)}{R} \tag{E-5}$$

where for convection, $R = \frac{1}{2\,\pi\,r\,h}$; $T_{ref} = T_\infty$ (E-6)

and for conduction, $R = \frac{1}{2\,\pi\,k_{nylon}\,\ln\left(\frac{r_{nylon}}{r_{sheath}}\right)}$; $T_{ref} = T_{stator}$. (E-7)

So, the expression for the first law of thermodynamics can be written as:

$$-kA_c \frac{\partial T}{\partial x}\Big|_x = -\,kA_c \frac{\partial T}{\partial x}\Big|_{x+\Delta x} + \frac{\left(T - T_{ref}\right)\Delta x}{R} \tag{E-8}$$

Taking the limit as the length of the infinitesimal system approaches zero yields:

$$\lim_{\Delta x \to 0} \frac{\left[kA_c \frac{\partial T}{\partial x}\Big|_{x+\Delta x} - kA_c \frac{\partial T}{\partial x}\Big|_x\right]}{\Delta x} - \frac{\left(T - T_{ref}\right)}{R} = 0$$

Since the temperature is assumed to be a function of x only, the partial derivatives can be written as total derivatives. Further, if the conduction area, A_c and the thermal conductivity, k, are not considered to be functions of x, the above equation simplifies to:

$$\frac{d^2\,T}{d\,x^2} - \frac{1}{kA_cR}\left(T - T_{ref}\right) = 0 \tag{E-9}$$

Defining $\Theta(x) \equiv T(x) - T_{ref}$, the differential equation can be written as:

$$\frac{d^2\,\Theta}{d\,x^2} - m^2\,\Theta = 0\,. \text{ where } m = +\sqrt{\frac{1}{kA_cR}}\,. \tag{E-10}$$

This differential equation has the general solution: $\Theta(x) = A\,e^{mx} + B\,e^{-mx}$ and the values of the coefficients are determined by the boundary conditions. This solution was applied to each of the four domains of the thermocouple with the following results.

Region 1 **$0 < x < L_1$**

$T_{ref} = T_{amb}$ and $\Theta_1(x) = T_1(x) - T_{amb} = A\,e^{m_1 x} + B\,e^{-m_1 x}$

$$m_1 = \sqrt{\frac{1}{(kA_c)_1 R_1}} \tag{E-11}$$

$$(kA_c)_1 = k_{chromel} A_{chromel\ wire} + k_{alumel} A_{alumel\ wire} + k_{MgO} A_{MgO} + k_{sheath} A_{sheath} \tag{E-12}$$

$R_1 = \dfrac{1}{2\,\pi\,r_{sheath}\,h_1}$ where h_1 is the value of h in region 1. (E-13)

The first Boundary Condition is the assumption that at x = 0, the temperature gradient is zero.

$$\text{B.C. 1: } \left.\frac{\partial T_1}{\partial x}\right|_{x=0} = 0 \tag{E-14}$$

This yields the equation $A - B = 0$ (E-15)

Region 2 **$L_1 < x < L_2$**

$T_{ref} = T_{stator}$ and $\Theta_2(x) = T_2(x) - T_{stator} = C\,e^{m_2 x} + D\,e^{-m_2 x}$

$$m_2 = \sqrt{\frac{1}{(kA_c)_2 R_2}} \tag{E-16}$$

$$(kA_c)_2 = (kA_c)_1 \tag{E-17}$$

$$R_2 \approx \frac{1}{2\,\pi\,k_{nylon}} \ln\left(\frac{r_{nylon}+y}{r_{sheath}}\right) \tag{E-18}$$

B.C. 2: $T_1(L_1) = T_2(L_1)$ Continuity of temperature at the interface. (E-19)

$$A\,e^{m_1 L_1} + B\,e^{-m_1 L_1} - C\,e^{m_2 L_1} - D\,e^{-m_2 L_1} = T_{stator} - T_{amb} \tag{E-20}$$

B.C. 3: $-\left[kA_c \frac{dT_1}{dx}\right]_{x=L_1} = -\left[kA_c \frac{dT_2}{dx}\right]_{x=L_1}$ Continuity of heat flux at the interface. (E-21)

$$A\,m_1\,e^{m_1 L_1} - B\,m_1\,e^{-m_1 L_1} - C\,m_2\,e^{m_2 L_1} + D\,m_2\,e^{-m_2 L_1} = 0 \tag{E-22}$$

Region 3 $\quad$ $L_2 < x < L_3$

$T_{ref} = T_{gap}$ and $\Theta_3(x) = T_3(x) - T_{gap} = E\,e^{m_3 x} + F\,e^{-m_3 x}$

$$m_3 = \sqrt{\frac{1}{(kA_c)_3 R_3}} \tag{E-23}$$

$$(kA_c)_3 = (kA_c)_2 = (kA_c)_1 \tag{E-24}$$

$$R_3 = \frac{1}{2\,\pi\,r_{sheath}\,h_3} \tag{E-25}$$

B.C. 4: $T_2(L_2) = T_3(L_2)$ Continuity of temperature at the interface (E-26)

$$C\,e^{m_2 L_2} + D\,e^{-m_2 L_2} - E\,e^{m_3 L_2} - F\,e^{-m_3 L_2} = T_{gap} - T_{stator} \tag{E-27}$$

B.C. 5: $-\left[kA_c \frac{dT_2}{dx}\right]_{x=L_2} = -\left[kA_c \frac{dT_3}{dx}\right]_{x=L_2}$ (E-28)

$$C\,m_2\,e^{m_2 L_2} - D\,m_2\,e^{-m_2 L_2} - E\,m_3\,e^{m_3 L_2} + F\,m_3\,e^{-m_3 L_2} = 0 \tag{E-29}$$

Region 4 $\quad$ $L_3 < x < L_4$

$T_{ref} = T_{gap}$ and $\Theta_4(x) = T_4(x) - T_{gap} = G\,e^{m_4 x} + H\,e^{-m_4 x}$

$$m_4 = \sqrt{\frac{1}{(kA_c)_4 R_4}} \qquad \text{(E-30)}$$

Here, $(kA_c)_4 = k_{chromel} A_{chromel\ wire} + k_{alumel} A_{alumel\ wire}$ (E-31)

$R_4 = \dfrac{1}{4\,\pi\, r_{sheath}\, h_4}$ (accounts for radial convection from the two exposed wires) (E-32)

B.C. 6: $T_3(L_3) = T_4(L_3)$ Continuity of temperature at the interface (E-33)

$$E\, e^{m_3 L_3} + F\, e^{-m_3 L_3} - G\, e^{m_4 L_3} - H\, e^{-m_4 L_3} = 0 \qquad \text{(E-34)}$$

B.C. 7: Equate the heat flux at the interface between Region 3 and Region 4.

$$-(kA_c)_3 \left.\frac{dT_3}{dx}\right|_{x=L_3} = -(kA_c)_4 \left.\frac{dT_4}{dx}\right|_{x=L_3} + h_4\,(A_3 - A_4)\big(T_3(L_3) - T_{gap}\big) \qquad \text{(E-35)}$$

where $A_3 = \pi\, r_{sheath}^2$ and $A_4 = \pi\, r_{wire}^2$

$$\begin{aligned} &E\left[-(kA_c)_3 m_3 - h_4(A_3 - A_4)\right] e^{m_3 L_3} + F\left[-(kA_c)_3 m_3 - h_4(A_3 - A_4)\right] e^{-m_3 L_3} \\ &+G\,(kA_c)_4 m_4\, e^{m_4 L_3} - H\,(kA_c)_4 m_4\, e^{-m_4 L_3} = 0 \end{aligned} \qquad \text{(E-36)}$$

B.C. 8: Analyze the heat flux at the thermocouple bead.

$$\dot{q}_{in} = \dot{q}_{out}$$

$$-(kA_c)_4 \left.\frac{dT_4}{dx}\right|_{x=L_4} = h_b A_b\left[T_4(L_4) - T_{gap}\right] \qquad \text{(E-37)}$$

where h_b = convective film coefficient for the thermocouple bead.

A_b = surface area of the spherical bead = $4\,\pi\, r_b^2$

$$G\left[h_b A_b + (kA_c)_4 m_4\right] e^{m_4 L_4} + H\left[h_b A_b - (kA_c)_4\, m_4\right] e^{-m_4 L_4} = 0 \qquad \text{(E-38)}$$

The boundary conditions generate a set of eight (8) linearly independent equations that can be solved for the eight constant coefficients, A through H. In matrix form,

$$M \bullet \begin{bmatrix} A \\ B \\ C \\ D \\ E \\ F \\ G \\ H \end{bmatrix} = \begin{bmatrix} 0 \\ T_{stator} - T_{amb} \\ 0 \\ T_{gap} - T_{stator} \\ 0 \\ 0 \\ 0 \\ 0 \end{bmatrix} \tag{E-39}$$

where M is the 8 x 8 matrix:

$$M = \begin{bmatrix} 1 & -1 & 0 & 0 & 0 & 0 & 0 & 0 \\ e^{m_1 L_1} & e^{-m_1 L_1} & -e^{m_2 L_1} & -e^{-m_2 L_1} & 0 & 0 & 0 & 0 \\ m_1 e^{m_1 L_1} & -m_1 e^{-m_1 L_1} & -m_2 e^{m_2 L_1} & m_2 e^{-m_2 L_1} & 0 & 0 & 0 & 0 \\ 0 & 0 & e^{m_2 L_2} & e^{-m_2 L_2} & -e^{-m_3 L_2} & -e^{-m_3 L_2} & 0 & 0 \\ 0 & 0 & m_2 e^{m_2 L_2} & -m_2 e^{-m_2 L_2} & -m_3 e^{m_3 L_2} & m_3 e^{-m_3 L_2} & 0 & 0 \\ 0 & 0 & 0 & 0 & e^{m_3 L_3} & e^{-m_3 L_3} & e^{m_4 L_3} & e^{-m_4 L_3} \\ 0 & 0 & 0 & 0 & \left[-(kA_t)_3 m_3 - h_4 (A_3 - A_4)\right] e^{m_3 L_3} & \left[-(kA_t)_3 m_3 - h_4 (A_3 - A_4)\right] e^{-m_3 L_3} & (kA_t)_4 m_4 e^{m_4 L_3} & -(kA_t)_4 m_4 e^{-m_4 L_3} \\ 0 & 0 & 0 & 0 & 0 & 0 & \left[h_5 A_5 + (kA_t)_4 m_4\right] e^{m_4 L_4} & \left[h_5 A_5 - (kA_t)_4 m_4\right] e^{-m_4 L_4} \end{bmatrix}$$

The unknown coefficients can then be solved as follows:

$$\begin{bmatrix} A \\ B \\ C \\ D \\ E \\ F \\ G \\ H \end{bmatrix} = M^{-1} \bullet \begin{bmatrix} 0 \\ T_{stator} - T_{amb} \\ 0 \\ T_{gap} - T_{stator} \\ 0 \\ 0 \\ 0 \\ 0 \end{bmatrix} \tag{E-40}$$

Since the primary concern is only the temperature of the thermocouple bead, it is only necessary to solve for the coefficients G and H since $T_b = T_4(L_4)$.

$$\begin{bmatrix} A \\ B \\ C \\ D \\ E \\ F \\ G \\ H \end{bmatrix} = \begin{bmatrix} - & - & - & - & - & - & - & - \\ - & - & - & - & - & - & - & - \\ - & - & - & - & - & - & - & - \\ - & - & - & - & - & - & - & - \\ - & - & - & - & - & - & - & - \\ - & - & - & - & - & - & - & - \\ - & Q & - & R & - & - & - & - \\ - & S & - & U & - & - & - & - \end{bmatrix} \begin{bmatrix} 0 \\ T_{stator} - T_{amb} \\ 0 \\ T_{gap} - T_{stator} \\ 0 \\ 0 \\ 0 \\ 0 \end{bmatrix} \tag{E-41}$$

To solve for G and H, only the elements Q, R, S and U of M^{-1} need to be evaluated.

Where

$Q = M^{-1}_{7,2}$ $S = M^{-1}_{8,2}$

$R = M^{-1}_{7,4}$ $U = M^{-1}_{8,4}$

$$G = Q\,(T_{stator} - T_{amb}) + R\,(T_{gap} - T_{stator}) \tag{E-42}$$

$$H = S\,(T_{stator} - T_{amb}) + U\,(T_{gap} - T_{stator}) \tag{E-43}$$

$$\begin{aligned} \Theta_4(L_4) = T_b - T_{gap} &= \left[Q\,(T_{stator} - T_{amb}) + R\left(T_{gap} - T_{stator}\right)\right] e^{m_4 L_4} \\ &\quad + \left[S\,(T_{stator} - T_{amb}) + U\left(T_{gap} - T_{stator}\right)\right] e^{-m_4 L_4} \end{aligned} \tag{E-44}$$

Dividing this equation by $\left(T_{gap} - T_{amb}\right)$ gives the dimensionless expression:

$$\frac{T_{bead} - T_{gap}}{T_{gap} - T_{amb}} = \left[Q\,x + R\,(1 - x)\right] e^{m_4 L_4} + \left[S\,x + U\,(1 - x)\right] e^{-m_4 L_4} \tag{E-45}$$

where $x \equiv \dfrac{T_{stator} - T_{amb}}{T_{gap} - T_{amb}}$.

Clearly, the relation between the dimensionless parameters $\frac{T_{bead} - T_{gap}}{T_{gap} - T_{amb}}$ and $\frac{T_{stator} - T_{amb}}{T_{gap} - T_{amb}}$ is linear.

The analysis was performed for the worst case scenario when the rotor speed would be low (5,000 rpm) and the least amount of air would flow past the thermocouple bead. Under these conditions, the film coefficient on the bead and on the sheathed portion inside the nylon rod was estimated to be 16.7 Btu/hr-ft^2-°F. The film coefficient acting on the thermocouple sheath exterior to the nylon was assumed to be 4 Btu/hr-ft^2-°F. The analysis was performed several times to assess the effect of the varying the height, y, of the nylon rod on the results. Figure E-3 is a presentation of the results for values of y ranging from 0 to 1 inch. The goal is for the bead temperature, T_{bead} to approach the gap temperature, T_{gap} and thus the ratio $\frac{T_{bead} - T_{gap}}{T_{gap} - T_{amb}}$ to approach zero.

Clearly, the thermocouple bead more closely approaches the gap temperature as the stator assumes the gap temperature rather than ambient conditions. This would be more likely after an initial data run when the rotor thermal test rig is warmed-up. However, it is desired to sufficiently isolate the thermocouple from the effects of the ambient and stator temperatures such that corrections are not necessary. To this end, the final design utilized a height, y, of 1", assuring that the thermocouple bead temperature was within 0.07% of the gap temperature compared to the ambient temperature.

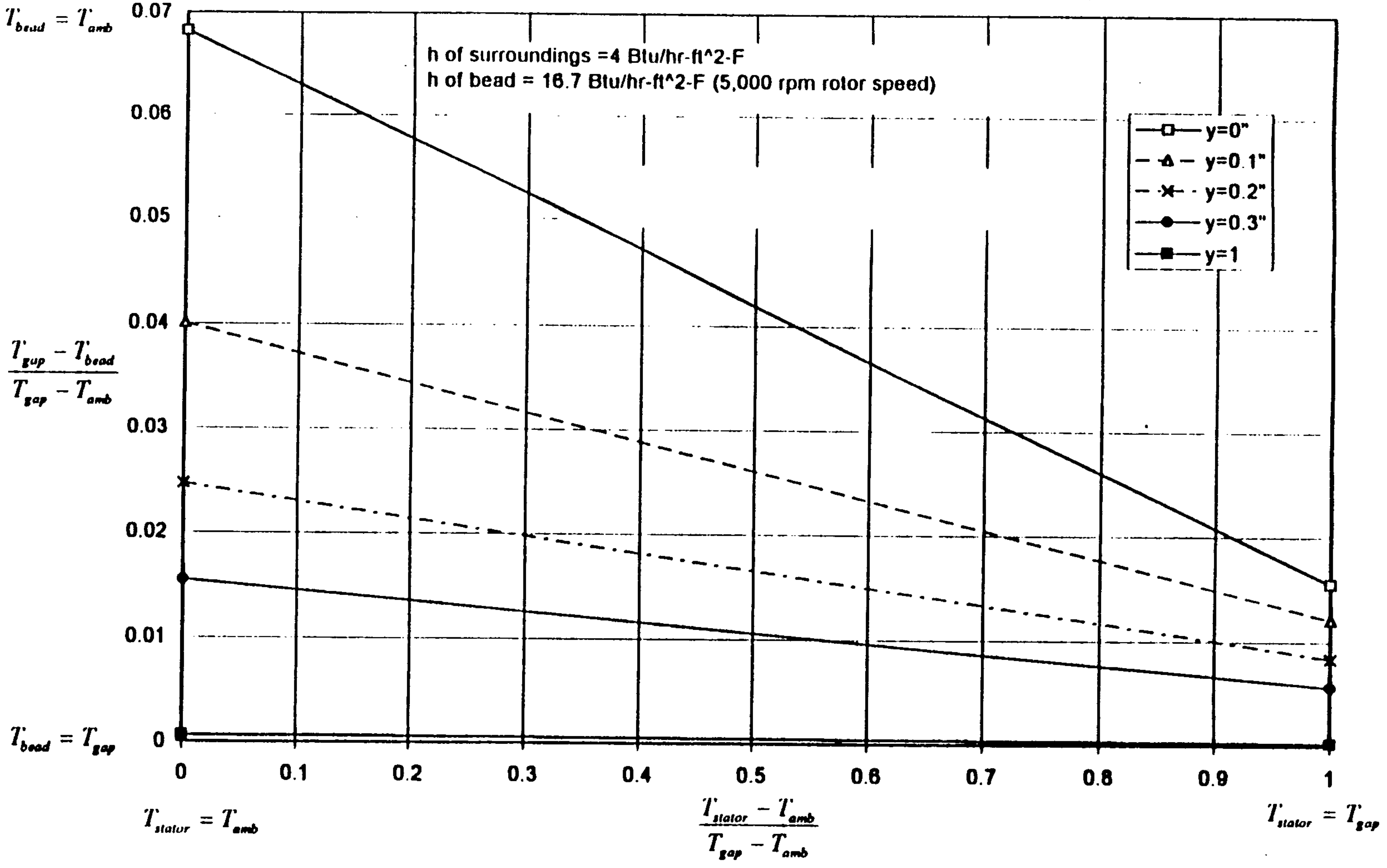

Figure 60: Effect of Stator and Ambient Temperature on Thermocouple Bead Temperature Thermocouple Measuring Gap Temperature

APPENDIX F

CALCULATION OF MASS FLOW RATE OF AXIAL AIRFLOW

A venturi flow meter was used to measure the axial flow rate of air delivered to the rotor thermal test rig. The differential pressure between the inlet and throat of the venturi and the inlet pressure to the venturi were measured with differential pressure transducers. The mass flow rate was calculated using equation 9.107 from Flow Measurement and Engineering Handbook[19]:

$$q_{lbm/s} = \frac{\pi}{4}\left[\frac{2g_c\left(\rho_w\right)_{T,go}}{12^5}\right]^{1/2}\frac{CY_1d_f^2}{\sqrt{1-\left(d_f/D_f\right)^4}}\sqrt{\rho_{f1}}\sqrt{h_w} \qquad \text{(F-1)}$$

The parameters in this equation are defined as follows:

$q_{lbm/s}$	Mass flow rate (lbm/s).
g_c	Dimensional conversion constant, 32.17405 lbm-ft/lbf-s^2.
$\left(\rho_w\right)_{T,go}$	Density of water at standard gravity (32.17405) and any temperature (lbm/ft^3).
C	Discharge coefficient, true flow rate divided by theoretical flow rate. C = 0.9797.
Y_1	Gas expansion factor based on upstream pressure.
d_f	Bore of the venturi at flowing conditions, 1.45 inches.
D_f	Inside pipe diameter at flowing conditions (nominal 3 inch Sch 40 PVC), inside diameter = 3.068 inches.
ρ_{f1}	Upstream density at flowing conditions (lbm/ft^3).
h_w	Differential pressure between inlet and throat (inches of water)

The gas expansion factor, Y_1, accounts for compressibility of the gas and is given in Table 9.26 of Flow Measurement Engineering Handbook as:

$$Y_1 = \left\{ \frac{\left(1-\beta^4\right)\left[k/(k-1)\right]\left(p_{f2}/p_{f1}\right)^{2/k}\left[1-\left(p_{f2}/p_{f1}\right)^{(k-1)/k}\right]}{\left[1-\beta^4\left(p_{f2}/p_{f1}\right)^{2/k}\right]\left(1-p_{f2}/p_{f1}\right)} \right\}^{1/2} \tag{F-2}$$

with the parameters in equation F-2 defined as:

β	Beta ratio d_f/D_f. $\beta = 0.4726$.
k	Isentropic exponent for a real gas. k = 1.4.
p_{f1}	Upstream-tap absolute pressure at flowing conditions (lbf/ft^2).
p_{f2}	Downstream-tap absolute pressure at flowing conditions (lbf/ft^2).

Using equations 9.34 and 9.35 of the Flow Measurement Engineering Handbook, the ratio p_{f2}/p_{f1} can also be expressed based on measured parameters as

$\frac{p_{f2}}{p_{f1}} = 1 - \frac{h_w}{27.73\, p_{f1}}$. For the range of pressures encountered in this experiment, a typical value of Y_1 is 0.9960. I.e. compressibility effects are small.

All of the variables in equation F-1 were measured and recorded by the data acquisition system except for ρ_{f1}. The density at flowing conditions was calculated based on the temperature, pressure and moisture content of the air at the venturi.

Calculation of the density of moist air as a function of pressure and temperature was conducted in accordance with the method presented on page 6.14 of the 1993 ASHRAE Fundamentals Handbook, Chapter 6, Psychometrics. This algorithm calculates moist air properties given dry-bulb temperature, wet-bulb temperature and pressure.

The density ρ of a moist air mixture is the ratio of the total mass to the total volume:

$$\rho = (M_a + M_w)/V = (1/v)(1+W) \tag{F-3}$$

where M_a and M_w are the masses of dry air and water vapor respectively contained in a sample and V is the volume of the sample. The humidity ratio W is defined as the ratio of the mass of water vapor to the mass of dry air contained in the sample and v is the moist air specific volume, ft^3/lbm dry air.

The moist air specific volume is given by:

$$v = \frac{R_a T(1 + 1.6078\,W)}{P} \tag{F-4}$$

where T is the absolute temperature, °R, P is the total pressure (partial pressure of dry air plus partial pressure of water vapor) lbf/ft^2, R_a is the gas constant for air, 53.35 ft-lbf/lbm-°R.

The humidity ratio may be approximated as:

$$W = \frac{(1093 - .556\,t^*)W_s^* - 0.240(t - t^*)}{1093 + .444\,t - t^*} \tag{F-5}$$

where t and t*, the dry bulb and wet bulb temperatures, are in °F. W_s is the saturation humidity ratio evaluated at a temperature, t. W_s^* is the saturation humidity ratio corresponding to saturation at the temperature t*. Note that the humidity ratio, W, does not change from ambient conditions to the conditions at the inlet to the venturi because heating of the air by the axial fan and friction in the ductwork are all sensible heating processes. Therefore, ambient dry-bulb and wet-bulb temperature measurements were made throughout the day as experimental data was collected.. These ambient conditions were used to calculate the humidity ratio. Local values of pressure (atmospheric plus static) and temperature were used in the calculation of density at the venturi.

W_s^* is evaluated using the following relation for W_s and evaluating p_{ws} at the wet bulb temperature t*.

$$W_s^* = \left. \frac{p_{ws}}{p - p_{ws}} \right|_{p_{ws} \text{ evaluated at } t^*} \tag{F-6}$$

The term p_{ws} represents the saturation pressure of water vapor in the absence of air at a given temperature.

The value of p_{ws} , the saturation pressure over liquid water for the temperature range 32 to 392°F, is given by the empirical relation:

$$\ln(p_{ws}) = C_8 / T + C_9 + C_{10}\,T + C_{11}\,T^2 + C_{12}\,T^3 + C_{13}\ln(T) \tag{F-7}$$

The constants in this formula are:

C_8 = -1.044 039 7 E+04

C_9 = -1.129 465 0 E+01

C_{10} = -2.702 235 5 E-02

C_{11} = 1.289 036 0 E-05

C_{12} = -2.478 068 1 E-09

C_{13} = 6.545 967 3

APPENDIX G

DESIGN DRAWINGS

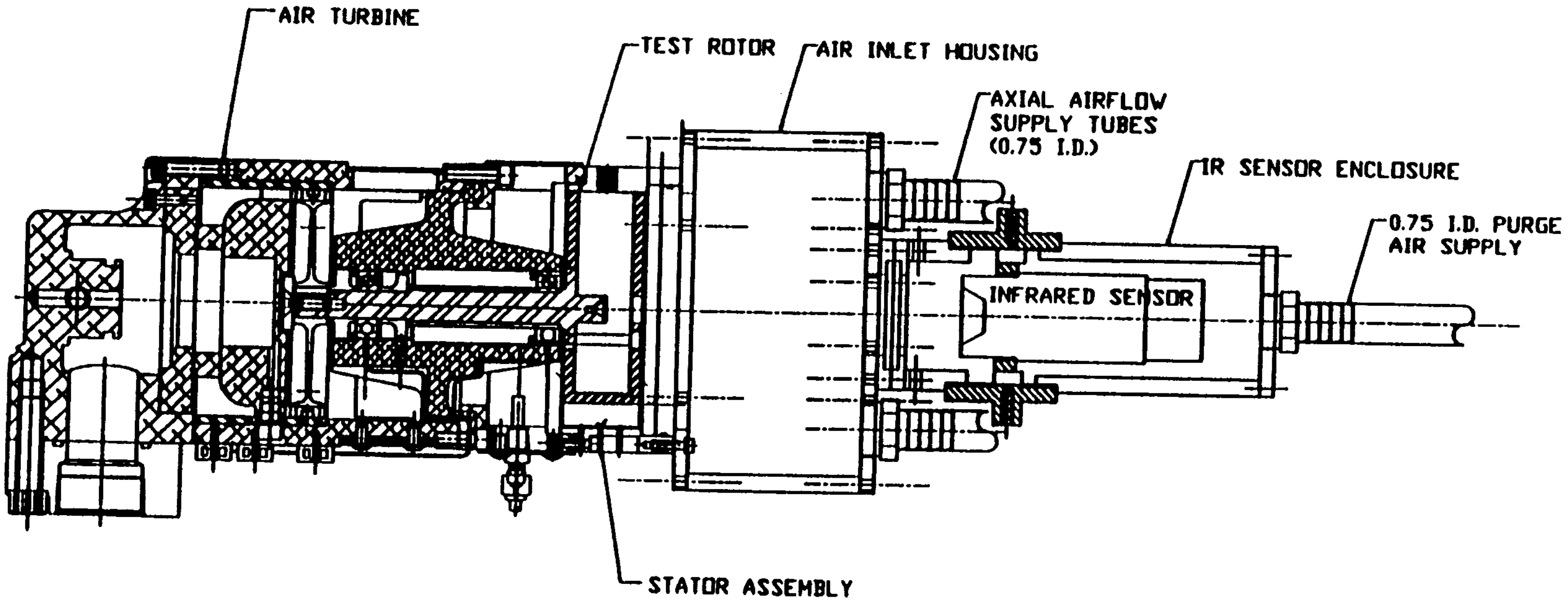
AIR TURBINE
TEST ROTOR
AIR INLET HOUSING
AXIAL AIRFLOW SUPPLY TUBES (0.75 I.D.)
IR SENSOR ENCLOSURE
0.75 I.D. PURGE AIR SUPPLY
INFRARED SENSOR
STATOR ASSEMBLY

Figure 61: Rotor Thermal Test Rig Assembly (Adapted from Tech Development, Inc., Dayton, Ohio)

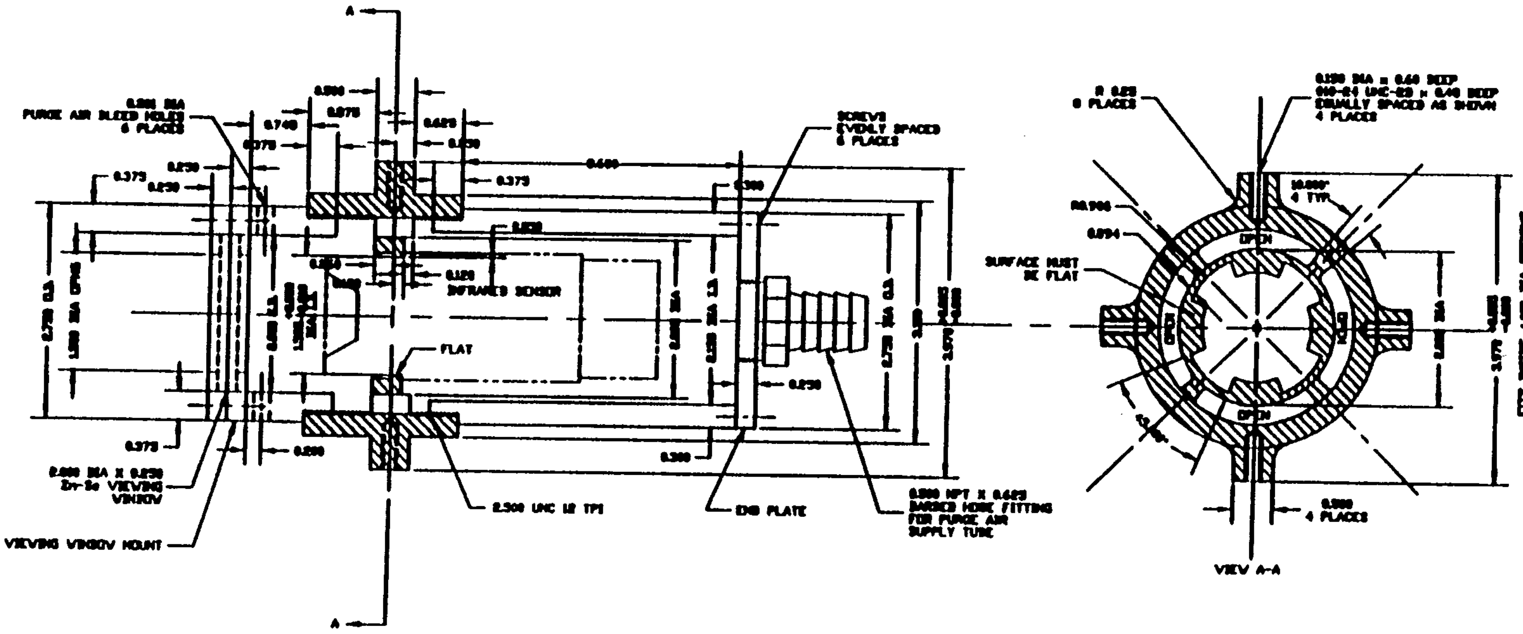
A
0.500
0.875
0.740
0.375
0.625
0.281 DIA
PURGE AIR BLEED HOLES
6 PLACES
0.373
0.250
0.250
0.375
0.400
0.120
INFRARED SENSOR
FLAT
0.375
0.200
2.000 DIA X 0.250
ZnSe VIEWING
WINDOW
VIEWING WINDOW MOUNT
2.500 UNC 12 TPI
SCREWS
EVENLY SPACED
6 PLACES
0.300
0.250
0.300
END PLATE
0.500 NPT X 0.625
BARBED HOSE FITTING
FOR PURGE AIR
SUPPLY TUBE
R 0.25
8 PLACES
R0.906
0.094
SURFACE MUST
BE FLAT
0.150 DIA x 0.40 DEEP
010-24 UNC-2B x 0.40 DEEP
EQUALLY SPACED AS SHOWN
4 PLACES
10.000°
4 TYP
OPEN
OPEN
OPEN
OPEN
0.500
4 PLACES
VIEW A-A
FITS INSIDE 4.000 DIA OPENING
NEED CLOSE TOLERANCE

Figure 62: Infrared Sensor Enclosure

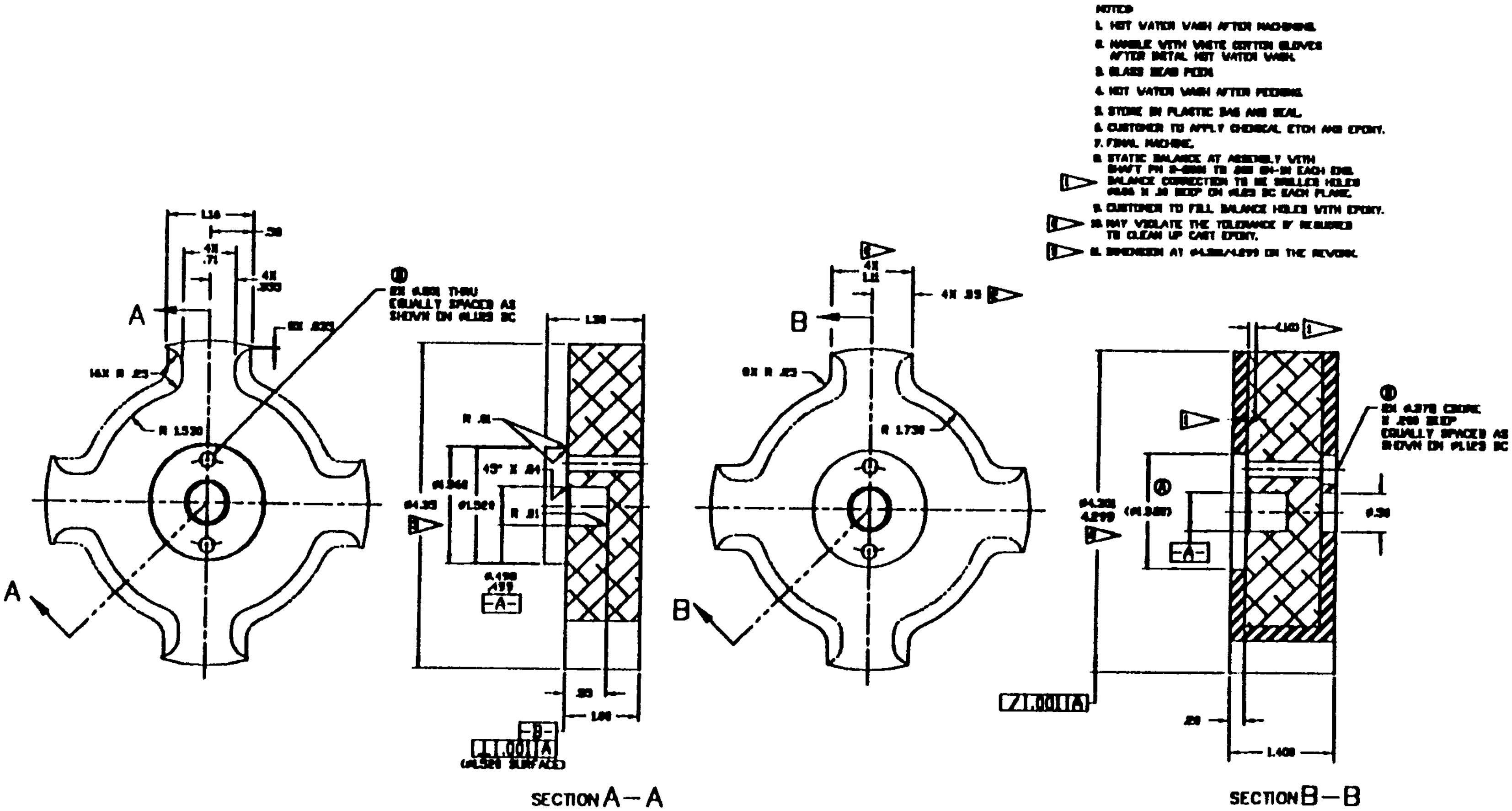
NOTES:
1. HOT WATER WASH AFTER MACHINING.
2. HANDLE WITH WHITE COTTON GLOVES AFTER INITIAL HOT WATER WASH.
3. GLASS BEAD PEEN
4. HOT WATER WASH AFTER PEENING.
5. STORE IN PLASTIC BAG AND SEAL.
6. CUSTOMER TO APPLY CHEMICAL ETCH AND EPOXY.
7. FINAL MACHINE.
8. STATIC BALANCE AT ASSEMBLY WITH SHAFT PN [illegible] TO [illegible] EACH END. BALANCE CORRECTION TO BE DRILLED HOLES [illegible] X .30 DEEP ON [illegible] BC EACH PLANE.
9. CUSTOMER TO FILL BALANCE HOLES WITH EPOXY.
10. MAY VIOLATE THE TOLERANCE IF REQUIRED TO CLEAN UP CAST EPOXY.
11. DIMENSION AT [illegible] ON THE REWORK.
A
A
B
B
16X R .25
R 1.530
8X R .25
R 1.730
4X .35
45° X .04
R .01
R .01
SECTION A—A
SECTION B—B
1.400

Figure 63: Rotor 1 Design Drawing (Adapted from Tech Development, Inc., Dayton, Ohio)

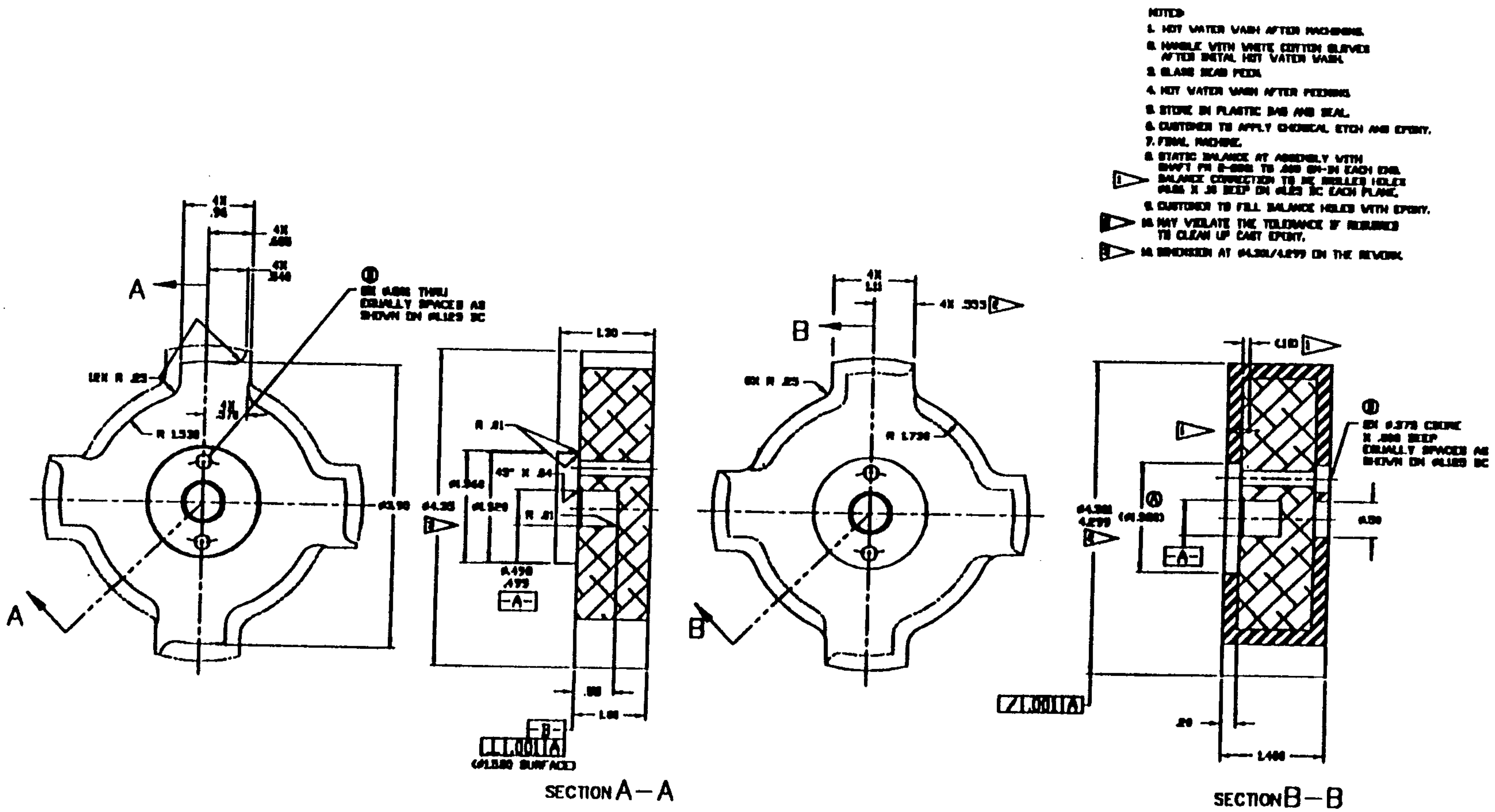
NOTES
1. HOT WATER WASH AFTER MACHINING.
2. HANDLE WITH WHITE COTTON GLOVES AFTER INITIAL HOT WATER WASH.
3. GLASS BEAD PEEN.
4. HOT WATER WASH AFTER PEENING.
5. STORE IN PLASTIC BAG AND SEAL.
6. CUSTOMER TO APPLY CHEMICAL ETCH AND EPOXY.
7. FINAL MACHINE.
8. STATIC BALANCE AT ASSEMBLY WITH SHAFT [illegible] EACH END. BALANCE CORRECTION TO BE DRILLED HOLES Ø.06 X .38 DEEP ON Ø1.23 BC EACH PLANE.
9. CUSTOMER TO FILL BALANCE HOLES WITH EPOXY.
10. MAY VIOLATE THE TOLERANCE IF REQUIRED TO CLEAN UP CAST EPOXY.
11. DIMENSION AT Ø4.301/4.299 ON THE REWORK.
A
A
4X .96
4X .486
4X .340
4X .370
12X R .25
R 1.530
8X Ø.086 THRU EQUALLY SPACED AS SHOWN ON Ø1.125 BC
Ø3.90
Ø4.35
1.30
R .01
45° X .04
Ø1.344
Ø1.320
R .01
Ø.498 .497
-A-
.80
1.00
-B-
(Ø1.580 SURFACE)
SECTION A—A
B
B
4X 1.11
4X .555
8X R .25
R 1.730
Ø4.301 4.299
(Ø1.980)
-A-
.110
8X Ø.375 CBORE X .080 DEEP EQUALLY SPACED AS SHOWN ON Ø1.125 BC
.20
1.400
SECTION B—B

Figure 64: Rotor 2 Design Drawing (Adapted from Tech Development, Inc., Dayton, Ohio)

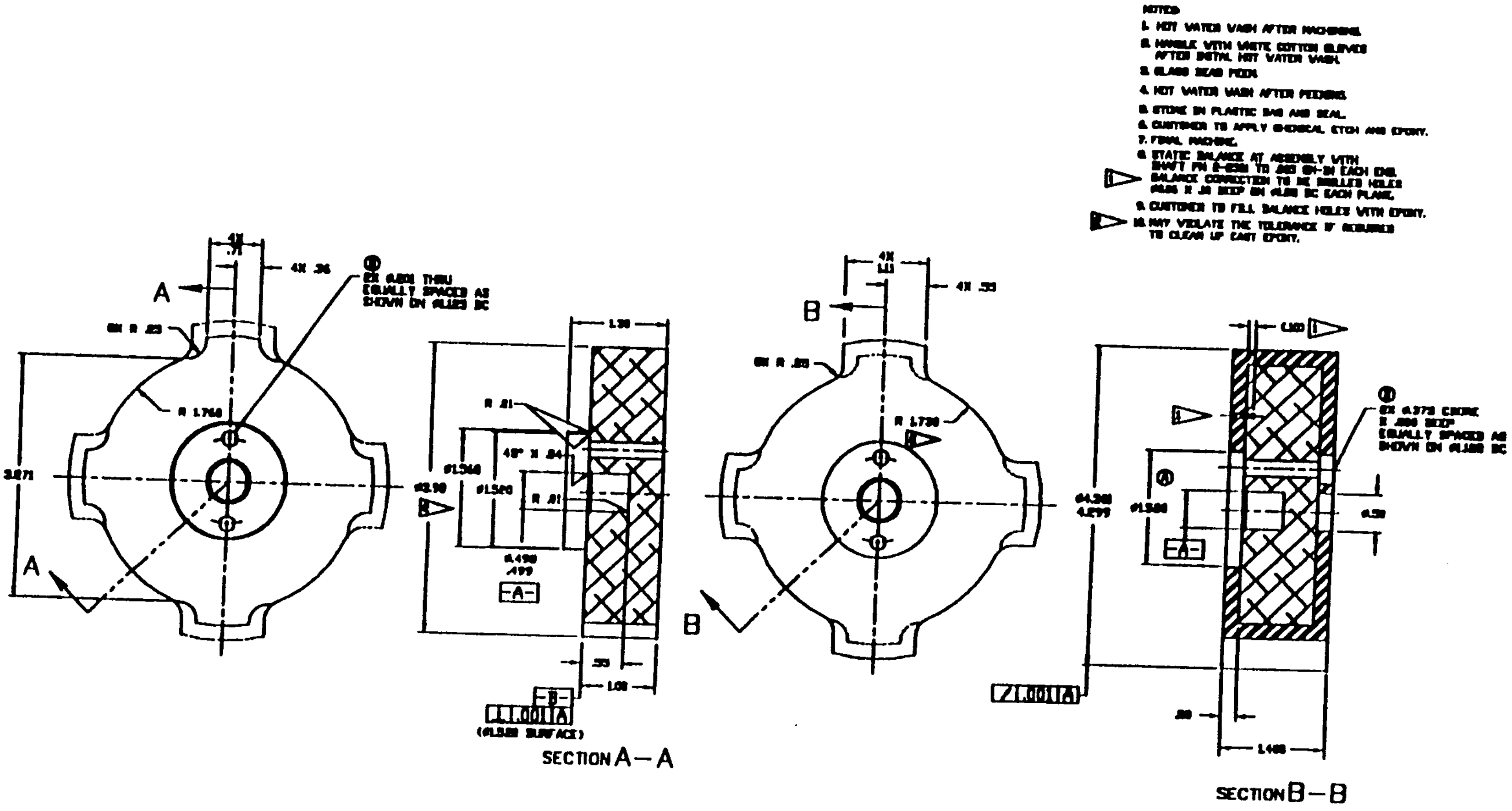

NOTES:
1. HOT WATER WASH AFTER MACHINING.
2. HANDLE WITH WHITE COTTON GLOVES AFTER INITIAL HOT WATER WASH.
3. GLASS BEAD PEEN.
4. HOT WATER WASH AFTER PEENING.
5. STORE IN PLASTIC BAG AND SEAL.
6. CUSTOMER TO APPLY CHEMICAL ETCH AND EPOXY.
7. FINAL MACHINE.
8. STATIC BALANCE AT ASSEMBLY WITH SHAFT PN [illegible] TO [illegible] OZ-IN EACH END. BALANCE CORRECTION TO BE DRILLED HOLES [illegible] X [illegible] DEEP ON [illegible] BC EACH PLANE.
9. CUSTOMER TO FILL BALANCE HOLES WITH EPOXY.
10. MAY VIOLATE THE TOLERANCE IF REQUIRED TO CLEAN UP CAST EPOXY.
A
A
4X .71
4X .36
8X R .03
R 1.744
3.271
EQUALLY SPACED AS SHOWN ON
R .01
45° X .04
Ø1.544
Ø1.520
Ø2.90
R .01
-A-
1.38
.55
1.08
-B-
(Ø1.500 SURFACE)
SECTION A—A
B
B
4X .55
8X R .03
R 1.730
Ø4.300
4.299
Ø1.500
-A-
EQUALLY SPACED AS SHOWN ON
1.400
SECTION B—B

Figure 65: Rotor 3 Design Drawing (Adapted from Tech Development, Inc., Dayton, Ohio)

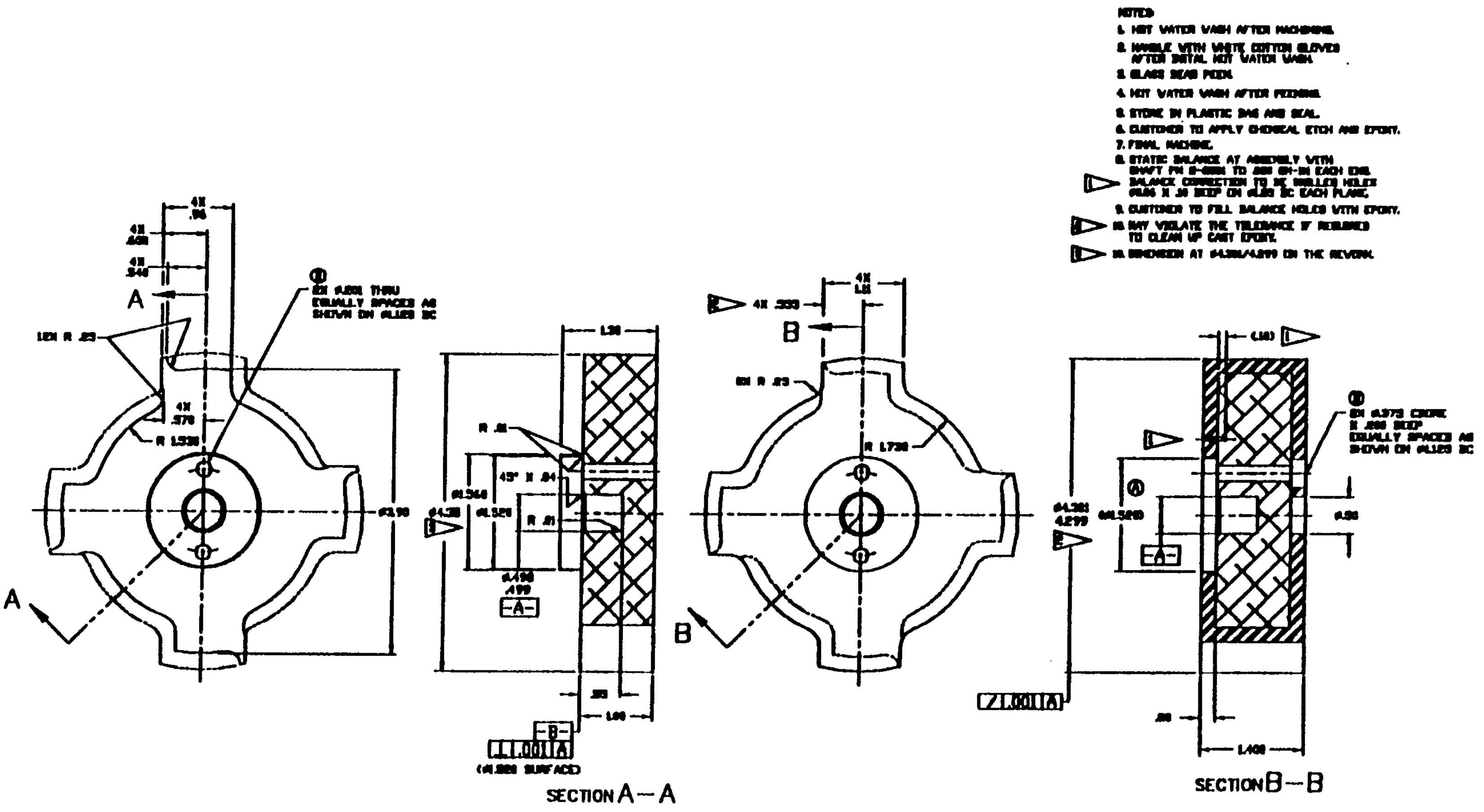
NOTES
1. HOT WATER WASH AFTER MACHINING.
2. HANDLE WITH WHITE COTTON GLOVES AFTER INITIAL HOT WATER WASH.
3. GLASS BEAD PEEN.
4. HOT WATER WASH AFTER PEENING.
5. STORE IN PLASTIC BAG AND SEAL.
6. CUSTOMER TO APPLY CHEMICAL ETCH AND EPOXY.
7. FINAL MACHINE.
8. STATIC BALANCE AT ASSEMBLY WITH SHAFT PN [illegible] TO [illegible] EACH END. BALANCE CORRECTION TO BE DRILLED HOLES [illegible] X .38 DEEP ON [illegible] BC EACH PLANE.
9. CUSTOMER TO FILL BALANCE HOLES WITH EPOXY.
10. MAY VIOLATE THE TOLERANCE IF REQUIRED TO CLEAN UP CAST EPOXY.
11. DIMENSION AT ⌀4.300/4.299 ON THE REVERSE.
A
A
B
B
SECTION A—A
SECTION B—B
R 1.530
R 1.730
⌀3.90
-A-
-B-
(⌀1.000 SURFACE)
45° X .04
1.40
1.400

Figure 66: Rotor 4 Design Drawing (Adapted from Tech Development, Inc., Dayton, Ohio)

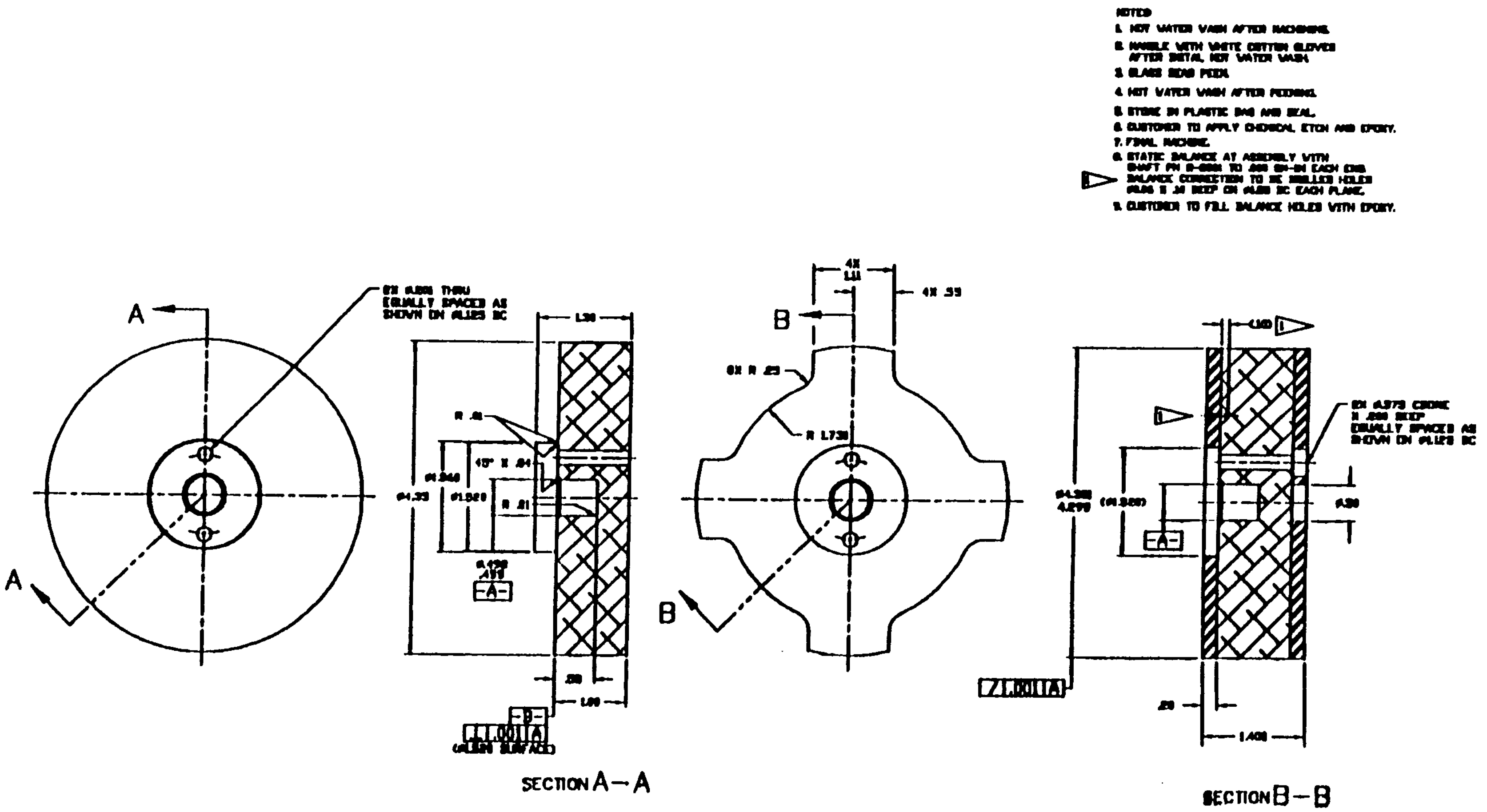
NOTES
1. HOT WATER WASH AFTER MACHINING.
2. HANDLE WITH WHITE COTTON GLOVES AFTER INITIAL HOT WATER WASH.
3. GLASS BEAD PEEN.
4. HOT WATER WASH AFTER PEENING.
5. STORE IN PLASTIC BAG AND SEAL.
6. CUSTOMER TO APPLY CHEMICAL ETCH AND EPOXY.
7. FINAL MACHINE.
8. STATIC BALANCE AT ASSEMBLY WITH SHAFT ... EACH END. BALANCE CORRECTION TO BE DRILLED HOLES ... EACH PLANE.
9. CUSTOMER TO FILL BALANCE HOLES WITH EPOXY.
A
A
EQUALLY SPACED AS SHOWN ON
1.30
45° X .04
⌀4.33
1.00
-B-
-A-
SECTION A—A
B
B
4X .59
8X R .25
R 1.730
(⌀1.500)
-A-
1.400
.25
SECTION B—B

Figure 67: Rotor 5 Design Drawing (Adapted from Tech Development, Inc., Dayton, Ohio)

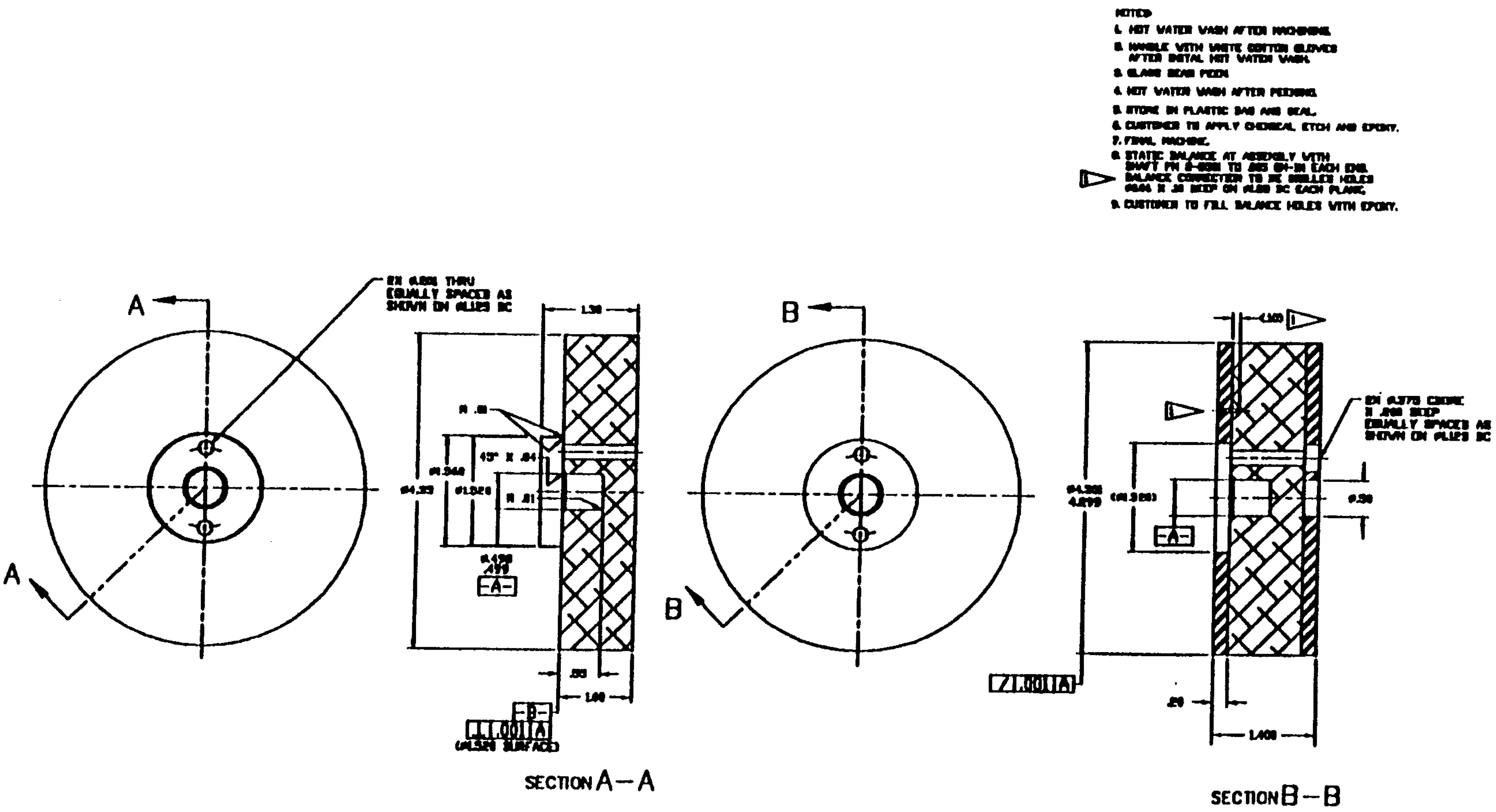
NOTES:
1. HOT WATER WASH AFTER MACHINING.
2. HANDLE WITH WHITE COTTON GLOVES AFTER INITIAL HOT WATER WASH.
3. GLASS BEAD PEEN
4. HOT WATER WASH AFTER PEENING.
5. STORE IN PLASTIC BAG AND SEAL.
6. CUSTOMER TO APPLY CHEMICAL ETCH AND EPOXY.
7. FINAL MACHINE.
8. STATIC BALANCE AT ASSEMBLY WITH
9. CUSTOMER TO FILL BALANCE HOLES WITH EPOXY.
A
A
THRU EQUALLY SPACED AS SHOWN ON BC
1.30
45° X .04
R .01
-A-
-B-
SECTION A—A
B
B
EQUALLY SPACED AS SHOWN ON BC
4.299
.20
1.400
-A-
SECTION B—B

Figure 68: Rotor 6 Design Drawing (Adapted from Tech Development, Inc., Dayton, Ohio)

APPENDIX H

MEASURED GAP SPACING BETWEEN ROTOR POLE TIP AND STATOR

The gap between the rotor pole tip and stator wall was measured for each rotor at four different stator locations and for each of the four pole tips (at 90° intervals for Rotor 6) for a total of 16 measurements for each rotor. Measurements were made by installing the rotor on the shaft and then screwing the stator housing in place. Viewing the front face of the rotor, measurement location were defined as shown in Figure 69.

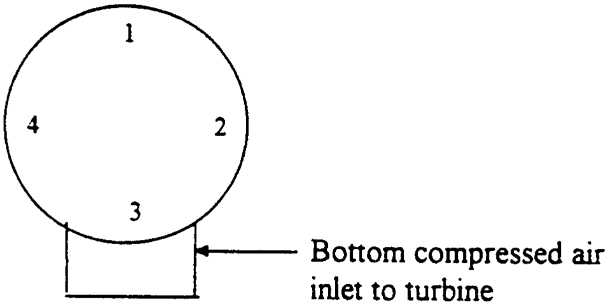

Figure 69: Stator Locations for Rotor Pole Gap Measurements

The results of the measurements are presented in Table 10.

Table 10: Measured Gaps Between Rotor Poles and Stator Wall

(All measurements are in inches)

Rotor	Location 1	Location 2	Location 3	Location 4	Average (16 values)
1	.035	.034	.035	.036	.035
	.033	.034	.036	.036	
	.032	.034	.036	.035	
	.033	.034	.036	.035	
	avg = .033	avg = .034	avg = .036	avg = .036	
2	.033	.033	.033	.033	.033
	.032	.033	.032	.032	
	.033	.033	.033	.033	
	.033	.033	.033	.032	
	avg = .033	avg = .033	avg = .033	avg = .033	
3	.030	.032	.027	.025	.027
	.028	.031	.027	.024	
	.025	.030	.025	.024	
	.028	.031	.025	.024	
	avg = .028	avg = .031	avg = .026	avg = .024	
4	.032	.033	.033	.033	.033
	.032	.033	.033	.033	
	.032	.033	.033	.033	
	.032	.033	.033	.033	
	avg = .032	avg = .033	avg = .033	avg = .033	
5	.024	.027	.028	.028	.027
	.024	.028	.028	.028	
	.025	.028	.028	.028	
	.025	.028	.030	.028	
	avg = .025	avg = .028	avg = .029	avg = .028	
6	.024	.025	.028	.027	.027
	.024	.028	.028	.028	
	.025	.028	.028	.028	
	.024	.028	.028	.028	
	avg = .024	avg = .027	avg = .028	avg = .028	

Measurements were made December 15, 1997.

APPENDIX I

ESTIMATE OF TIME FOR SHAFT HUB AND ROTOR CORE TO REACH THERMAL EQUILIBRIUM

I.1 Introduction

The multi-lump analysis and associated FORTRAN code used in analyzing the experimental data assume that the entire body of the rotor and the shaft hub are at the same temperature at the time the experiment begins. This appendix presents a brief investigation regarding the validity of this assumption.

As discussed in Chapter 3, the rotor is heated in an oven until its temperature is greater than 200°F. It is then mounted on the shaft hub and the RTTR is assembled. The RTTR is then installed in the safety enclosure and the six air lines are connected which provide axial airflow, and the compressed air line is attached to the air turbine. The elapsed time from connecting the rotor to the shaft hub until start of the test is typically 3 minutes. During this time, the hot rotor core and cool shaft hub exchange heat. This analysis estimates the time required for the rotor and shaft hub to reach thermal equilibrium assuming that rotor and shaft hub are taken together as a closed system.

I.2 Analysis

The closed system consists of the aluminum rotor core, epoxy insulation and stainless steel hub. Applying the law of conservation of energy to this system at the initial time and after thermal equilibrium, it is possible to determine the equilibrium temperature.

$$Energy\big|_{t=0} = Energy\big|_{t=final} \tag{I-1}$$

$$\begin{aligned}(\rho\, c_v\, V\, T_{initial})\big|_{epoxy} + (\rho\, c_v\, V\, T_{initial})\big|_{core} + (\rho\, c_v\, V\, T_{initial})\big|_{Hub} = \\ \left[(\rho\, c_v\, V)\big|_{epoxy} + (\rho\, c_v\, V)\big|_{core} + (\rho\, c_v\, V)\big|_{Hub}\right] T_{equilibrium}\end{aligned} \tag{I-2}$$

It is assumed that the initial temperature of the rotor core and epoxy insulation are the same. Substituting the values of thermophysical properties and volumes for the three components, a non-dimensionalized ratio of the equilibrium temperature to the initial temperatures of the rotor core, epoxy insulation and shaft hub is calculated to be:

$$\frac{T_{equilibrium} - T_{hub\ initial}}{T_{core/epoxy\ initial} - T_{hub\ initial}} = 0.975 \tag{I-3}$$

A finite element model of rotor 6 was employed to study the time required to achieve this equilibrium temperature condition. The finite element model was a 1/8th representation of rotor 6 and was comprised of 1,248 solid 8-node brick elements and 1,629 nodes. Node number 1584 represents the back face of the stainless steel hub where it connects to the shaft and is located on the centerline of the rotor and shaft. The temperature history of this node was used to determine the time to achieve steady state.

The hub achieves thermal equilibrium within 40 seconds, well before the start of data collection. Therefore, it is reasonable to assume that the rotor and hub are approximately the same temperature at the start of the test.

APPENDIX J

EXPERIMENTAL VALIDATION OF USING FORWARD BEARING TEMPERATURE AS SHAFT TEMPERATURE

J.1 Introduction

The multi-lump analysis assumes that the temperature of the end of the shaft, element 14, is known at any given time. Because this temperature could not be directly measured, it was assumed to be the same temperature as the forward bearing housing which was monitored by the data acquisition system. This appendix presents the results of an experimental investigation of the validity of this assumption.

J.2 Experiment

For data file r5_05k_2.prn, the data acquisition system was started at the same time that the hot rotor 5 was attached to the shaft hub instead of starting data collection just before supplying compressed air to the turbine. The assembled RTTR was then left with the rotor specimen cooling due to free convection and heat loss conducted through the shaft. The experimental data was analyzed assuming the same value of convection film coefficient applied to all surfaces.

J.3 Analysis

The analysis was performed twice, once with $h = 11$ W/m^2-K (2 Btu/hr-ft^2-°F) and once with $h = 23$ W/m^2-K (4 Btu/hr-ft^2-°F) which are reasonable ranges for the film coefficient for free convection. The data was analyzed between the time period 80 and

130 seconds. The shaft temperature was prescribed to be the measured forward bearing temperature. The results, presented in Figure 70 clearly show that the measured core temperature is bounded by the multi-lump analysis predicted core temperature using the two estimated values of film coefficient.

J.4 Conclusions

This experiment provides a positive indication that the forward bearing temperature may be a reasonable estimate of the shaft temperature. Thus, the FORTRAN program used to analyze the experimental data assumes that the thermal resistance between the shaft and the forward bearing is zero.

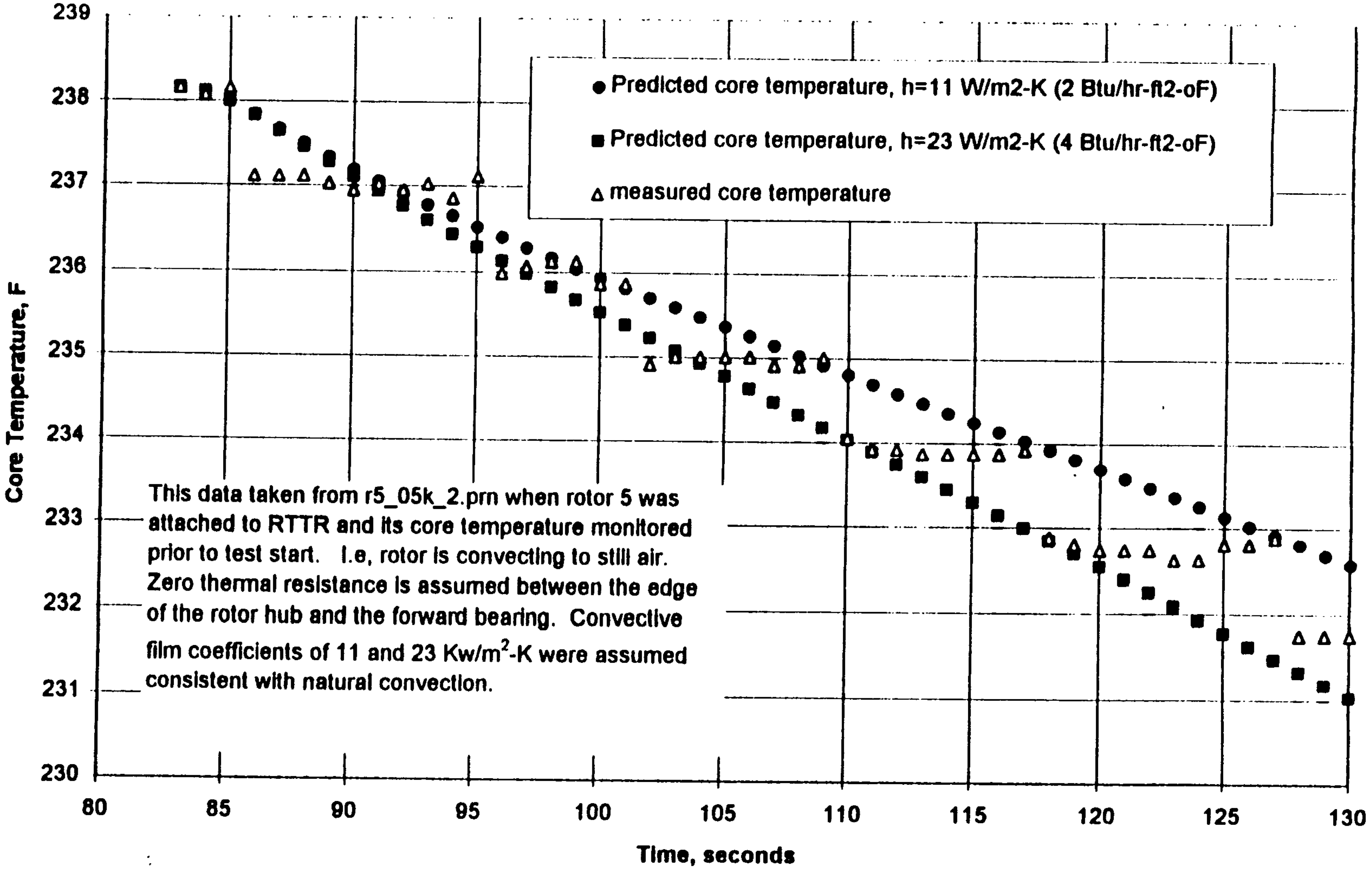

This data taken from r5_05k_2.prn when rotor 5 was attached to RTTR and its core temperature monitored prior to test start. I.e, rotor is convecting to still air. Zero thermal resistance is assumed between the edge of the rotor hub and the forward bearing. Convective film coefficients of 11 and 23 Kw/m^2-K were assumed consistent with natural convection.

Figure 70: Analysis of Thermal Resistance from Shaft to Forward Bearing

APPENDIX K

MATHCAD™ PROGRAM DEVELOPED FOR HIGH SPEED, WALL-DRIVEN FLOW ANALYSIS

Mathcad program used to analyze temperature distribution. adiabatic wall temperature. recovery factors. and film coefficients for high speed wall driven flow

$RPM := 30000$

gap height $h := 0.027 \cdot .0254$ $h = 0.0007$ meters

outer radius $r := 2.15 \cdot .0254$ $r = 0.0546$ meters

$\omega := 2 \cdot \pi \cdot \frac{RPM}{60}$ $\omega = 3141.5927$ rad/s

$V := r \cdot \omega$ $V = 171.5624$ m/s Tip speed

$U := \frac{V}{2}$ $U = 85.7812$ m/s "free-stream velocity"

Air properties at 343K (158 F)

$\rho := 1.0291$ Density, kg/m^3

$\nu := 19.89 \cdot 10^{-6}$ Kinematic viscosity m^2/s

$k := 29.21 \cdot 10^{-3}$ Thermal conductivity W/(m-K)

$Cp := 1.008 \cdot 10^{3}$ Specific heat J/(Kg-K)

$\alpha := \frac{k}{\rho \cdot Cp}$ Thermal diffusivity m^2/s

$\alpha = 2.8159 \cdot 10^{-5}$ m^2/s

$Prt := 0.85$ Turbulent Prandtl number

$\tau := 0.0225 \cdot \rho \cdot U^2 \cdot \left(\frac{\frac{h}{2} \cdot U}{\nu} \right)^{-.25}$ Estimate wall shear stress using Blasius Relation

$\tau = 27.4753$ N/m^2

$edot := \tau \cdot V$ $edot = 4713.7339$ W/m^2 Viscous energy dissipated due to shear work

$u\tau := \sqrt{\frac{\tau}{\rho}}$ $u\tau = 5.1671$ m/s Friction or shear velocity

$\delta = 4.4777 \cdot 10^{-5}$ Thickness of viscous sublayers such that the speed at y=h is equal to the tip speed. V

$TR := 400$ Arbitrary assignment of the rotor temperature. K (260 F)

Equations describing velocity and temperature fields of air in gap region

Region 1:

$$T1(y,qR) := TR - \frac{edot}{4\cdot\alpha\cdot\rho\cdot Cp}\cdot\frac{y^2}{\delta} - \frac{qR\cdot y}{\alpha\cdot\rho\cdot Cp}$$

$$u1(y) := \frac{\tau}{\rho\cdot\nu}\cdot y$$

Region 2:

$$A := \frac{1}{2.44}\cdot u\tau$$

$$T2(y,qR) := \left(\frac{qR}{\rho\cdot Cp} + \frac{edot}{2\cdot\rho\cdot Cp}\right)\cdot\frac{Prt}{A}\cdot\ln\left(\frac{\delta}{y}\right) - T1(\delta,qR)$$

$$u2(y) := 2.44\cdot u\tau\cdot\ln\left(\frac{y}{\delta}\right) + u1(\delta)$$

Region 3:

$$T3(y,qR) := \left(\frac{qR}{\rho\cdot Cp} + \frac{edot}{2\cdot\rho\cdot Cp}\right)\cdot\frac{Prt}{A}\cdot\ln\left[\frac{h-y}{\left(\frac{h}{2}\right)}\right] + T2\left(\frac{h}{2},qR\right)$$

$$u3(y) := u2\left(\frac{h}{2}\right) + 2.44\cdot u\tau\cdot\ln\left[\frac{h}{2\cdot(h-y)}\right]$$

Region 4

$$T4(y,qR) := \frac{edot}{2\cdot\rho\cdot Cp\cdot\alpha\cdot\delta}\cdot\left(h\cdot y - \frac{y^2}{2}\right) - \frac{qR + edot}{\rho\cdot Cp\cdot\alpha}\cdot y + T3(h-\delta,qR) + \frac{qR + edot}{\rho\cdot Cp\cdot\alpha}\cdot(h-\delta) - \frac{edot}{2\cdot\rho\cdot Cp\cdot\alpha\cdot\delta}\cdot\left[h\cdot\right.$$

$$u4(y) := -\frac{\tau}{\rho\cdot\nu}\cdot(h-y) + u3(h-\delta) + \frac{\tau}{\rho\cdot\nu}\cdot\delta$$

$$T(y,qR) := \begin{cases} T1(y,qR) & \text{if } 0 \le y \le \delta \\ T2(y,qR) & \text{if } \delta < y \le \frac{h}{2} \\ T3(y,qR) & \text{if } \frac{h}{2} < y \le (h-\delta) \\ T4(y,qR) & \text{if } (h-\delta) < y \le h \end{cases}$$

$$u(y) := \begin{cases} u1(y) & \text{if } 0 \le y \le \delta \\ u2(y) & \text{if } \delta < y \le \frac{h}{2} \\ u3(y) & \text{if } \frac{h}{2} < y \le (h-\delta) \\ u4(y) & \text{if } (h-\delta) < y \le h \end{cases}$$

$u(h) = 171.5403$ Need to check to assure that u(h) = V. If not, adjust viscous sublayer thickness, δ, until they match

$Tm(qR) := \frac{1}{h} \cdot \int_0^h T(y,qR)\,dy$ Definition of Mixed Temperature

$$Tavg(qR) := \frac{T(0,qR) + T(h,qR)}{2}$$

$rc1 := \dfrac{(T(0,0) - Tavg(0)) \cdot 2 \cdot Cp}{u\left(\frac{h}{2}\right)^2}$ Definition of r_c recovery factor $rc1 = 1.4989$

$rc2 := \dfrac{(T(0,0) - Tm(0)) \cdot 2 \cdot Cp}{u\left(\frac{h}{2}\right)^2}$ Definition of r_c recovery factor $rc2 = 1.0255$

$Taw(qR) := Tm(qR) + rc2 \cdot \dfrac{u\left(\frac{h}{2}\right)^2}{2 \cdot Cp}$ Definition of adiabatic wall temperature

$$\mathrm{rotorfilm}(qR) := \frac{qR}{T(0,qR) - \mathrm{Taw}(qR)}$$

Definition of film coefficients for rotor and stator. Note that they use adiabatic wall temperature as reference.

$$\mathrm{statorfilm}(qR) := \frac{qR + \mathrm{edot}}{\mathrm{Taw}(qR) - T(h,qR)}$$

$$\mathrm{aero}(qR) := \mathrm{Taw}(qR) - \mathrm{Tm}(qR)$$

$qR := 0, 250 .. 500$ Heat loss from rotor, W/m2-K

$qS(qR) := qR + \mathrm{edot}$ Heat gain to stator, W/m2-K

$rc1 = 1.4989$ $\quad \mathrm{aero1} := rc1 \cdot \dfrac{u\left(\frac{h}{2}\right)^2}{2 \cdot Cp}$ $\quad \mathrm{aero1} = 5.4695$ K $\quad \mathrm{aero1} \cdot 1.8 = 9.845$ F

$rc2 = 1.0255$ $\quad \mathrm{aero2} := rc2 \cdot \dfrac{u\left(\frac{h}{2}\right)^2}{2 \cdot Cp}$ $\quad \mathrm{aero2} = 3.7421$ K $\quad \mathrm{aero2} \cdot 1.8 = 6.7357$ F

W/m2	W/m2	K	K	K	K	K	W/(m2-K)	K
qR	qS(qR)	T(0,qR)	Taw(qR)	T(h,qR)	Tavg(qR)	Tm(qR)	rotorfilm(qR)	aero(qR)
0	4713.7339	400	400	389.0611	394.5305	396.2579	0	3.7421
250	4963.7339	400	399.4198	387.9007	393.9504	395.6778	430.9133	3.7421
500	5213.7339	400	398.8397	386.7404	393.3702	395.0976	430.9133	3.7421

$\mathrm{rotorfilm}(500) = 430.9133$

$\mathrm{statorfilm}(500) = 430.9133$

Note that the film coefficient for the rotor and stator are equal independent of the heat fluxes associated with the rotor and stator

$\dfrac{\mathrm{rotorfilm}(500)}{5.677} = 75.9051$ Film coefficient, Btu/hr-ft2-oF